Doctoral theses at NTNU, 2019:190

Yuna Zhao

Numerical Modeling and Dynamic Analysis of Offshore Wind Turbine Blade Installation

Yuna Zhao

Doctoral Thesis

ISBN 978-82-326-3976-2 (printed version)
ISBN 978-82-326-3977-9 (electronic version)
ISSN 1503-8181

Doctoral theses at NTNU, 2019:190

NTNU
Norwegian University of
Science and Technology
Faculty of Engineering
Department of Marine Technology

NTNU
Norwegian University of
Science and Technology

NTNU

NTNU
Norwegian University of
Science and Technology

Yuna Zhao

Numerical Modeling and Dynamic Analysis of Offshore Wind Turbine Blade Installation

Thesis for the degree of Philosophiae Doctor

Trondheim, June 2019

Norwegian University of Science and Technology
Faculty of Engineering
Department of Marine Technology

NTNU
Norwegian University of
Science and Technology

NTNU
Norwegian University of Science and Technology

Thesis for the degree of Philosophiae Doctor

Faculty of Engineering
Department of Marine Technology

ISBN 978-82-326-3976-2 (printed version)
ISBN 978-82-326-3977-9 (electronic version)
ISSN 1503-8181

Doctoral theses at NTNU, 2019:190

Printed by Skipnes Kommunikasjon as

Abstract

Installing offshore wind turbine blades is very challenging and risky due to large lifting height and high required installation precision. Offshore single blade installation is frequently adopted because of small deck space requirement. Current practice in the industry is to install offshore wind turbine blades by jack-up crane vessels in shallow waters. The typical operational environmental condition is mean wind speed less than 10m/s and significant wave height lower than 1.5∼2m. Compared with jack-up crane vessels, floating ones are flexible with respect to operational water depth and efficiency in relocation. The latter might be an alternative for installing offshore wind turbine blades, especially in intermediate and deep waters.

Numerical studies of the critical operational scenarios during the planning phase is important aid for planning and execution of a safe and efficient installation. During offshore single blade installation, the final blade mating operation is generally considered to be the critical phase. To assess the dynamic responses of offshore single blade installation systems during mating operations, coupled simulation methods that account for blade aerodynamics, vessel hydrodynamics and crane flexibilities are needed, but are currently limited.

In this thesis, a fully coupled method, SIMO-RIFLEX-Aero, is established for numerical modeling and analysis of offshore single blade installation by jack-up or floating crane vessels. It can account for blade aerodynamics, vessel hydrodynamics, structural dynamics and wire coupling mechanics. The leg-soil interaction is also considered for jack-up vessels. The blade aerodynamic loads are calculated in the Aero code developed in this study based on the instantaneous blade displacement and velocity according to the cross-flow principle.

The coupled method is used to study offshore single blade installation of the DTU 10 MW wind turbine blade by a typical jack-up crane vessel. The jack-up crane vessel is modeled in details with consideration of wave loads on the legs, wind loads on the hull, structural flexibility of legs and crane, as well as soil-leg interaction. The wave-induced vessel motion and crane flexibility are found to have significant influence on the blade motion. The influence is dependent on site-specific parameters such as soil properties. Detailed modeling of soil behavior using linear springs with dampers is recommended. Simple models using pinned or fixed foundations lead to large overestimation and underestimation of blade motion, respectively, which may affect estimation of operational safety and efficiency.

A preliminary feasibility study on single blade installation by using large

floating crane vessels is carried out, by comparing their performance with a typical jack-up crane vessel. Two typical floating crane vessels are considered, i.e., a mono-hull and a semi-submersible. They are assumed to be equipped with DP systems that can well eliminate their slowing varying horizontal motions. The results indicate that single blade installation by floating vessels is feasible. The feasibility depends on vessel type and size, as well as site conditions. The semi-submersible vessel is more feasible than the mono-hull vessel. However, the life cycle cost versus benefit needs further assessment. The efficiency of floating vessel installation is higher in short wave conditions. Utilization of weather orientation for floating vessels can greatly reduce the installed blade motion and thus reduce the operational cost.

Allowable operational limits in terms of environmental conditions are also evaluated for single blade installation by the semi-submersible crane vessel. They, together with weather forecasts, can assist the planning and decision-making during the execution of installation operation. The critical events, limiting parameters and criteria are firstly identified. The critical events are excessive radial motion of the blade root or bent guide pins at blade root. The corresponding limiting parameters are radial motion and radial impact velocity at the blade root, respectively. For instance, the impact criterion to avoid bent guide pins at blade root which is related to the radial impact velocity, is determined based on nonlinear finite element analysis. Slacks in tugger lines should be avoided and are considered as restrictive events. Fully coupled time domain simulations are then conducted to estimate the characteristic values of the limiting parameters. The operational limits, in terms of wind and wave conditions, are thus derived by using response-based criteria. The impact criterion is considered to be conservative since the turbine hub is assumed to be rigid.

In summary, the author develops a fully coupled method for numerical modeling and analysis of single blade installation and conducts a systematic study on installation by jack-up and floating crane vessels. The coupled method can also be used to investigate demounting or replacing offshore wind turbine blades and can be extended to study installation of rotor, and fully assembled tower-rotor-nacelle for offshore wind turbines. In practice, it can be utilized to assist the planning and execution phases of installation and to develop simulators for personnel training.

Preface

This thesis is submitted to the Norwegian University of Science and Technology (NTNU) for partial fulfilment of the requirements for the degree of philosophiae doctor.

This doctoral work has been performed at the Centre for Autonomous Marine Operations and Systems (AMOS), Department of Marine Technology, NTNU, Trondheim, with Professor Torgeir Moan as main supervisor and with co-supervisors Professor Zhen Gao at Department of Marine Technology, NTNU and Peter Christian Sandvik at SINTEF Ocean.

I was financially supported by a scholarship from China Scholarship Council (CSC) from August 2014 to July 2018, which is greatly appreciated. Moreover, I also acknowledge the financial support from Equinor (previously Statoil) to attend academic conferences.

Acknowledgement

I would like to express my sincere thanks to my supervisor Prof. Torgeir Moan. He gave me the opportunity to pursue my PhD study at the Department of Marine Technology, NTNU. I also appreciate his illuminating guidance and instructions for my PhD work, and the opportunities to present my work on various occasions.

I would also like to thank my co-supervisor Prof. Zhen Gao, for his valuable guidance on my work and generous support on cooperations and communications with industrial and academic professionals.

I would like to extend my gratitude to my co-supervisor Peter Christian Sandvik. He gave me careful guidance on modeling of marine operations and provided valuable discussions about my research.

I am thankful to my colleagues Dr. Zhengshun Cheng and Amrit Shankar Verma, as well as Eric Van Buren from Fred Olsen Windcarrier for their nice collaboration. I also appreciate Zhengshun's help with coding and proofreading of papers.

Many other people have contributed to my work. Dr. Jingzhe Jin from SINTEF Ocean and Mr. Petter Faye Søyland from Fred Olsen Windcarrier are acknowledged for valuable discussions. Many thanks to Mr. Mahmoud Etemaddar for detailed discussions and valuable inputs on wind turbine installation. Thanks are also extended to Drs. Lin Li, Wilson Guachamin Acero, Chenyu Luan and Wei Chai for valuable discussions.

There are also a great number of friends and colleagues who brighten the days at Tyholt and color life in Trondheim. I cherished the get-togethers, skiing trips, cabin trips, hikings and travelings we had during the last four years. Warm thanks go to Ping and Thomas, for their encouragement and help during my difficult times.

Finally, I want to express my deep gratitude towards my parents and my elder brother for their love, support and understanding. A special thank goes to my boyfriend Zhifei, for his love, companionship and encouragement.

Yuna Zhao
July 2018
Trondheim, Norway

List of Appended Papers and a Report

This thesis consists of an introductory part, five papers and one report. They are given in Appendix A.

Paper 1:
An integrated dynamic analysis method for simulating installation of a single blade for wind turbines.
Authors: Yuna Zhao, Zhengshun Cheng, Peter Christian Sandvik, Zhen Gao, Torgeir Moan
Published in *Ocean Engineering*, 2018, Vol. 152, pp. 72-88.

Paper 2:
Numerical modeling and analysis of the dynamic motion response of an offshore wind turbine blade during installation by a jack-up crane vessel.
Authors: Yuna Zhao, Zhengshun Cheng, Peter Christian Sandvik, Zhen Gao, Torgeir Moan, Eric Van Buren
Published in *Ocean Engineering*, 2018, Vol. 165, pp. 353-364.

Paper 3:
Effect of foundation modeling of a jack-up crane vessel on the dynamic motion response of an offshore wind turbine blade during installation.
Authors: Yuna Zhao, Zhengshun Cheng, Zhen Gao, Torgeir Moan
Published in *Proceedings of the International Offshore Wind Technical Conference (IOWC)*, San Francisco, USA, November 4-7, 2018.

Paper 4:
Numerical study on the feasibility of offshore single blade installation by floating crane vessels.
Authors: Yuna Zhao, Zhengshun Cheng, Zhen Gao, Peter Christian Sandvik, Torgeir Moan
Published in *Marine Structures*, 2019, Vol. 64, pp. 442-462.

Paper 5:
Explicit structural response-based methodology for assessment of operational limits for single blade installation for offshore wind turbines.
Authors: Amrit Shankar Verma, Yuna Zhao, Zhen Gao, Nils Petter Vedvik
Published in *Proceedings of the 4th International Conference in Ocean Engineering (ICOE 2018)*, Chennai, India, February 18-21, 2018.

Report 1:

Assessment of operational limits for offshore single blade installation using response based criteria
Authors: Yuna Zhao, Zhen Gao, Torgeir Moan, Peter Christian Sandvik.
Report, Norwegian University of Science and Technology, 2019.

Declaration of Authorship

All the five papers that serve as the core content of this thesis are co-authored. For *papers 1, 2, 3, and 4*, I was the first author and responsible for initiating ideas, establishing the models, performing the analysis and calculations, providing the results and writing the papers. Dr. Zhengshun Cheng (the second co-author) assisted me in developing the Aero code and provided valuable discussions. Peter Christian Sandvik contributed with his expertise in modeling and analysis of marine operations. Professor Torgeir Moan and Professor Zhen Gao have contributed to the support, corrections and constructive comments to increase the scientific quality of the publications.

Regarding the *paper 5*, I was the second author and responsible for calculating the stochastic responses of the wind turbine blade, analyzing the results, plotting figures and contributing to methods for global dynamic responses. Amrit Shankar Verma initiated the idea and wrote the other parts. Professor Zhen Gao and Professor Nils Petter Vedvik gave valuable comments to this paper.

For the report, I was the first author and did most of the work. Professor Torgeir Moan and Professor Zhen Gao have contributed to the support, corrections and constructive comments to increase the scientific quality of the report.

Additional Paper

The following publication has been produced during the doctoral work but is not included in this thesis because of scope.

Paper 6:

Study on lift-off of offshore wind turbine components from a barge deck with emphasis on snatch loads in crane wire.
Authors: Yuna Zhao, Zhen Gao, Torgeir Moan, Peter Christian Sandvik
Published in *Proceedings of the third Marine Operation Specialty Symposium (MOSS),* National University of Singapore, Singapore, September 20-21, 2016.

Symbols and abbreviations

θ_B Blade initial pitch angle

θ_{wd} Wind incident angle

θ_{wv} Wave incident angle

H_s Significant wave height

$O - XYZ$ Global coordinate system

$O_b - X_bY_bZ_b$ Blade-related coordinate system

$O_v - X_vY_vZ_v$ Vessel-related coordinate system

T_I Turbulence intensity

T_p Wave peak period

U_w Mean wind speed

CFD Computational Fluid Dynamics

COG Center of Gravity

DLL Dynamic Link Library

DNVGL Det Norske Veritas and Germanischer Lloyd

DOF Degree of Freedom

DP Dynamic Positioning

FEM Finite Element Method

GW Gigawatt

HAWC2 Horizontal Axis Wind turbine simulation Code 2nd generation

IEC	International Electrotechnical Commision
ISO	International Orgnisation for Standardization
JONSWAP	Joint North Sea Wave Project
LC	Load case
MW	Megawatt
MWh	Megawatt hour
RAO	Response Amplitude Operator
RNA	Rotor Nacelle Assembly
STD	Standard deviation
TLP	Tension Leg Platform

Contents

xvi

List of Tables

xviii

List of Figures

 xxiv

Chapter 1

Introduction

1.1 Background and motivation

As one of the clean, renewable and reliable energy sources, offshore wind energy has been developing fast in the last decades. By the end of 2017, the global cumulative capacity of offshore wind energy reaches almost 19 GW, which is over three times larger than that in 2011.

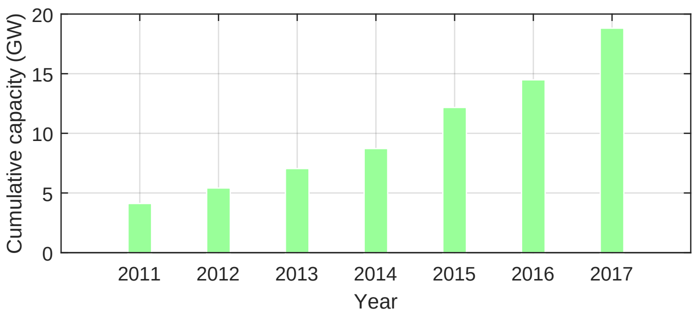

Figure 1.1: Global offshore wind energy annual cumulative capacity [34]

The individual capacity of offshore wind turbines also increases fast, as shown in Figure 1.2. During 2001∼2015, over 80% of offshore wind turbine orders were below 3MW, while there are few orders on this size now. Nowadays, 5MW or larger offshore wind turbines account for more than 50% of the market share [12]. In 2016, 32 8MW wind turbines were successfully installed at Burbo Bank Extension offshore wind farm [73]. In 2018, a 12MW wind turbine design has been announced by GE Renewable Energy [32]. The increase in turbine capacity is closely linked with the increasing turbine size and hub height, as indicated by comparing the properties of

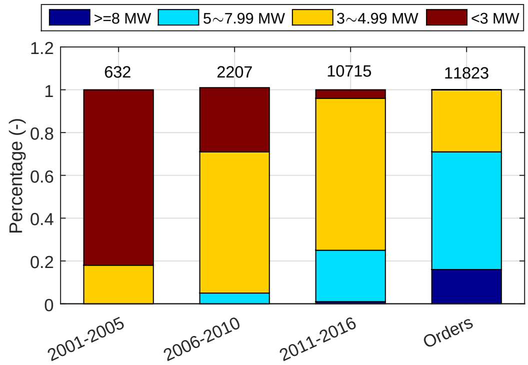

Figure 1.2: Development of offshore wind turbine size based on commercial orders since 2001: segmented by grid connection date. Orders include turbines planned to be installed in 2017 and beyond [12]

blades for various offshore wind turbines in Table 1.1. Such increases add challenges to the installation of offshore wind turbines, requiring larger crane capacity and higher lifting height, and making the installation more sensitive to offshore environmental conditions.

Table 1.1: Offshore wind turbine capacity and blade dimensions

Turbine model	Capacity [MW]	Blade weight [tons]	Blade length [m]	Hub height [m]	Reference wind farm
Bonus B76/2000 [110]	2	6.5	36.5	64	Middelgrunden
Siemens SWT-3.6-107 [93]	3.6	15.8	52	83.5	Burbo Bank
Senvion 5MW [2]	5	20.8	61.5	92	Alpha Ventus
Vestas V164-8.0MW[106]	8	35	80	105	Burbo Bank Extension
DTU 10MW[4]	10	41.7	86.4	119	Research model
Haliade-X 12MW [32]	12	Unknown	107	150	Recently announced

Depending on the water depth, offshore wind turbines are supported by different types of support structures, as shown in Figure 1.3. In shallow waters up to 60m in depth, bottom-fixed supported structures are preferred. Gravity based structures, suction buckets and monopiles are suitable for offshore sites shallower than 40m [72]. Tripods, triples and jackets can be used in water depths up to 60m [11]. The deep water zones are highly attractive to the offshore wind industry due to their potential of much higher power production due to stronger and more stable wind there [6]. Floating support structures are more cost-effective in deep water over 100m. As shown in Figure 1.3, three typical types of floating wind turbines have been widely studied, i.e., TLP [3, 71], semi-submersible [64, 87] and spar [24, 52, 79]. The world's first floating wind farm, i.e., Hywind Scotland, was

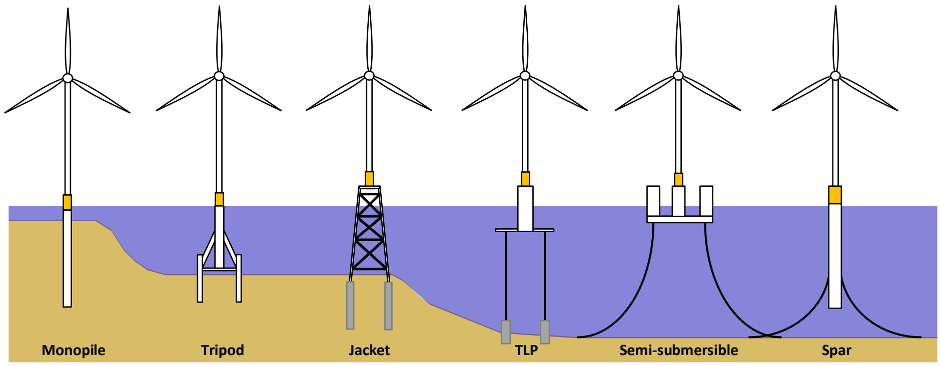

Figure 1.3: Offshore wind turbines supported by different types of support structures in various water depths

installed in 2017 [27], indicating the spar-type support structures entering the market. Until now, the majority of offshore wind turbines are supported by bottom-fixed structures. Monopiles are the dominant support structures with 87% of the market share. Jackets and gravity based support structures account for 9% and 2% respectively [109].

Figure 1.4 shows the average water depth and distance from shore for European offshore wind farms by the end of 2016. Both average water depth and distance to shore of offshore wind farms keep increasing. Distance to shore and water depth are of significant economic importance, because they affect both the investment costs and the operation and maintenance costs [99]. A 10% increase in either water depth or distance to shore will imply a 1% increase in investment costs [54].

The installation is an important phase during the life cycle of every offshore wind turbine. On one hand, the structural integrity of wind turbine components needs to be ensured during installation. On the other hand, the installation cost for offshore wind turbines is very high, accounting for approximately 19% of the total budget which is significantly larger than the 3% for land-based wind turbines [97]. From the technical point of view, the high installation cost is due to the complexity of the operation and the harsh environmental conditions offshore. In addition, the increase in turbine size, water depth and distance from shore add more challenges to the installation, leading to higher cost. Nowadays, there is an urgent need to bring down the installation cost of offshore wind turbines. The significant cost reduction for offshore wind farms in the bidding phase is therefore encouraging [68, 47].

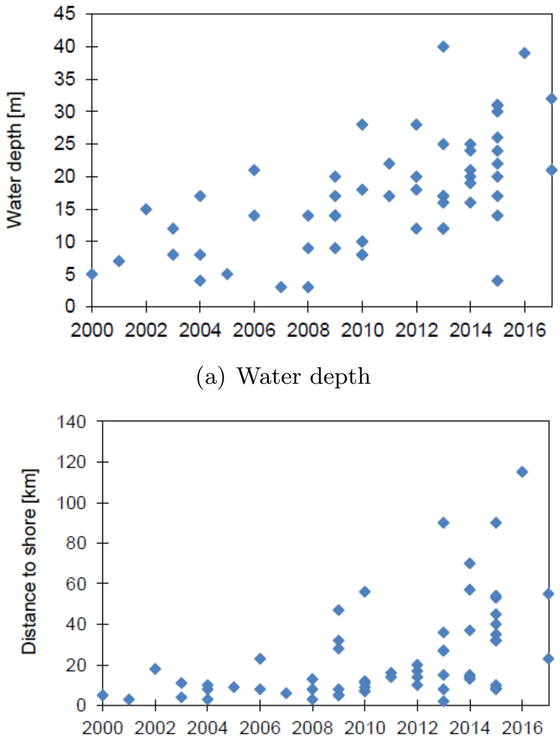

(a) Water depth

(b) Distance to shore

Figure 1.4: Water depth and distance to shore for European offshore wind farms between 2000 and 2016 [54]

1.2 Offshore wind turbine installation methods

At present, the majority of offshore wind turbines are bottom-fixed ones. Thus, offshore installation is necessary. During the installation process, the components of offshore wind turbines including support structures, tower, nacelle and blades, need to be assembled and installed together at the designated offshore location. A review of the current installations methods for offshore bottom-fixed wind turbines is summarized in this section. Most of these methods are dependent on offshore lifting using crane vessels, which is also commonly used for installations in the oil and gas industry [8, 40, 58, 67].

Support structures

The installation methods of support structures are dependent on the structure types.

Monopiles are generally being upended and lowered to the sea bed by crane vessels, either jack-up or floating ones [41]. Before installation, they are traditionally transported on the deck of crane vessels [88]. To reduce the operational cost, it is also common to transport them on the deck of barges. With the fast increase of monopiles' size and weight, wet-towing of monopiles with capped ends is used to ease the demand of larger crane vessels.

Jackets and tripods are normally transported on the deck of crane vessels or transportation barges. Upon arrival at the offshore site, they are lifted and installed by the on-board crane.

Gravity-based structures are very heavy, the mass of which can be over 2800 tons [28]. Using crane vessels to lift them is a challenge due to limited crane capacities. Thus, they are generally being towed to the offshore sites, and ballasted and lowered into the prepared seabed.

(a) (b) (c)

Figure 1.5: Installation of bottom-fixed offshore wind turbine support structures (a) monopile upending operation [88]; (b) jacket lifting operation [13]; (c) gravity-based structure towing operation [89].

Turbines

Different from support structures, the turbine components can only be dry-transported, either on the crane vessel or by transportation barges. The installation of turbines offshore is mainly based on lifting operations by crane vessels, mostly jack-up crane vessels for bottom-fixed wind turbines [76]. There are many alternative methods for turbine installation, depending on the number of lifts for per turbine, as shown in Figure 1.6.

The cost-effectiveness of those installation methods is dependent on the turbine size, crane vessel size and capacity, and distance from port to off-

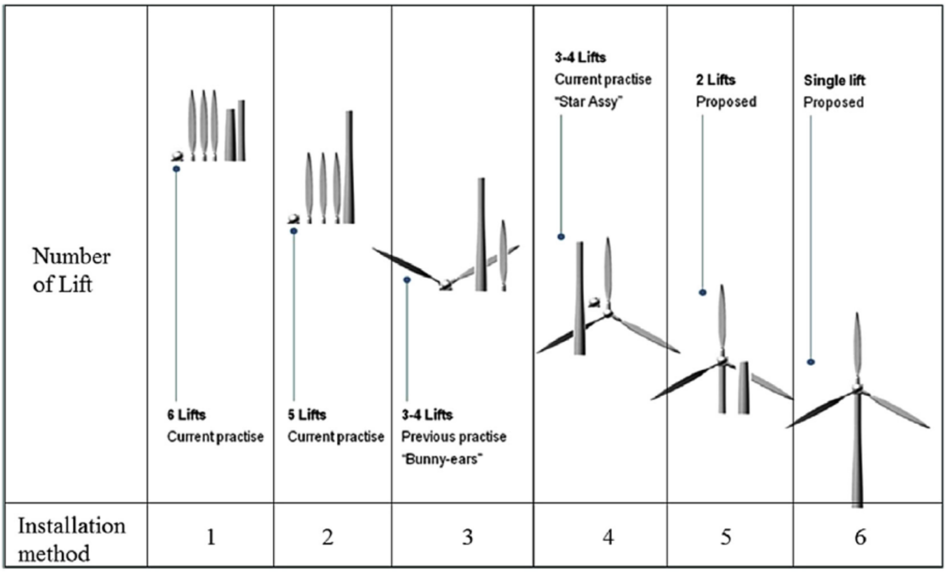

Figure 1.6: Offshore wind turbine installation methods categorized by required number of lifts [1]

shore site, etc [101]. In the past, pre-assembly onshore methods were mainly used for bottom-fixed offshore wind turbines. For small capacity turbines, pre-assembly onshore reduces the offshore construction and hence is more economical. There are also innovative concepts proposed to install fully assembled tower, rotor and nacelle in recent years. Sarkar and Gudmestad [86] developed a floatable subsea structure to install complete turbines with telescope towers. The turbine rotor needs to be oriented in the horizontal plane in order to keep it out of water. Ku et al. [55] studied the dynamic responses of an offshore wind turbine (tower-nacelle-rotor assembly) during lifting operation by a floating crane barge. Guachamin Acero et al. [37] proposed a novel procedure to install complete turbines based on the inverted pendulum principle. In addition, single lift of completely assembled turbine was also adopted during the installation of floating wind turbines at the Hywind Scotland wind farm [27].

However, pre-assembly onshore methods become less competitive with an increase of turbine size due to their large demand of vessel deck space and crane capacity. Nowadays, the split methods 1 and 2 are more commonly used for bottom-fixed wind turbines, for example, at the Race bank offshore wind farm in 2017 [74].

The large installation height of wind turbine components makes the operation more weather sensitive and challenging, compared to support structures. Particularly, wind loads on the turbine blades are significant since they are designed to extract energy from wind. As a result, installation of blades becomes the most challenging and risky operations in offshore wind turbine installation.

Single blade installation is most frequently used in recent years, due to small deck space requirement and flexible blade orientations during installation. During the installation process, the blade is lifted and installed in a feathered position, which is kept during the whole installation operation [56, 42]. As shown in Figure 1.7, the single blade can be installed in various orientations such as horizontal, vertical or even inclined. For inclined-blade installation, longer crane boom is required as the blade needs to be lifted higher than the hub height. The vertical-orientated installation needs to rotate the blade prior to installation since it is horizontally stored on the vessel deck, which makes the process more complex. The horizontal orientation installation is commonly preferred since no rotation of blade is required.

(a) (b) (c)

Figure 1.7: Single blade installation of offshore wind turbine blades with various orientations: (a) horizontal mounting [92]; (b) vertical mounting [63]; (c) inclined mounting [63]

Installation vessels

Installation of offshore wind turbines are generally carried out by crane vessels, either jack-up or floating ones.

The jack-up crane vessels are now extensively used during the installation of bottomed-fixed wind turbines. They can sit on the seabed via their legs during operation and thus provide a stable working platform. However, the jack-up leg lowering and retrieval processes are very time consuming and weather sensitive. In addition, they are also limited by water depth [26]. Table 1.2 shows several typical jack-up crane vessels used in offshore wind farm construction.

Table 1.2: Jack-up crane vessels used in offshore wind farm installation

Vessel	Max. water depth (m)	Crane capacity (t)	Max. lifting height (m)	Wind farms
Sea Installer	55	900	112	Race Bank (2017) [74]
Bold Tern	60	800	120	Veja Mate (2017) [102]
MPI Adventure	40	1000	105	Rampion (2017) [81]
Seajacks Scylla	65	1500	104	Walney Extension (2017) [75]

To date, limited research work has been carried out on jack-up crane vessels used in offshore wind turbine installation. Duan et al. [25] and Ringsberg et al. [85] studied the soil impact loads on the spudcans of a jack-up crane vessel during the leg lowering and retrieval phases. It was found that the soil impact loads are smaller in longer waves. Dalfsen [10] studied the dynamic structural response of the jack-up crane vessel in survival conditions, focusing on the effects of soil load modeling. The results indicated that advanced soil models are essential in the design check of jack-up crane vessels in extreme sea states. Stettner [98] studied the dynamic responses of a jacket foundation during installation by a jack-up crane vessel which is fixed with no crane tip motion. In these studies, the dynamic motion response of the vessels during crane operations was not addressed.

Compared with jack-ups, floating crane vessels are more flexible with respect to operational water depth and are much faster in relocation. The drawback of the floating vessels is their wave-induced motions which make the operations very challenging. As listed in Table 1.3, they are also involved in offshore wind farm construction, mostly for support structure or substation installations. Dynamic analysis of floating crane vessels installing different kinds of wind turbine foundations has been investigated in Refs. [86, 14, 59, 117] with respect to innovative installation methods, dynamic response analysis and derivation of operational environmental limits. In addition, floating crane vessels are also used in floating wind turbine installations. For example, Conlift vessel installed Hywind Demo floating wind turbine [53] and Saipem 7000 vessel installed Hywind Scotland floating wind farm [27].

Table 1.3: Floating crane vessels used in offshore wind farm installation (mainly for installing foundations and substations)

Vessel	Positioning	Crane capacity (t)	Wind farms
Olegs Strashnov	DP+ mooring	5000	Beatrice (2017) [5]
Rambiz	DP+ mooring	3300	Karehamn (2012) [66]
Svanen	DP+ mooring	8000	Walney Extension (2017) [75]

1.3 Guidelines, numerical modelling and analysis of offshore wind turbine installation activities

The installation of offshore wind turbines is a temporary condition, which is a branch of marine operation. For such operations, safety and efficiency are important. The purpose of numerical studies is to develop effective simulation methods, use them to analyze the dynamic responses of the system and to further guide operations with the aim of safe and efficient operations.

The planning and execution of such operations are based on standards and guidelines such as DNVGL-RP-C205 [18] for modeling of environmental conditions and loads, DNVGL-RP-N103 [22] and DNV-OS-H205 [21] for analysis of typical lifting operations, and DNV-OS-H101 [19] and DNVGL-ST-N001 [20] for requirements of operational limits and planning of marine operations. In recent years, guidelines specifically focusing on offshore wind turbine transportation and installations, such as ISO 29400:2015 [49] and DNVGL-ST-0054 [23], have been issued.

Numerical modeling and analysis of such operation typically involve multiple disciplines, such as hydrodynamics, aerodynamics, structure mechanics, soil mechanics, as well as stochastic and probabilistic methods. The important system response parameters include, for example, motions of installation vessel and installed components, structural response of the installed components, loads in lift wires, etc. To address novel problems such as marine operations, a combination of computer codes, such as SIMO [95] and RIFLEX [94], Orcaflex and Ansys-AQWA, and MOSES [100], are capable for consideration of motion response, structural dynamics and mechanical couplings. In addition, SIMO and RIFLEX, and Orcaflex also have programming interfaces provided via DLL (dynamic link library), providing links with user-defined functions. It allows for development of more advanced numerical methods to capture the important features of marine operations. For instance, Li et al. [61] developed a coupled method to account for shielding effect of crane vessel on monopile during the lowering process.

The dynamic analysis of marine operations provides loads and responses which can be used to assist the planning and execution of the operations. An important way of achieving this is to transform the required safety criteria into limits on vessel motions or environmental conditions that can be forecasted before operations or directly monitored during the execution phase. A generic methodology has been developed by Guachamin Acero et al. [38] to assess the operational limits of marine operations. It was further applied to derive the operational limits of transition piece mating [36], monopile hammering [62] and fully assembled turbine installation [35]. Ringsberg et al. [85] assessed the allowable sea states for a jack-up vessel during its installation at the seabed, in terms of H_s and T_p, by comparing spudcan impact force from seabed with criteria derived via FEM analysis. Li. et al. [60] studied the effect of different numerical methods on the operational sea states of monopile-lowering. In addition to H_s and T_p, wind conditions also need to be considered when assessing the operational limits for wind turbine rotor or blade installation [33].

The current thesis focuses on the advanced modeling and assessment of operational limits in terms of both wind and wave conditions for offshore wind turbine blade installation.

1.4 Review of research work on offshore wind turbine blade installation

So far, only a few studies have been published on offshore wind turbine blade installations. Some studies focus on the aerodynamic modeling of blades during installation or under standstill conditions. The characteristics of aerodynamic loads acting on a blade under installation conditions are quite different from a blade of an operating wind turbine. Wang et al. [108] studied the hoisting forces on a wind turbine blade during installation using computational fluid dynamics (CFD) under constant wind conditions. CFD analyses require significant computational efforts and cost. Hence, more sophisticated methods need to be used to determine aerodynamic loads marine operations. In 2014, Gaunaa et al. [30] proposed a first-order engineering model to describe the aerodynamic forces on a blade using the cross-flow principle. Later on, Gaunaa et al. [31] also used CFD analysis to correct the engineering model for the DTU 10MW reference blade, in large blade pitch and wind yaw angles.

Some focus on the installation process of blades for wind turbines. Wang et al. [107] studied the hoisting force of a 1.5 MW wind turbine rotor using Bladed. Kuijken [56] investigated possible ways to improve single blade installation in higher wind speed using HAWC2, by varying the lifting wires' arrangement without considering crane tip motion. Jiang et al. [50] studied the mating process of a 5MW blade considering the wind-induced blade motion and hub movement caused by wave-induced monopile motion. Modeling of vessel motion and crane flexibility and the subsequent influence on blade motion are not considered in these studies.

Studies investigating wind turbine blade installation from the perspective of structural integrity have been carried out. Verma et al. [103] investigated the impact behaviour of an offshore wind turbine blade when the blade collides with turbine tower during the installation process. The results showed that only less than 20% of the impact energy is dissipated by plastic deformation of the blade while the rest is elastic energy. Verma et al. [104] also studied the blade root impacts with hub during mating based on non-linear FEM analysis and established the blade root structural damage criteria with respect to impact velocity.

Development of controlling strategies to reduce blade motion during installation is another important aspect. Ren et al. [84] developed and verified a modularized simulation toolbox for single wind turbine blade installation in MATLAB/Simulink, with focus on control design. An active crontrol algorithm of tugger lines was later developed to compensate blade motion during installation [83].

The environmental condition limits used in industry for installing offshore wind turbine blades (and nacelles) are simply given in terms of wind speed and significant wave height, i.e., the average wind speed less than 10$\sim$12m/s at 10 m above the sea level and the significant wave height lower than 1.5$\sim$2m [65, 1, 77]. One of the purposes of this study is to derive these operational limits using response-based criteria, based on fully coupled numerical modelling and analysis of the installation system, and considering wave peak period as an additional important factor for the operation limits.

1.5 Aim and scope

The main goal of the work in this thesis is to study the offshore single blade installation, including development of a fully coupled method for numerical modelling and analysis, study of the blade dynamic motion characteristics during installation, and assessment of operational environmental limits using response-based criteria. To accomplish it, the following sub-objectives are defined.

- To develop an external code (named Aero) for calculating aerodynamic loads on a wind turbine blade during installation and to validate it by comparison with other numerical models.

- To establish a coupled simulation tool SIMO-Aero by integrating the developed Aero code with SIMO for modeling and analysis of single blade installation.

- To develop a fully coupled aero-hydro-soil-elastic-mechanical simulation tool for modeling and analysis of offshore single blade installation using jack-up crane vessels, considering detailed modeling of crane dynamics and jack-up vessel motion during blade installation.

- To demonstrate the system dynamic response characteristics of blade installation by a jack-up crane vessel and study influences of simplified modeling of soil reaction force on the system responses.
- To investigate the feasibility of using floating crane vessels during offshore single blade installation by comparing the dynamic responses of the installation systems with the jack-up vessel.
- To assess the operational limits of offshore single blade installation using blade response-based criteria.

This thesis is written as a summary of five published papers and one report, including three journal articles and two conference papers, as attached in the Appendix. The scope of the thesis is shown in Figure 1.8 where the main topics and the interconnection between appended papers are illustrated.

Paper 1 This paper deals with the development of a fully coupled simulation method for single blade installation for both onshore and offshore wind turbines [114]. The aerodynamic model for single blades during installation, i.e., the Aero code, is established based on the cross-flow principle, accounting for the effect of wind turbulence and dynamic stall. It is verified by code-to-code comparisons with HAWC2. The Aero code is coupled with SIMO to achieve the integrated simulation tool SIMO-Aero. The coupled code can account for blade aerodynamics and system mechanical couplings. It is applied in case studies on the wind-induced dynamic responses of a DTU 10MW blade during installation using a jack-up crane vessel. The vessel is assumed to be rigid, including the crane, and rigidly fixed to the seabed.

Paper 2 This paper deals with the detailed modeling of the jack-up vessel and crane tip motions [115]. A coupled model for a typical elevated jack-up crane vessel is first developed, considering the hydrodynamic and aerodynamic loads on the vessel, the soil-structure interaction, and the structural flexibility of the jack-up legs and crane. The developed vessel model is further coupled with the SIMO-Aero code to achieve a fully coupled aero-hydro-soil-elastic-mechanical code SIMO-RIFLEX-Aero for numerical modeling and dynamic analysis of offshore single blade installation using jack-up crane vessels. The code is

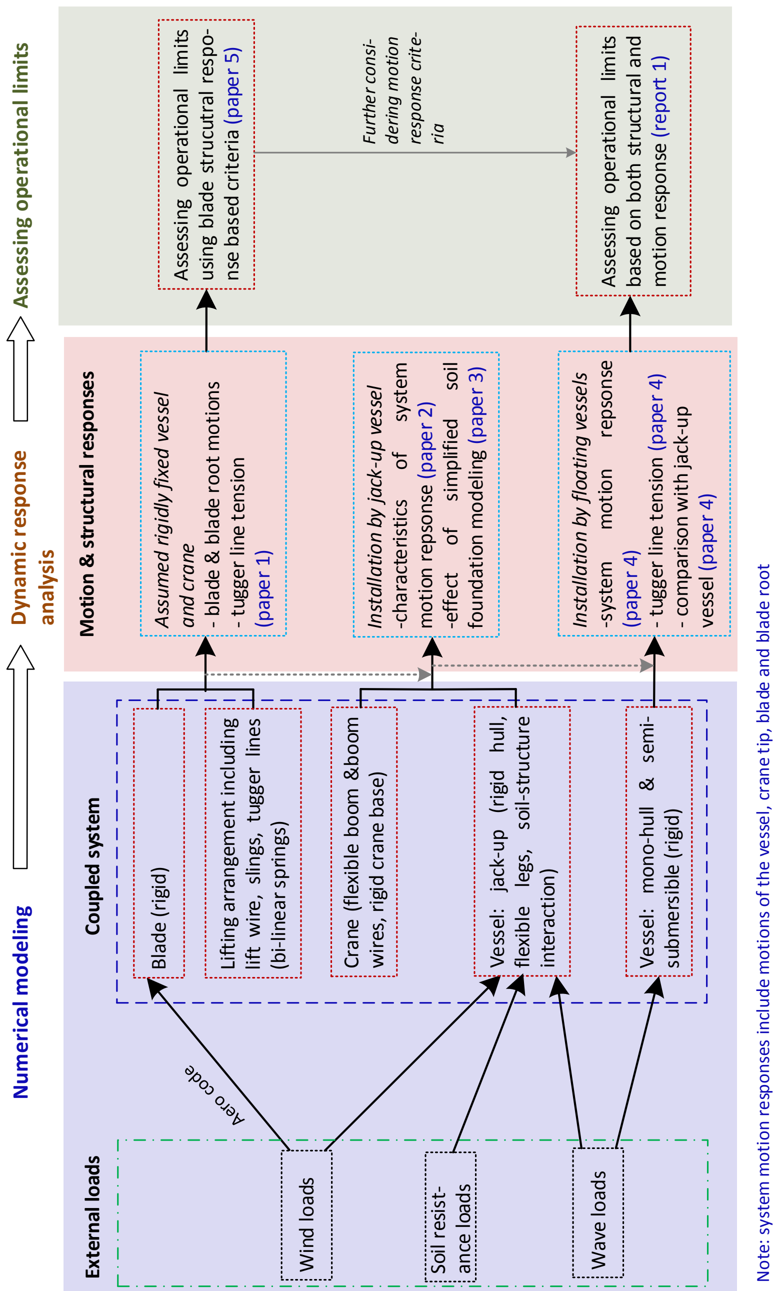

Figure 1.8: Scope of the thesis and interconnection between the appended papers

then applied to study the dynamic response of the DTU 10MW wind turbine blade installed by a typical jack-up crane vessel under various wind and wave conditions.

Paper 3 This paper further addresses the effects of soil behaviour modeling on the dynamic motion response of a wind turbine blade installed by a typical jack-up crane vessel using the SIMO-RIFLEX-Aero code [112]. Three foundation models and two types of soil are considered, including pinned foundation, fixed foundation and linear springs combined with dampers considering dense sand and hard clay soil. The foundation modeling is found to have vital effects on the system dynamic motion response. The characteristics of system motions differ under different types of soil. Pinned and fixed foundations are respectively shown to give significant underestimation or overestimation of system dynamic responses, compared with the detailed soil modeling using linear springs and dampers. To ensure safe and efficient offshore operations, detailed site specific soil properties should be used in numerical studies of offshore crane operations using jack-up crane vessels.

Paper 4 This paper deals with a preliminary feasibility study on offshore single blade installation using floating crane vessels. Two large floating crane vessels are considered, i.e., a mono-hull vessel and a semi-submersible vessel [113]. They are assumed to be equipped with dynamic positioning systems that can well mitigate the slowly varying horizontal motions. Their overall performance during the blade installation is numerically evaluated by comparing their performance against a typical jack-up crane vessel. The crane dynamics play a less important role for blade installation by floating vessels, compared to the jack-up crane vessel. The results indicate that it is feasible to install offshore wind turbine blades by using floating crane vessels provided that the vessel type is properly selected. Semi-submersible vessels are more feasible than mono-hull vessels for offshore wind turbine installations.

Paper 5 This paper outlines a structural-response method to assess the allowable operational limits of offshore single blade installation [105]. It is done by considering the structural damage criteria for the lifted blade linked with global response analysis during installation.

Report 1 An approach to assess the operational limits for offshore single blade installation based on response criteria including both global motion and structural integrity, developed on the basis of paper 5. The approach is demonstrated by a case study on the final mating operation of the DTU 10 MW wind turbine blade during installation by a semi-submersible crane vessel [116].

1.6 Thesis outline

The summary of the thesis includes six chapters. A brief description of each chapter is provided as follow:

Chapter 1: Introduction
This chapter includes introduction, background, motivation, aim and scope and outline of the thesis. A review of offshore wind turbine installation methods, crane vessels, and numerical studies of marine operations is discussed.

Chapter 2: Installation Systems and Procedures
This chapter summarizes the considered installation systems for offshore single blade installation, including the blade, lifting arrangement and crane vessels. The installation procedures are discussed and the critical installation phase is identified.

Chapter 3: Numerical modeling of the Installation System
This chapter addresses the detailed numerical modeling of the blade installation systems, including the fully coupled simulation method, and detailed structural and external forces models, used in all papers.

Chapter 4:
This chapter presents the dynamic responses of the single blade installation systems under various wind and wave conditions, of papers $1 \sim 4$. The characteristics of the vessel motion (6 DOFs), the crane tip movement (3 DOFs), the blade motion at its COG and the corresponding translational motion at the blade root (3 DOFs) are investigated. Tensions in the tugger lines are also discussed.

Chapter 5:
This chapter addresses the method and results for assessing allowable operational wind and wave conditions for offshore single blade installation using response-based criteria in report 1.

Chapter 6:

Conclusions, original contributions and the recommendations for future research work are presented.

Chapter 2

The installation system and installation procedure

2.1 General

Compared to the installation of foundations and towers, installation of offshore wind turbine blades is more challenging, due to the large installation height and required high installation precision. Although installation of pre-assembled rotor has been used, single blade installation by lifting operation is most frequently used for offshore wind turbine blade installation in recent years, due to its small deck space requirement and flexible blade orientations during installation. A review of offshore single blade installation, installation vessels has been discussed in Sections 1.2 in Chapter 1.

This chapter discusses the installation procedures and main system components for offshore single blade installation, and summarizes the main system parameters used in this thesis, including blade, lifting arrangement, crane and different types of vessels investigated. The DTU 10MW wind turbine blade [4] and the jack-up crane vessel are used in all five papers. In addition, floating crane vessels are considered in *Paper 4* and *Report 1* shown in Chapter 5.

2.2 Installation procedure

Generally the wind turbine blades are transported on board the installation vessel and are installed by lifting operations. The installation procedure, as illustrated in Figure 2.1, is summarized into the following steps:

Step 1. The blade is loaded in the yoke which is to protect the blade

18

(a) Step 1: lift the blade off vessel deck [7]

(b) Step 2: lift the blade to the hub height [91]

(c) Step 3: the blade root approach the hub [91]

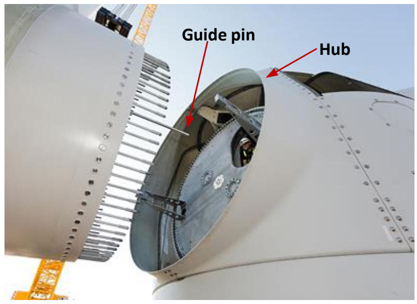

(d) Step 4: monitor the blade root motion [90]

(e) Step 5: mate the blade root into the hub [80]

Figure 2.1: Illustration of the procedure of offshore single blade installation (pictures from different references are used in order to give a clear illustration of each phase.)

integrity during installation. The yoke and the blade are lifted off the vessel deck by running the crane winch. There are tugger lines attached to the yoke, from a trolley running on the crane boom.

Step 2. The blade is gradually lifted to the installation height. The orientation of the blade is controlled by the pre-tensioned tugger lines.

Step 3. The blade approaches the turbine hub by operating the crane. The blade is suspended in a safe position, minimizing risk for impacts.

Step 4. The crane and the tugger lines are adjusted to ensure good alignment of the blade root with the hub opening. The blade root motion is monitored to decide whether the mating operation is possible or not.

Step 5. Once mating is expected to be possible, the blade root is mated into the hub.

The final mating operation, including steps 4 and 5 are generally considered to be critical for the blade installation. In the monitoring phase in step 4, too large motion at the blade root would make it impossible to start the mating operation. In step 5, the mating operation fails if damages occur in the guide pins at the blade root.

The thesis deals with the numerical studies of single blade installation for offshore wind turbines with focus on the dynamic analysis of the coupled system during steps 4 and 5.

2.3 Installation systems

A typical blade installation system consists of three main parts, i.e., the installed blade and the lifting arrangements, the crane, and the vessels. This thesis considers the installation using three different kinds of crane vessels, i.e., a jack-up crane vessel, a semi-submersible crane vessel and a mono-hull crane vessel.

2.3.1 Coordinate systems

As shown in Figure 2.2, three right-handed coordinate systems are defined and used for each blade installation system, i.e., a global coordinate system $O - XYZ$, a vessel-related coordinate system $O_v - X_vY_vZ_v$ and a blade-related coordinate system $O_b - X_bY_bZ_b$.

The blade-related coordinate system $O_b - X_bY_bZ_b$ has its origin on the blade's COG. Y_b is in the blade's longitudinal direction and is positive towards the blade tip; Z_b is positive upwards; X_b follows the right-hand rule. The $O_b - X_bY_bZ_b$ parallels with the global coordinate system $O - XYZ$ when the blade is at rest.

 20

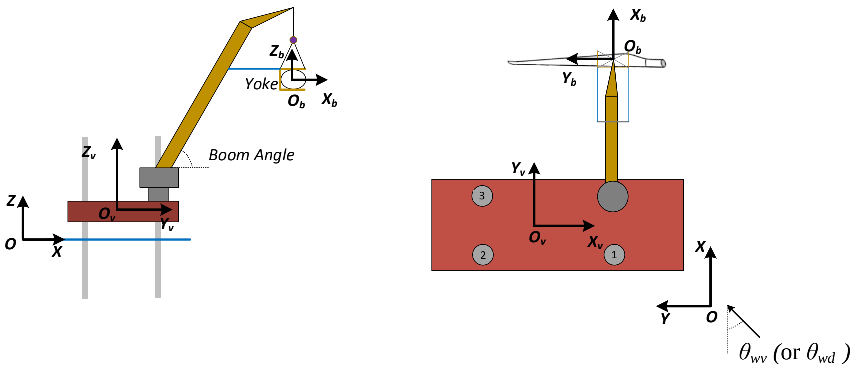

(a) Jack-up vessel: side view and top view

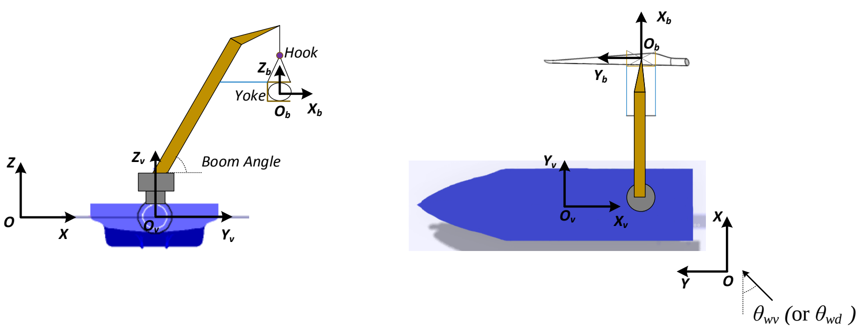

(b) Mono-hull vessel: side view and top view

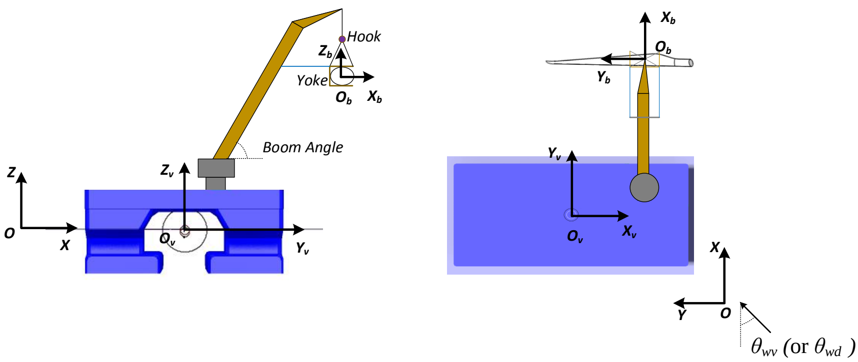

(c) Semi-submersible vessel: side view and top view

Figure 2.2: Definition of coordinate systems for the blade installation system

For the vessel-related coordinate system $O_v - X_vY_vZ_v$, its origin is located at the water-plane center of the floating vessel at rest, while it sits on the geometrical center of the elevated jack-up hull. X_v is in the vessels' longitudinal direction and Z_v is positive upwards; Y_v follows the right-hand rule. When the vessel is at rest, $O_v - X_vY_vZ_v$ will parallel with the global coordinate system $O - XYZ$ if it rotates around the Z_v axis by 90 deg.

The global coordinate system $O - XYZ$ has its origin located at the mean sea surface. Z is positive upwards. X parallels with the Y_v when the vessels are at rest. The Y follows the right hand rule.

The incident wave angle is defined as the relative angle of wave direction and the positive X direction in the global coordinate system. The incident wind angle has a similar definition while the wind and waves do not always have the same incident angle.

2.3.2 Blade and lifting arrangement

The DTU 10MW wind turbine blade is designed to be installed at the hub height of 119 m above the mean sea surface. The main system properties used in this study are presented in Table 2.1. In this study, the blade is considered to be straight and rigid. The blade COG is located 26.2m from its root, along the blade span.

A yoke weighting 47 tons is used to hold the blade around the blade COG. The yoke is lifted by the hook via four slings. The lift wire runs through the crane tip to the hook. Two horizontal tugger lines are deployed from the yoke to the crane structure. Both tugger lines have an arm length of 10m, as shown in Figure 2.3. Pretension is applied in tugger lines to prevent slack lines.

Table 2.1: Main properties of the blade lifting system

Parameter	Value	Unit
Hook mass	10	tons
Yoke mass	47	tons
Blade mass	41.67	tons
Blade length	86.37	m
Blade COG*	26.2	m
Installation height	119	m
Tugger line arm length	10	m

* The position of blade COG is presented relative to the blade root and along the blade span.

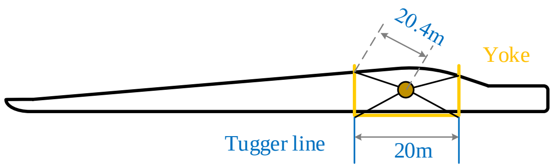

Figure 2.3: Illustration of tugger line system

2.3.3 Crane

The same typical pedestal crane is used for all three crane vessels in this study, as shown in Figure 2.4. In *Papers 1 and 5*, a rigid crane was assumed. The detailed modeling of the crane is developed in *Papers 2, 3 and 4*. The crane consists of crane supports, a wire overhang system and a lattice boom. The crane is connected to the vessel via the crane supports. The main parameters of the crane are listed in Table 2.2. The crane had the same orientation on all three vessels. The height of the crane tip remained the same, i.e., 144.9 m above the mean sea surface.

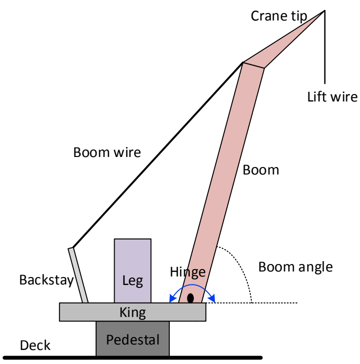

Figure 2.4: Illustration of a typical offshore pedestal crane [115]

2.3.4 Vessels

Three vessels are used in this study, i.e., a jack-up crane vessel, a semi-submersible crane vessel and a mono-hull crane vessel.

The jack-up vessel was considered in *Papers 1∼5*. The jack-up crane vessel has four legs with its hull elevated above the mean sea surface during operations. In *Papers 1 and 5*, the jack-up vessel was assumed rigidly fixed to the seabed without any motion. A detailed model of the jack-up vessel was developed in *Paper 2* and used in *Papers 3 and 4*. Main parameters of

Table 2.2: Main parameters of the crane [113]

Crane properties [115]	
Boom length [m]	107.6
Crane boom angle [deg]	67.6
No. of equivalent boom wires [-]	2
Equivalent boom wire stiffness [kN/m]	9048
Equivalent boom wire damping [kNs/m]	90.5
Crane tip positions on the vessels *	
Semi-submersible vessel	(66m, 65.3m, 144.9m)
Mono-hull vessel	(74.2m,65.6m,144.9m)
Jack-up vessel	(34.2m,49.3m,133.2m)

* It is given in the vessel-related coordinate system. The height of crane tip on all three vessel are the same in the global coordinate system, i.e., 144.9m above the mean sea surface.

the jack-up vessel are listed in Table 2.3.

Table 2.3: Main parameters of the jack-up vessel [115]

Parameters	Unit	Values
Hull length, breadth and depth	[m]	132, 39, 9
Displacement during transportation	[m^3]	2.20×10^4
Total elevated load	[t]	1.69×10^4
Leg length and diameter	[m]	92.4, 4.5
Long. and trans. leg spacing	[m]	68.3, 30.6
Airgap	[m]	7.2
Leg below hull	[m]	49
Soil type		Dense sand
K_x, K_y and K_z *	[kN/m]	1.35×10^6, 1.35×10^6, 1.47×10^6
K_ϕ, K_θ and K_ψ *	[kNm/deg]	6.4×10^5, 6.4×10^5, 8.3×10^5

* Equivalent linear spring stiffness of the soil in six DOFs, a detailed explanation of which can be in Section 3.5.

Table 2.4: Main parameters of the floating crane vessels [113]

Parameters		Semi-submersible	Mono-hull
Length	[m]	175	183
Breadth	[m]	87	47
Operational draught	[m]	26.1	12
Displacement	[m^3]	1.638×10^5	6.190×10^4

Two typical floating vessels were used in *Paper 4*, including a semi-submersible vessel and a mono-hull vessel, with their main properties shown in Table 2.4. The semi-submersible vessel has two longitudinal pontoons that are completely submerged. Each of the pontoon is connected to the main deck via three vertical columns. Both the semi-submersible vessel and the mono-hull vessel are assumed to be equipped with dynamic positioning (DP) systems. Their slowly-varying motions in surge, sway and yaw are well mitigated by the DP systems.

Chapter 3

Numerical modelling of the installation system

3.1 General

Even though installation of wind turbine blades is challenging and risky, limited relevant studies have been carried out and published, as discussed in Section 1.4. To ensure the operational safety and improve the installation efficiency, it is important to establish and use advanced numerical simulation tools to study the system dynamic response during installation.

In this thesis, a fully coupled method SIMO-RIFLEX-Aero for simulating offshore single blade installation is established. It can account for blade aerodynamics, crane flexibility, detailed modeling of installation vessel motions and wire coupling mechanics.

This chapter gives a summary of the coupled method (*Papers 1 and 2*), and structural modeling and external force modeling of the blade installation systems. Detailed modeling of jack-up vessel and crane was developed in *Paper 2* and considered in *Paper 3 and 4*. Floating crane vessels, including a mono-hull and a semi-submersible, were considered in *Paper 4*. The semi-submersible crane vessel was further used in *Report 1*.

Both wind and wave loads are important to consider during the numerical modelling and analysis of offshore wind turbine installation. The wind turbine blades are sensitive to wind loads while the installation vessels, including both jack-up and floating vessels, are sensitive to the wave loads. For commonly used jack-up crane vessels, the typical sea states considered for practical installation of offshore wind turbine blades are the mean wind speed at the turbine hub height less than 10$\sim$12m/s and the significant wave height smaller than 1.5$\sim$2m [1, 77]. The crane vessels' wave-induced motion contributes to a significant motion at the crane tip, which makes the installation very challenging. However, the motions, specially of the floating crane vessels, are sensitive to wave periods. The motions of the elevated jack-up crane vessels are mainly caused by the wave loads on the jack-up legs, leg structural flexibility and soil foundation rigidity. Floating crane vessels typically have DP and (or) mooring systems to mitigate their slow drift motions. Their first-order wave induced motions are significant, and sensitive to incoming wave directions. Compared to monohull type floating vessels, the semi-submersible type ones lead to relatively less crane tip motion due to the fact that the natural periods of their rigid body motions are generally beyond upper limit of typical wave periods.

3.2 Coupled simulation method

As shown in Figure 3.1, the coupled simulation method is developed by integrating an Aero code with SIMO [95] and being further linked with RIFLEX [94]. The Aero code calculates the aerodynamic forces and moments acting on the installed blade. It is integrated with SIMO via using the external dynamic link library (DLL). The SIMO and RIFLEX codes were developed by SINTEF Ocean and have been widely used in the offshore wind, oil and gas industries. SIMO models the blade as a rigid body. SIMO and RIFLEX provide detailed modeling of the crane vessel and system mechanical couplings, including wind loads, hydrodynamics, structural flexibility and soil-structure interaction, etc.

Figure 3.2 shows the step-by-step development of both the structural models and external force models for the blade installation systems in the coupled code. First, modeling of the blade and lifting arrangement (lift wires, slings and tugger lines) was established in SIMO-Aero by assuming a jack-up crane vessel without any motion (*Paper 1 and 5*). In addition to the blade and lifting arrangement, the second model considers the wind loads on the jack-up hull, wave loads on the jack-up legs, structural flexibility of the legs and the crane, and soil-structure interaction (*Paper 2 and 3 and 4*). After that, the floating crane vessels were considered in the third model (*Paper 4*).

The following sections summarize the details of the system modeling, including aerodynamic loads, hydrodynamic loads, soil-structure interaction, structural modeling and mechanical couplings.

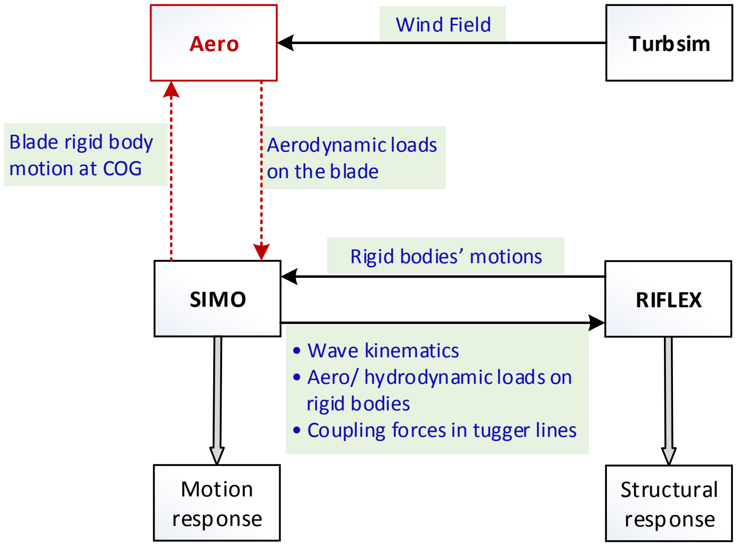

Figure 3.1: Overview of the coupled simulation method. The author's contribution is highlighted in red.

3.3 Aerodynamic loads

Aerodynamic loads on the blade and the elevated hull were considered. The former is calculated in the Aero code while the latter is computed in SIMO.

3.3.1 Aerodynamic loads on the blade

The aerodynamic forces and moments acting on the installed blade are computed by the Aero code. The Aero code is developed based on the cross-flow principle, accounting for effects of wind shear, wind turbulence and dynamic stall. It is coupled with the SIMO via DLL (dynamic link library). During the aerodynamic load calculation, the blade is divided into a number of elements. The aerodynamic load on each blade element is first computed in the local element coordinate system. The total aerodynamic loads are the sum of that on all elements, acting on the blade COG in the global coordinate system. The coordinate systems are shown in Figure 3.3.

The aerodynamic load on each blade element is calculated based on the cross-flow principle [44, 43]. It is applicable for calculation of aerodynamic forces on a wind turbine blade, where the local blade element suits a 2D approximation. In the cross-flow principle, the inflow velocity normal to the cross section, i.e., $\mathbf{V}_{A,i}$ along y_c is neglected, as shown in Figure 3.4.

 28

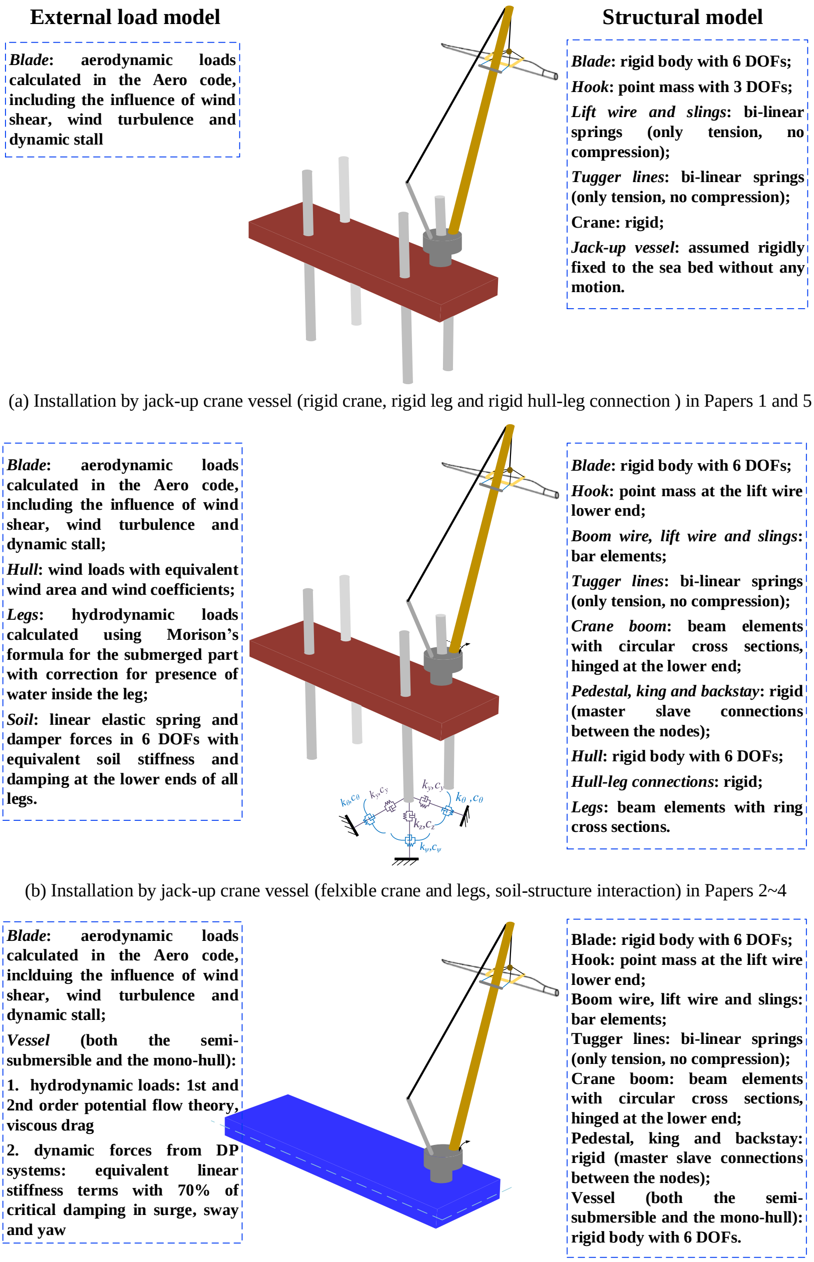

(a) Installation by jack-up crane vessel (rigid crane, rigid leg and rigid hull-leg connection) in Papers 1 and 5

(b) Installation by jack-up crane vessel (felxible crane and legs, soil-structure interaction) in Papers 2~4

(c) Installation by floating crane vessels (detailed modeling of vessel and crane) in Paper 4

Figure 3.2: Structural and external force models of the blade installation systems

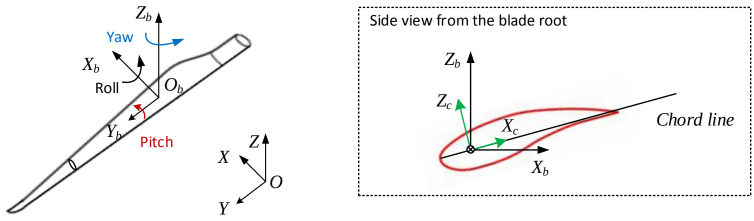

Figure 3.3: Definition of coordinate systems $O-XYZ$, $O-X_bY_bZ_b$ and $O-X_cY_cZ_c$ are respectively the global, blade-related and local blade element coordinate systems [114].

Hence, the relative wind velocity used in the aerodynamic load calculation $\mathbf{V}_{rel}$ can be expressed as:

$$\mathbf{V}_{rel} = [V_{A,i,xc} \quad 0 \quad V_{A,i,zc}]^T \tag{3.1}$$

where $V_{A,i}$ is the relative wind velocity seen by the element i. $V_{A,i,xc}$ and $V_{A,i,zc}$ are respectively its projection on x_c and z_c. $V_{A,i}$ is obtained using Eq. (3.2)

$$\mathbf{V}_{A,i} = \mathbf{T}_{GC,i}(\mathbf{V}_{WG,i} - \mathbf{V}_i + \mathbf{V}_{IG,i}) \tag{3.2}$$

where $\mathbf{V}_{WG,i}$, $-\mathbf{V}_i$ and $\mathbf{V}_{IG,i}$ are respectively the global wind velocity, element velocity and wake-induced velocity at the ith element. The $\mathbf{V}_{IG}$ is expected to have marginal influence for blades during installation, which is different from an operational blade with large rotational speed because the installed blade motion is very small. Thus, Eq. (3.2) can be simplified as

$$\mathbf{V}_{A,i} = \mathbf{T}_{GC,i}(\mathbf{V}_{WG,i} - \mathbf{V}_i) \tag{3.3}$$

The angle of attack α is determined using $\mathbf{V}_{rel}$. α is further used to find the C_L and C_D coefficients based on a 2D look-up table which gives the relationship between C_L, C_D and α. In addition, there is an option to include dynamic stall effect before the table look-up.

The Beddoes-Leishman dynamic stall model is used. It was originally proposed by Leishman and Beddoes [57] for helicopter aerodynamics. Later, Gupta and Leishman [39] adapted it for application in wind turbine aerodynamics. As shown on the right side of Figure 3.5, there are three parts in the Beddoes-Leishman dynamic stall model, i.e., unsteady attached flow, unsteady separated flow and dynamic vortex lift. In the unsteady attached flow regime, the aerodynamic loading consists of a circulatory and an impulsive part. The circulatory component is due to the change of angle of attack

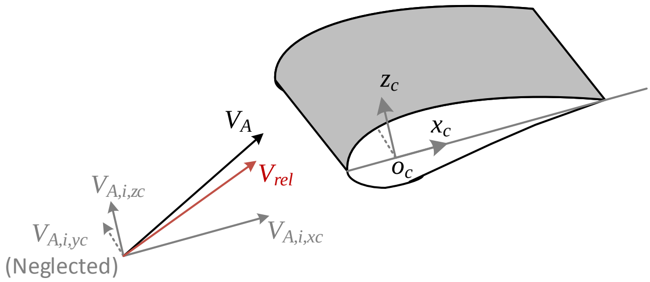

Figure 3.4: Illustration of cross-flow principle: $\mathbf{V}_{A,i} = [V_{A,i,xc} V_{A,i,yc} V_{A,i,zc}]^T$ *[114]*

while the impulsive component is related to the change rate of α and pitch moment. Furthermore, the attached flow results are modified due to flow separation on the low-pressure side of the airfoil, including leading edge and trailling edge separations. The final part of the model is the vortex build-up and shedding. The vortex lift contribution is empirically modeled as an excess circulation in the vicinity of the airfoil using the difference between the normal force coefficient C_N from attached flow and separated flow. The total loading on the airfoil is the sum of the aforementioned components.

Then the lift and drag forces on the blade element is computed using the obtained C_L and C_D. The total aerodynamic loads on the blade are the sum of these on all elements. Figure 3.5 shows a flow diagram for calculating the aerodynamic load on a lifted blade.

Verification of the Aero code

The Aero code is verified by code-to-code comparison against HAWC2 using the DTU 10MW Reference Wind Turbine blade. Figure 3.6 show the comparison of lift and drag force. It is shown that the results from the developed code are in good accordance with the HAWC2 results. However, it should be noted that this code-to-code comparison only verifies the aerodynamic code but does not validate the model against experimental data since they are very difficult to obtain.

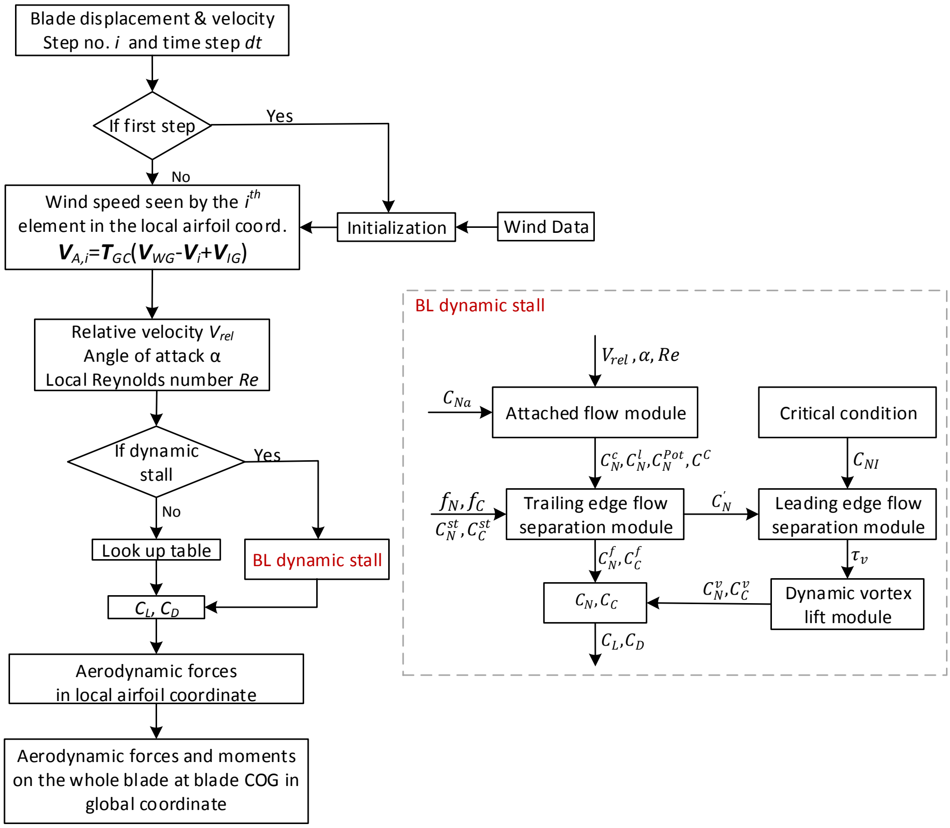

Figure 3.5: Flow chart for aerodynamic modeling [114]

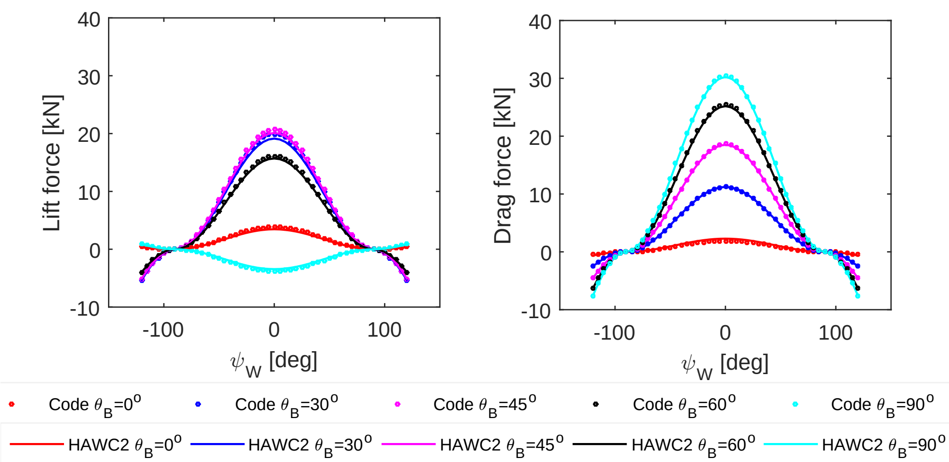

Figure 3.6: Verification of the Aero Code against HAWC2: constant wind 10m/s [114].

 32

Distribution of aerodynamic force on a lifted blade

The distribution of aerodynamic forces on a lifted blade is quite different from a rotating one. Figure 3.7 compares the lift and drag force distribution on a blade during rotation and lifted condition. As shown in Figure 3.7,

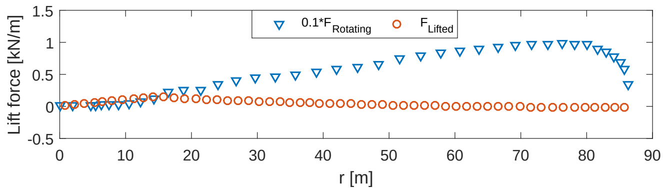

(a) Lift force F_z

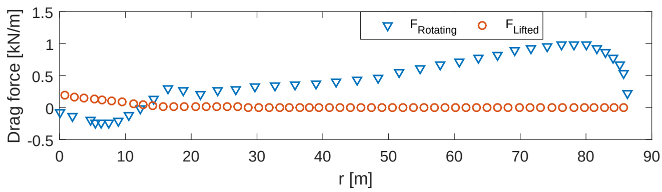

(b) Drag force F_x

Figure 3.7: Distribution of lift and drag forces on a blade under rotating condition and lifting condition: blade pitch angle 0^o*; rotational speed for the rotating blade 8.029 rpm; constant wind 10m/s [114].*

both lift and drag forces for the rotating blade experience an increasing trend towards the tip. The aerodynamic center of the rotating blade stays close to the blade tip. It indicates that the rotational speed plays an important role in the aerodynamic force distribution of a rotating blade.

For the lifted blade, the main contribution of the aerodynamic loads comes from the middle and root part of the blade. Thus, the aerodynamic center of a lifted blade is located close to the blade root. Compared to the inflow wind velocity, the velocity of a lifted blade is insignificant.

Importance of blade velocity in aerodynamic load calculation

It is important to consider the blade velocity during calculation of aerodynamic loads in Eq. (3.3), as shown in Figure 3.8. Even though the blade velocity has minor influence on the magnitude of aerodynamic loads, it plays an important role in terms of aerodynamic damping. An overestimation of blade motion is expected if the blade velocity is neglected during the aerodynamic response calculation.

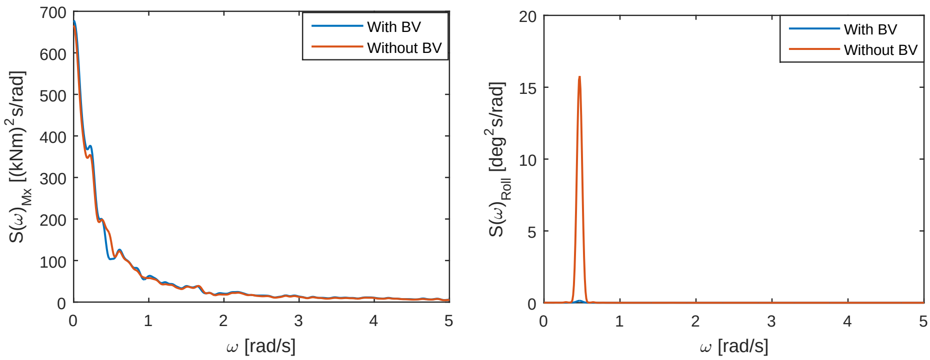

(a) Spectrum of blade aerodynamic roll moment

(b) Spectrum of blade roll motion

Figure 3.8: Comparison of aerodynamic loads and motions calculated with consideration of blade velocity (With BV) and without consideration of blade velocity (Without BV); blade initial pitch angle $\theta_B = 0^o$*; turbulent wind with mean speed* $10m/s$ *and turbulence intensity* $T_I = 15.72\%$*; it assumes a rigid jack-up crane vessel without motion [114].*

3.3.2 Wind loads on the jack-up hull

During offshore wind turbine installation, the wind loads on the jack-up crane vessel consists of contributions from the jack-up house, legs, as well as the wind turbine components and equipment loaded on the vessel deck. The wind area and shape coefficients of each component are different. The wind load on one component may be greatly affected by shielding effect from others. Detailed coefficients from wind tunnel test are needed in order to achieve an accurate estimation of wind loads. However, these coefficients are not available at present. Under such a circumstance, the wind area above the hull baseline is considered as a block with equivalent area and wind coefficients. The wind loads on the parts of the legs between the wave crest and the hull baseline are neglected as recommended [16]. The simplification is acceptable since the motion of the jack-up vessel is mainly wave-induced during operations. The wind load is calculated as [16]:

$$F_{x,wd} = \frac{1}{2}\rho_{air}C_S AV^2 cos\alpha \tag{3.4}$$

$$F_{y,wd} = \frac{1}{2}\rho_{air}C_S AV^2 sin\alpha \tag{3.5}$$

$$F_{z,wind} = 0 \tag{3.6}$$

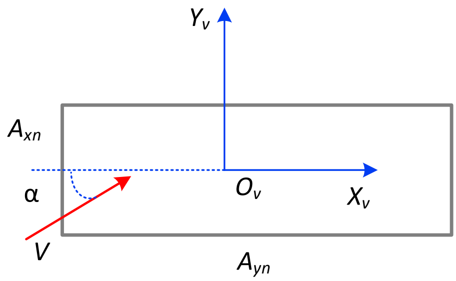

Figure 3.9: Illustration of wind area and relative wind inflow angle (top view) [115]

where ρ_{air} is the density of air; α is the relative wind inflow angle, as shown in Figure 3.9; V is the relative wind speed; C_S is the overall shape coefficient , i.e., $C_S = 1.1$; A is the area normal to the inflow wind:

$$A = A_{xn}|cos\alpha| + A_{yn}|sin\alpha| \tag{3.7}$$

where A_{xn} and A_{yn} are respectively the wind area normal to X_v and Y_v axis. The corresponding wind moments can be expressed as:

$$M_{x,wd} = -z_c F_{y,wd} \tag{3.8}$$

$$M_{y,wd} = z_c F_{x,wd} \tag{3.9}$$

$$M_{z,wd} = x_c F_{y,wd} - y_c F_{x,wd} \tag{3.10}$$

where $[x_c \quad y_c \quad z_c]$ is the position vector for the center of the equivalent wind block.

3.4 Hydrodynamic loads

3.4.1 Wave loads on the jack-up legs

A jack-up crane vessel usually has its hull elevated well above the mean sea surface when installing offshore wind turbines. The wave loads acting on the submerged legs can be calculated by integration of wave force from the seabed to the instantaneous free sea surface using strip theory based on the linear wave kinematics, as shown in Figure 3.10.

Since the ratio of leg diameter to wave length is less than 1/5, the instantaneous wave load normal to the leg can be calculated using Morison's

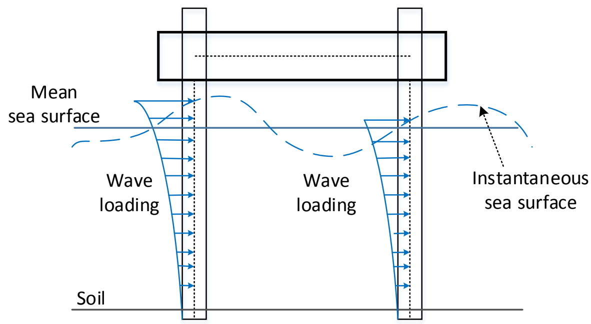

Figure 3.10: Wave loads on jack-up legs [115]

formula by accounting for relative motion, i.e.:

$$\mathbf{F} = \int_{-h}^{\eta} [\rho A_{ext}(1 + C_A)\dot{\mathbf{u}}(z) - \rho A_{ext} C_A \ddot{\mathbf{r}}(z) \\ + \frac{1}{2}\rho D_{ext} C_D |\mathbf{u}(z) - \dot{\mathbf{r}}(z)|(\mathbf{u}(z) - \dot{\mathbf{r}}(z)) - \rho A_{int}\ddot{\mathbf{r}}(z)]dz \tag{3.11}$$

where the dots denote time derivatives; ρ is the mass density of water; D_{ext} is the external diameter of the leg; A_{ext} and A_{int} are respectively the external and internal cross-sectional areas of the leg; C_A and C_D are respectively the non-dimensional 2D added mass and quadratic drag coefficients; $\mathbf{u}$ and $\mathbf{r}$ are respectively the velocity vector of undisturbed wave field and motion vector of the leg; h is the water depth and η is the instantaneous wave elevation.

The presence of water in leg is also considered in the model. The water mass inside the legs introduces extra load due to the acceleration of the water in leg together with the leg [94], which are presented as the last term in Eq. (3.11).

3.4.2 Wave loads on the floating vessels

For the floating vessels, the hydrostatic restoring coefficients are computed using the mean position of the vessels. The hydrodynamic loads are calculated based on the potential flow theory. The added mass, potential damping and first order wave excitation forces are obtained using a first order potential flow model and applied in the time domain using the convolution techniques [95]. Additional viscous roll damping is incorporated as 3% of the vessel's critical damping in roll [78].

In addition to the first order hydrodynamic forces, the mean wave drift loads are also considered. The Newman's approximation is used to estimate the second order difference frequency wave excitation loads on the monohull vessel in surge, sway and yaw. For the semi-submersible vessel, second order difference frequency wave excitation forces in all 6 DOFs are important in shallow water. Hence, integration of second order mean wave pressure over its wetted surface is used to estimate the corresponding second order difference frequency wave loads in all 6 DOFs, as recommended in the DNV-RP-C205 guideline [15].

The restoring forces from the DP system are simplified into equivalent linear stiffness terms in surge, sway and yaw. Besides, large damping, i.e., 70% of the critical damping of the vessels' surge, sway and yaw motion, is applied to eliminate the corresponding slowly varying motion. This is a reasonable assumption since it can be achieved by use of DP systems in practical operations [95].

3.5 Jack-up soil-structure interaction

For the jack-up vessel, the soil reaction force is represented by using equivalent linear elastic springs combined with dampers, without detailed modeling of the spudcans, as shown in Figure 3.11. It is a feasible simplification for modeling of soil behavior for jack-up crane vessels under operational sea states which typically have a significant wave height below 2.5-3.0m [1, 76]. In such conditions, the loads acting on the spudcans are much smaller than those required to reach the soil yield surface. Hence, the linear elastic soil modes can be used [9, 111].

As shown in Figure 3.11, linear springs and dampers in 6 DOFs at the reference point are used to represent the soil resistant force. The reference point of the soil model is at the lower end of each jack-up leg where the spudcan locates. The corresponding soil reaction force can be expressed as a function of spudcan displacement, i.e.:

$$\mathbf{F}_s = \mathbf{K_s}\mathbf{X_{sc}} + \mathbf{C_s}\dot{\mathbf{X}}_{\mathbf{sc}} \tag{3.12}$$

where the dots denote time derivative; $\mathbf{K_s} = [k_x \quad k_y \quad k_z \quad k_\phi \quad k_\theta \quad k_\psi]$ is the soil stiffness vector in 6 DOFs without considering coupling effects. The stiffness coefficient are dependent on the soil properties, the dimension and the penetration depth of the spudcans. They could be calculated using recommended empirical formula [96, 48] or estimated based on site-specific soil properties. The $\mathbf{C_s}$ is the corresponding vector of the soil damping. $\mathbf{X_{sc}}$ is the displacement vector, i.e.:

$$\mathbf{X_{sc}} = [x \quad y \quad z \quad \phi \quad \theta \quad \psi] \tag{3.13}$$

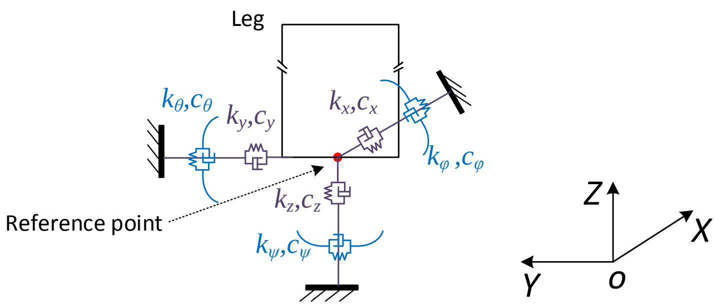

Figure 3.11: Modeling of soil resistance force on the spudcan using linear springs and dampers [115]

where x, y, z are the translation motion of the reference point (lower end node of jack-up leg); ϕ, θ and ψ are the rotational motion of the leg at its lower end.

3.6 Structural modeling

The blade is modeled as a rigid body. The blade structural flexibility is found to have a minor contribution to blade rigid body motion during installation [30].

Regarding the crane, the crane boom is modeled using beam elements. The lower end of the boom is hinged on the crane base. The boom inclination is controlled by the boom wires. The boom wires are represented by bar elements. The deformation of the crane supports, including king, pedestal and back-stay is neglected, assuming that the crane deformation is mainly due to the flexibility of the boom and boom wires.

The floating vessels are modeled as rigid bodies with 6 DOFs. The jack-up hull is also represented as a rigid body with 6 DOFs. Structural flexibility in the jack-up legs are accounted for by use of beam elements. The jack-up hull-leg connections are modeled as rigid connections. The spudcans are modeled as point mass at the lower end of each leg.

For slender structures, such as crane boom and jack-up legs, structural damping are accounted for using the Rayleigh damping model [82]. The damping matrix can be expressed as:

$$c = \alpha_1 m + \alpha_2 k \tag{3.14}$$

where α_1 and α_2 are receptively the mass- and stiffness-proportional damping coefficients. Coefficients of $\alpha_1 = 0$ and $\alpha_2 = 0.005$ were specified for the slender structures.

3.7 Mechanical couplings

The non-compressive tugger line coupling forces are modeled as bi-linear spring forces:

$$T = \begin{cases} k\Delta L, & \text{if} \quad \Delta L >= 0 \\ 0, & \text{otherwise} \end{cases} \tag{3.15}$$

where T is the wire tension and ΔL is the wire elongation. Besides, k is the wire axial stiffness. Damping in wires is considered by using stiffness-proportional damping, which is taken as 1% of the wire stiffness.

Lift wire and slings are always tensioned because of the blade gravity force. In paper 1 and 5, they are modeled as bi-linear springs. In paper 2, 3 and 4, they are represented using bar elements with equivalent stiffness properties.

3.8 Identification of system natural periods

The natural periods of the three blade installation systems are estimated in this section. Since the blade installation systems are very complex, the natural periods are identified module by module.

3.8.1 Blade motion

The natural frequencies of blade rigid body motion are obtained by eigenvalue analysis, together with the hook while keeping the vessel and the crane fixed, based on Eq.(3.16).

$$[-\omega^2\mathbf{M} + \mathbf{K}] \cdot \mathbf{X} = 0 \tag{3.16}$$

where $\mathbf{M}$ and $\mathbf{K}$ are the mass and restoring matrix of the BY and hook. In addition, the restoring matrix $\mathbf{K}$ mainly comes from the gravity of involved bodies, lift wire, slings and tugger lines.

The dominant motions of the blade rigid body motion and corresponding periods and frequencies are listed in Table 3.1. The blade-hook in-phase pendulum motion has the longest natural period of 12s, followed by the blade yaw resonant motion with a period around 5s. The third mode is caused by the out-of-phase double pendulum motion of the blade and hook around the crane tip in the vertical $O_bY_bZ_b$ plane [114].

Table 3.1: Natural periods and dominant motion of the blade rigid body motion (defined in the blade-related coordinate systems in Figure 2.2) [113]

Dominant response	Period [s]	Frequency [rad/s]
Blade roll resonance (in phase pendulum motion)	12.0	0.52
Blade yaw resonance (due to tugger lines)	5.11	1.23
Blade-hook double pendulum around the crane tip in the $O_b - Y_bZ_b$ plane (blade and hook motion out of phase)	3.63	1.73

3.8.2 Crane movement

The natural period of the crane motion is identified by using decay tests while the vessel is fixed. A vertical force is applied at the crane tip and removed after some time. The natural period of the crane is calculated by analyzing the time series of the crane tip motion. The natural period is caused by the rotational motion of the crane boom around its hinged lower end due to the boom wire deformation. The crane boom itself has marginal deformation, compared to that of the boom wires. The natural period of the crane is affected by the lifted components and lifting gears. The crane itself has a natural period of 2.0s without lifting anything. However, when the installed blade and the lifting gear are considered, the crane natural period is shifted to approximately 2.9s.

3.8.3 Vessel motions

Eigenvalue analyses are conducted to identify the natural periods of the vessels' motion, excluding the crane and blade.

For the floating vessels, their natural frequencies are obtained by solving Eq.(3.17).

$$[-\omega^2(\mathbf{M} + \mathbf{A}_\infty) + \mathbf{K}] \cdot \mathbf{x} = 0 \tag{3.17}$$

where $\mathbf{M}$ is the vessel mass matrix; $\mathbf{A}_\infty$ is the added mass matrix at infinite frequency; $\mathbf{K}$ is the restoring matrix which is the sum of the hydrostatic restoring and the equivalent restoring from the DP system.

The eigenvalue analysis for the jack-up vessel is made by using the Lanczos method [94], considering the flexibilities in the jack-up legs and the soil foundations.

The results are presented in Table 3.2. The natural periods of the semi-submersible vessel are above 18s. The natural periods of the mono-hull vessel motion in heave, roll and pitch are between 9s∼14s, which are within

 40

typical wave period range. The natural periods of the jack-up vessel motion are much shorter than those of the two floating vessels.

Table 3.2: Natural periods of vessels' motions (defined in the vessel-related coordinate systems in Figure 2.2) [113]

Vessel	Surge	Sway	Heave	Roll	Pitch	Yaw
Semi-submersible	83.68 s	75.29 s	22.64 s	23.56 s	18.20 s	86.72 s
Mono-hull	87.27 s	75.23 s	10.00 s	13.51 s	9.07 s	85.69 s
Jack-up	2.912 s	3.087 s	2.363 s	0.479 s	0.594 s	0.451 s

3.9 Time domain simulations

This thesis focuses on the most critical phase of the blade installation process, i.e., the final mating phase of blade root into the turbine hub. Steady-state time-domain simulations were carried out to study the dynamic responses of the blade installation systems during the final blade mating phase. The blade installation procedures from lifting the blade from vessel deck to the hub height, are not addressed.

The 3D turbulent wind field used in the time domain simulations is generated by TurbSim [51], based on the IEC Kaimal Model defined in IEC 61400 [45]. Wind shear is also considered using the normal wind profile [45], where the mean wind speed U_z is calculated as a function of height z above the mean sea level, based on the power law principle, i.e.:

$$U(z) = U_{ref}(\frac{z}{z_{ref}})^{\alpha} \tag{3.18}$$

where U_{ref} is the reference mean wind speed at the reference height z_{ref} while α is the power law exponent. In this study, z_{ref} is 119m which is the designed hub height of the DTU 10MW wind turbine. The value of α is set to 0.14 for offshore wind field according to IEC 61400-3 [46]. The waves are simulated as long crested irregular waves based on the Joint North Sea Wave Project (JONSWAP) spectrum i.e.:

$$S(\omega) = \frac{\alpha g^2}{\omega^5} exp[-\beta(\frac{\omega_p}{\omega})^4]\gamma^{exp[\frac{(\frac{\omega}{\omega_p}-1)^2}{2\sigma^2}]} \tag{3.19}$$

where ω_p is the wave peak frequency; α is the spectral parameter; β is the form parameter and γ is the peakedness parameter[15].

For each sea state, a total of 30∼42 samples of 20 min steady-state simulations are carried out. In each sample, the first 10 min are removed, to exclude the numerical transient effects. Based on the time domain simulations, the characteristic values of the blade motion responses during the final mating phase are derived by extreme value distribution using either exceedance probability or mean-upcrossing rate [70]. Extrapolation techniques [69] are used for extreme value estimation corresponding to very low exceedance probability level in order to reduce computation efforts.

 42

Chapter 4

Global dynamic response analysis of the installation system

4.1 Overview

In this chapter, the dynamic response characteristics of offshore single blade installation by both jack-up and floating crane vessels are investigated using fully coupled time domain simulations. It addresses the installation by jack-up crane vessel (*paper 1, 2 and 3*) in Section 4.2, and the response characteristics and feasibility of floating crane vessel installation (*paper 4*) in Section 4.3, by a detailed comparison with jack-up crane vessel installation.

4.2 Offshore single blade installation by jack-up crane vessel

Figure 4.1 shows the scenario where an offshore wind turbine blade is installed using a jack-up crane vessel. During the installation process, the motions of the jack-up vessel and the crane are also important. The vessel motion can cause significant crane tip motion during lifting operations at large heights. The crane tip motion due to the vessel motion and crane flexibility also greatly increase the motion of the installed blade.

This section addresses the characteristics of the vessel motion (6 DOFs), the crane tip movement (3 DOFs), the blade motion at its COG and the corresponding translational motion at the blade root (3 DOFs). The blade root is considered as a point on the blade which is modeled as a rigid body.

 44

Therefore, the translational motion of the blade root is obtained from the 6 DOF rigid-body motion of the blade.

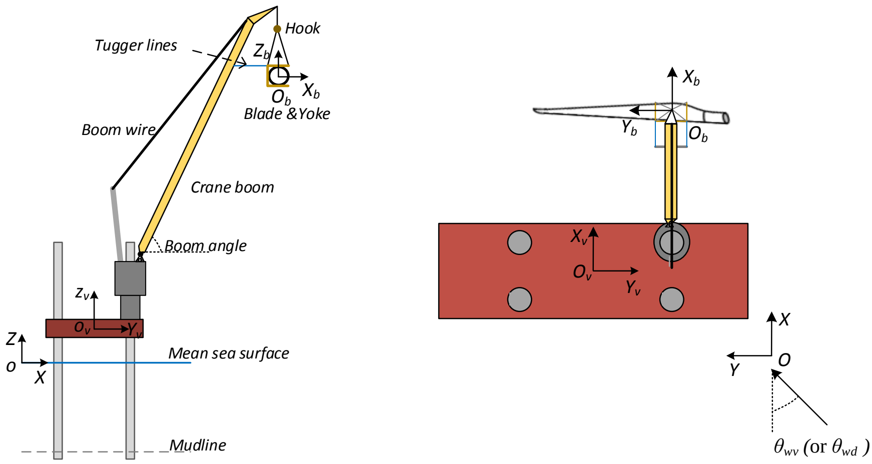

(a) Side view (b) Top view

Figure 4.1: Scenario of single blade installation using a jack-up crane vessel.

4.2.1 Jack-up vessel motion

The 6 DOF motion of the jack-up vessel is defined as for a floating vessel. The jack-up hull is considered as a rigid body. The vessel motion is mainly induced by the deformation of jack-up legs and soil-structure interaction. The wave loads on the legs are the main source of excitation. The wind loads on the vessel hull have minor contributions to the vessel motion, compared to the waves loads on legs. In addition, the soil properties have significant impacts on the jack-up vessel motion. It is revealed by a detailed comparison of system responses with various soil behaviours.

As shown in Figure 4.2(a), the characteristics of jack-up vessel motion are significantly affected by the soil-structure interactions. Compared to the modeling using linear springs combined with dampers, using simply pinned or fixed foundations is expected to give large discrepancies in the vessel motion. The pinned foundation modeling shifts the natural periods of vessel motion closer to wave frequencies, as shown in Figure 4.2(b). As a result, the vessel gets larger wave load excitations, leading to overestimated vessel motion. The fixed foundation modeling does the opposite and underestimates the JP motion. Hence, site-specific soil behavior modeling is essential.

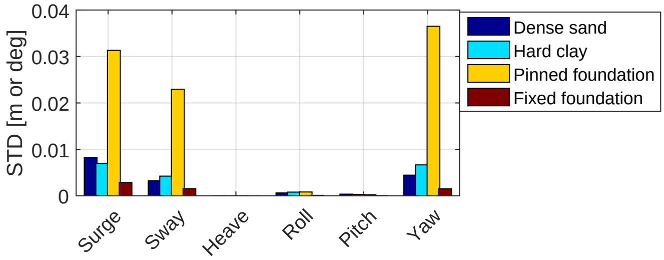

(a) Standard deviations

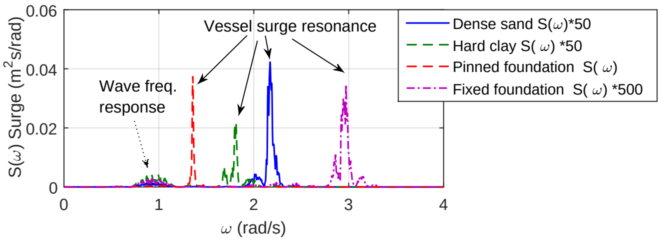

(b) Power spectra of the surge motion [112]

Figure 4.2: Standard deviations and power spectra of jack-up vessel motion with different soil models: $U_w = 10.23m/s$, $\theta_{wd} = 0deg$; $H_s = 2.4m$, $T_p = 8.55s$, $\theta_{wv} = 65.87deg$.

4.2.2 Crane tip motion

The crane tip motion gets remarkable contributions from the wave-induced vessel motion, as indicated by the results in Figure 4.3(a). Besides, the crane tip motion also gets significant contribution from the crane flexibility caused by the deformation of boom wires. As the crane is deployed in the vertical $O_vY_vZ_v$ plane during the operation. It gives significant contributions to the crane tip motion along Y_v and Z_v, as can be observed in the power spectra in Figure 4.3(b).

As revealed by Figure 4.4, the calculated crane tip motion is affected by the soil behavior modeling. The crane tip motion in hard clay soil is found to be slightly different from that in dense sand. In addition, the crane tip motion is dependent on modeling of soil reaction forces. Compared to the modeling using linear springs combined with dampers, the pinned foundation model gives a significant overestimation of crane tip motion, especially along X_v and Y_v, caused by the overestimated vessel motion. Likewise, the crane tip motion is remarkably underestimated by the fixed foundation model.

 46

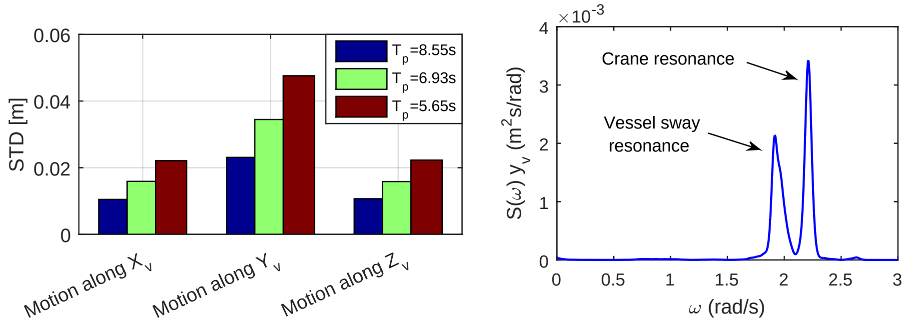

(a) (b)

Figure 4.3: Standard deviations and power spectrum of the crane tip motion: the soil is dense sand modeled using linear springs combined with dampers, $U_w = 10.23m/s$, $\theta_{wd} = 0deg$; $H_s = 2.4m$, $\theta_{wv} = 65.87deg$; (a) Standard deviations the crane tip motion with varying T_p; (b) power spectrum of the crane tip motion along Y_v with $T_p = 8.55s$ [115].

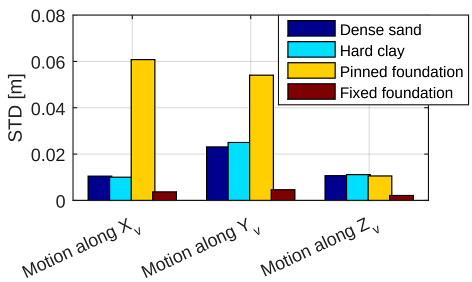

Figure 4.4: Standard deviations of the crane tip motion with different models of soil reaction forces: $U_w = 10.23m/s$, $\theta_{wd} = 0deg$, $H_s = 2.4m$, $T_p = 8.55s$, $\theta_{wv} = 65.87deg$.

4.2.3 Blade motion

The 6 DOF rigid-body motion of the blade at its COG is defined in the blade-related coordinate system in Figure 2.2(a).

Results in Figure 4.5(a) shows that significant underestimation in blade motion is expected if the crane tip is assumed fixed. As indicated by the power spectra of blade sway motion in Figure 4.5(a), the blade motion gets significant contributions from both jack-up vessel motion and crane flexibility, as can be observed in Figure 4.5(a).

The blade surge, heave and pitch motions are mainly caused by the vessel motion and crane deformation, as shown in Figure 4.5(a). They show large dependencies on the wave conditions.

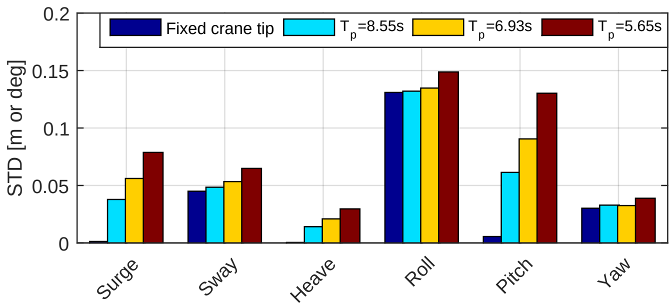

(a) Standard deviations of blade motion

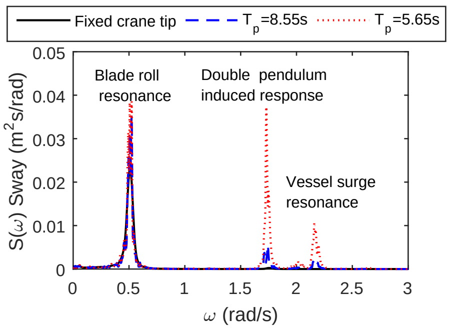

(b) Power spectra of blade sway motion

Figure 4.5: Comparison of blade motion in varying wave conditions with dense sand soil. The fixed crane tip case considers only wind loads on the blade; for the other three cases, the vessel and the crane tip are free to move, both wind and waves are considered. $U_w = 10.23m/s$, $\theta_{wd} = 0deg$; $H_s = 2.4m$, $\theta_{wv} = 65.87deg$.

The blade sway, roll and yaw motions are mainly induced by the blade aerodynamic loads while they are affected by the vessel and crane tip motions. As shown in Figure 4.5(b), the blade sway motion is completely dominated by the blade roll resonant response when the crane tip is assumed fixed. Considering the vessel motion and crane flexibility introduce another two peaks into its power spectrum, due to the double pendulum induced response and the vessel surge resonant motion. Overall, their effects increase significantly in short waves.

As shown in Figure 4.6, the modeling of soil behavior significantly affects the blade motion during installation by jack-up vessels. The blade motion installed by jack-up crane vessel with hard clay soil is observed to have larger

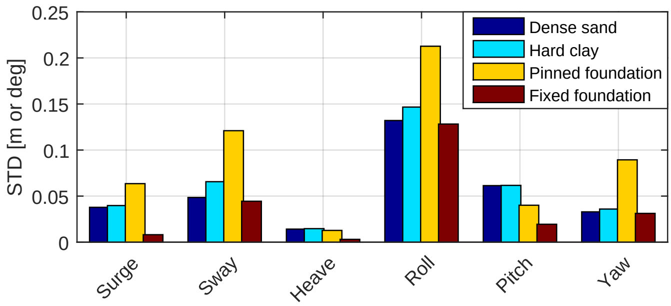

Figure 4.6: Standard deviations of the blade motions with different soil models: $U_w = 10.23m/s$, $\theta_{wd} = 0deg$; $H_s = 2.4m$, $T_p = 8.55s$; $\theta_{wv} = 65.87deg$.

motion than in dense sand soil. Compared to the linear spring combined with damper model, the pinned foundation modeling and fixed foundation modeling of soil respectively overestimates and underestimates the blade motion.

4.2.4 Blade root motion

The blade root motion is critical during the final mating phase. It is defined in the blade related coordinate system in Figure 2.2(a). An illustration of the blade root motion in time domain is shown in Figure 4.7.

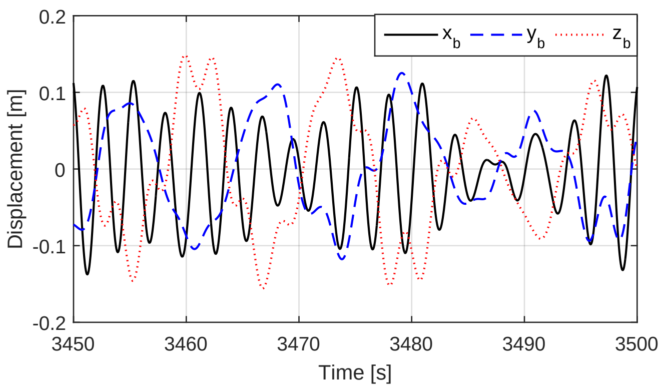

Figure 4.7: Example time series of blade root motion after removing mean: $U_w = 10.23m/s$, $\theta_{wd} = 0deg$, $H_s = 2.4m$, $T_p = 6.93s$, $\theta_{wv} = 65.87deg$; the soil is dense sand modeled using linear springs combined with dampers.

Figure 4.8(a) shows the standard deviations of blade root motion. Com-

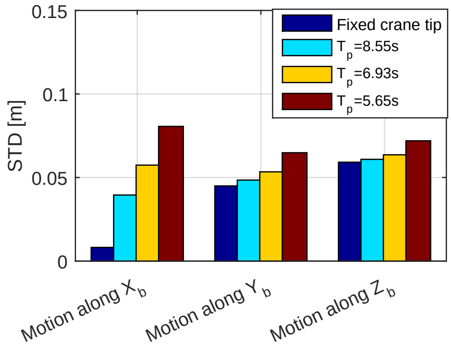

(a) with varying wave conditinos

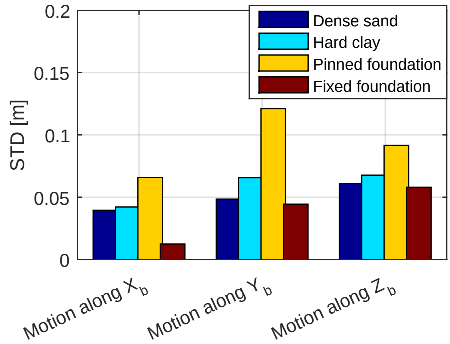

(b) with different soil models

Figure 4.8: Standard deviations of the blade root motion: $U_w = 10.23m/s$, $\theta_{wd} = 0deg$; *(a)* $H_s = 2.4m$, $\theta_{wv} = 65.87deg$; *the soil is dense sand modeled using linear springs combined with dampers. (b)* $H_s = 2.4m$, $T_p = 8.55s$; $\theta_{wv} = 65.87deg$.

paring results in Figure 4.8(a) shows that the blade root motion would be significantly underestimated, especially along X_b, if the detailed modeling of vessel and crane motion is not considered. Larger underestimation is expected to occur in shorter waves.

As revealed in Figure 4.8(b), site-specific soil properties are essential for better estimation of blade root motion during installation by jack-up crane vessels. Simple modeling of soil behavior using pinned (fixed) foundations gives large overestimation (underestimation) of blade root motion. This is caused by the differences in the corresponding contributions from vessel motion, which can be observed in the power spectra of blade root motion along Z_b shown in Figure 4.9.

4.3 Single blade installation using floating crane vessels

Floating crane vessels are flexible with respect to working water depth and are much faster in relocation. They are thus a promising alternative to install offshore wind turbine components, especially in intermediate and deep water.

In this thesis, the single blade installation by floating crane vessels is numerically studied, by a detailed system response comparison with jack-up crane vessel installation which has dens sand soil modeled using linear

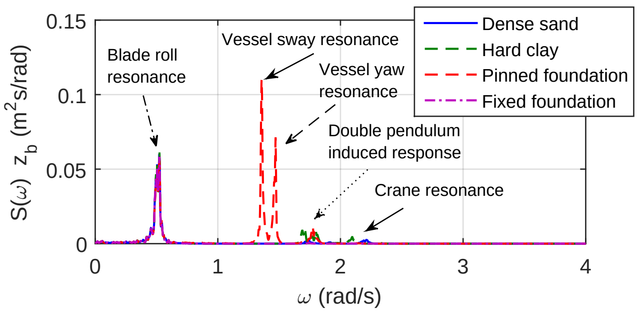

Figure 4.9: Power spectra of blade root motion along Z_b with different soil models: $U_w = 10.23m/s$, $\theta_{wd} = 0deg$; $H_s = 2.4m$, $T_p = 8.55s$; $\theta_{wv} = 65.87deg$ [112].

springs combined with dampers. Figure 4.10 illustrates the installation scenarios.

4.3.1 Vessels' motion

The floating vessels' motions are mainly induced by the wave loads. They are marginally affected by the blade aerodynamic loads and blade motion. Figure 4.11 shows the standard deviations of the floating vessels' motion with varying incident wave directions, comparing with the jack-up vessel motion. The vessels' motions are defined in the vessel-related coordinate systems shown in Figure 2.2. The floating vessels' motions are much larger than that for the jack-up vessel. Compared to the mono-hull vessel, the semi-submersible vessel has smaller motion and is less sensitive to varying wave directions. Because the semi-submersible vessel has natural periods of motion much larger than typical wave periods, leads to better motion performance within general wave frequency range, as shown in Figure 4.12.

4.3.2 Crane tip motion

The crane tip motion is defined in the vessel-related coordinate system for each installation system shown in Figure 2.2. The standard deviations of crane tip motion with varying incident wave directions are shown in Figure 4.13. The crane tip motion on the floating vessels is much larger than that on the jack-up vessel. Different from the jack-up crane vessel, the crane tip motion on the floating vessels is mainly resulted from the wave-induced vessel motion while the crane flexibility gives a minor contribution, which

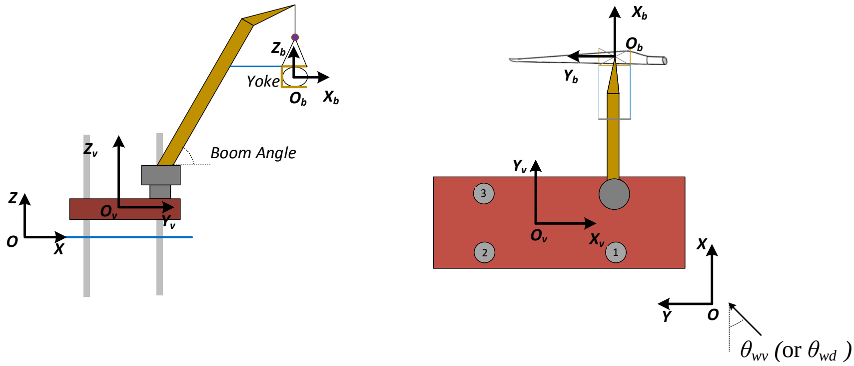

(a) Jack-up vessel: side view and top view

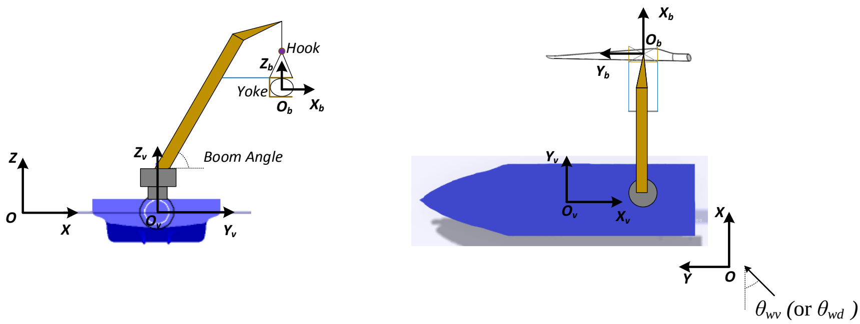

(b) Mono-hull vessel: side view and top view

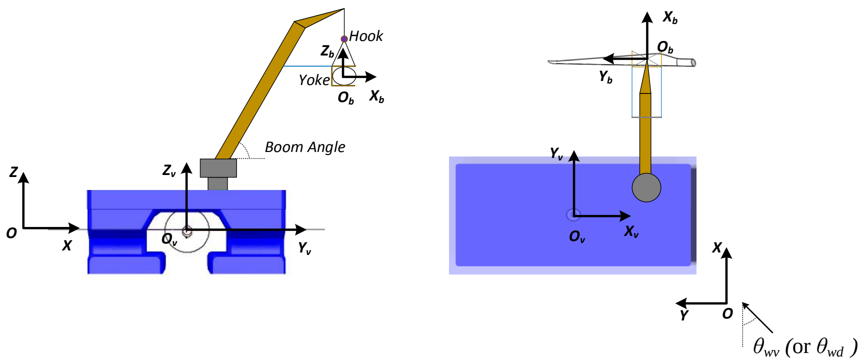

(c) Semi-submersible vessel: side view and top view

Figure 4.10: Illustration of installation scenarios of floating vessel installations in comparison with jack-up vessel installation.

 52

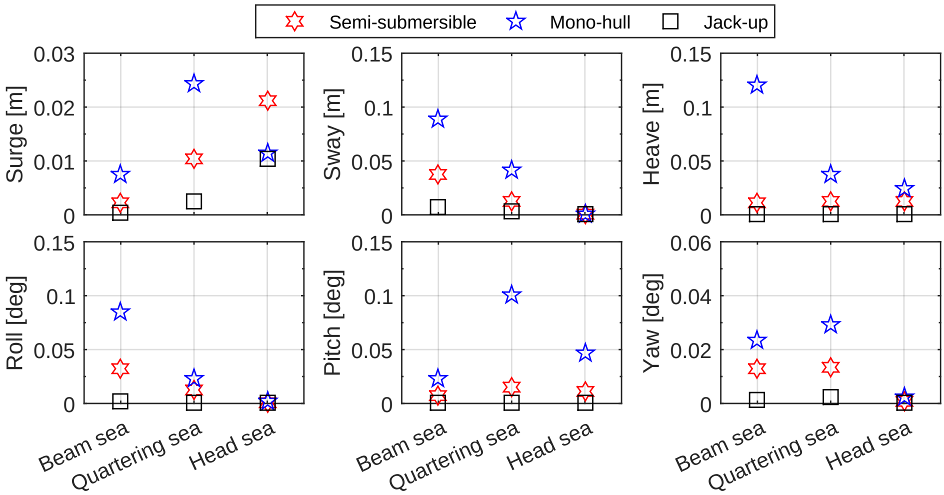

Figure 4.11: Standard deviations of floating vessels' motion with varying wave directions: $H_s = 1m$, $T_p = 7.3s$; beam sea $\theta_{wv} = 0deg$, quartering sea $\theta_{wv} = 315deg$ and head sea $\theta_{wv} = 270deg$.

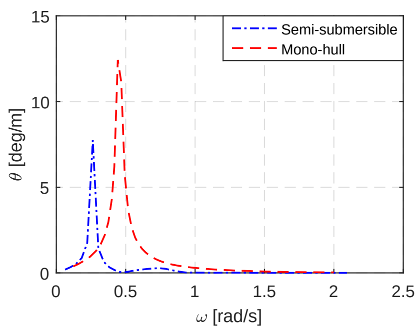

Figure 4.12: RAO of the floating vessels' roll motion. The transfer functions are estimated with incident wave angle of 0^o *[113].*

can be observed in Figure 4.14. Overall, the semi-submersible vessel has a much smaller crane tip motion than the mono-hull vessel.

Comparing Figures 4.11 and 4.13, the amplitude of crane tip motion is generally larger than the vessel translational motion, for crane operations at large lifting height, since the vessel's rotational motion greatly contributes to the crane tip motion. However, the former can be smaller than the latter in some cases. For example, for the mono-hull vessel in beam sea condition, the crane tip motion in Z_v direction is smaller than the vessel heave motion.

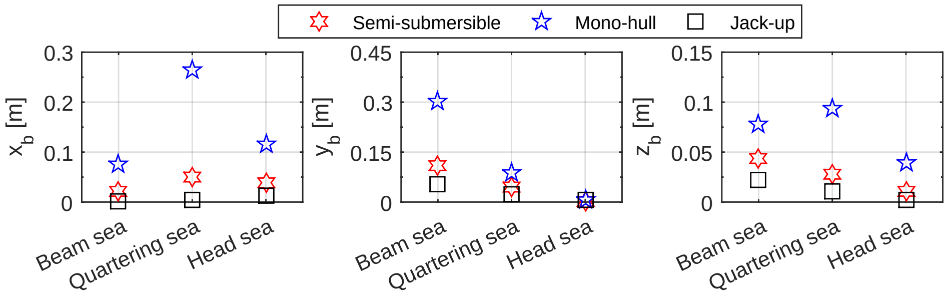

Figure 4.13: Standard deviations of the crane tip motion with varying wave direction: $H_s = 1m$*,* $T_p = 7.3s$*; beam sea* $\theta_{wv} = 0deg$*, quartering sea* $\theta_{wv} = 315deg$ *and head sea* $\theta_{wv} = 270deg$*.*

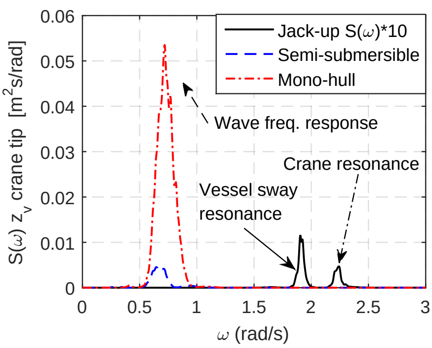

Figure 4.14: Power spectra of crane tip motion along Z_v*:* $H_s = 1m$*,* $T_p = 7.3s$*; quartering sea* $\theta_{wv} = 315deg$ *[113].*

Because the former gets significant contribution from the mono-hull vessel's roll motion which is out of phase with and counteracts the latter.

4.3.3 Blade motion

The blade motion, referring to its COG, is defined in the blade-related coordinate system for each installation system in Figure 2.2.

Figure 4.16 identifies the relative importance of wave-induced vessel motion and blade aerodynamic loads on the blade motion. The blade surge, heave and pitch motions are mainly resulted from the wave-induced vessel motion, for both floating and jack-up crane vessels. The blade motion in other DOFs has contributions from both factors. When being installed by the jack-up crane vessel, the aerodynamic loads have a dominant effect on

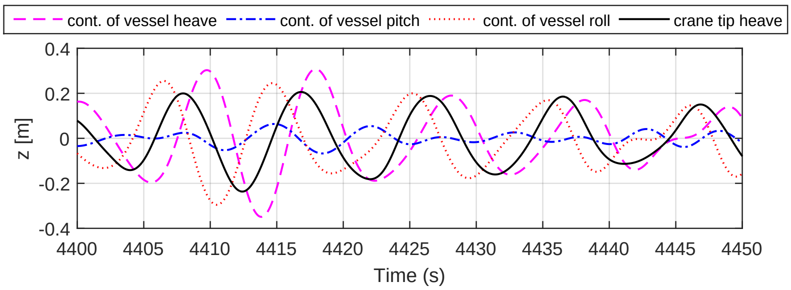

Figure 4.15: Contributions of the mono-hull vessel's motion to the crane tip motion in Z_v direction in beam sea condition: $H_s = 1m$, $T_p = 7.3s$ [113].

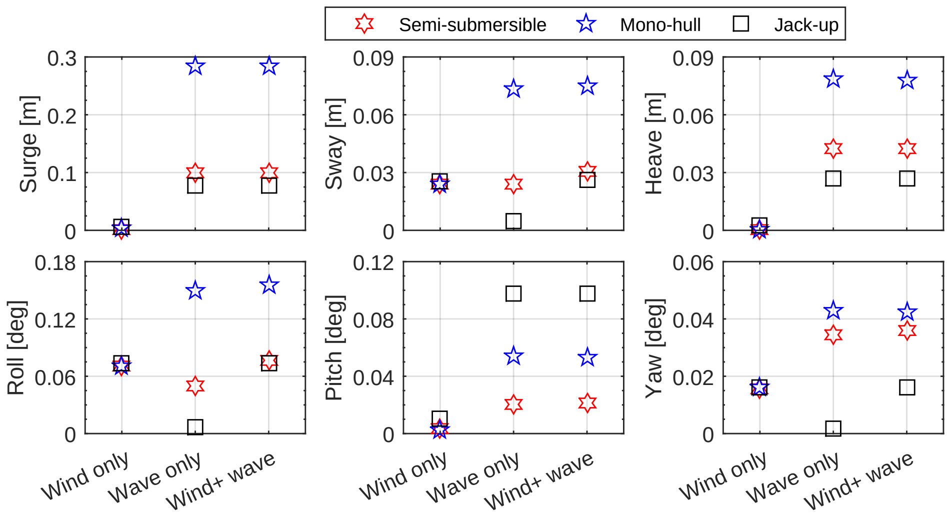

Figure 4.16: Standard deviations of blade motion in wind only, wave only and combined wind and wave conditions: $U_w = 7.0m/s$, $\theta_{wd} = 0deg$; $H_s = 1m$, $T_p = 7.3s$, beam sea $\theta_{wv} = 0deg$.

blade motion in sway, roll and yaw. When floating crane vessels are used, both aerodynamic loads and wave-induced motion are important. As shown by the power spectra of blade roll motion in Figure 4.17, both the wave-induced vessel motion and blade aerodynamic loads can excite the blade roll resonant response for floating vessels. Besides, the wave frequency response in blade roll motion is caused by the floating crane vessels. Compared to the semi-submersible vessel, the wave frequency motion is significant when the blade is installed by the mono-hull vessel and the double-pendulum motion

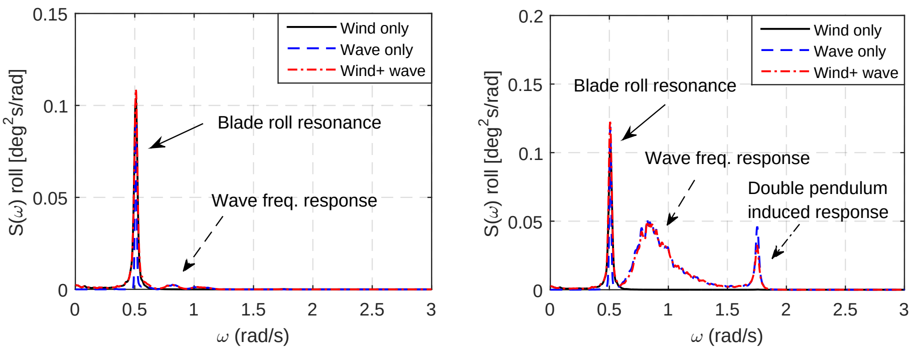

(a) By semi-submersible vessel

(b) By mono-hull vessel

Figure 4.17: Power spectra of blade roll motion: $U_w = 7.0m/s$, $\theta_{wd} = 0deg$; $H_s = 1m$, $T_p = 7.3s$, *beam sea* $\theta_{wv} = 0deg$ *[113].*

is excited as a result.

Figure 4.18 compares the blade motion with varying incident wave direction. Due to the significant wave frequency response of the mono-hull vessel, the installed blade has much larger motion amplitudes and are more sensitive to varying wave direction, than the semi-submersible and the jack-up vessels. The blade motion on the semi-submersible vessel is slightly larger than that on the jack-up vessel. Overall, the installed blade motion is the smallest when the crane vessels are in head sea condition.

Similar to the crane tip motion, the blade motion on the floating vessels has relatively less important contributions from the crane dynamics, as shown in Figure 4.19. On the jack-up vessel, the crane resonant response is important for the blade motion.

4.3.4 Blade root motion

The blade root translational motion is given in the blade-related coordinate system for each installation system shown in Figure 2.2. Figure 4.20 shows the standard deviations of blade root motion with varying wave direction. The blade root motion is found to have large dependency on the wave conditions, especially during installation by the mono-hull vessel. The mono-hull vessel has the largest blade root motion, followed by the semi-submersible vessel which has slightly larger values than the jack-up vessel. The blade root motion is observed to reach its minimum in head sea condition.

To reduce the blade root motion during installation, the wave direction of 285 deg, close to the vessel head sea condition, is used to utilize the

 56

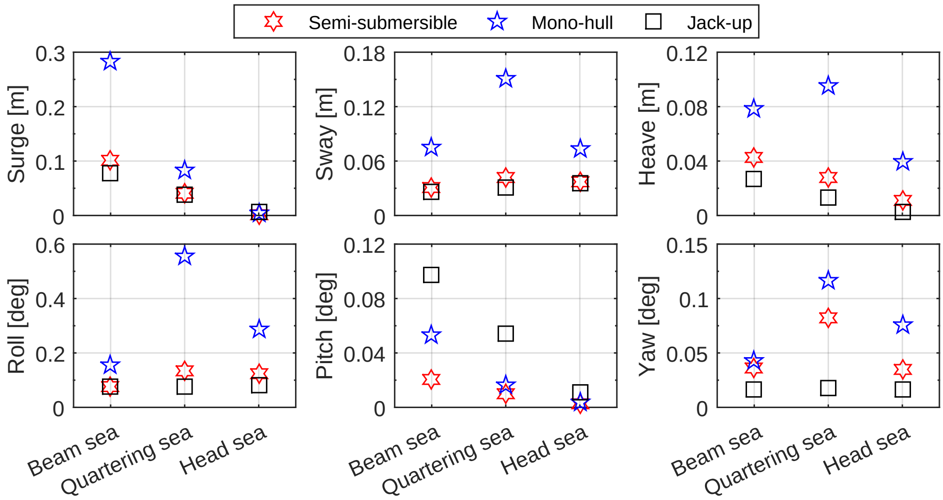

Figure 4.18: Standard deviations of blade motion with varying wave direction: $H_s = 1m$, $T_p = 7.3s$; beam sea $\theta_{wv} = 0deg$, quartering sea $\theta_{wv} = 315deg$ and head sea $\theta_{wv} = 270deg$.

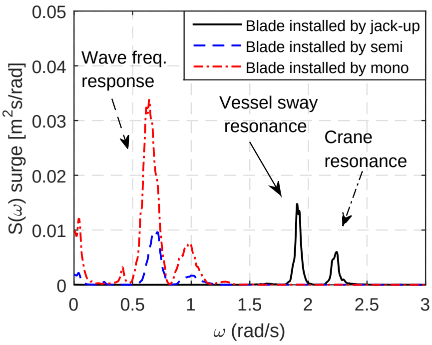

Figure 4.19: Power spectra of blade surge motion: $U_w = 7.0m/s$, $\theta_{wd} = 0deg$; $H_s = 1m$, $T_p = 7.3s$, quartering sea $\theta_{wv} = 315deg$ [113].

wave orientation to improve vessel performance. The 15 deg offset from the head sea direction is recommended by DNVGL-RP-N103 [22] to represent a practical head sea condition during operation. Figure 4.21 further compares the standard deviations of blade root motion with varying wave peak period T_p. The jack-up crane vessel causes the smallest motions, followed by the semi-submersible vessel and the mono-hull vessel. The motion of blade root on the jack-up vessel decreases with increasing T_p, since the vessel gets decreasing wave excitations. On the contrary, the floating crane vessels

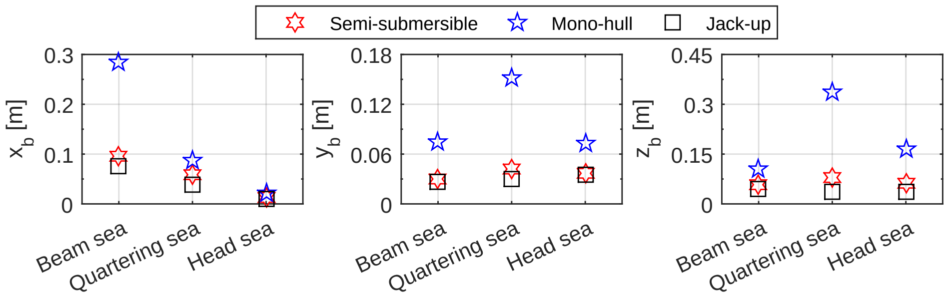

Figure 4.20: Standard deviations of blade root motion with varying wave direction: $U_w = 7.0m/s$, $\theta_{wd} = 0deg$; $H_s = 1m$, $T_p = 7.3s$; beam sea $\theta_{wv} = 0deg$, quartering sea $\theta_{wv} = 315deg$ and head sea $\theta_{wv} = 270deg$.

have remarkable increases in blade root motion, as shown in Figure 4.21. A much smaller increase is observed for the semi-submersible vessel than the mono-hull vessel, since the semi-submersible vessel causes much less wave frequency response in blade root motion.

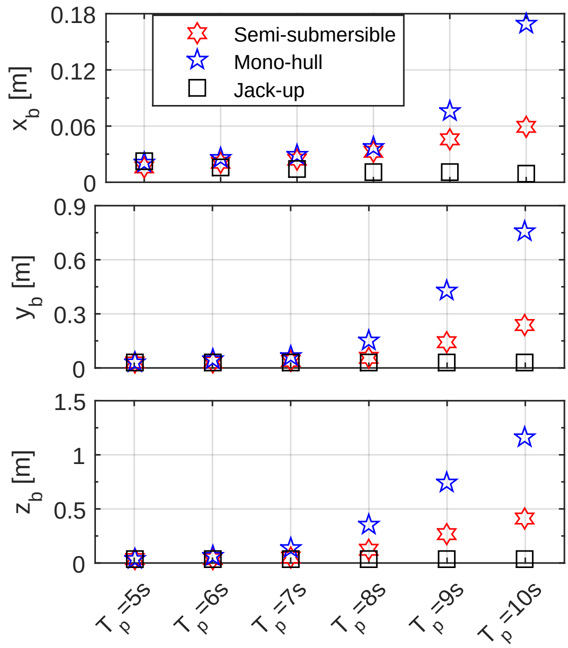

Figure 4.21: Standard deviations of blade root motion with varying wave peak period: $U_w = 7.0m/s$, $\theta_{wd} = 0deg$; $H_s = 1m$, $\theta_{wv} = 285deg$ close to head sea.

 58

Figure 4.22 further compares the translational movements at blade root with that at blade COG and crane tip in the global coordinate system, during installation by all three crane vessels. The motions at crane tip, blade COG and blade root are found to be quite different from each other. The blade COG movement is quite different from that of the crane tip. When the jack-up crane vessel is used, the former is overall larger than the latter. For floating crane vessels, the former is observed to be smaller than the latter on the mono-hull vessel, especially along global X and Y directions, when T_p is smaller than 8s. Besides, the blade root movement along the global Z direction is found to be much larger than that of the blade COG during installations by all three vessels. Hence, detailed system modeling and analysis are recommended during the planning phase of offshore wind turbine installation, including the modeling of vessel motion, crane dynamics, lifting arrangement and lifted component, to ensure safe and efficient operations.

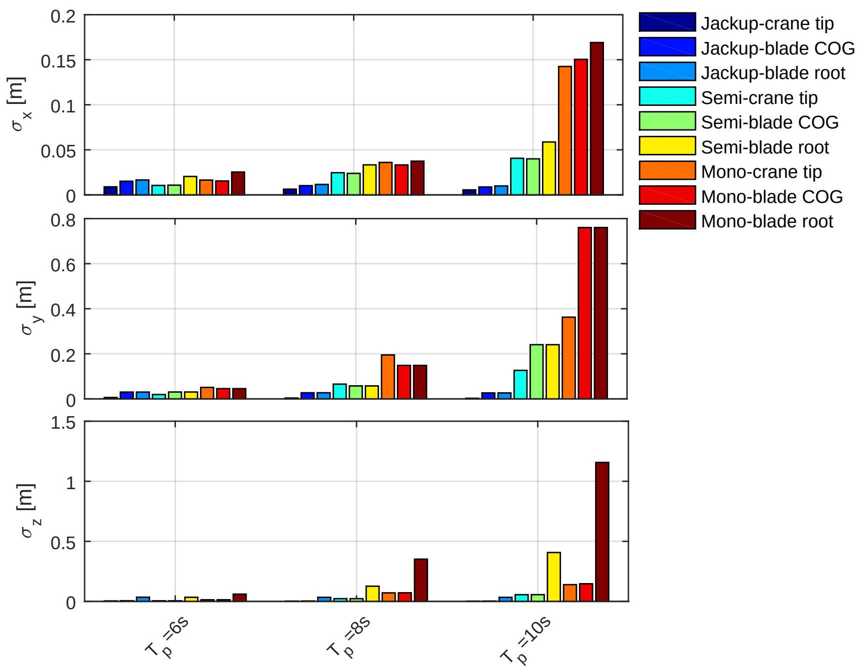

Figure 4.22: Comparison of blade root motion with that of blade COG and crane tip in the global coordinate system during installation by jack-up, mono-hull and semi-submersible crane vessels: $U_w = 7.0m/s$, $\theta_{wd} = 0deg$; $H_s = 1m$, $\theta_{wv} = 285deg$ *close to head sea.*

4.3.5 Tension in tugger lines

Identical tugger line system with two horizontally deployed tugger lines are used to control the heading of the blade during installation by the three crane vessels. The tugger line 1 is close to blade root while tugger line 2 is close to blade tip. During the simulations, no slack event is observed within the tugger lines.

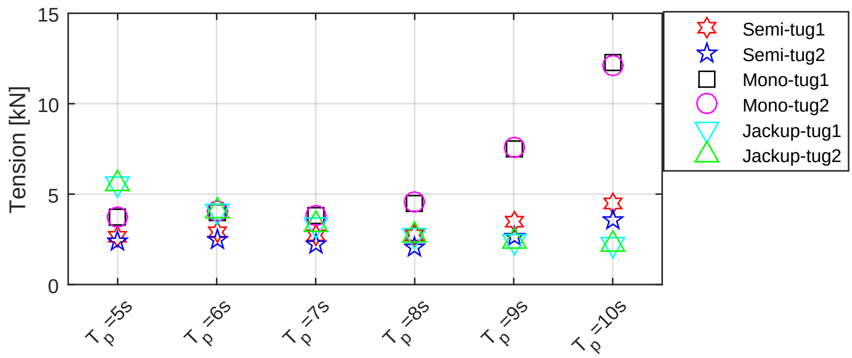

Figure 4.23: Standard deviations of tugger line tension with varying wave peak period: $U_w = 7.0m/s$, $\theta_{wd} = 0deg$; $H_s = 1m$, $\theta_{wv} = 285deg$ close to head sea.

Figure 4.23 compares the standard deviations of tugger line tension with varying wave peak period. When the T_p is 5s, the tugger lines on the jack-up vessel have larger tension fluctuations than floating vessels. With the increase of T_p, the tugger lines on the jack-up vessel experience a decrease in variation of tension while those on the floating vessels have a remarkable increase. Compared with the tugger lines on the mono-hull vessel, those on the semi-submersible vessel experience much lower fluctuation in tension.

Overall, the system response of single blade installation by the jack-up crane vessel decreases with increasing wave period. On the contrary, it increases significantly with the increase of wave period when floating crane vessels are used. The crane flexibility plays a relatively important role in the dynamic responses of installation by jack-up vessel while it is less important for floating vessel installations.

4.3.6 Feasibility of floating crane vessel installation

During single blade installation for offshore wind turbines, the mating operation is not feasible or successful if one of the following scenarios occur during the mating phase:

 60

- Too large blade root displacement in the radial direction of the hub opening, since it can make mating operation not possible.
- Excessive blade root velocity, especially in the radial direction of the hub opening, since it can cause impact with the hub opening and consequently damage guide pins at the blade root. The guide pins are much stronger in taking axial force than bending moment [104].

Therefore, the blade root displacement (R_{xz}) and velocity (V_{xz}) in the radial direction of the hub opening are two critical parameters that strongly affect the feasibility of single blade installation by floating vessels. Nevertheless, relevant quantitative criteria with respect to these two critical parameters are difficult to obtain.

In order to assess the feasibility of single blade installation by floating crane vessels, the criteria are assumed to be the characteristic values of R_{xz} and V_{xz} of the blade root during installation by a typical jack-up crane vessel ($U_w = 8.3m/s$, $\theta_{wd} = 0deg$; $H_s = 1.5m$, $T_p = 7.7s$, beam sea $\theta_{wv} = 0deg$) [113]. The criteria considered are conservative as the environmental condition is below the operational limits for single blade installation by jack-up crane vessels.

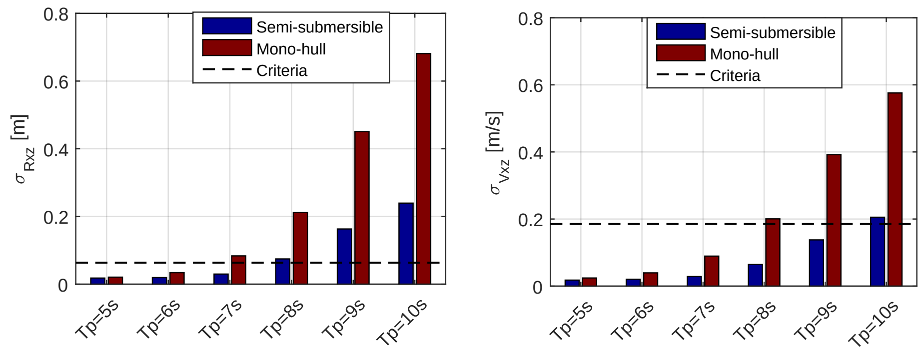

(a) Displacement (b) Velocity

Figure 4.24: Comparison of blade root motion R_{xz} and V_{xz} in the radial direction of the hub opening in the global coordinate system: $U_w = 7.0m/s$, $\theta_{wd} = 0deg$; $H_s = 1m$, $\theta_{wv} = 285deg$ close to head sea [113].

Figure 4.24 presents the comparison of R_{xz} and V_{xz} with varying wave peak period, against the selected criteria. The significant wave height and wind condition are kept constant. As shown in Figure 4.24, both R_{xz} and V_{xz} increase significantly with increasing T_p. Single blade installation by the mono-hull crane vessel is feasible under wave conditions with T_p less

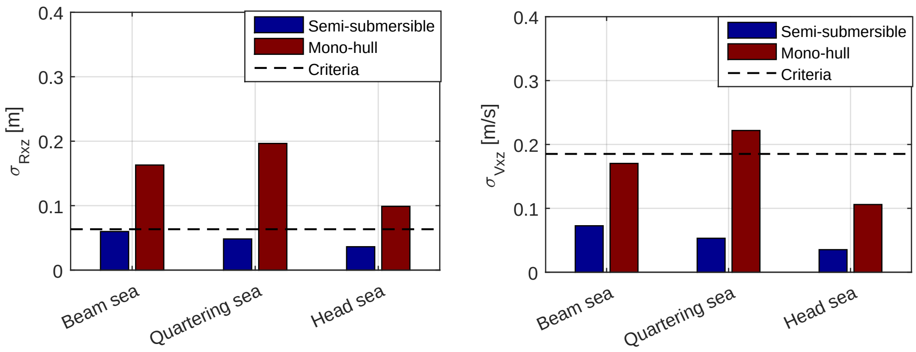

(a) Displacement (b) Velocity

Figure 4.25: Comparison of blade root motion R_{xz} and V_{xz} in the global coordinate system with varying incident wave direction: $U_w = 7.0m/s$, $\theta_{wd} = 0deg$; $H_s = 1m$, $T_p = 7.3s$ [113].

than 7s. The semi-submersible vessel installation is feasible with a larger T_p of about 8s. Thus, the feasibility of single blade installation by floating vessels is dependent on the probability of peak period T_p, or the probability of operational weather window.

The feasibility of single blade installation by floating vessels is expected to be larger at offshore wind farm sites characterized by relatively short waves, such as in the North Sea, rather than sites dominated by long waves. Because the blade during installation by floating vessels has smaller motion in short waves than in long waves, as can be observed in Figure 4.24.

To increase feasibility and performance of floating crane vessels in single blade installation, the vessels should be carefully selected. Increase of vessel size is one possible solution from the technical point of view, but it will increase the vessel construction cost and consequently the operational cost. Another possible solution is to use a floating vessel with better hydrodynamic performance, e.g., with natural periods of vessel motion outside typical wave period range. A suitable vessel type is semi-submersible. The geometrical parameters of a semi-submersible vessel, such as pontoons, columns, cross section and overall size, usually can make its natural periods of motion beyond upper limit of typical wave periods.

Utilization of weather orientation is another way to improve the floating vessels' performance when installing wind turbine blades, as shown by the comparison in Figure 4.25. By adjusting the vessel heading relative to the wave direction, such as head sea, the blade root radial motion is greatly reduced for both of the floating vessels.

 62

Floating crane vessels can more easily be relocated during offshore wind turbine installation, than jack-up vessels. The installation process of a jack-up vessel, such as leg lowering and retrieval, is sensitive to wave conditions and very time consuming (over 4 hours in total) [29]. Nevertheless, it is not necessary for floating vessels, and hence the time spent on relocation can be significantly shorter.

Chapter 5

Assessment of operational environmental limits using response-based criteria

5.1 General

By ensuring a safe and efficient final mating of the blade would greatly reduce the overall installation costs. The physical limits during the mating are the annular mating gap between the blade root and the hub, and no structural bending damage in the blade root guide pins. Expressing these physical limits in terms of allowable environmental conditions, such as wind and waves, would be very helpful for the planning and execution phases of the operation, since the environmental conditions can be forecasted prior to and tracked during execution of operations. By using numerical modelling and analysis, derivation of the environmental limits of offshore single blade installation could be achieved.

Acero et. al has proposed a generic methodology to assess the environmental limits of offshore wind turbine installation [38]. The methodology was applied to establish the environmental limits of transition piece mating [36], monopile hammering [62] and fully assembled turbine installation [35]. In those application, only waves are considered as the main source of excitation loads. When assessing the operational limits wind turbine blade installation, wind conditions also need to be considered, in addition to wave conditions.

In this chapter, a systematic approach to assess the operational limits based on response criteria for offshore blade mating operation is proposed.

 64

The approach is demonstrated by a case study considering single blade installation for a jacket wind turbine by a semi-submersible crane vessel. The hub motion of a typical jacket wind turbine is assumed small and not considered in this study.

5.2 Methodology

First of all, the potentially critical events should be identified based on the system configuration, installation procedure and numerical modelling of the sequentially defined installation activities. A general description of the wind turbine blade installation procedures was given in Chapter 2. The final mating operation is found to be critical. Then the corresponding limiting parameters are identified for those events. The establishment of the environmental limits includes a combination of three main aspects, i.e., the allowable limits of the limiting parameters based on the physical limits, safety factors, and the characteristic response values. The characteristic values of the limiting parameters need to be computed based on time domain analysis using the numerical model and extreme value distribution theories. The allowable environmental limit for each event can be identified by comparing the characteristic values of the limiting parameter at various environmental conditions with the allowable response limit. In principle, safety factors need to be considered in the operational limits due to uncertainties, for instance, from numerical modelling and human actions in practical operations. However, the safety factor is assumed to be 1 in this study.

5.2.1 Identification of critical events and limiting parameters

The motion monitoring phase is pre-requisite for the mating operation. In this phase, the blade root motion is monitored to see if mating attempts are possible or not. The critical event is failure of mating attempts due to excessive blade root motion relative to the radial direction of turbine hub opening. The corresponding limiting parameter is the blade root motion in the hub opening's radial direction.

During the mating phase, plastic deformation in blade root guide pins may occur when the blade root collides with the hub. Particularly, radial impacts are much more critical than axial impacts. Because radial impacts may result in bent guide pins, leading to failure of mating operation. Thus, the critical event is plastic bending deformation in guide pins. The deformation is closely related to impact velocity. The limiting parameter is taken as the radial impact velocity of the blade root. The relationship between the impact velocity and deformation could be established based on advanced structural analysis of the impact scenario[105]. The core principle of the structural analysis is the same with that for blade tip collision with neighbouring structures in Paper 5. The dependency of structural damage on impact velocity can be obtained by a series of structural analysis based on the detailed modelling of impact scenario. The threshold impact velocity which causes nearly zero damage energy (corresponds to zero plastic deformation) could be further captured. The threshold impact velocity can be further used to quantify the environmental limits.

During the whole operation, structural integrity in wire and ropes needs to be ensured . On one hand, the maximum wire tension should be within the wire design capacity. The wires are assumed to have sufficient capacities since they are also used to install much heavier wind turbine components such as transition pieces. On the other hand, slacks in wires should be avoided, especially in tugger lines. The lift wire and slings are found to be always tensioned during the operation due to the gravity of the installed blade. Since slacks in tugger wires can be adjusted by increasing the pretension, they are considered as a restrictive event.

Figure 5.1 list a summary of the critical events and corresponding limiting parameters.

	Operation	Potential critical events	Limiting parameter	Allowable limit
Motion monitoring phase	- Align blade root with hub opening - Monitor blade root motion	- Failure of mating attempts due to excessive blade root relative to hub opening	- Radial motion of blade root relative to hub opening	- Radius of mating gap
Mating phase	- Mate blade root onto the hub	- Guide pins at blade root bent - Wire slack (restrictive)	- Radial impact velocity - Tension in tugger lines	- Established based on FEM analysis - Tension larger than zero

Figure 5.1: Potential critical events, corresponding limiting parameters and allowable limits for the blade mating operation [116]

5.2.2 Allowable limits for and characteristic values of the limiting parameters

In the monitoring phase, the allowable limit for the annular mating gap is quite straight forward which is the gap between the hub opening and blade root. In practical operations, the actual value of mating gap radius can be

 66

obtained based on the detailed dimensions of the blades and the turbine hub.

In the final mating phase, the allowable limit of impact velocity is related to impact damage criteria. For wind turbine blades, the specific value of the allowable limit need to be established based on FEM analysis of the impact scenario, as discussed in the previous section. The structural damage criteria can be expressed in terms of impact velocity.

The characteristic values of the identified limiting parameters need to be calculated based on time domain coupled analysis of the operational scenario. Details of the discussion about the numerical model can refer to Chapter 3. The characteristic values of the limiting parameters can be derived on the basis of extreme value distribution using either exceedance probability or target percentile. The exceedance probability is dependent on the consequences of failure events. In the monitoring phase, the mating attempts can always be tried again. Thus, the consequence of failure is relatively less severe and a larger exceedance probability can be designed. However, damaged guide pins in the mating phase lead to irreversible operation and severe consequence. Therefore, a small exceedance probability should be considered.

5.2.3 Operational limits for the complete mating operation

The complete blade mating operation consists of the motion monitoring phase and the mating phase. The operational limits for each of these two activities can be identified by comparing the characteristic value of the limiting parameter with the corresponding allowable limit, under various possible environmental conditions. By combining the operational limits of both activities and taking the lower envelope, the operational limits for the complete operation can be obtained.

The procedures are summarized in the flowchart shown in Figure 5.2.

5.3 Case study

In this section, the methodology is demonstrated by using the scenario that a semi-submersible crane vessel installing a DTU 10MW wind turbine blade onto a jacket foundation located at water depth of 39m. Typically, jacket wind turbines have relatively small hub motion. In the case study, the hub motion is not considered. Figure 5.3(a) shows an illustration of the system. Main parameters of the system components can be found in Chapter 2.

For the motion monitoring phase, the allowable limit is the annular

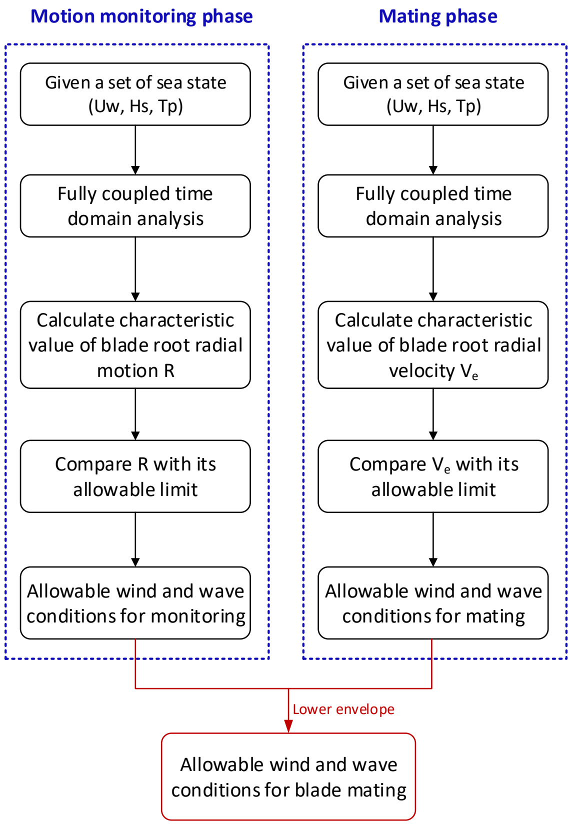

Figure 5.2: Flowchart of assessing allowable wind and wave conditions for the blade mating operation[116]

mating gap between the hub radius and blade root. In this case study, it is assumed to be proportional with the radius of blade root:

$$r = \lambda R_{root} \tag{5.1}$$

where λ is a factor, which is assuemed to be between 10%$\sim$20%. The characteristic value of blade root radial motion (R) is quantified based on average outcrossing rate. The failure of mating attempts has low consequence. It is assumed that the mating is possible if the blade root crosses the circular boundary once per minute. More accurate value can be assigned based on specific operations. The characteristic value of the blade root radial motion is the value corresponding to a mean upcorssing rate of $\nu^+ = 0.0167s^{-1}$, as illustrated in Figure 5.4(a).

In the blade mating phase, the limiting parameter is the blade radial

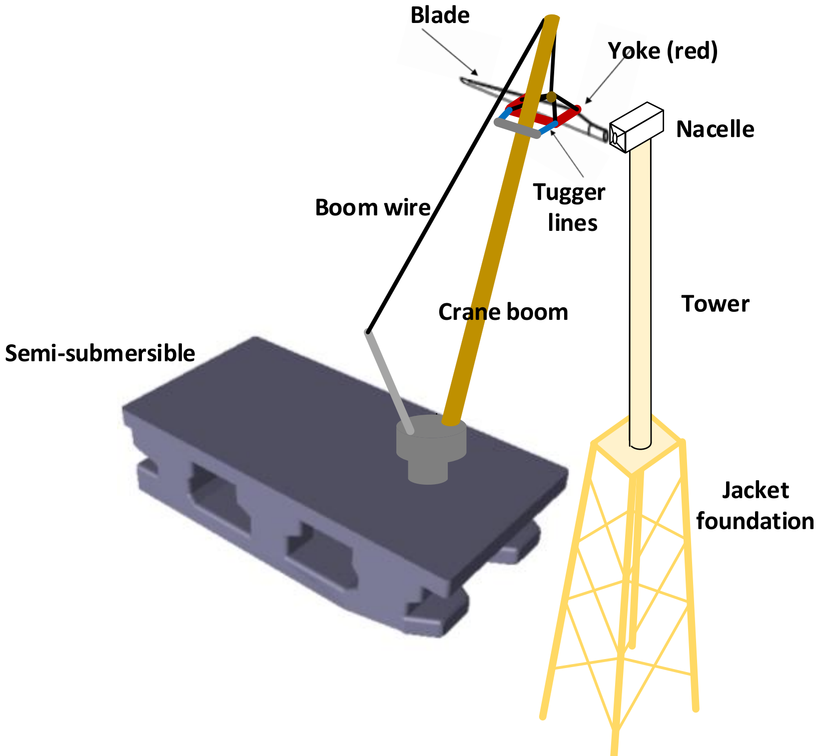

(a) System for offshore single blade installation(Note: the figure is for illustration purpose, system components may not be in scale.)

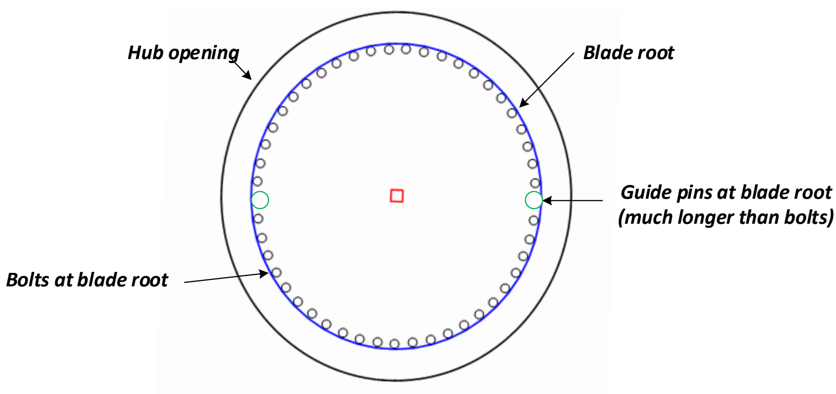

(b) Illustration of the mating gap

Figure 5.3: Illustration of the offshore single blade installation system and mating gap [116]

velocity. The corresponding allowable limit causing no damage is found to be around 0.7m/s, based on non-linear finite element analysis of the impact scenario of DTU 10MW wind turbine blade by [104]. The consequence of damaged guide pins is dramatic. The probability of occurrence is limited to 10^{-4}, which is a representative value for typical marine operations, according to DNV-OS-H101 [17]. The characteristic value of blade root radial impact velocity (V_e) is taken as the 10-min extreme value with a exceedance probility to 10^{-4}. Figure 5.4(b) shows an example. The results are based on stationary time domain analysis. They do not include transient effects if impact occurs between the blade root guide pins and the hub opening, since modeling of impacts is not accounted for. The environmental limits may be reduced by transient effects.

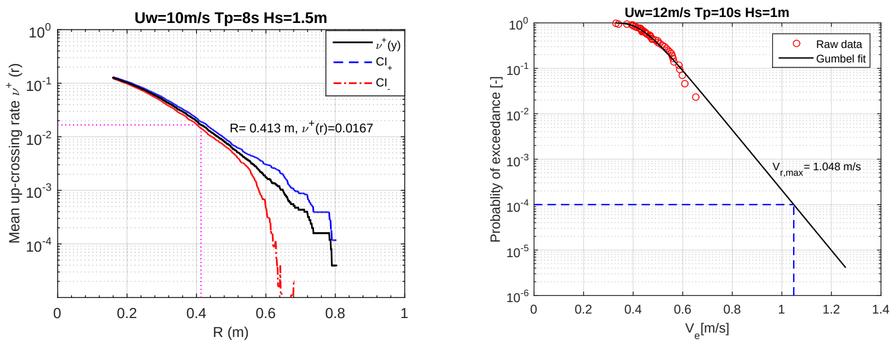

(a) (b)

Figure 5.4: Characteristic values of limiting parameters [116]. (a)Example of getting characteristic values of blade root radial motion based on mean upcrossing rate. Legends: time domain simulation(-), empirical 95% confidence band. (b) Example of getting blade root radial velocity based on Gumbel distribution fit

A wide range of wind and wave conditions are considered. The mean wind speed at hub height varies from 2 m/s to 12 m/s in steps of 2m/s. The significant wave height varies from 0.5 m to 3.0 m in steps of 0.5 m and the wave peak period varies from 4 s to 12 s in steps of 2 s. The wind inflow angle is $\theta_{wd} = 0\ deg$. The incident wave angle is $\theta_{wv} = 285\ deg$, slightly off head sea.

The characteristic values of the limiting parameters for all the combination of these environmental conditions are calculated using the aforementioned approach.

5.4 Assessment of operational limits

The allowable operational sea states for each phase are identified by mapping the characteristic values of limiting parameters against their allowable limits. The overall allowable wind and wave conditions for the complete blade mating operation can be found by combining those of the monitoring and mating phases, and taking the lower envelope, as illustrated in Figure 5.5. These environmental limits are vessel and installation dependent. Nevertheless, they can be used in combination with statistical environmental data to find weather window for installation or to assist decision making during operation.

As can be observed in Figure 5.5, in short waves ($T_p <= 6s$), mating attempts are safe to carry out for H_s of 3m and wind speed of 12m/s. With the increase of wave peak period, the allowable environmental limits decrease sharply.

Overall, the mating operation is governed by the motion monitoring phase when the mating gap $r = 0.1R_{root}$. In such a case, the complete blade mating operation is mainly failed by unsuccessful mating attempts during the motion monitoring phase. In this case, increasing the limiting criteria of impact velocity does not necessarily lead to increases in the overall environmental limits. However, if the mating gap is $0.2R_{root}$ and the allowable impact velocity is 0.7m/s, the overall environmental limit would be governed by the bent guide pins in the mating phase. Under such a circumstance, an increase in the allowable impact velocity can widen the overall environmental limits.

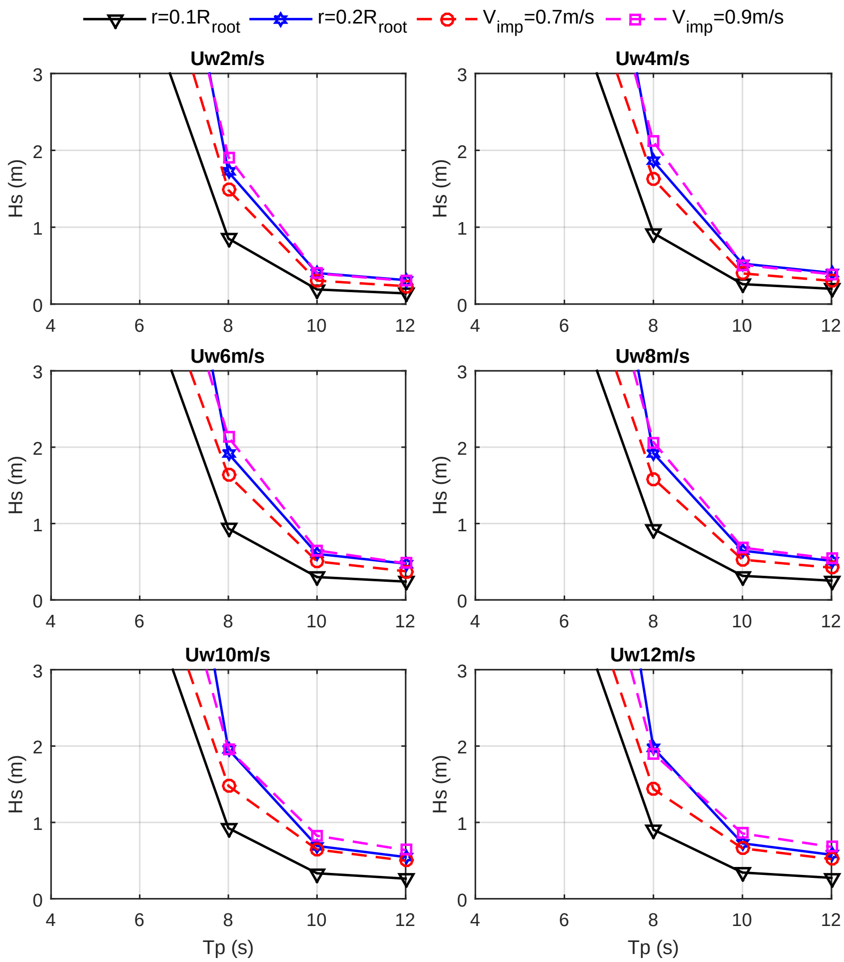

Figure 5.5: Allowable limits of wave and wind conditions for blade-hub mating [116]

 72

Chapter 6

Conclusions

This thesis addresses the single blade installation for offshore wind turbines, focusing on the final mating of blade root to the hub. First, a coupled method for simulating the single blade installation is developed. Based on this method, dynamic analysis was carried out to study the installation system responses. It also demonstrates that the methodology can be used to assess the operational limits in terms of allowable wind and wave conditions. The main conclusions, original contributions, and recommendations for future work are presented in this final chapter.

6.1 Original contributions

The main contributions of the thesis can be summarized as follow:

• *Establishing a coupled method for simulating single blade installation for wind turbines*

The coupled simulation method SIMO-Aero was established by developing an external aerodynamic code Aero and integrating it with SIMO. The Aero code calculates the aerodynamic loads on the installed blade based on the cross-flow principle. It was developed in an external dynamic link library (DLL) and was validated against HAWC2. The coupled method can be used to analyse removal or replacement of wind turbine blades, installation of rotor, and integrated tower, nacelle and rotor assembly (RNA).

• *Response analysis of offshore single blade installation by jack-up crane vessels using a fully coupled aero-hydro-soil-elastic-mechanical model*

Jack-up crane vessels are commonly used to install wind turbine blades. Detailed modeling of a typical jack-up crane vessel was developed, considering wave loads on jack-up legs, soil-structure interaction, structural flexibility in legs and crane. The developed vessel model was integrated with coupled method SIMO-Aero to formulate a fully coupled aero-hydro-soil-elastic-mechanical model for simulating single blade installation by jack-up crane vessels.

• *Demonstrate the feasibility of offshore single blade installation by floating crane vessels using a fully coupled model*

The floating crane vessels are attractive because they can relocate and are flexible with respect to operational water depth. Use of floating crane vessels are inevitable in deep water if on site installation is needed. The feasibility of using floating crane vessels (mono-hull and semi-submersible types) is evaluated by comparing the blade response with that of a typical jack-up crane vessel.

• *Assessing operational limits of offshore single blade installation*

The operational limits involving both wind and wave conditions for single blade installation were assessed, accounting for both global motion response and structural integrity. They can be used during the planning and execution phases of operations, together with weather forecasts.

6.2 Conclusions

• A coupled simulation tool SIMO-Aero was developed and verified for modeling and analysis of single blade installation for wind turbines. The Aero code calculates the aerodynamic loads on the blade based on the cross-flow principle. The blade is modeled as a rigid body. Its structural flexibility have minor contributions to the blade motion during installation. The aerodynamic damping due to blade motion is found to be important in the blade dynamic response.

• A fully coupled aero-hydro-soil-elastic-mechanical model, SIMO-RIFLEX-Aero was developed to analyze offshore single blade installation by jack-up crane vessels. The vessel motion is mainly induced by wave loads. The wind loads were found to have marginal influence in the vessel motion. Both vessel motion and crane flexibility contribute to significant motions at crane tip and installed blade. Modeling of soil based on site-specific soil properties was found to be important for the blade dynamic response during installation by jack-up crane vessels. It indicates that detailed modeling and analysis of the installation system are essential for planning offshore operations.

• A preliminary feasibility study was carried out on offshore single blade installation by floating crane vessels. Two types of crane vessels are considered, i.e., a mono-hull and a semi-submersible. The results indicated that it is feasible to use floating crane vessels to install offshore wind turbine blades provided that the slowly varying motion of floating vessels are well mitigated by the DP system. The feasibility lies in the allowable operational weather window, and is site- and vessel-dependent. Offshore sites with short wave conditions has higher feasibility in floating vessel installation than at sites with long wave conditions. Floating vessels with small wave frequency motion responses are expected to have a higher feasibility, such as semi-submersibles. Utilization of weather orientation for floating vessels can greatly reduce the blade motion and hence increase the feasibility and reduce the operational cost.

• The coupled method was applied to determine the operational environmental limits for offshore single blade installation, considering both wind and wave conditions. The critical events for the mating phase were identified to be failure of mating attempts due to too large blade root motion and bent blade guide pins during radial impact with the turbine hub. The limiting parameters are blade root motion and velocity in the radial direction of hub opening. The limiting sea states are derived using blade response-based criteria. The results are conservative since the turbine hub is assumed to be rigidly fixed without motion.

6.3 Limitations and recommendations for future work

• *Validation of the coupled method via comparisons with experiments or offshore field measurements*

The developed coupled method for simulating offshore single blade installation has been verified module by module. SIMO and RIFLEX have been widely validated and used. The Aero code is verified by code-to-code comparison with HAWC2 results. However, a comprehensive validation of the coupled method has not been done in this thesis. Since the purpose of the coupled method is to aid the planning and execution of practical installation operations, it is essential to be validated by comparison with measurements of the system response during offshore operations of single blade installation or in experiments. Such a validation is recommended if the condition allows in the future.

- *Further study on methods for better estimation of aerodynamic loads on a wind turbine blade during installation*

Future work is recommended to study the aerodynamics of an installed blade. The characteristics of a wind turbine blade during installation are quite different from the operational condition. In this study, the aerodynamic loads on the installed blade is calculated based on cross-flow principle. It should be noted that the method based on cross-flow gives a good estimation of aerodynamic loads on installed blades when the wind yaw angle and blade pitch angle are relatively small. Otherwise, the estimated aerodynamic loads have been shown to have deviations from results based on CFD analysis. Therefore, future efforts are recommended for better estimation of aerodynamic loads on an installed blade during large yaw and pitch conditions. One possible way is to further introduce generalized correction model or factors on detailed CFD studies or wind tunnel experiments.

- *Study on methods to reduce blade motion during installation*

The single blade installation studied in this thesis is based on reasonable estimated tugger line arrangement and crane deployment. Results in this study show that the motion at blade root during the final mating phase is significant. To improve the installation efficiency and to reduce the installation cost, it is important to develop methods reducing the blade motion and thus widen the operational weather window. Future work could be using active tugger line control system or advanced yoke system to compensate the blade motion during installation. Thus, the blade installation could be carried out in under environmental conditions with higher wind speeds and (or) larger sea states.

- *Effect of wind turbine foundation motion on the allowable operational environmental limits*

In this study, the developed coupled method is applied to estimate the environmental limits for offshore single blade installation. However, the motion of the bottom-fixed wind turbine supported structure is not considered. Future work is recommended to account for the wind turbine support structure in the coupled method, and further asses the influence of motions of different types of offshore wind turbine foundations on the corresponding operational limits for offshore single blade installation.

- *Study of installation vessel design*

Traditional installation methods for offshore wind turbines require lifting operations by crane vessels. The wave-induced crane vessel motions cause significant motion in installed components, particularly at large lifting heights. The design of installation vessels or concepts, especially floating ones, are recommended to reduce the wind and wave-induced system motions during offshore winf turbine installation operations.

 78

References

[1] D. Ahn, S.-C. Shin, S.-Y. Kim, H. Kharoufi, and H.-c. Kim. Comparative evaluation of different offshore wind turbine installation vessels for Korean west–south wind farm. *International Journal of Naval Architecture and Ocean Engineering*, 9(1):45–54, 2017.

[2] Alpha ventus. Alpha ventus offshore wind farm. `https://www.alpha-ventus.de/english/`, 2015. (Accessed on 12/28/2018).

[3] E. Bachynski and T. Moan. Design considerations for tension leg platform wind turbines. *Marine Structures*, 29(1):89–114, 2012.

[4] C. Bak, F. Zahle, R. Bitsche, T. Kim, A. Yde, L. C. Henriksen, M. H. Hansen, and A. Natarajan. Description of the DTU 10 MW reference wind turbine. Tech. Rep. DTU Wind Energy Report-I-0092, Technical University of Denmark, 2013.

[5] Beatrice Offshore Windfarm Ltd. Beatrice Wind Farm. `https://www.beatricewind.com/`, 2017. (Accessed on 07/09/2018).

[6] T. Burton, N. Jenkins, D. Sharpe, and E. Bossanyi. *Wind energy handbook*. John Wiley & Sons Ltd, UK, 2011.

[7] Business Green. World's biggest wind turbine installed at Burbo Bank offshore extension. `https://www.businessgreen.com/bg/news/2470309/worlds-biggest-wind-turbine-installed-at-burbo-bank\-offshore-extension`, 2016. (Accessed on 02/24/2019).

[8] J.-H. Cha, M.-I. Roh, and K.-Y. Lee. Dynamic response simulation of a heavy cargo suspended by a floating crane based on multibody system dynamics. *Ocean Engineering*, 37(14-15):1273–1291, 2010.

[9] M. M. Christopher. *Physical and numerical modelling of offshore foundations under combined loads*. PhD thesis, University of Oxford, 1994.

 80

[10] V. A. Dalfsen. *Integral soil-jack-up modelling-Modelling site-specific jack-up response and performing safety assessment.* Master thesis, Delft University of Technology, 2016.

[11] R. Damiani, K. Dykes, and G. Scott. A comparison study of offshore wind support structures with monopiles and jackets for us waters. In *Journal of Physics: Conference Series*, volume 753, page 092003, 2016.

[12] J. Deign. An illustrated guide to the growing size of wind turbines. `https://www.greentechmedia.com/articles/read/an-illustrated-guide-to-the-growing-size-of-wind-turbines#gs.Ll3YGYQ`, August 2017. (Accessed on 07/07/2018).

[13] DEME. Ormonde offshore wind farm. `https://www.deme-group.com/geosea/references/ormonde-offshore-wind-farm`, 2018. (Accessed on 07/08/2018).

[14] S. Deng. Numerical simulations for lift-off operation of an offshore wind turbine monopile. Master's thesis, Norwegian University of Sicence and Technology, 2016.

[15] DNV. DNV-RP-C205 Environmental conditions and environmental loads. Standard, DET NORSKE VERITAS, Olso, Norway, 2007.

[16] DNV. DNV-RP-C104: Self-elevating units. Standard, DET NORSKE VERITAS, Olso, Norway, 2011.

[17] DNV. Recommended Practice DNV-OS-H101: marine operations. Standard, DET NORSKE VERITAS, Olso, Norway, 2011.

[18] DNV. DNV-OS-H205 Lifting Operations, Part 2-5. Standard, DET NORSKE VERITAS, Olso, Norway, 2014.

[19] DNVGL. DNV-OS-H101 Marine Operations, General. Standard, DET NORSKE VERITAS, Olso, Norway, 2016.

[20] DNVGL. Recommended practice DNVGL-ST-N001, Marine operations and marine warranty. Standard, DNV GL, Olso, Norway, 2016.

[21] DNVGL. DNVGL-RP-C205 Environmental conditions and environmental loads. Standard, DNV GL AS, 2017.

[22] DNVGL. DNVGL-RP-N103, Modelling and Analysis of Marine Operations. Standard, DNV GL AS, 2017.

[23] DNVGL. DNVGL-ST-0054 Transportation and instalaltion of wind power plants. Standard, DNV GL AS, 2017.

[24] F. Duan, Z. Hu, and J. Niedzwecki. Model test investigation of a spar floating wind turbine. *Marine Structures*, 49:76–96, 2016.

[25] V. Duan and F. Olsson. *Impact loads on a self-elevating unit during jacking operation*. Master thesis, Chalmers University of Technology, 2014.

[26] M. A. El-Reedy. *Offshore structures: design, construction and maintenance*. Gulf Professional Publishing, 2012.

[27] Equinor. Hywind-the leading solution for floating offshore wind power. `https://www.statoil.com/en/what-we-do/hywind-where-the-wind-takes-us.html`, 2018. (Accessed on 05/01/2018).

[28] M. Esteban, B. Couñago, J. López-Gutiérrez, V. Negro, and F. Vellisco. Gravity based support structures for offshore wind turbine generators: Review of the installation process. *Ocean Engineering*, 110:281–291, 2015.

[29] Fred. Olsen Windcarrier AS. Specifications for Jack-up Installation vessels Brave Tern and Bold Tern. Report, Fred. Olsen Windcarrier AS, Oslo, 2016.

[30] M. Gaunaa, L. Bergami, S. Guntur, and F. Zahle. First-order aerodynamic and aeroelastic behavior of a single-blade installation setup. *Journal of Physics: Conference Series*, 524(1):012073, 2014.

[31] M. Gaunaa, J. Heinz, and W. Skrzypiński. Toward an engineering model for the aerodynamic forces acting on wind turbine blades in quasisteady standstill and blade installation situations. *Journal of Physics: Conference Series*, 753(2):022007, 2016.

[32] GE Renewable Energy. World's Largest Offshore Wind Turbine: Haliade-X. `https://www.ge.com/renewableenergy/wind-energy/turbines/haliade-x-offshore-turbine`, 2018. (Accessed on 12/28/2018).

[33] T. Gintautas, J. D. Sørensen, and S. R. Vatne. Towards a risk-based decision support for offshore wind turbine installation and operation & maintenance. *Energy Procedia*, 94:207–217, 2016.

[34] Global Wind Energy Council. GLOBAL WIND STATISTICS 2017. Report, Global Wind Energy Council, 2018.

[35] W. Guachamin Acero, Z. Gao, and T. Moan. Assessment of the dynamic responses and allowable sea states for a novel offshore wind turbine installation concept based on the inverted pendulum principle. *Energy Procedia*, 94:61–71, 2016.

[36] W. Guachamin Acero, Z. Gao, and T. Moan. Methodology for assessment of the allowable sea states during installation of an offshore wind turbine transition piece structure onto a monopile foundation. *Journal of Offshore Mechanics and Arctic Engineering*, 139(6):061901, 2017.

[37] W. Guachamin Acero, Z. Gao, and T. Moan. Numerical study of a novel procedure for installing the tower and rotor nacelle assembly of offshore wind turbines based on the inverted pendulum principle. *Journal of Marine Science and Application*, 16(3):243–260, 2017.

[38] W. Guachamin Acero, L. Li, Z. Gao, and T. Moan. Methodology for assessment of the operational limits and operability of marine operations. *Ocean Engineering*, 125:308–327, 2016.

[39] S. Gupta and J. G. Leishman. Dynamic stall modelling of the S809 aerofoil and comparison with experiments. *Wind Energy*, 9(6):521–547, 2006.

[40] Y. Ha, B. Nam, S. Hong, D. Jung, and H. Kim. Experimental and numerical study on mating operation of a topside module by a floating crane vessel in waves. *Ocean Engineering*, 154:375–388, 2018.

[41] S. Herman. Offshore wind farms: Analysis of transport and installation costs. Report, Energy Research Centre of the Netherlands, 2002.

[42] High Wind NV. Boom lock. `http://www.high-wind.eu/boomlock/`, 2015. (Accessed on 01/09/2017).

[43] S. F. Hoerner and H. V. Borst. *Fluid-dynamic lift: practical information on aerodynamic and hydrodynamic lift.* Hoerner Fluid Dynamics, Vancouver, WA, 1985.

[44] S. Horner. Fluid dynamic drag: Practical information on aerodynamic drag and hydrodynamic resistance. *Hoerner Fluid Dyn., Midland Park, NJ*, 1965.

[45] IEC. International standard 61400-1, wind turbines, part 1: Design requirements, 2005.

[46] IEC. IEC 61400-3, wind turbines, part 3: Design requirements for offshore wind turbines, 2009.

[47] IEEFA. Lower biding pricing trends in UK offshore wind auctions. `http://ieefa.org/ieefa-europe-technology-gains-help-drive-rush-capital-markets-offsh` 2017. (Accessed on 12/29/2018).

[48] ISO. ISO/DIS 19905-1: Petroleum and natural gas industries- Site-specific assessment of mobile offshore units- Part 1: Jack-ups. Standard, International Organization for Standardization, 2009.

[49] ISO. ISO 29400:2015 Ships and marine technology – Offshore wind energy – Port and marine operations. Standard, International Organization for Standardization, 2015.

[50] Z. Jiang, Z. Gao, Z. Ren, Y. Li, and L. Duan. A parametric study on the final blade installation process for monopile wind turbines under rough environmental conditions. *Engineering Structures*, 172:1042–1056, 2018.

[51] B. J. Jonkman. Turbsim user's guide: Version 1.50, 2009.

[52] M. Karimirad and T. Moan. Feasibility of the application of a spar-type wind turbine at a moderate water depth. *Energy Procedia*, 24:340–350, 2012.

[53] N. Keseric. Norway's solution: Hywind world's first full scale floating turbine. Report, Statoil (now Equinor), 2014.

[54] L. Kitzing and P. E. Morthorst. Trends in offshore wind economics–the past and the future. In *Proceedings-14th Wind Integration Workshop, 20-22 October 2015, Brussels*, 2015.

[55] N. Ku and M.-I. Roh. Dynamic response simulation of an offshore wind turbine suspended by a floating crane. *Ships and Offshore Structures*, 10(6):621–634, 2015.

[56] L. Kuijken. *Single Blade Installation for Large Wind Turbines in Extreme Wind Conditions.* Master thesis, Technical University of Denmark, 2015.

[57] J. G. Leishman and T. Beddoes. A semi-empirical model for dynamic stall. *Journal of the American Helicopter society*, 34(3):3–17, 1989.

[58] B. Li, W. Huang, and X. Chen. A numerical study of dynamic response of crane semi-submersible along tlp in tender-assisted drilling operation. *Ships and Offshore Structures*, pages 1–14, 2018.

[59] L. Li, Z. Gao, and T. Moan. Comparative study of lifting operations of offshore wind turbine monopile and jacket substructures considering vessel shielding effects. In *The Twenty-fifth International Ocean and Polar Engineering Conference, June 21-26, 2015, HAwaii, US*, 2015.

[60] L. Li, Z. Gao, and T. Moan. Operability analysis of monopile lowering operation using different numerical approaches. *International Journal of Offshore and Polar Engineering*, 26(2):88–99, 2016.

[61] L. Li, Z. Gao, T. Moan, and H. Ormberg. Analysis of lifting operation of a monopile for an offshore wind turbine considering vessel shielding effects. *Marine structures*, 39:287–314, 2014.

[62] L. Li, W. Guachamin Acero, Z. Gao, and T. Moan. Assessment of allowable sea states during installation of offshore wind turbine monopiles with shallow penetration in the seabed. *Journal of Offshore Mechanics and Arctic Engineering*, 138(4):041902, 2016.

[63] Liftra. Blade dragon. `http://www.liftra.com/product/product-2/`, 2012. (Accessed on 01/09/2017).

[64] Y. Liu, S. Li, Q. Yi, and D. Chen. Developments in semi-submersible floating foundations supporting wind turbines: A comprehensive review. *Renewable and Sustainable Energy Reviews*, 60:433–449, 2016.

[65] B. Maples, G. Saur, M. Hand, R. van de Pieterman, and T. Obdam. Installation, operation, and maintenance strategies to reduce the cost of offshore wind energy. Technical report, National Renewable Energy Lab.(NREL), USA, 2013.

[66] MHI VESTAS OFFSHORE WIND. Krehamn offshore wind farm — mhi vestas. `http://www.mhivestasoffshore.com/kaarehamn/`, 2013. (Accessed on 07/09/2018).

[67] P. Mukerji. Hydrodynamic responses of derrick vessels in waves during heavy lift operation. In *20th Offshore Technology Conference, Houston*, 1988.

[68] W. Musial, P. Beiter, P. Schwabe, T. Tian, T. Stehly, P. Spitsen, A. Robertson, and V. Gevorgian. 2016 Offshore Wind Technologies Market Report. Technical report, National Renewable Energy Laboratory (NREL),US, 2017.

[69] A. Naess and O. Gaidai. Monte carlo methods for estimating the extreme response of dynamical systems. *Journal of Engineering Mechanics*, 134(8):628–636, 2008.

[70] A. Naess and T. Moan. *Stochastic dynamics of marine structures*. Cambridge University Press, UK, 2013.

[71] E. Oguz, D. Clelland, A. H. Day, A. Incecik, J. A. López, G. Sánchez, and G. G. Almeria. Experimental and numerical analysis of a tlp floating offshore wind turbine. *Ocean Engineering*, 147:591–605, 2018.

[72] K.-Y. Oh, W. Nam, M. S. Ryu, J.-Y. Kim, and B. I. Epureanu. A review of foundations of offshore wind energy convertors: Current status and future perspectives. *Renewable and Sustainable Energy Reviews*, 88:16–36, 2018.

[73] Ørsted. Burbo Bank Extension offshore wind farm. `https://orsted.co.uk/Generating-energy/Offshore-wind/Our-wind-farms`, 2017. (Accessed on 07/09/2018).

[74] Ørsted. Race Bank offshore wind farm. `https://orsted.com/en/Media/Newsroom/News/2018/02/Full-power-at-Race-Bank-Offshore-Wind-Farm`, 2018. (Accessed on 07/08/2018).

[75] Ørsted. Walney Extension wind farm. `https://walneyextension.co.uk/en`, 2018. (Accessed on 07/09/2018).

[76] J. Paterson, F. D'Amico, P. Thies, R. Kurt, and G. Harrison. Offshore wind installation vessels–A comparative assessment for UK offshore rounds 1 and 2. *Ocean Engineering*, 148:637 – 649, 2018.

[77] J. Paterson, F. DAmico, P. Thies, R. Kurt, and G. Harrison. Offshore wind installation vessels- a comparative assessment for UK offshore rounds 1 and 2. *Ocean Engineering*, 148:637–649, 2018.

[78] E. A. Pedersen. Motion analysis of semi-submersible. Master's thesis, Department of Marine Technology, Norwegian University of Science and Technology, 2012.

[79] S. Rahmdel, B. Wang, C. Han, K. Kim, and S. Park. A parametric study of spar-type floating offshore wind turbines (FOWTs) by numerical and experimental investigations. *Ships and Offshore Structures*, 11(8):818–832, 2016.

[80] Rampion Offshore Wind. The rampion offshore wind farm. `https://www.bbc.com/news/uk-england-sussex-44287014`, 2018. (Accessed on 02/24/2019).

[81] Rampion Offshore Wind. The south coast's first offshore wind farm — rampion offshore wind. `https://www.rampionoffshore.com/`, 2018. (Accessed on 07/09/2018).

[82] L. Rayleigh. *Theory of Sound (two volumes)*. Dover Publications, New York, 1877.

[83] Z. Ren, Z. Jiang, Z. Gao, and R. Skjetne. Active tugger line force control for single blade installation. *Wind Energy*, 21(12):1344–1358, 2018.

[84] Z. Ren, Z. Jiang, R. Skjetne, and Z. Gao. Development and application of a simulator for offshore wind turbine blades installation. *Ocean Engineering*, 166:380–395, 2018.

[85] J. W. Ringsberg, V. Daun, and F. Olsson. Analysis of impact loads on a self-elevating unit during jacking operation. *Journal of Offshore Mechanics and Arctic Engineering*, 139:031602–1– 031602–9, 2017.

[86] A. Sarkar and O. T. Gudmestad. Study on a new method for installing a monopile and a fully integrated offshore wind turbine structure. *Marine structures*, 33:160–187, 2013.

[87] T. Sauder, V. Chabaud, M. Thys, E. Bachynski, and L. O. Sæther. Real-Time Hybrid Model Testing of a Braceless Semi-Submersible Wind Turbine: Part I - The Hybrid Approach. In *ASME 2016 35th International Conference on Ocean, Offshore and Arctic Engineering.* American Society of Mechanical Engineers, June 1924, 2016, Busan, South Korea.

[88] Seaway Heavy Lifting. Oleg Strashnov. `https://www.seawayheavylifting.com.cy/vessels/oleg-strashnov`, 2018. (Accessed on 07/08/2018).

[89] C. Shelton. Gravity base foundations leaving the Port of Tyne for the Blyth Offshore Demonstrator Wind Farm. https://www.khl.com/international-cranes-and-specialized-transport/uk-port-serves-offshore-wind-sector/128787.article, 2017. (Accessed on 07/08/2018).

[90] Siemens. Offshore wind turbine blade installation. https://www.siemens.com/press/en/feature/2012/energy/2012-07-rotorblade.php, 2012. (Accessed on 12/27/2018).

[91] Siemens. Picture from online video. https://www.youtube.com/watch?v=zUQifpcGTrg, 2014. (Accessed on 02/24/2019).

[92] Siemens. Siemens wind turbine blade being positioned. https://www.siemens.co.uk/en/news_press/index/news_archive/2014/major-uk-offshore-wind-manufacturing-site-to-be-built-by-siemens.htm, 2014. (Accessed on 01/09/2017).

[93] Siemens. Siemens SWT-3.6-107 specifications. https://www.siemens.com/content/dam/internet/siemens-com/global/market-specific-solutions/wind/data_sheets/data-sheet-wind-turbine-swt-3-6-107.pdf, 2015. (Accessed on 12/28/2018).

[94] SINTEF Ocean. RIFLEX- Theory Manual 4.10.1. SINTEF Ocean, Trondheim, Norway, 2017.

[95] SINTEF Ocean. SIMO-Theory Manual Version 4.10. SINTEF Ocean, Trondheim, Norway, 2017.

[96] SNAME. Technical & Research Bulletin 5-5A: Guidelines for Site Specific Assessment of Mobile Jack-Up Units, 2008.

[97] T. J. Stehly, D. M. Heimiller, and G. N. Scott. 2016 Cost of Wind Energy Review. Technical report, National Renewable Energy Lab (NREL), US, 2017.

[98] O. Stettner. *Numerical Simulation for Installation of Jacket Foundation of Offshore Wind Turbines*. Master thesis, Delft University of Technology and Norwegian University of Sicence and Technology, 2014.

[99] R. Swart, C. Coppens, H. Gordijn, M. Piek, P. Ruyssenaars, J. Schrander, P. de Smet, M. Hoogwijk, M. Papalexandrou, E. de Visser, et al.

Europe's onshore and offshore wind energy potential: An assessment of environmental and economic constraints. Technical report, European Environment Agency, 2009.

[100] Ultramarine. MOSES Reference Manual 7.07, 2013.

[101] E. Uraz. Offshore wind turbine transportation & installation analyses planning optimal marine operations for offshore wind projects. Master's thesis, Gotland University, 2011.

[102] Veja Mate Offshore Project GmbH. Veja mate offshore project gmbhabout us. `http://www.vejamate.net/#aboutus`, 2017. (Accessed on 07/09/2018).

[103] A. S. Verma, Z. Gao, N. P. Vedvik, and Z. Gao. A comprehensive numerical investigation of the impact behaviour of an offshore wind turbine blade due to impact loads during installation. *Ocean Engineering*, 172:127–145, 2019.

[104] A. S. Verma, Z. Jiang, N. P. Vedvik, Z. Gao, and Z. Ren. Impact assessment of a wind turbine blade root during an offshore mating process. *Engineering structures*, 180:205–222, 2019.

[105] A. S. Verma, Y. Zhao, Z. Gao, and N. P. Vedvik. Explicit structural response-based methodology for assessment of operational limits for single blade installation for offshore wind turbines. In *Proceedings of the 4th International Conference in Ocean Engineering (ICOE 2018), Chennai, India, February 18-21*, 2018.

[106] Vestas. V164-8MW specifications. `http://www.homepages.ucl.ac.uk/~uceseug/Fluids2/Wind_Turbines/Turbines/V164-8MW.pdf`, 2012. (Accessed on 12/28/2018).

[107] Y. Wang, W. He, and D. Tian. Calculation of hoisting forces of the wind turbine rotor based on wind conditions. *Renewable energy*, 39(1):323–328, 2012.

[108] Y. Wang, D. Tian, and W. He. Computation of hoisting forces on wind turbine blades using computation fluid dynamics. *Applied Mechanics and Materials*, 446:452–457, 2014.

[109] Wind Europe. Offshore wind in Europe- Key trends and statistics 2017. Report, Wind Europe, 2018.

[110] Wind-turbine-models. Bonus b76/2000 - 2,00 mw - wind turbine. `https://en.wind-turbine-models.com/turbines/121-bonus-b76-2000`, 2012. (Accessed on 12/28/2018).

[111] J. Zeng, H. Yuan, C. Wang, Y. Wang, and J. Mo. The research on the fatigue analysis of the jack-ups leg based on sesam software. In *ASME 2015 34th International Conference on Ocean, Offshore and Arctic Engineering, May 31-June 5, 2015, St. John's, Newfoundland, Canada*, pages V007T06A068–V007T06A068. American Society of Mechanical Engineers, 2015.

[112] Y. Zhao, Z. Cheng, Z. Gao, and T. Moan. Effect of foundation modeling on the dynamic motion response of an offshore wind turbine blade during installation by a jack-up crane vessel. In *Proceedings of the International Offshore Wind Technical Conference (IOWC), San Francisco, USA, November 4-7*, 2018 (accepted).

[113] Y. Zhao, Z. Cheng, Z. Gao, P. C. Sandvik, and T. Moan. Numerical study on the feasibility of offshore single blade installation by floating crane vessels. *Marine Structures*, 64:442–462, 2019.

[114] Y. Zhao, Z. Cheng, P. C. Sandvik, Z. Gao, and T. Moan. An integrated dynamic analysis method for simulating installation of a single blade for offshore wind turbines. *Ocean Engineering*, 152:72–88, 2018.

[115] Y. Zhao, Z. Cheng, P. C. Sandvik, Z. Gao, T. Moan, and E. V. Buren. Numerical modeling and analysis of the dynamic motion response of an offshore wind turbine blade during installation by a jack-up crane vessel. *Ocean Engineering*, 165:353–364, 2018.

[116] Y. Zhao, Z. Gao, T. Moan, and P. C. Sandvik. Assessment of operational environmental limits for offshore single blade installation using response-based criteria. Technical report, Norwegian University of Science and Technology (NTNU), Trondheim, Norway, 2019.

[117] H. Zhu, L. Li, and M. Ong. Study of lifting operation of a tripod foundation for offshore wind turbine. In *IOP Conference Series: Materials Science and Engineering*, volume 276(1), page 012012, 2017.

90

Appendix A

Appended papers

A.1 Paper 1

Paper 1:
An integrated dynamic analysis method for simulating installation of a single blade for wind turbines.
Authors: Yuna Zhao, Zhengshun Cheng, Peter Christian Sandvik, Zhen Gao, Torgeir Moan
Published in *Ocean Engineering*, 2018,
DOI:10.1016/j.oceaneng.2018.01.046.

An integrated dynamic analysis method for simulating installation of single blades for wind turbines

Yuna Zhao[a,c,*], Zhengshun Cheng[a,b,c], Peter Christian Sandvik[d], Zhen Gao[a,b,c], Torgeir Moan[a,b,c]

[a] *Centre for Autonomous Marine Operations and Systems (AMOS), NTNU, NO-7491 Trondheim, Norway*
[b] *Centre for Ship and Ocean Structures (CeSOS),NTNU, NO-7491 Trondheim, Norway*
[c] *Department of Marine Technology, NTNU, NO-7491 Trondheim, Norway*
[d] *PC Sandvik Marine, Trondheim, Norway*

Abstract

Installation of blades for wind turbines is challenging due to large lifting height and high precision. Assessment of blade dynamic responses during installation needs advanced simulation tools which are limited at present. This paper aims at developing an integrated simulation tool SIMO-Aero for single blade installation for both onshore and offshore wind turbines. Based on the cross-flow principle, the aerodynamic model is established by accounting for the effect of wind turbulence and dynamic stall. Then it is coupled with SIMO to achieve the integrated simulation tool SIMO-Aero which can account for blade aerodynamics, vessel hydrodynamics and system mechanical couplings. The aerodynamic code is verified by code-to-code comparisons with HAWC2. Furthermore, SIMO-Aero is applied in case studies on the wind-induced dynamic responses of a DTU 10MW blade during installation using a jack-up crane vessel which is assumed to be rigid, including the crane, and rigidly fixed to the seabed. The characteristics of system dynamic responses prior to mating the blade onto the hub are studied. It is shown that the blade motions are dominated by the pendulum motion. Critical parameters of the installation process are identified. The extreme responses of critical parameters are further studied under turbulent winds and wind gusts.

*Corresponding author
Email address: yuna.zhao@ntnu.no (Yuna Zhao)

Keywords: Wind turbine, blade installation, fully coupled method, extreme response

1. Introduction

In recent years, air pollution and global warming have become important issues to the world, leading to an urgent need of clean, renewable and reliable energy sources such as wind energy. The wind industry has grown significantly in the last decades. The global cumulative installed wind capacity reached 487GW by the end of 2016, which includes about 14.4GW installed offshore (Global Wind Energy Council, 2017). At the same time, the size of wind turbines also increases fast. In 2016, 8MW wind turbines were successfully installed at Burbo Bank offshore wind farm (DONG energy, 2016). The trend towards larger turbine size leads to larger blade size, higher installation height and increased sensitivity to wind condition (and also wave condition for offshore turbines), which adds difficulties to the installation of turbine components, especially the blades.

(a) Horizontal mounting (Siemens, 2014b) (b) Vertical mounting (Liftra, 2012) (c) Inclined mounting (Liftra, 2012)

Figure 1: Single blade installation of offshore wind turbine blades with various orientations

The three most commonly used methods for blade installation are respectively single blade installation, bunny ear and whole rotor lift (Uraz, 2011). Among those, single blade installation is most frequently used for offshore installation in recent years, due to small deck space requirement and flexible blade orientations during installation (Ahn et al., 2017). During the installation process, the blade is lifted and installed in a feathered position, which is kept during the whole installation operation (Kuijken, 2015; Siemens, 2014b; High Wind NV, 2015). As shown in Figure 1, the single blade can be installed in various orientations such as horizontal, vertical or even inclined.

For inclined-blade installation, longer crane boom is required as the blade needs to be lifted higher than the hub height. The vertical-orientated installation needs to rotate the blade prior to installation since it is horizontally stored on the vessel deck, which makes the process more complex. The horizontal orientation installation is most preferred since no rotation of blade is required. Besides, installations of blades for offshore wind turbines are commonly conducted by jack-up crane vessels rather than floating ones since they provide a very stable working platform.

Wind condition is the one of the main constraints for blade installation wind turbines since it directly affects the waiting time for suitable weather window, which causes large economic cost. By now, most of the lifting equipment for single blade installation can operate under wind speed of 10 m/s. There are also advanced installation equipment such as Blade Dragon (Liftra, 2012), B75 lifting yoke (Siemens, 2014a) and Boom Lock (High Wind NV, 2015). The Blade Dragon, which is shown in Figure 1(b)$\sim$1(c), has a remote control system and can install blades with all orientations. It claims that installation of blades can take place at a speed below $12m/s$. The B75 lifting yoke is claimed to be capable of installing blades in average wind speed up to $14m/s$. It has automatic sling connection and can actively yaw itself to adjust the blade position during installation. The Boom Lock is a system mounted on crane boom to control the blade movement, which is claimed to allow installation of blades in average wind speed up to $15m/s$.

(a) (b)

Figure 2: Advanced equipment for installation of blades for offshore wind turbines:(a)B75 lifting yoke (Siemens, 2014a); (b)Boom Lock (High Wind NV, 2015)

Since the installation of blades for wind turbines is challenging, it is of importance to establish and use advanced numerical simulation tools to study the dynamic response of blade during installation. The dynamic response could be further used to predict the available weather windows if the installation criteria are known.

However, so far a limited number of studies on blade installations for wind turbines have been published. Some studies focus on the aerodynamic modeling of blades during installation or under standstill conditions. The characteristics of aerodynamic loads acting on a blade under installation conditions are quite different from a blade of an operating wind turbine. Wang et al. (2014) studied the hoisting forces on a wind turbine blade during installation using computational fluid dynamics (CFD) under constant wind conditions. Gaunaa et al. (2016) assessed the performance of cross-flow principle on the DTU 10MW reference blade in standstill situations using extensive three-dimensional CFD calculations. The authors concluded that the cross-flow principle gives a good estimation of aerodynamic loading when the blade pitch angle is within $[-50^o \quad 50^o]$. These CFD analyses specialize in accurate estimation of aerodynamic loads based on solving Navier-Stokes equations. However, they require significant computational efforts and cost. Thus, it is not suitable for simulation of marine operations.

Others focus on the installation process of blades for wind turbines. Wang et al. (2012) studied the hoisting force of a 1.5 MW wind turbine rotor using Bladed (GL Garrad Hassan, 2010). Gaunaa et al. (2014) proposed a general scaling method regarding the mean and standard deviations of aerodynamic loads on a single blade in yawed and pitched wind conditions. Kuijken (2015) examined possible ways to improve single blade installation in higher wind speed using HAWC2 (Larsen and Hansen, 2015). However, Bladed and HAWC2 are designed to calculate time-domain responses for wind turbine systems which are already in operation. Moreover, they cannot provide accurate models for mechanical couplings such as lift wires, slings and tugger lines, which are of great importance in the modeling of blade installation for wind turbines. Therefore, more sophisticated simulation tools for analysis of blade installation for wind turbines should be developed.

In this paper, a novel coupled simulation tool SIMO-Aero is developed for wind turbine blade installation in which an aerodynamic code is fully coupled with SIMO, a software specialized in numerical simulation of marine operations. The aerodynamic modeling is firstly described considering the effect of turbulent wind inflow and dynamic stall. Then the aerodynamic code is coupled with SIMO to establish the integrated simulation tool SIMO-Aero. SIMO-Aero is similar to SIMO-Riflex-Aerodyn (Kvittem et al., 2012) and SIMO-Riflex-AC (Cheng et al., 2016) which are fully coupled simulation tools integrating an external aerodynamic model with SIMO and Riflex for time-domain simulations of offshore wind turbine systems during installation. The SIMO-Aero proposed in this paper can be used to study the dynamic responses of single-blade-installation system for both onshore and offshore installations. Moreover, it has great potential to develop more efficient methods for installation or removal of blades for offshore wind turbines using a floating crane vessel.

The aerodynamic code in the integrated simulation tool is verified against HAWC2 results using the DTU 10 MW reference wind turbine blade (Bak et al., 2013). The developed simulation tool is applied in a series of load cases to study the characteristics of wind-induced dynamic responses of the blade installation system in turbulent winds and extreme operating gust winds.

2. Aerodynamic modeling

In this section, the aerodynamic modeling of a single blade is presented based on the cross-flow principle. Before going into details of the aerodynamic model, the coordinate systems used in the modeling are clearly defined.

2.1. Reference Frame

As shown in Figure 3, three coordinate systems were used, i.e., the global coordinate system $OXYZ$, body-fixed coordinate system for the blade $oxyz$ and local airfoil (blade cross-section) coordinate system $o_c x_c y_c z_c$, which are all right-handed coordinate systems. The origin o of the blade body-fixed coordinate is located at the blade center of gravity (COG). The y-axis is in the spanwise direction and x-axis is positive towards the trialling edge while z-axis follows the right-hand rule. The instantaneous rotational motions of the blade around X, Y and Z axis are respectively roll(ϕ), pitch(θ) and yaw(ψ). When ϕ, θ and ψ are all zero, $oxyz$ parallels with the global coordinate $OXYZ$. The y_c-axis of the local airfoil coordinate coincides with the y-axis while the x_c-axis is along the chord line.

Given a vector represented by $\mathbf{L}_G$ in the global coordinate system, its representation in the blade body-fixed coordinate system is:

$$\mathbf{L}_b = \mathbf{T}_{GB}\mathbf{L}_G \tag{1}$$

Furthermore, the representation of L_b in the local airfoil coordinate system is:

$$\mathbf{L}_c = \mathbf{T}_{BC}\mathbf{L}_b \tag{2}$$

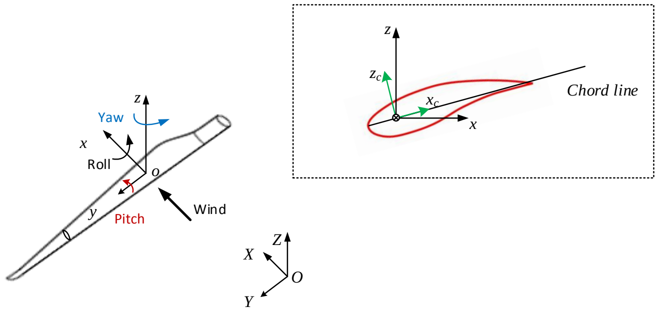

Figure 3: Definition of coordinate systems

where $\mathbf{T}_{GB}$ and $\mathbf{T}_{BC}$ are the coordinate transformation matrix. The $\mathbf{T}_{GB}$ is a function of instantaneous blade rotational motion ϕ, θ, ψ while $\mathbf{T}_{BC}$ is a function of structural twist angle of blade local cross-sections.The transformation matrix from the global coordinate to the local airfoil coordinate $\mathbf{T}_{GC}$ is:

$$\mathbf{T}_{GC} = \mathbf{T}_{BC}\mathbf{T}_{GB} \tag{3}$$

2.2. Cross-flow principle

In the aerodynamic force calculation, the blade is divided into a number of elements. For each element, the calculation of aerodynamic loads is based on the cross-flow principle (Horner, 1965; Hoerner and Borst, 1985), which has been widely used in wind energy industry. In the cross-flow principle, the inflow velocity normal to the cross section is neglected, as shown in Figure 4. Thus, the component of relative inflow velocity $\mathbf{V}_{A,i}$ on y_c axis is neglected, i.e.:

$$\mathbf{V}_{rel} = [V_{A,i,xc} \quad 0 \quad V_{A,i,zc}]^T \tag{4}$$

where $V_{A,i,xc}$ and $V_{A,i,zc}$ are respectively the projection of $\mathbf{V}_{A,i}$ on axis x_c and y_c. This principle is applicable for calculation of aerodynamic forces on a wind turbine blade, where the local blade element suits a 2D approximation.

The characteristics of $\mathbf{V}_{rel}$ for an element on a lifted blade are quite different from that on a rotating one. For an element a rotating blade, the large rotational speed has a significant contribution to $\mathbf{V}_{rel}$. However, the $\mathbf{V}_{rel}$ for an element on a lifted blade is mainly from the inflow wind velocity. It leads to significant discrepancies in aerodynamic loading on the whole

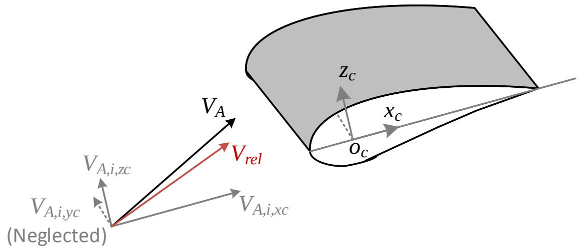

Figure 4: Illustration of cross-flow principle: $\mathbf{V}_{A,i} = [V_{A,i,xc} \quad V_{A,i,yc} \quad V_{A,i,zc}]^T$

blade. The overall difference in aerodynamic load between a lifted blade and a rotating blade is further discussed in Section 6.1.

2.3. Calculation of aerodynamic forces

Figure 5 shows a flow diagram for calculating the aerodynamic load on a lifted blade. The instantaneous displacement and velocity of the blade are respectively $\mathbf{X}_B$ ($[x(t)\ y(t)\ z(t)\ \phi(t)\ \theta(t)\ \psi(t)]^T$) and $\mathbf{V}_B$ ($[v_x(t)\ v_y(t)\ v_z(t)$ $v_\phi(t)\ v_\theta(t)\ v_\psi(t)]^T$) at each time step. The whole blade is divided into a number of elements. The total force on the blade is the sum of those on all elements.

For each element, its instantaneous position and velocity in the global coordinate system is calculated:

$$\mathbf{X}_i = \mathbf{X}_B^{1\sim3} + \mathbf{T}_{GB}^T(t)\mathbf{r}_{i,b} \tag{5}$$

$$\mathbf{V}_i = \mathbf{V}_B^{1\sim3} + \mathbf{V}_B^{4\sim6} \times [\mathbf{T}_{GB}^T(t)\mathbf{r}_{i,b}] \tag{6}$$

where $\mathbf{X}_i = [x_i(t) \quad y_i(t) \quad z_i(t)]^T$ and $\mathbf{V}_i = [v_{x,i}(t) \quad v_{y,i}(t) \quad v_{z,i}(t)]^T$; $\mathbf{r}_{i,b}$ is the position vector of element i in the blade body-fixed coordinate. Based on the global position of the i^{th} element, the wind inflow velocity at this element could be obtained, i.e., $\mathbf{V}_{WG,i}$. The corresponding relative inflow velocity $\mathbf{V}_{A,i}$ in the local airfoil coordinate can be derived from:

$$\mathbf{V}_{A,i} = \mathbf{T}_{GC,i}(\mathbf{V}_{WG,i} - \mathbf{V}_i + \mathbf{V}_{IG,i}) \tag{7}$$

The $\mathbf{V}_{IG}$ is the wake induced velocity. It is significant for an rotating blade with large rotational speed. However, it has marginal influence for blades

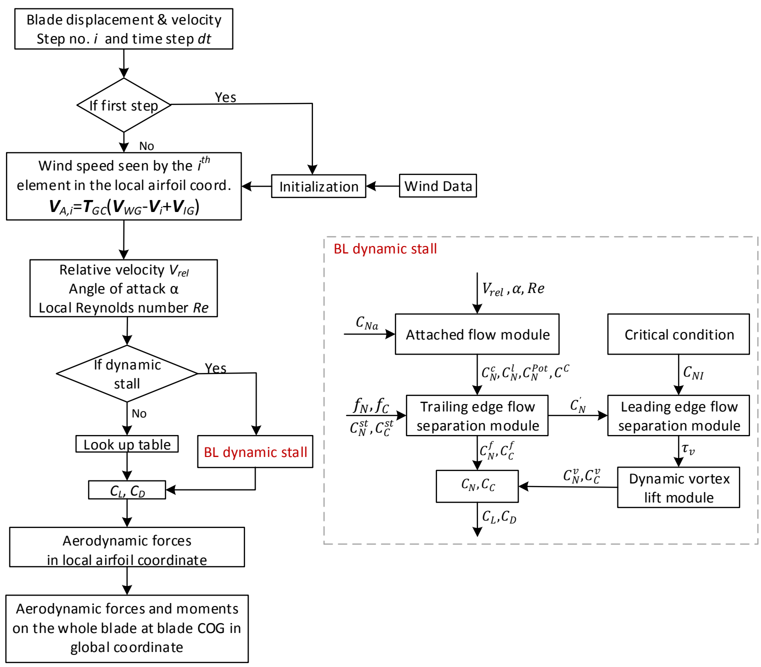

Figure 5: Flow chart for aerodynamic modeling, adapted from Ref.(Cheng et al., 2017)

during installation because the blade motion is very small. Therefore, it is neglected here.

Afterwards, the relative velocity $\mathbf{V}_{rel}$ used for further aerodynamic calculation is obtained using $\mathbf{V}_{A,i}$ based on the cross-flow principle, which was discussed in detail in Section 2.2. Then, the angle of attack α is determined. It is used to calculate the lift coefficient C_L and drag coefficient C_D based on a 2D look-up table. The table gives the relationship between C_L, C_D and α. Based on the calculated C_L and C_D coefficients for each element, the aerodynamic lift, drag force are calculated. Furthermore, the aerodynamic forces on the whole blade are obtained as the sum of those on all elements. The total aerodynamic forces are given in the global coordinate system at blade COG.

Moreover, there is an option to include dynamic stall effect before the table look-up. The Beddoes-Leishman dynamic stall model is used, which is explained in the next section.

2.4. Beddoes-Leishman stall model

The Beddoes-Leishman dynamic stall model was originally proposed by Leishman and Beddoes (1989) for helicopter aerodynamics. Later, Gupta and Leishman (2006) adapted it for application in wind turbine aerodynamics. As shown on the right side of Figure 5, there are three parts in the Beddoes-Leishman dynamic stall model, i.e., unsteady attached flow, unsteady separated flow and dynamic vortex lift.

In the unsteady attached flow regime, the aerodynamic loading consists of a circulatory and an impulsive part. The circulatory component is due to the change of angle of attack while the impulsive component is related to the change rate of α and pitch moment. Furthermore, the attached flow results are modified due to flow separation on the low-pressure side of the airfoil, including leading edge and trailling edge separations. The final part of the model is the vortex build-up and shedding. The vortex lift contribution is empirically modeled as an excess circulation in the vicinity of the airfoil using the difference between the normal force coefficient C_N from attached flow and separated flow. The total loading on the airfoil is the sum of the aforementioned components.

2.5. Inflow wind

The developed simulation tool can account for steady wind, turbulent wind and gust wind. The steady wind is constant in time and space. The turbulent wind is described by the IEC Kaimal Model (IEC, 2005). For the turbulent wind, the three-dimensional full-field wind file is generated by using the NREL's TurbSim program (Jonkman, 2009). The extreme operating gust wind is defined according to IEC 6400-1 (IEC, 2005).

The effects of wind shear is considered in the inflow wind. The wind shear effect is described by the power law wind profile, i.e.:

$$V(z) = V(z_{ref})(\frac{z}{z_{ref}})^{\alpha_s} \tag{8}$$

where $V(z)$ is the wind speed at height z while $V(z_{ref})$ is the wind speed at reference height z, which is normally the hub height. In addition, α_s is the wind shear exponent (IEC, 2009).

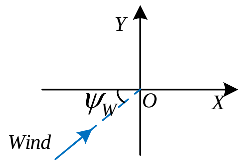

Figure 6: Illustration of wind inflow direction

The wind yaw angle ψ_W is defined as the angle between the wind inflow direction and the global X-axis in OXY plane. It is positive in the anti-clockwise direction. As shown in Figure 6, the wind flows along the positive global X axis when ψ_W is zero.

3. Development of the integrated simulation tool

The developed aerodynamic code is coupled with SIMO (MARINTEK, 2015a,b) to formulate the integrated simulation tool SIMO-Aero for blade installation. SIMO is widely used in time-domain simulations of marine operations in the offshore oil&gas and renewable energy industries. It could be used to simulate dynamic loads and responses for onshore foundations and offshore jack-up crane vessels or floating vessels. The coupled SIMO-Aero code could account for aerodynamics of the installed blade, hydrodynamics of the installation vessel and mechanical couplings between bodies in the multi-body system.

The SIMO-Aero code developed in this paper is a fully coupled code. As shown in Figure 7, the instantaneous blade displacement and velocity in the global coordinate system is calculated by SIMO at each time step. The instantaneous displacement is used to update the transformation matrix from global to local blade element coordinate systems. Then the blade velocity and wind inflow velocity in the global coordinate system are transferred into the local blade element coordinate system, to update the relative velocity seen by the local blade element and the angle of attack. The corresponding lift and drag coefficients are determined from a look-up table, and are used to estimate the lift and drag forces in the local blade element coordinate system. These aerodynamic forces are then transferred into the global coordinate system, and are sent back to SIMO to calculate the blade displacement and velocity for the next time step.

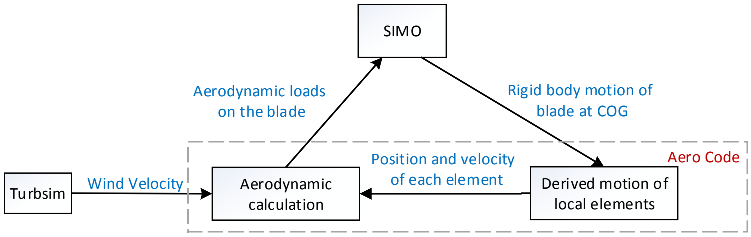

Figure 7: Overview of the coupled simulation tool

Figure 8 shows the modeling of external loads and internal coupling for the blade installation system. The system for blade installation usually consists of a crane vessel, a hook, a yoke and the blade to be installed. The hook is connected to the crane via the lift wire. Four slings spread down from the hook to the yoke which holds the blade. The blade and the yoke are modeled as one rigid body denoted by BY. Two horizontal tugger lines run from the yoke to the crane boom in order to control the blade motions.

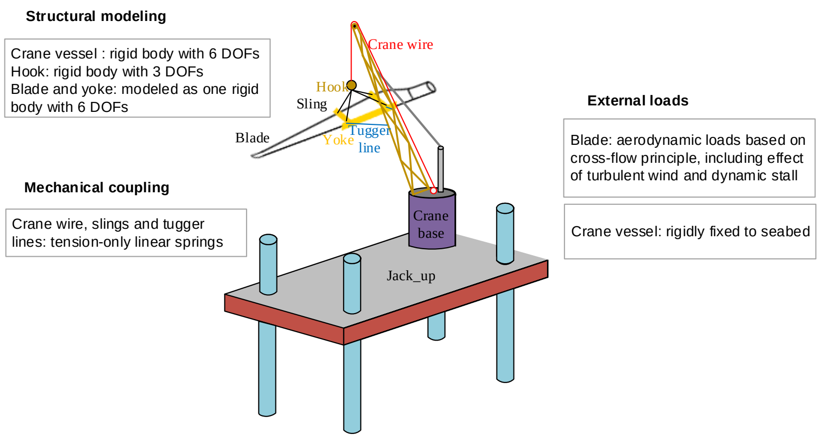

Figure 8: Illustration of overall modeling for offshore blade installation system

In the present paper, the coupled SIMO-Aero code was applied in case studies with focus on the wind-induced responses of the blade. A jack-up crane vessel which is assumed to be rigid and rigidly fixed to the seabed is used. The wave load, hydrostatic loads and current loads are all not considered for the jack-up crane vessel.

3.1. Aerodynamic model

The aerodynamic model is extensively described in Section 2. It is based on the cross-flow principle and accounts for the effect of turbulence and dynamic stall. However, there are still limitations in the aerodynamic model. The dynamic inflow effect, the wind loads on yoke and influence of yoke geometry on the flow field are assumed to be insignificant and not included. For the case study presented later, a straight blade is considered. Besides, the blade is assumed to be rigid. Gaunaa et al. (2014) studied the importance of structural flexibility for a wind turbine blade during installation using the DTU 10MW blade. It was found that the influence of structural flexibility is negligible as long as the natural frequency of blade rigid body motion is below 2.51rad/s (0.4Hz). The results in Section 7.1 show that the natural frequency of blade rigid motion is 0.5rad/s, which is well below 2.51rad/s. Thus, the blade flexibility has minor effect on the dynamic response of the blade during the installation phase.

3.2. Mechanical coupling model

The bodies involved in the blade installation system are coupled with each other via lift wire, slings or tugger lines. The coupling forces in the wires are modeled as linear spring forces (zero compression):

$$T = k\Delta L \qquad (T > 0) \tag{9}$$

where T is the wire tension and ΔL is the wire elongation. Besides, k is the axial stiffness of the wire, which is given by:

$$\frac{1}{k} = \frac{L}{EA} + \frac{1}{k_0} \tag{10}$$

where L and A are respectively the length and cross-sectional area of the wire, E the modulus elasticity of the material of the wire and $1/k_0$ the connection flexibility.

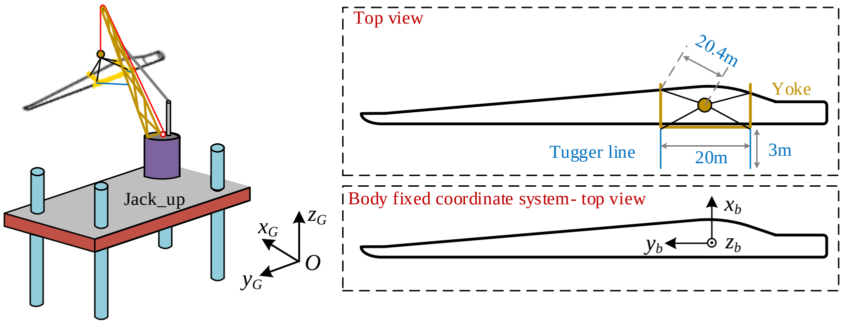

Figure 9: Illustration of blade installation system

4. System description

Since jack-up crane vessels are most commonly used for blade installations of offshore wind turbines, a jack-up crane vessel is used in the following case studies, as shown in Figure 9.

The blade used in this study is the DTU 10MW reference wind turbine blade (Bak et al., 2013). The hub height is 119 m above the mean sea surface. The blade is considered to be straight, which is 86.37m long and weighs about 42 tons. The blade COG is located 26.2m from its root. The blade is divided into 55 elements during the calculation of aerodynamic loads. The corresponding chord length, twist angle, thickness and airfoil coefficients at each blade element are interpolated based on those described by Bak et al. (2013).

A yoke weighting 47 tons is placed around the blade COG to hold the blade. Two horizontal tugger lines are deployed from the yoke to the crane structure. Both tugger lines are 3m long and have an arm length of 10m, as shown in Figure 9. Table 1 is a summary of the system properties.

The detailed wire properties in the system are presented in Table 2. The crane wire is a typical metal wire rope with diameter of 60mm (Lankhorst ropes, 2013). The flexibility of the lift wire is due to the deformation of the crane boom and wires from crane tip to crane winch. The slings have a diameter of 30mm while the diameter of the tugger lines is 5mm. In addition, material damping in wire is included in the model, which is about 1% of the wire stiffness according to the SIMO Theory Manual (MARINTEK, 2015a).

Table 1: Main properties of the blade lifting system

Parameter	Value	Unit
Hook mass	10	tons
Yoke mass	47	tons
Blade mass	41.67	tons
Blade length	86.37	m
Installation height	119	m
Tugger line arm length	10	m

Table 2: Main parameters of the mechanical coupling

Parameter	Unit	Lift wire	Slings	Tugger lines
L	[m]	4.7	20.4	3.0
EA/L	[kN/m]	1.06e5	5.87e3	1.17e3
k_0	[kN/m]	5.0e3	–	–
Damping	[kNs/m]	1.06e3	5.87e1	1.17e1

4.1. Eigenvalue analysis

Eigenvalue analysis is conducted to evaluate the eigen periods of rigid body motions of the hook, blade and yoke. In the numerical model, the blade and yoke are modeled as one body, which is denoted by BY. The eigen periods and modes are obtained by solving Eq.(11):

$$[-\omega^2(\mathbf{M}+\mathbf{A})+\mathbf{K}]\cdot\mathbf{X}=0 \tag{11}$$

where **M**, **A** and **K** are the mass, added mass and restoring matrix of the BY and hook. Since they are in air, the added mass matrix **A** is zero. In addition, the restoring matrix **K** mainly comes from the gravity of involved bodies, lift wire, slings and tugger lines.

As shown in Table 3, the BY and hook coupled motions have 9 eigen modes. The dominated motion(s) of each eigen mode is emphasized in bold. The 1^{st} mode has the largest eigen period 13.63s, corresponding to the system pendulum motion in the blade local y_bz_b plane shown in Figure 9. The 2^{nd} is dominated by the yaw motion of the BY. The 3^{rd} mode is a combination of transnational motions in the horizontal plane and rotational motion in the vertical plane. The eigen periods of these two modes are much shorter due to the influence of the tugger lines. The last 6 modes have short natural periods, which are below 3s. The first mode is the most important for the

Table 3: Eigen modes and natural periods for BY (blade and yoke) and hook rigid body motions

Mode		1	2	3	4	5	6	7	8	9
$x_{BY,1}$	[m]	0.00	0.00	0.00	0.13	-0.09	0.12	0.00	0.01	0.00
$x_{BY,2}$	[m]	0.37	**0.70**	-0.14	0.00	0.00	0.00	-0.11	0.00	0.00
$x_{BY,3}$	[m]	0.00	0.00	0.00	-0.01	0.03	**1.00**	0.00	0.00	-0.09
$x_{BY,4}$	[deg]	**1.00**	**-0.94**	0.31	0.00	0.00	0.00	0.15	0.00	0.00
$x_{BY,5}$	[deg]	0.00	0.00	0.00	**-1.00**	**-1.00**	0.35	0.00	**-1.00**	-0.02
$x_{BY,6}$	[deg]	0.10	**-0.84**	**-1.00**	0.00	0.00	0.00	0.00	0.00	0.00
$x_{H,1}$	[m]	0.00	0.00	0.00	-0.19	-0.51	0.40	0.00	0.02	0.04
$x_{H,2}$	[m]	0.01	**1.00**	-0.26	0.00	0.00	0.00	**1.00**	0.00	0.00
$x_{H,3}$	[m]	0.00	0.00	0.00	0.00	0.05	**0.79**	0.00	0.00	**1.00**
T_n	[sec]	13.63	3.72	3.45	1.59	1.15	0.99	0.24	0.18	0.13

Note: $x_{BY,1} \sim x_{BY,6}$– BY motion in six degrees of freedom; $x_{H,1} \sim x_{H,3}$– translational motions of the hook.

dynamics of the system, as demonstrated by the spectral analysis of blade motion in Section 7.1.

5. Load cases and environmental conditions

A series of load cases are defined for code verification and time domain simulations, as given in Table 4 and 5. It should be noted that these load cases are not from design codes, but are only chosen for the numerical study in this paper. However, the largest turbulence intensity 15.72% in the load cases is chosen according to the desgin class C in IEC 6400-1 (IEC, 2005).

Load case LC1 is the steady wind case, which is used to verify the aerodynamic code.

In load case LC2, turbulent wind is applied. It is used to demonstrate the necessity of using an advanced aerodynamic model and how much inaccuracy a simplified aerodynamic model might cause as discussed in Section 6. The simplification made means that blade velocity is neglected in the calculation of aerodynamic loads.

Load case LC3 is a turbulent wind case with varying turbulence intensity T_I. LC3 is designed to study the characteristics of the blade installation system under turbulent wind condition, including global motion of the blade, aerodynamic loads acting on the blade and tension in crane wire and tugger lines.

Turbulent wind is also used in load cases LC4 and LC5 while their initial blade pitch angles θ_B are different from LC3. The θ_B represents the initial orientation of blade relative to the horizontal plane. LC4 and LC5 are used

Table 4: Definition of load cases with steady or turbulent wind

	U_W[m/s]	ψ_W[deg]	T_I[%]	$\theta_B[deg]$	T_S[s]	N_S
LC1	10	[-120∼120]	0	[0 30 45 60 90]	100	1
LC2	10	0	15.72	[0 45]	600	50
LC3	10	0	[1 3 5 7 9 11 13 15.72]	0	600	50
LC4	10	0	[1 3 5 7 9 11 13 15.72]	30	600	50
LC5	10	0	[1 3 5 7 9 11 13 15.72]	45	600	50
LC6	10	[0 15 30 45 60 75]	15.72	0	600	50

Note: U_W– mean wind speed at hub height; ψ_W– wind yaw angle; T_I– inflow wind turbulence intensity; θ_B– blade initial pitch angle; T_S– simulation time of each run; N_S– number of runs for each sub-case.

for comparison against LC3 to analyze the influence of blade pitch angle on two vital parameters during installation system, i.e., the blade root motion and loads in tugger lines.

In load case LC6, the turbulence intensity T_I is constant while the wind inflow angle ψ_W varies from 0^o to 75^o. The corresponding results show the influence of ψ_W on the extreme responses.

In load case LC1, only one run with duration of 100s is conducted since the blade is fixed and the wind is steady. However, 50 runs are executed for each simulation with duration of 600s in the turbulent wind load cases LC2 $\sim$ LC6. The reason for using 10min as the simulation time is that the duration of mating the blade onto hub usually takes approximately 10min. Fifty runs are to ensure the robustness of the obtained statistics. Moreover, 500s is used before the turbulent wind starts in each simulation to remove the transient effect due to simulation start up.

Extreme operating gust wind (EOG) represents rapid change in wind speed. It is applied to study the dynamic responses of the blade installation system under sudden transient change of inflow wind speed. Table 5 lists the EOG load cases. Load cases LC7 and LC8 have the same gust wind while their blade pitch angles θ_B are different. The purpose is to study the dynamic response of the blade installation system under extreme operating gust wind and the influence of θ_B on the dynamic responses. The wind speed of an EOG is given as:

$$V(z,t) = \begin{cases} V(z) - 0.37V_{gust}sin(3\pi t/T_G)(1-cos(2\pi t/T_G)) & \text{for} \quad 0 \leqslant t \leqslant T_G \\ V(z) & \text{otherwise} \end{cases} \tag{12}$$

where T_G is the duration of wind gust, i.e. $10.5s$ (IEC, 2005). Besides, V_{gust}

Table 5: Definition of load cases with gust wind

	U_W[m/s]	ψ_W[deg]	θ_B[deg]	T_G[s]	T_S[s]	N_S
LC7	10	0	0	10.5	600	1
LC8	10	0	45	10.5	600	1

Note: T_G– duration of gust wind.

is the gust velocity at the hub height, which is determined by the hub height wind speed, etc. In addition, V_z is the wind speed at height z, which is determined by the wind shear effect and wind speed at hub height.

6. Verification of the coupled simulation tool

Verification of the coupled simulation tool is carried out module by module. SIMO has been widely validated and used in the offshore oil&gas and renewable energy industries. Therefore, only verification of the Aero Code is carried out. Code-to-code comparison against HAWC2 is conducted using the DTU 10MW Reference Wind Turbine blade under load case LC1. Figure 10 show the comparison of lift and drag force. It is shown that the results from the developed code are in good accordance with the HAWC2 results. However, it should be noted that this code-to-code comparison only verifies the aerodynamic code but does not validate the model against experimental data since they are very difficult to obtain.

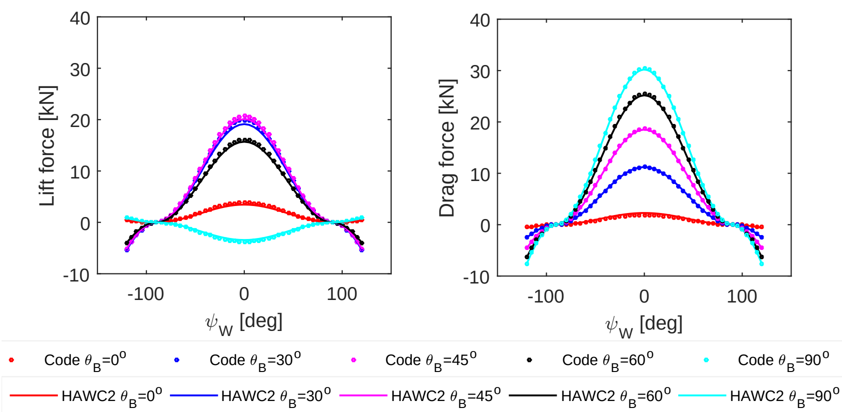

Figure 10: Verification of the Aero Code against HAWC2 in LC1

Figure 10 reveals the influence of blade pitch angle θ_B ($0^o < \theta_B < 90^o$) and wind yaw angle ψ_W ($-120^o < \psi_W < 120^o$) on the blade aerodynamic loads. With the increase of θ_B, the aerodynamic lift force F_z firstly experiences an increasing trend before θ_B reaches 45^o and then starts to decrease until $\theta_B = 90^o$. However, the aerodynamic drag force F_x experiences a consistent increase until $\theta = 90^o$. At the mean time, both F_z and F_x scale with the cosine function of ψ_W. The peak value of F_x at $\psi_W = 0^o$ is over $30kN$, which is 50% larger than the peak of F_z at the same yaw angle. The roll moment M_x shown in Figure 11(a) shares the same trend with F_z because it is the integration of lift force along the blade with an arm around the blade COG. Similar to F_D, the yaw moment M_z increases until θ_B reaches 90^o.

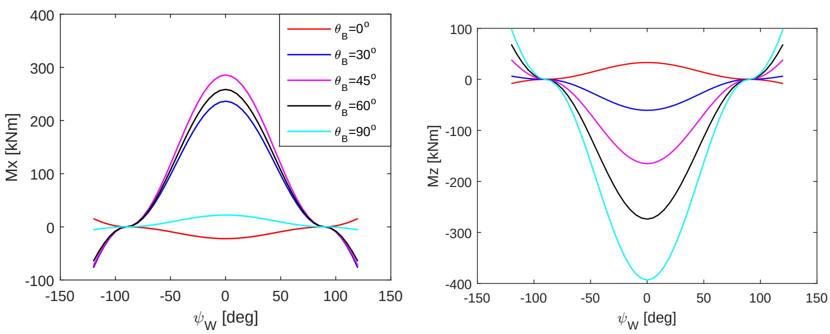

(a) Roll moment M_x

(b) Yaw moment M_z

Figure 11: Blade aerodynamic roll and yaw moment calculated from code at different blade pitch angle and wind yaw angle in LC1

6.1. Comparison of aerodynamic force distribution on a lifted blade and a rotating blade

The distribution of aerodynamic forces on a lifted blade is quite different from a rotating one. Figure 12 compares the lift and drag force distribution on a blade during rotation and lifted condition in LC1. The blade has zero initial pitch angle in both conditions. Besides, the rotating blade has a rotational speed of 8.029 rpm. As shown in Figure 12, both lift and drag forces for the rotating blade experience an increasing trend towards the tip. The aerodynamic center of the rotating blade stays close to the blade tip. It indicates that the rotational speed plays an important role in the aerodynamic force distribution of a rotating blade. For the lifted blade, the main contribution of the aerodynamic loads comes from the middle and root part of the blade. Thus, the aerodynamic center of a lifted blade is located close to the blade root. Compared to the inflow wind velocity, the velocity of a lifted blade is insignificant.

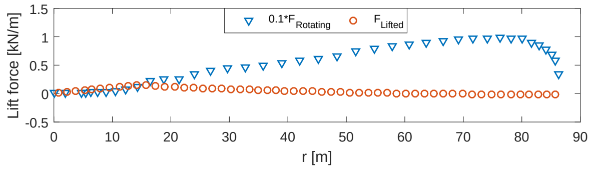

(a) Lift force F_z

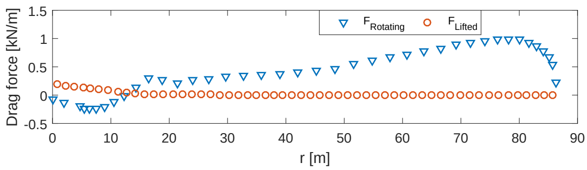

(b) Drag force F_x

Figure 12: Comparison of distribution of lift and drag forces on a blade under rotating condition and lifted condition in LC1: $\theta_B = 0^o$ and blade rotational speed 8.029 rpm.

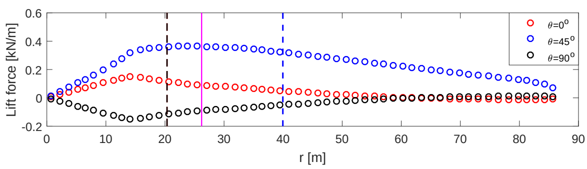

(a) Lift force F_z

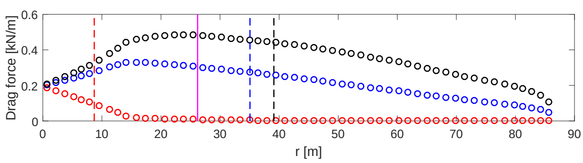

(b) Drag force F_x

Figure 13: Lift and drag force distribution of a lifted blade in LC1: $\psi_W = 0^o$

Figure 13 shows the aerodynamic distribution on a lifted blade with variation of blade pitch angle in LC1. The pink dense line Figure 13 represents the blade COG while the dotted lines stands for the aerodynamic center at different θ_B. As shown in Figure 13(a), the aerodynamic center of lift force for $\theta_B = 0^o$ is 20m from the blade root. Then it moves to around 40m from root at $\theta_B = 45^o$. Afterwards, it moves back towards the blade root as θ_B increases. When the blade pitch angle is 90^o, the aerodynamic center of lift force is the same with zero pitch angle. On the contrary, the aerodynamic center of drag force consistently moves towards blade tip as θ_B increases.

6.2. Influence of blade velocity on the system response

In the current method for calculation of aerodynamic loads, the velocity $\mathbf{V}_i$ at blade elements due to blade motion, i.e., $\mathbf{V}_{MG}$, is taken into consideration, as shown in Eq.(7). Since the blade velocity is small compared with wind inflow velocity, there might be thoughts to neglect the blade velocity (BV) in the aerodynamic load calculation. In this section, the influence of blade velocity in the aerodynamic load calculation is discussed.

- Approach With BV: considering $\mathbf{V}_i$ in the calculation of aerodynamic loads; the relative inflow velocity in the local airfoil coordinate system is:

$$\mathbf{V}_{A,i} = \mathbf{T}_{GC,i}(\mathbf{V}_{WG,i} - \mathbf{V}_i) \tag{13}$$

- Approach Without BV: neglecting $\mathbf{V}_i$ in the calculation of aerodynamic loads; the relative inflow velocity in the local airfoil coordinate system is:

$$\mathbf{V}_{A,i} = \mathbf{T}_{GC,i}\mathbf{V}_i \tag{14}$$

In addition, it should be noted that the instantaneous position of the blade is used in the coordinate transformation matrix $\mathbf{T}_{GC,i}$ in both approaches. Load case LC2 is used in the comparison of these two approaches. The blade roll motion and aerodynamic roll moment on the blade are taken as examples in the comparison.

Figures 14 and 15 respectively compare the time series and spectra of the blade roll motion and aerodynamic roll moment on the blade calculated based on approach With BV (with consider blade velocity in the calculation of aerodynamic load) and Without BV (without consider blade velocity in the calculation of aerodynamic load) in LC2 with blade initial pitch angle

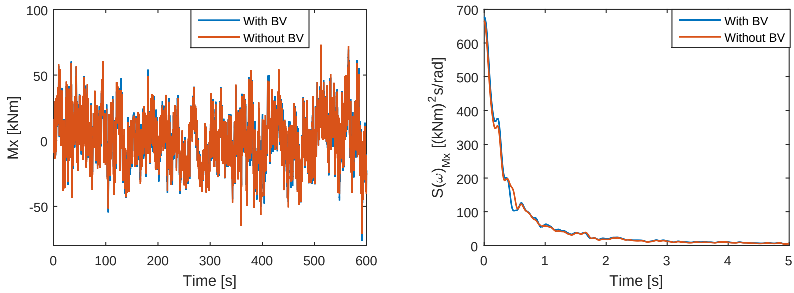

(a) Time series of M_x (b) Spectrum of M_x

Figure 14: Comparison of aerodynamic roll moment on the blade calculated based on the approach With and Without BV using load case LC2 with blade initial pitch angle $\theta_B = 0^o$

$\theta_B = 0^o$. As shown in Figures 14(a) and 14(b), neglecting the blade velocity during the calculation of aerodynamic loads leads to a marginal decrease of the amplitude of aerodynamic roll moment M_x at $\omega = 0.46 rad/s$ which is the resonant frequency of roll motion. As a consequence, neglecting the blade velocity leads to significant discrepancies in the blade motion, as shown in Figures 15(a) and 15(b). Similar trends are seen in the comparison of these two approaches in LC2 with blade initial pitch angle $\theta_B = 45^o$, as

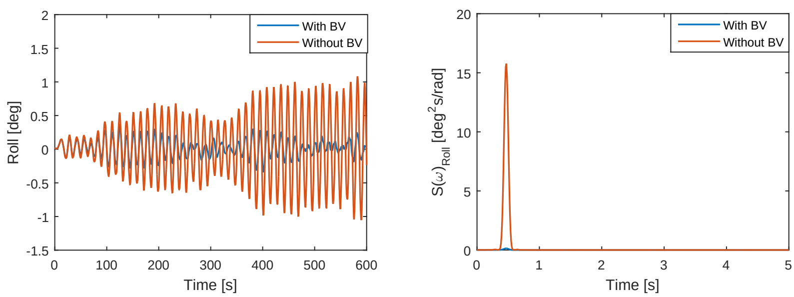

(a) Time series of blade roll motion (b) Spectrum of blade roll motion

Figure 15: Comparison of blade roll motion calculated based on approach With BV and Without BV using load case LC2 with blade initial pitch angle $\theta_B = 0^o$

shown in Figures 16 and 17. However, neglecting the blade velocity during the calculation of aerodynamic loads at $\theta_B = 45^o$ leads to a much smaller difference in blade roll motion. Because the total aerodynamic roll moment on the blade at $\theta_B = 45^o$ is less sensitive to the variation of angles of attack at all blade elements induced by neglecting the blade velocity than at $\theta_B = 0^o$.

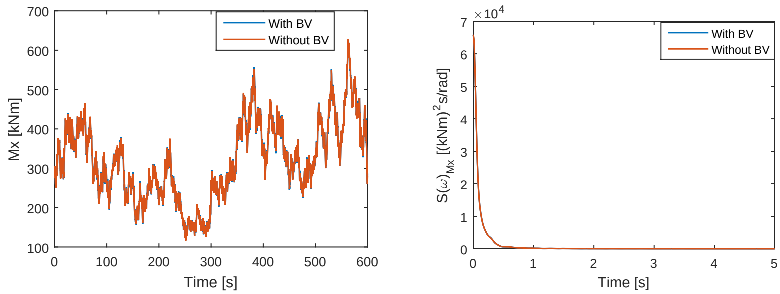

(a) Time series of M_x (b) Spectrum of M_x

Figure 16: Comparison of aerodynamic roll moment calculated based on approach With BV and Without BV using load case LC2 with blade initial pitch angle $\theta_B = 45^o$

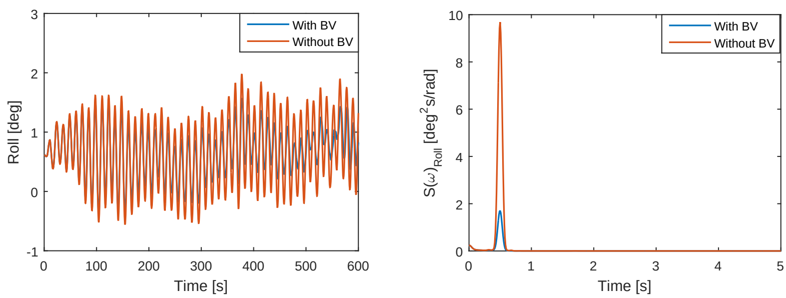

(a) Time series of blade roll motion (b) Spectrum of blade roll motion

Figure 17: Comparison of blade roll motion calculated based on approach With BV and Without BV using load case LC2 with blade initial pitch angle $\theta_B = 45^o$

Even though the blade velocity has marginal impact on the amplitude of aerodynamic loads, it is essential to include it in the aerodynamic load calculations, since it plays an important role in terms of aerodynamic damping. The blade motion is highly dominated by pendulum motion, for which the damping is small. Thus, the aerodynamic damping due to blade motion is crucial for the dynamic response of the blade. When it is neglected, the blade motion will be significantly overestimated.

6.3. Influence of tugger line arrangement on blade dynamic motion

As mentioned in Section 4, a representative value of the tugger line arm length 10m (relative to the blade COG) was used, which is also shown in Figure 18(a). To investigate the impact of tugger line arrangement on the dynamic characteristics of blade motion, a shorter tugger line arm length, i.e., 5m was applied as illustrated in Figure 18(b) for comparison. The results are shown in Figure 19.

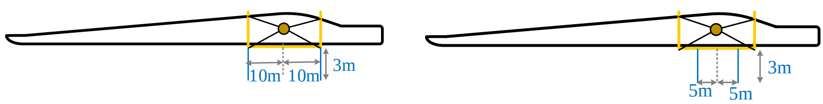

(a) Arm length 10m

(b) Arm length 5m

Figure 18: Illustration of different tugger line arm length relative to blade COG

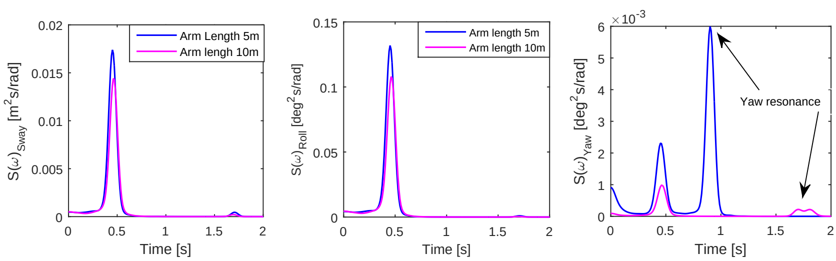

(a) Sway

(b) Roll

(c) Yaw

Figure 19: Comparison of spectra of blade motions at its COG with different tugger line arm length in LC2 with blade initial pitch angle $\theta_B = 0^o$

As shown in Figure 19(a) and 19(b), the dynamic responses of blade sway and roll with tugger line arm length of 10m are slightly smaller than that for the 5m case. However, significant reduction of blade yaw motion is seen in Figure 19(c) by increase of the tugger line arm length from 5m to 10m. That is because the tugger line arm length of 10m increases the resonant frequency of blade yaw motion to a high level where resonant response is greatly reduced.

7. Results and discussions

The developed coupled simulation tool SIMO-Aero is applied to study the wind-induced dynamic response of the system prior to the mating process. The characteristics of stochastic dynamic response of the blade installation system is analyzed. The study is further extended by analyzing the extreme responses of the system under turbulent wind and extreme operating gust wind conditions.

7.1. Stochastic dynamic responses of the blade installation system in turbulent wind

The global responses of the blade installation system in load case LC2 are studied in this section. In load case LC3, the wind yaw angle ψ_W and blade initial pitch angle θ_B are both zero while the turbulence intensity T_I of the inflow wind varies from 1% to 15.72%.

Table 6 shows the mean values of the global responses, such as blade motions, aerodynamic loads on the blade and tensions in crane wire and tugger lines. The non-zero mean values of roll and yaw are respectively resulted from the aerodynamic roll and yaw moment. The roll motion leads to difference of tension in tugger lines, which causes the non-zero blade sway motion.

The standard deviations (STDs) of blade surge, heave and pitch are not presented since they are almost zero. The STDs of blade sway, roll and yaw with variation of wind turbulence intensity T_I are shown in Figure 20(a). The blade roll motion is much larger than its yaw. As mentioned in Section 4, the tugger lines are deployed in the horizontal plane, which control the blade yaw motion. However, constraints in the vertical plane are much weaker, leading to significant blade roll motion. Moreover, the STDs of blade sway, roll and yaw scale linearly with T_I. Besides, the STD variation of aerodynamic loads and tensions in crane wire and tugger lines, which are respectively shown in Figures 20(b) $\sim$ 20(d), experience a similar linear trend over T_I. The linear-scale relationship between system response and wind turbulence intensity

Table 6: Mean value of global response in LC2

	Parameter	Mean value	Unit
Blade motion	Surge	0.0016	[m]
	Sway	0.0046	[m]
	Heave	0.001	[m]
	Roll	0.014	[deg]
	Pitch	-0.0101	[deg]
	Yaw	0.0095	[deg]
Forces	F_x	2.145	[kN]
	F_z	5.5619	[kN]
	M_x	2.1596	[kNm]
	M_z	33.9096	[kNm]
	F_{cw}	965.4169	[kN]
	F_{tugg1}	21.0743	[kN]
	F_{tugg2}	24.4876	[kN]

Note: F_x and F_z– Aerodynamic drag and lift force; M_x and M_z– Aerodynamic roll and yaw moment; F_{cw}– Tension in the crane wire; F_{Tugg}– Tension in tugger lines.

can be expressed as:

$$\begin{bmatrix} \sigma_{sway} & \sigma_{roll} & \sigma_{yaw} \\ \sigma_{Fx} & 0 & \sigma_{Fz} \\ \sigma_{Mx} & 0 & \sigma_{Mz} \\ \sigma_{Fcw} & \sigma_{Ftug1} & \sigma_{Ftug2} \end{bmatrix} = T_I \mathbf{A} \tag{15}$$

where $\mathbf{A}$ is a matrix of the scale parameters, which are determined by the inflow wind characteristics and properties of the blade, such as mean wind speed, density of air, aerodynamic and structural properties of the blade, etc. This indicates that the STDs of blade motions, aerodynamic loads and wire tensions are proportional to the wind turbulent intensity. It agrees with and further extends one of the conclusions in Ref.(Gaunaa et al., 2014). The agreed conclusion is that the aerodynamic loading on a lifted blade is proportional to T_I. In LC2, $\mathbf{A}$ is found to be:

$$\mathbf{A} = \begin{bmatrix} 0.0026 & 0.0071 & 0.0008 \\ 0.0365 & 0 & 0.1029 \\ 1.1376 & 0 & 0.6176 \\ 0.1018 & 0.0842 & 0.0980 \end{bmatrix} \tag{16}$$

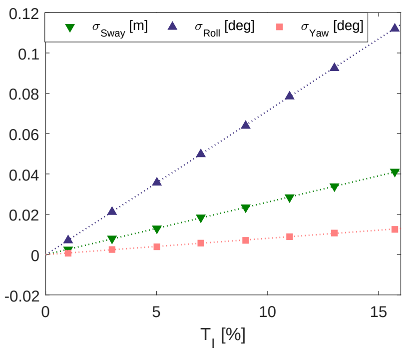

(a) Blade motion

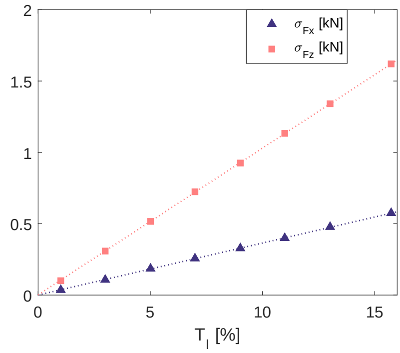

(b) Aerodynamic forces

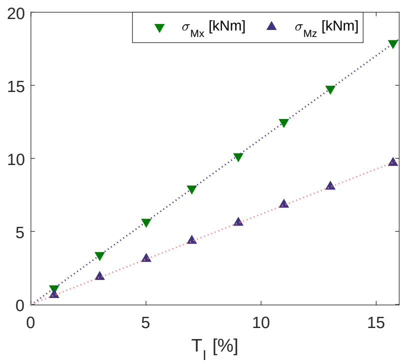

(c) Aerodynamic moments

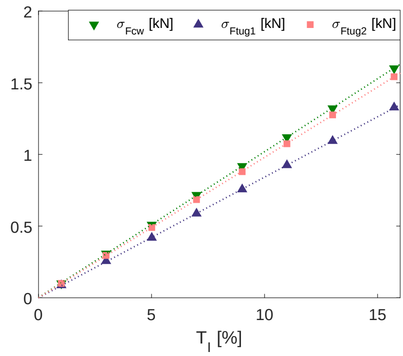

(d) Crane wire and tugger line tension

Figure 20: Standard deviation of aerodynamic loads on the blade in LC3: the dashed lines are the linearly fitted lines

Furthermore, spectral analysis for blade motions is conducted, particularly for sway, roll and yaw motions. As shown in Figures 21, all of the three spectra have a peak around $\omega = 0.46 rad/s$. The corresponding peak period is approximately $13.63s$, which is the natural period of the 1^{st} mode of the system rigid body motion shown in Table 3. It indicates that the pendulum motion dominates the system responses. Besides, the yaw spectrum has other two small peaks between $\omega = 1.5 rad/s$ and $\omega = 2.0 rad/s$, which are respectively the eigen periods of the 7th and 8th modes shown in Table 3. Moreover, the spectrum peaks also increase with increasing turbulence intensity, which indicates that the blade motion is larger at higher turbulent intensity.

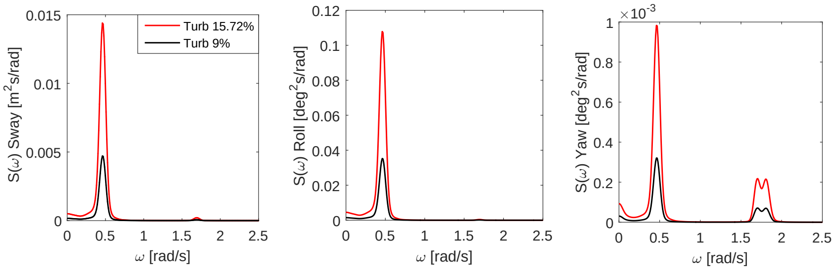

(a) Sway (b) Roll (c) Yaw

Figure 21: Spectra of blade motions at its COG in LC3

7.2. Stochastic motion response at blade root in turbulent wind

The blade root displacement relative to the hub position can be expressed as:

$$[\Delta x \quad \Delta y \quad \Delta z]^T = [x - x_0 \quad y - y_0 \quad z - z_0]^T \tag{17}$$

where x_0, y_0 and z_0 are the position of hub center. Figure 22 shows an example of the time series of blade root displacements and velocities.It is shown that the surge motion at blade root is the smallest while the heave motion is the largest. The horizontal tugger lines provide significant restoring in surge. However, the restoring in sway and heave relies on the slings and crane wires, which are quite limited.

Moreover, the spectral analysis for motions at blade root is conducted, as shown in Figure 23. The heave spectrum at blade root, shown in Figure 23(c) has the largest values, which is due to the significant blade roll motion. The surge spectrum at blade root in Figure 23(a) has a similar trend with the blade yaw spectrum in Figure 21(c). This indicates that the surge motion at blade root is mainly resulted from the blade yaw motion. The amplitude in sway spectrum at blade root in Figure 23(b) is very close to the amplitude of blade sway spectrum in Figure 21(a). It indicates that the blade rotational motions have marginal contribution to the sway motion at blade root, compared with blade sway.

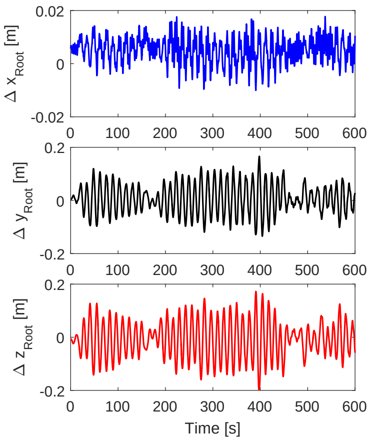

(a) Displacement

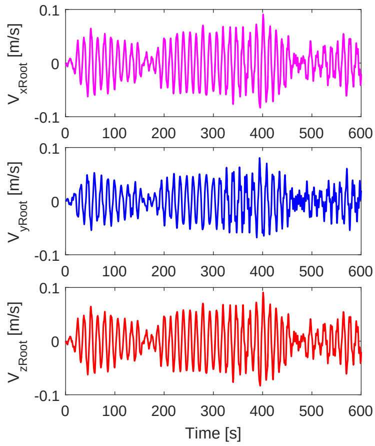

(b) Velocity

Figure 22: Example of time series for blade root displacement and velocity in LC3 with $T_I = 15.72\%$

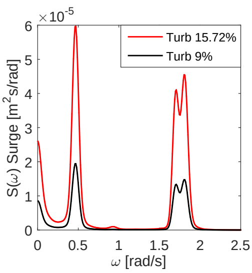

(a) Surge

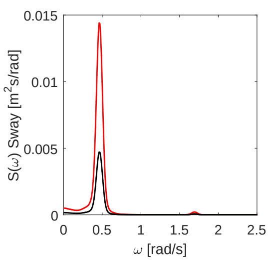

(b) Sway

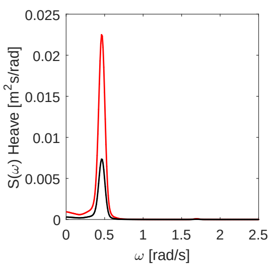

(c) Heave

Figure 23: Spectra of motions at blade root in LC3

7.3. Extreme response in turbulent wind

In this section, the extreme values of critical parameters in the lifting system during the blade mating process are studied. For the mating process of the blade onto hub, the blade root motion in the XZ plane is very critical. If the blade root motion in XZ plane is too large, the blade cannot be mated onto the hub. In this study, the blade root motion in the XZ plane is denoted as R_{root}:

$$R_{root} = \sqrt{(\Delta x)^2 + (\Delta z)^2} \tag{18}$$

The sway motion at blade root is also important because it might lead to destructive collisions. The sway motion at blade root is expressed as:

$$Y_{root} = \Delta y \tag{19}$$

Besides, the sway velocity at blade root is denoted as $V_{y,root}$.

The tension in crane wire is not considered as a critical parameter since it has small variation from its mean value. The extreme tension in tugger lines F_{tug} is considered to be critical as it adds extra force and moment to the crane boom.

7.3.1. Extreme value estimation

The extreme values in this study are calculated based on the mean up-crossing rate method (Naess and Moan, 2012). In this method, it is assumed that the high threshold up-crossings are statistically independent, thus a Poisson probability distribution can be applied for the extreme values. Let $M(T) = max\{Y(t); 0 \leq t \leq T\}$ denotes the extreme value for a random process $Y(t)$ over the duration of T. If the process is stationary, the corresponding probability of exceedance for extreme values is given by:

$$P(M(T) > y) = 1 - exp\Big(-\bar{v}^{+}(y)T\Big) \tag{20}$$

where $\bar{v}^{+}(y)$ is the mean up-crossing rate.The sample-estimated mean value of $\bar{v}^{+}(y)$ can be calculated from simulated time series:

$$\hat{\bar{v}}^{+}(y) = \frac{1}{kT}\sum_{j=1}^{k} n_j^{+}(y;T) \tag{21}$$

where $n_j^{+}(y;T)$ represents the number of up-crossings at level y of the jth time history during $[0 \quad T]$. Besides, k is the number of time series. With enough number of time series, a good approximation of 95% confidence interval (CI) can be obtained, i.e.:

$$CI_{\pm}(y) = \hat{\bar{v}}^{+}(y) \pm \frac{1.96\hat{s}(y)}{\sqrt{k}} \tag{22}$$

Eq.(21 $\sim$ 22) are the basics for the empirical estimation of the mean upcrossing rate from direct numerical simulations, i.e., Monte Carlo simulation. However, direct numerical simulations are very time-consuming especially for low probability levels (Chai et al., 2015). To be more time-efficient, an extrapolation technique is applied (Naess and Gaidai, 2008).

The 10-min extreme values are studied with 3.3% probability of exceedence, which corresponds to occur once within 300min according to DNV-RP-H103 standard (Det Norske Veritas , 2011). The corresponding mean upcrossing rate is 5.593×10^{-5}. Fifty time series are used for the extreme value estimation of each sub-case. Figure 24(a) and 24(b) present two examples of the fitting and extrapolation.

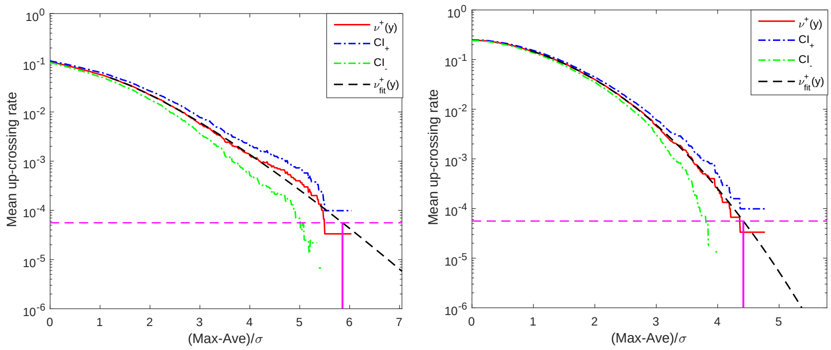

(a) Blade root displacement R

(b) Tugger line tension

Figure 24: Illustration of mean upcrossing rate extrapolation: LC3 with $T_I = 15.72\%$

7.3.2. Effects of turbulence intensity

The influence of wind turbulence intensity T_I on the system extreme responses is studied in this section. Load cases LC3, LC4 and LC5 are used. The turbulence intensity T_I varies within each load case while the blade initial pitch angle θ_B increases from 0^o in LC3 to 45^o in LC5. Figure 25 shows the results. Specifically, Figure 25(a) shows the extremes of R_{root}. Figures 25(b) and 25(c) present respectively the extreme sway displacement Y_{root} and velocity $V_{y,root}$ at blade root. Figure 25(d) shows the extreme tension in tugger lines F_{tug}.

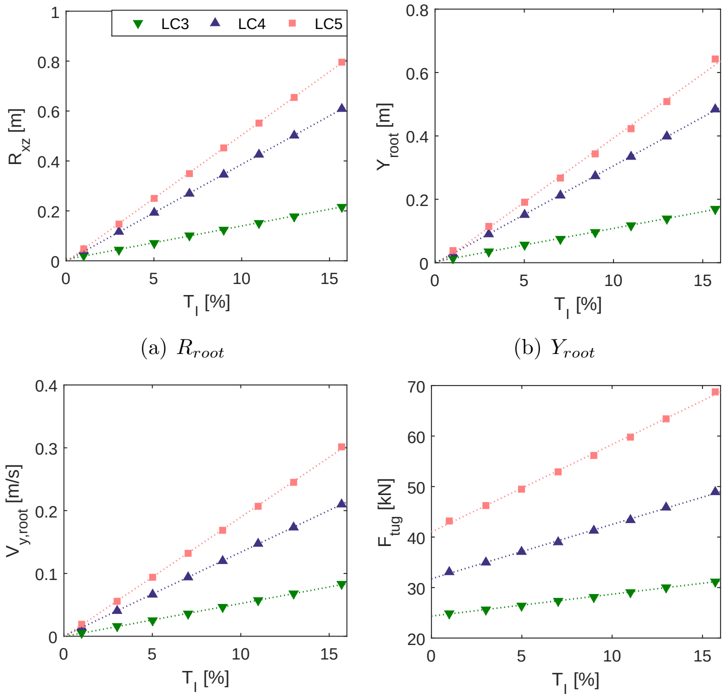

(a) R_{root} (b) Y_{root}

(c) $V_{y,root}$ (d) F_{tug}

Figure 25: Extreme responses of blade root motion and tension in tugger lines in LC3 $\sim$ LC5: the dashed lines are the linearly fitted lines

Similar to the standard deviations of the system response in Section 7.1, the system extreme responses also increase linearly with increasing T_I. At the same time, the extreme responses experience a non-linear increasing trend with the increase of θ_B. The extreme responses at $\theta_B = 0^o$ is small. A dramatic increase occurs when θ_B increases to 30^o in LC4. The extreme responses at $\theta_B = 45^o$ in LC5 reach their respective peak values. The variation trend over θ_B is similar to that of the aerodynamic forces and moments shown in Figure 10 and 11.

Take the extreme values of R_{root} as an example, the extreme value of R_{root} at $T_I = 15.72\%$ is over three times larger than the corresponding extreme at $T_I = 5\%$. Besides, the extreme value of R_{root} also varies a lot with increasing blade pitch angle. At $T_I = 15.72\%$, the extreme value of R_{root} increases over two times when θ_B increases from 0^o to 45^o. Compared with R_{root}, the extreme value of Y_{root} is slightly smaller. At large pitch angle, the extreme value of $V_{y,root}$ is significant. This indicates that large blade pitch angle makes it more difficult to mate the blade onto hub and increases the chance of blade root collision with hub.

7.3.3. Effects of wind direction

Figure 26(a) shows the influence of wind yaw angle ψ_B on the extreme responses of the system using load case LC6. Six yaw angles are simulated, varying between 0^o and 75^o.

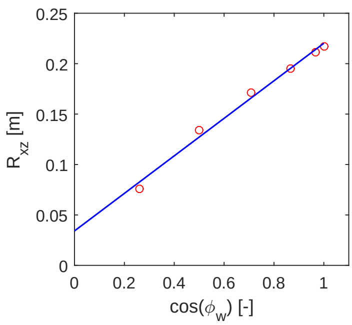

(a) R_{root}

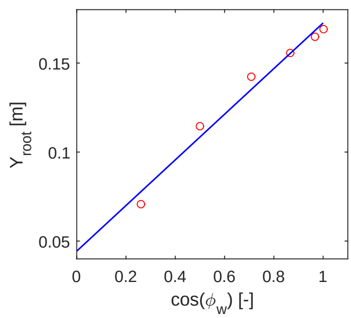

(b) Y_{root}

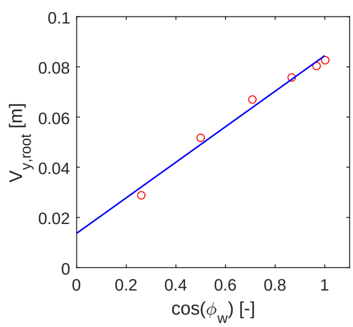

(c) $V_{y,root}$

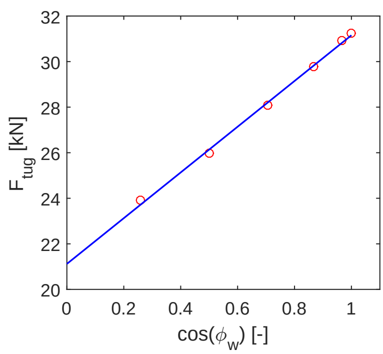

(d) F_{tug}

Figure 26: Extreme root displacement and tugger line tension in LC6

It is shown that all the extreme responses are linear functions of the cosine functions of ψ_B. The fitted line is presented as the blue curve in Figure 26(a). It is shown that the system extreme responses decrease with increasing wind yaw angle. This indicates that larger wind yaw angle makes the mating operation of a blade onto hub easier.

7.4. Stochastic dynamic response of the system in extreme operating gust wind

The influence of extreme operating wind gust on the dynamic response of the system is studied in this section, as shown in Figure 27. Different blade initial pitch angles θ_B are applied, i.e. 0^o in LC7 and 45^o in LC8. The same gust wind is used for both cases. The gust wind inflow angle ψ_B is zero and the mean wind speed is 10m/s. Figure 27(b) shows the time series of the gust wind speed. The wind gust starts at 300s and ends at 310.5s. The other graphs in Figure 27 show the blade root motion and aerodynamic loading on the blade. To have a better illustration of the response, time series between 290s and 350 is presented.

As shown in Figures 27(b) and 27(c), the aerodynamic loads on the blade follow the gust wind simultaneously. Compared with LC7, the aerodynamic loads in LC8 have a much larger peak. Nevertheless, the aerodynamic loads in both cases become stable after the gust wind ends, which indicates that the aerodynamic loads on a lifted blade are mainly dominated by inflow wind velocity.

However, compared with the blade aerodynamic loads, the motion responses at blade root experience a different trend. As shown in Figures 27(d) $\sim$ 27(f), the blade root motions fluctuate a lot. Moreover, much larger fluctuations are seen by blade root motion in LC8. The fluctuation of blade root surge motion (Δx) is dominated by two cycles, which agrees with the spectrum of blade root surge motion in Figure 23(a). Apparently, the sway (Δy) and heave (Δz) motions at blade root fluctuate with the natural frequency of the 1^{st} eigen mode shown in Figures 23(b) and 23(c).

The maximum responses of blade root motions are listed in Table 7. In load case LC7, the maximum values of R_{root}, Y_{root} and $V_{y,root}$ are all very small. Nevertheless, in LC8, the maximum values of R_{root} and Y_{root} are respectively 0.43m and 0.33m. Compared with results in Figure 25, the maximum responses in the extreme operating gust wind are equivalent to the extreme responses under turbulent wind with turbulence intensity of 7%.

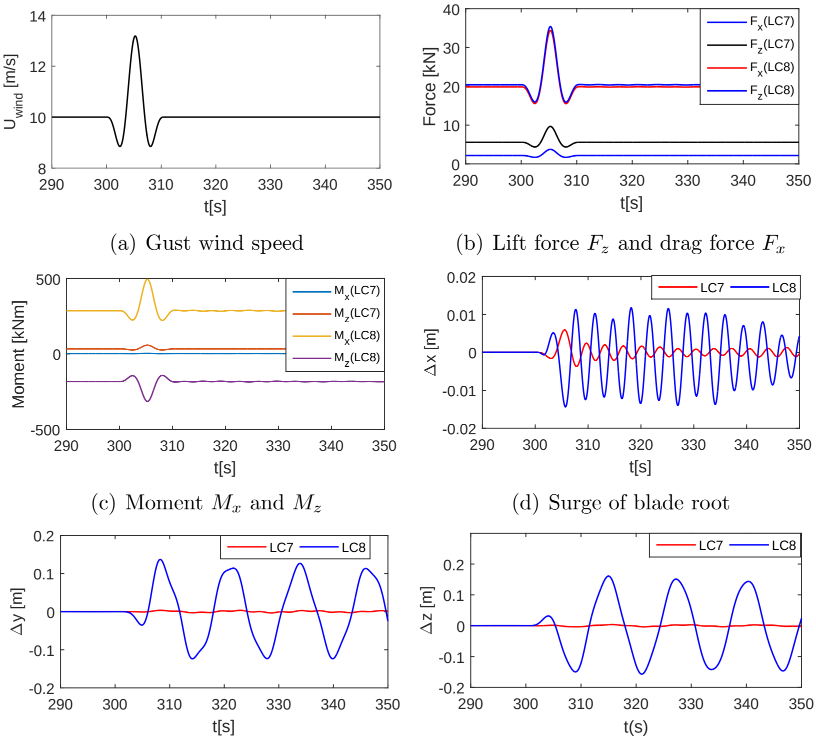

(a) Gust wind speed

(b) Lift force F_z and drag force F_x

(c) Moment M_x and M_z

(d) Surge of blade root

(e) Sway of blade root

(f) Heave of blade root

Figure 27: Blade root motion and blade aerodynamic loads in LC7 and LC8

Table 7: Maximum responses of blade root motion in LC7 and LC8

Parameter	Maximum		Unit
	LC7	LC8	
R_{root}	0.0060	0.4257	[m]
Y_{root}	0.0034	0.3308	[m]
$V_{y,root}$	0.0030	0.0852	[m/s]

8. Conclusions

This paper deals with the development, verification and application of an integrated simulation tool for modeling and dynamic analysis of single blade installation for wind turbines. On the basis of cross-flow principle, an aerodynamic code denoted as Aero code is developed considering the effect of wind turbulence, extreme operating gusts and dynamic stall. The developed Aero code is then coupled with SIMO to formulate the integrated simulation tool, i.e., SIMO-Aero code. The coupled SIMO-Aero code could be used to evaluate the system performance during single blade installation for offshore as well as onshore wind turbines, accounting for aerodynamics, hydrodynamics and wire coupling mechanics.

Verification of the simulation tool is conducted module by module. SIMO has been widely verified and used. The Aero code is verified by code-to-code comparisons against HAWC2 results. It is shown that the Aero code gives accurate estimation of the aerodynamic loads. The characteristics of aerodynamic loads on a lifted blade are quite different from a rotating one. For a lifted blade, the main contributions of aerodynamic loads come from the middle and root part of the blade. Furthermore, the aerodynamic damping is of great importance in the dynamic response of blade during installation.

The developed integrated simulation tool is then applied to simulate the wind-induced dynamic responses of a DTU 10MW reference wind turbine blade prior to mating using a jack-up crane vessel. Stochastic dynamic analysis reveals the characteristics of the blade installation system. The blade motions are dominated by pendulum motions. Sway and roll motion of the blade are significant, leading to large sway and heave motion at the blade root. Furthermore, the system critical responses are identified, which are respectively blade root surge and heave motion, displacement and velocity of root sway and tension in tugger lines. Moreover, the critical responses are further studied in turbulent wind and gust wind. The results indicate that a larger wind yaw angle and a smaller blade pitch angle ease the difficulty of mating the blade onto the hub. Besides, installing a blade under extreme operating gust wind is less difficult than in strong turbulent wind.

The horizontally deployed tugger lines are commonly used in offshore blade installation. However, they do not provide enough constraints in the lateral and vertical directions, leading to significant blade root motions in sway and heave. To reduce motions at blade root, increasing damping in the tugger lines or adjusting tugger line configurations might help. Besides, a yoke with automatic motion compensation is expected to have a better control of motions at the blade root.

Moreover, the blade root motion is highly sensitive to the initial pitch angle of the blade, wind turbulence intensity and wind direction. During the planning and operational phases of offshore wind turbine blade installation, these factors are recommended to be considered together with the mean wind speed. In this way, the offshore blade installation could be conducted safely, economically and more efficiently.

9. Future work

In this study, the jack-up crane vessel including the crane were assumed to be rigid and rigidly fixed to the seabed. In reality, the crane tip of the jack-up crane vessel moves due to the motion of the jack-up vessel under wave loads and the deformation of the crane at large lifting height. This movement has some impacts on the dynamic response of the blade during installation. A future study will be conducted to evaluate the influence of wave-induced loads on the jack-up crane vessel and deformation of the jack-up crane vessel and the crane on the dynamic behavior of the blade during installation.

Study on blade installation by a floating crane vessel is also to be conducted by using the developed simulation tool in the future. It is expected to be favored by the offshore wind industry, due to the rapid development of offshore wind energy.

Acknowledgment

The authors appreciate the support from the Department of Marine Technology, Centre for Ships and Ocean Structures (CeSOS) and Centre for Autonomous Marine Operations and Systems (AMOS), NTNU. The work is financially supported by the China Scholarship Council (CSC).

Reference

Ahn, D., Shin, S.-C., Kim, S.-Y., Kharoufi, H., Kim, H.-C., 2017. Comparative evaluation of different offshore wind turbine installation vessels for korean west–south wind farm. International Journal of Naval Architecture and Ocean Engineering 9 (1), 45–54.

Bak, C., Zahle, F., Bitsche, R., Kim, T., Yde, A., Henriksen, L. C., Hansen, M. H., Natarajan, A., 2013. Description of the DTU 10 MW reference wind turbine. Tech. Rep. DTU Wind Energy Report-I-0092, Technical University of Denmark.

Chai, W., Naess, A., Leira, B. J., 2015. Stochastic dynamic analysis and reliability of a vessel rolling in random beam seas. Journal of Ship Research 59 (2), 113–131.

Cheng, Z., Madsen, H. A., Gao, Z., Moan, T., 2016. Aerodynamic modeling of floating vertical axis wind turbines using the actuator cylinder flow method. Energy Procedia 94, 531–543.

Cheng, Z., Madsen, H. A., Gao, Z., Moan, T., 2017. A fully coupled method for numerical modeling and dynamic analysis of floating vertical axis wind turbines. Renewable Energy 107, 604–619.

Det Norske Veritas , 2011. Modelling and analysis of marine operations, standard DNV-RP-H103.

DONG energy, 2016. Burbo Bank Extension. http://www.dongenergy.co.uk/uk-business-activities/wind-power/operational-offshore-wind-farms, (Accessed on 24/10/2017).

Gaunaa, M., Bergami, L., Guntur, S., Zahle, F., 2014. First-order aerodynamic and aeroelastic behavior of a single-blade installation setup. Journal of Physics: Conference Series 524 (1), 012073.

Gaunaa, M., Heinz, J., Skrzypiński, W., 2016. Toward an engineering model for the aerodynamic forces acting on wind turbine blades in quasisteady standstill and blade installation situations. Journal of Physics: Conference Series 753 (2), 022007.

GL Garrad Hassan, 2010. Bladed theory manual version 4.0.

Global Wind Energy Council, 2017. GLOBAL WIND STATISTICS 2016.

Gupta, S., Leishman, J. G., 2006. Dynamic stall modelling of the S809 aerofoil and comparison with experiments. Wind Energy 9 (6), 521–547.

High Wind NV, 2015. Boom lock. http://www.high-wind.eu/boomlock/, (Accessed on 01/09/2017).

Hoerner, S. F., Borst, H. V., 1985. Fluid-dynamic lift: practical information on aerodynamic and hydrodynamic lift. Hoerner Fluid Dynamics, Vancouver, WA.

Horner, S., 1965. Fluid dynamic drag: Practical information on aerodynamic drag and hydrodynamic resistance. Hoerner Fluid Dyn., Midland Park, NJ.

IEC, 2005. International standard 61400-1, wind turbines, part 1: Design requirements.

IEC, 2009. IEC 61400-3, wind turbines, part 3: Design requirements for offshore wind turbines.

Jonkman, B. J., 2009. Turbsim user's guide: Version 1.50.

Kuijken, L., 2015. Single blade installation for large wind turbines in extreme wind conditions. Master thesis, Technical University of Denmark.

Kvittem, M. I., Bachynski, E. E., Moan, T., 2012. Effects of hydrodynamic modelling in fully coupled simulations of a semi-submersible wind turbine. Energy Procedia 24, 351–362.

Lankhorst ropes, 2013. Offshore steel wire ropes. http://www.lankhorstropes.com/files/uploads/Offshore/brochures/Steel_Wire_Rope_brochure__100dpi__April_2013.pdf, (Accessed on 02/13/2017).

Larsen, T. J., Hansen, A. M., 2015. How 2 HAWC2, the user's manual, version 12.2. User manual version 12.2, Risø National Laboratory, DTU.

Leishman, J. G., Beddoes, T., 1989. A semi-empirical model for dynamic stall. Journal of the American Helicopter society 34 (3), 3–17.

Liftra, 2012. Blade dragon. http://www.liftra.com/product/product-2/, (Accessed on 01/09/2017).

MARINTEK, 2015a. Simo-theory manual version 4.6.

MARINTEK, 2015b. Simo-user manual version 4.4.1.

Naess, A., Gaidai, O., 2008. Monte Carlo methods for estimating the extreme response of dynamical systems. Journal of Engineering Mechanics 134 (8), 628–636.

Naess, A., Moan, T., 2012. Stochastic dynamics of marine structures. Cambridge University Press: Cambridge, UK.

Siemens, 2014a. Innovative yoke for safe wind turbine blade lifting. http://www.offshorewind.biz/2014/06/26/innovative-yoke-for-safe-wind-turbine-blade-lifting/, (Accessed on 01/09/2017).

Siemens, 2014b. Siemens wind turbine blade being positioned. https://www.siemens.co.uk/en/news_press/index/news_archive/2014/major-uk-offshore-wind-manufacturing-site-to-be-built-by-siemens.htm, (Accessed on 01/09/2017).

Uraz, E., 2011. Offshore wind turbine transportation & installation analyses planning optimal marine operations for offshore wind projects. Master thesis, Gotland University.

Wang, Y., He, W., Tian, D., 2012. Calculation of hoisting forces of the wind turbine rotor based on wind conditions. Renewable energy 39 (1), 323–328.

Wang, Y., Tian, D., He, W., 2014. Computation of hoisting forces on wind turbine blades using computation fluid dynamics. Applied Mechanics and Materials 446, 452–457.

A.2 Paper 2

Paper 2:

Numerical modeling and analysis of the dynamic motion response of an offshore wind turbine blade during installation by a jack-up crane vessel.

Authors: Yuna Zhao, Zhengshun Cheng, Peter Christian Sandvik, Zhen Gao, Torgeir Moan, Eric Van Buren

Published in *Ocean Engineering*, 2018.,
DOI:10.1016/j.oceaneng.2018.07.049

Numerical modeling and analysis of the dynamic motion response of an offshore wind turbine blade during installation by a jack-up crane vessel

Yuna Zhao[a,c,*], Zhengshun Cheng[a,b,c], Peter Christian Sandvik[d], Zhen Gao[a,b,c], Torgeir Moan[a,b,c], Eric Van Buren[e]

[a] *Centre for Autonomous Marine Operations and Systems (AMOS), NTNU, NO-7491 Trondheim, Norway*
[b] *Centre for Ship and Ocean Structures (CeSOS),NTNU, NO-7491 Trondheim, Norway*
[c] *Department of Marine Technology, NTNU, NO-7491 Trondheim, Norway*
[d] *PC Sandvik Marine, Trondheim, Norway*
[e] *Fred. Olsen Windcarrier, Olso, Norway*

Abstract

Jack-up crane vessels are commonly used to install offshore wind turbine blades and other components. A jack-up crane vessel is subjected to wind and wave loads, which cause motion at crane tip. Excessive motion at crane tip can lead to failure of lifting operations. Therefore, the crane tip motion should be properly assessed for jack-up crane vessels. In this study, a fully coupled model is developed for a typical elevated jack-up crane vessel, considering the hydrodynamic and aerodynamic loads on the vessel, the soil-structure interaction, and the structural flexibility of the jack-up legs and crane. The vessel model developed is further coupled with the SIMO-Aero code to achieve a fully coupled aero-hydro-soil-elastic-mechanical code SIMO-RIFLEX-Aero for numerical modeling and dynamic analysis of offshore single

*Corresponding author
Email address: yuna.zhao@ntnu.no (Yuna Zhao)

blade installation using jack-up crane vessels. The SIMO-RIFLEX-Aero code is then applied to study the dynamic response of the DTU 10MW wind turbine blade installed by a typical jack-up crane vessel under various wind and wave conditions. The results show that significant motion is induced at crane tip, mainly due to wave loads. It is important to consider the structural flexibility of the jack-up legs and crane when modeling the installation of offshore wind turbine blades.
Keywords: Offshore wind turbine blade installation, jack-up crane vessel, soil-structure interaction, structural flexibility, fully coupled method, dynamic motion response

1. Introduction

Offshore wind turbines can be installed by either floating or jack-up crane vessels, as shown in Figure 1. Compared to jack-up vessels, floating vessels provide more flexibility for offshore operations and accessibility in deep water. They have been used to install fully assembled wind turbine towers with rotors and nacelle for floating and jacket-supported offshore wind turbines, as presented in Figures 1(a) and 1(b). However, such operations are very challenging and rarely used due to the wave-induced motion of the floating crane vessels.

Jack-up crane vessels are commonly used to install offshore wind turbines in shallow water, because they can provide a stable working platform. They are able to install the components of offshore wind turbines (such as foundation, tower, nacelle and blades) separately and in sequence, as shown in Figure 1(c) (Ahn et al., 2017). Due to the growing market for offshore wind

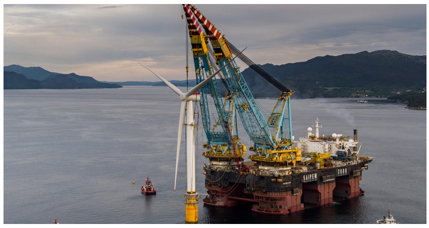

(a)

(b)

(c)

Figure 1: Installation of offshore wind turbines : (a) and (b) Installation of fully assembled tower by floating crane vessels (Carbon Brief Ltd, 2017; Scaldis Salvage & Marine Contractors NV, 2018); (c) Single blade installation for using a vessel (Fred. Olsen Windcarrier AS, 2017)

energy, the demand for use of jack-up crane vessels keeps increasing (Global Data, 2014).

Compared to traditional jack-up platforms used in the offshore oil and gas industry, the jack-up crane vessels for offshore wind turbine installation usually have shallower leg penetration into the seabed because of the frequent repositioning. As a result, the vessels are more sensitive to wind and wave loads. The tip of the crane on the vessel is observed to have notable motion during offshore operations. Large crane tip motion can lead to damaged guide pins at blade root during the blade installation. To ensure safe and cost efficient operations, it is of great importance to study the dynamic response of the jack-up crane vessel, especially of the crane tip and the installed components.

To date, limited work has been carried out on jack-up crane vessels used in offshore wind turbine installation. Duan and Olsson (2014) and Ringsberg et al. (2017) studied the soil impact loads on the spudcans of a jack-up crane vessel during the lowering and retrieval phases of jack-up legs. Weather window assessments were also conducted based on the spudcan impact force criteria. It was found that the leg lowering and retrieval operations are possible under larger wave heights in long waves. Van Dalfsen (2016) studied the effects of soil load modeling on the dynamic structural response of the jack-up crane vessel under survival conditions. The results indicated that advanced soil models are essential in the design check of jack-up crane vessels in extreme sea states. However, the dynamic motion response of the vessels during crane operations are not considered in these studies.

Zhao et al. (2018) developed an integrated dynamic analysis method for simulating installation of a single blade for wind turbines. The coupled aero-hydro-mechanical code SIMO-Aero was developed and verified, which is capable of accounting for blade aerodynamics, vessel hydrodynamics and system mechanical couplings. The SIMO-Aero code was used to study the dynamic response of a single blade installed by a jack-up crane vessel; however, the motions of the vessel and the crane were not considered by Zhao et al. (2018).

In the present study, a fully coupled model is developed for a typical jack-up crane vessel by using the SIMO (SINTEF Ocean, 2017b) and RIFLEX (SINTEF Ocean, 2017a) codes. The SIMO and RIFLEX codes were developed by SINTEF Ocean and have been widely used in the offshore wind, oil and gas industries. The vessel model can account for the wave loads on the jack-up legs, the wind loads on the vessel, the structural flexibility of the vessel legs and the on-board crane, and the soil-structure interaction. Eigen value analysis is conducted to identify the eigen periods and mode shapes of the vessel. The first two longest natural periods are compared against values calculated according to standard recommended formula to evaluate the numerical model. Then the vessel model developed is integrated with the SIMO-Aero code developed by Zhao et al. (2018) to achieve a fully coupled aero-hydro-soil-elastic-mechanical code, i.e., SIMO-RIFLEX-Aero, for offshore wind turbine blade installation by a jack-up crane vessel. Afterwards, a series of time domain simulations are carried out to study the dynamic response characteristics of the vessel, the cane tip and the installed blade under different wind and wave conditions. The effects of crane tip motion on the dynamic response of the installed blade are also investigated.

2. Numerical modeling of the elevated jack-up crane vessel

In this section, a coupled model is developed for typical elevated jack-up crane vessels based on the SIMO-RIFLEX code, as shown in Figure 2. The vessel model accounts for the structural flexibility of the legs and the crane, the soil-spudcan interaction, the wave loads on the legs and the wind loads acting on the vessel. The vessel model developed is later integrated with the SIMO-Aero code in Section 5 to formulate the the SIMO-RIFLEX-Aero code, a fully aero-hydro-soil-elastic-mechanical coupled code, for simulating offshore wind turbine blade installed by jack-up crane vessels.

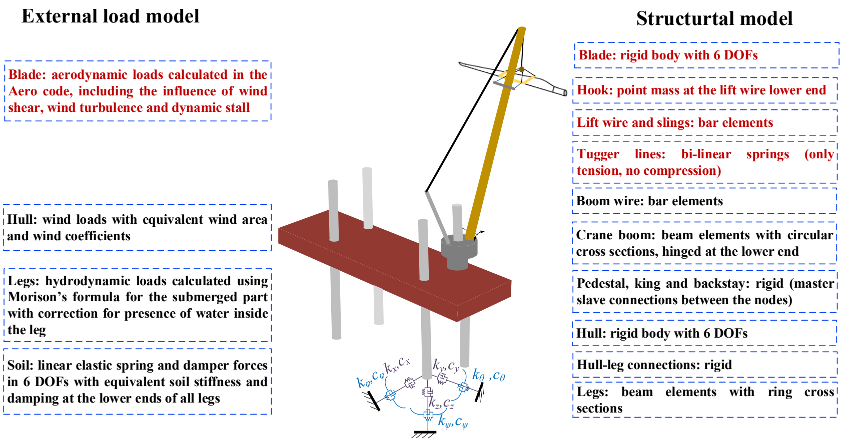

Figure 2: The structural and external force models of a typical elevated jack-up crane vessel. The blade and the lifting gear are also illustrated here to give an overview of the fully coupled aero-hydro-soil-elastic-mechanical code, i.e., SIMO-RIFELX-Aero, for simulating installation of offshore wind turbine blades by jack-up crane vessels. The integration of the codes and the modeling of the blade and the lifting gear are discussed in details in Section 5.

The hull of the vessel is modeled as a rigid body with 6 degrees of freedom (DOFs) in SIMO, because it is generally much stiffer in all directions, compared to the jack-up legs and the crane. The jack-up legs are modeled by use of flexible beam elements in RIFLEX. The spudcans are modeled as nodal bodies at the lower end of each leg.

The jack-up legs are connected to the hull by jacking systems installed in the white jacking houses shown in Figure 3(a). Figure 3(b) shows the rock-chock type jacking system which is commonly used in modern jack-up

(a) Jacking houses (A2SEA, 2017)

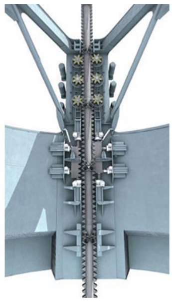

(b) Rack-chock type jacking system (Friede & Goldman Ltd., 2017)

Figure 3: Hull-leg connections for typical offshore jack-up crane vessels

vessels. It forms very stiff clamped connections between the legs and the hull. The flexibility of such jacking system has negligible influence on the system natural periods (Global Maritime, 2003). Thus, the hull-leg connections are modeled as rigid connections in the present model.

Pedestal crane is a typical type of cranes equipped on jack-up crane vessels. As shown in Figure 4(a), a pedestal crane consists of crane supports, a wire overhang system and a lattice boom. In the numerical model, it is assumed that the deformation of the crane system are mainly due to the flexibility of the boom and boom wires. The deformation of the crane supports, including king, pedestal and back-stay, is neglected. The lattice boom is simplified into a circular RIFLEX beam with equivalent structural stiffness properties. The lower end of the boom is hinged on the crane base. The boom inclination is controlled by the boom wires which are modeled as RIFLEX bar elements.

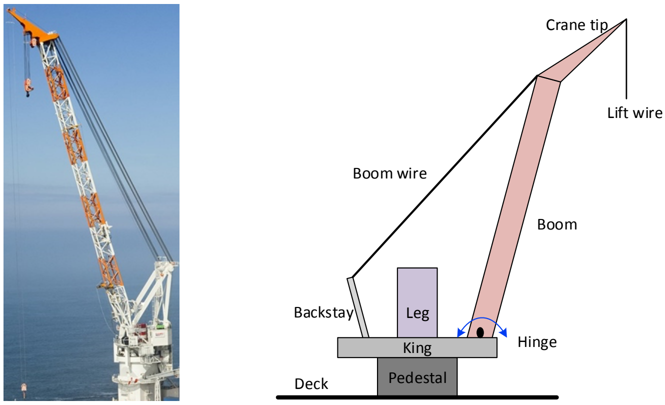

(a) Pedestal crane (b) Simplified numerical model

Figure 4: Illustration of a typical offshore pedestal crane and its numerical model

2.1. Modeling of soil-spudcan interaction

In the present model, the soil reaction force is represented by using equivalent linear elastic springs combined with linear dampers to consider the soil damping effects, without detailed modeling of the spudcans, as shown in Figure 5. It is a feasible simplification for modeling of soil behavior for jack-up crane vessels under operational sea states which typically have a significant wave height below 2.5-3.0m (Ahn et al., 2017; Paterson et al., 2017). In such conditions, the loads acting on the spudcans are much smaller than those required to reach the soil yield surface. Hence, the linear elastic soil modes can be used (Martin, 1994; Zeng et al., 2015).

As shown in Figure 5, linear springs and dampers in 6 DOFs at the reference point are used to represent the soil resistant force. The reference point of the soil model is at the lower end of each jack-up leg where the

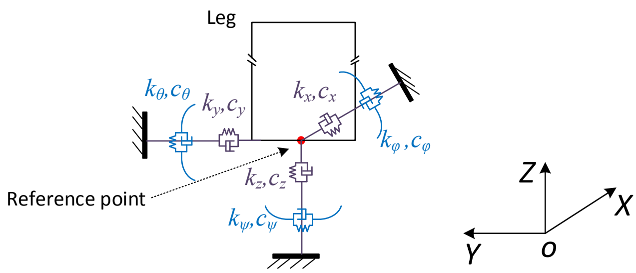

Figure 5: Modeling of soil resistance force on the spudcan using linear springs and dampers

spudcan locates. The corresponding soil reaction force can be expressed as a function of spudcan displacement, i.e.:

$$\mathbf{F}_s = \mathbf{K_s X_{sc}} + \mathbf{C_s \dot{X}_{sc}} \tag{1}$$

where the dots denote time derivative; $\mathbf{K_s} = [k_x \quad k_y \quad k_z \quad k_\phi \quad k_\theta \quad k_\psi]$ is the soil stiffness vector in 6 DOFs without considering coupling effects. The stiffness coefficient are dependent on the soil properties, the dimension and the penetration depth of the spudcans. They could be calculated using recommended empirical formula (SNAME, 2008; ISO, 2009) or estimated based on site-specific soil properties. The $\mathbf{C_s}$ is the corresponding vector of the soil damping. $\mathbf{X_{sc}}$ is the displacement vector, i.e.:

$$\mathbf{X_{sc}} = [x \quad y \quad z \quad \phi \quad \theta \quad \psi] \tag{2}$$

where x, y, z are the translation motion of the reference point (lower end node of jack-up leg); ϕ, θ and ψ are the rotational motion of the leg at its lower end.

2.2. Modeling of the wave loads

A jack-up crane vessel usually has its hull elevated well above the mean sea surface when installing offshore wind turbines. Only the lower parts of the legs are submerged. As shown in Figure 6, the instantaneous wave load normal to the leg can be calculated using Morison's formula (leg diameter to wave length ratio $< 1/5$):

$$\begin{aligned}\mathbf{F} = \int_{-h}^{\eta} [\rho A_{ext}(1 + C_A)\dot{\mathbf{u}}(x) - \rho A_{ext} C_A \ddot{\mathbf{r}}(x) \\ + \frac{1}{2}\rho D_{ext} C_D |\mathbf{u}(x) - \dot{\mathbf{r}}(x)|(\mathbf{u}(x) - \dot{\mathbf{r}}(x)) - \rho A_{int}\ddot{\mathbf{r}}(x)] dx\end{aligned} \tag{3}$$

where the dots denote time derivatives; ρ is the mass density of water; D_{ext}

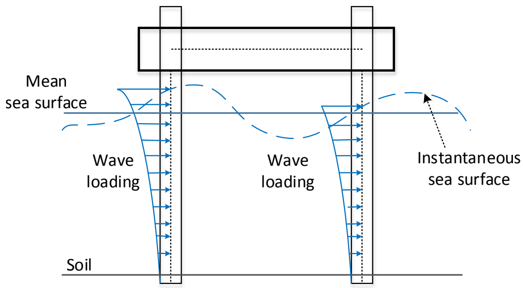

Figure 6: Wave loads on legs of the vessel

is the external diameter of the leg; A_{ext} and A_{int} are respectively the external and internal cross-sectional areas of the leg; C_A and C_D are respectively the non-dimensional 2D added mass and quadratic drag coefficients; $\mathbf{u}$ and $\mathbf{r}$ are respectively the velocity vector of undisturbed wave field and motion vector of the leg; h is the water depth and η is the instantaneous wave elevation. The last term in Eq. (3) represents the effect of water inside leg (SINTEF Ocean, 2017a).

2.3. Modeling of the wind loads

During offshore wind turbine installation, the wind loads on the jack-up crane vessel consists of contributions from the jack-up house, legs, as well as the wind turbine components and equipment loaded on the vessel deck. The wind area and shape coefficients of each component are different. The wind load on one component may be greatly affected by shielding effect from others. Detailed coefficients from wind tunnel test are favorable in order to achieve an accurate estimation of wind loads. However, these coefficients are not available at present. Under such a circumstance, the wind area above the hull baseline is considered as a block with equivalent area and wind coefficients. The wind loads on the parts of the legs between the wave crest and the hull baseline are neglected as recommended (DNVGL, 2015). The simplification is acceptable since the motion of the jack-up vessel is mainly wave-induced during operations. The wind load is calculated as (DNVGL, 2015):

$$F_{x,wd} = \frac{1}{2}\rho_{air} C_S A V^2 cos\alpha \tag{4}$$

$$F_{y,wd} = \frac{1}{2}\rho_{air} C_S A V^2 sin\alpha \tag{5}$$

$$F_{z,wind} = 0 \tag{6}$$

where ρ_{air} is the density of air; α is the relative wind inflow angle, as shown in Figure 7; V is the relative wind inflow velocity; C_S is the overall shape coefficient , i.e., $C_S = 1.1$; A is the area normal to the inflow wind:

$$A = A_{xn}|cos\alpha| + A_{yn}|sin\alpha| \tag{7}$$

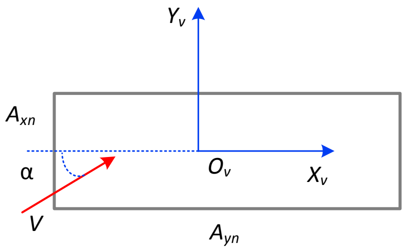

Figure 7: Illustration of wind area and relative wind inflow angle (top view)

where A_{xn} and A_{yn} are respectively the wind area normal to X_v and Y_v axis. The corresponding wind moments can be expressed as:

$$M_{x,wd} = -z_c F_{y,wd} \tag{8}$$

$$M_{y,wd} = z_c F_{x,wd} \tag{9}$$

$$M_{z,wd} = x_c F_{y,wd} - y_c F_{x,wd} \tag{10}$$

where $[x_c \quad y_c \quad z_c]$ is the position vector of the center of the equivalent wind block.

2.4. Modeling of $P - \Delta$ effect and influence of leg inclination

For slender and flexible jack-up structures, the second order effects need to be considered, such as the $P-\Delta$ effect and the influence of leg inclination (SNAME, 2008).

The $P-\Delta$ effect is illustrated in Figure 8(a). The deformation of jack-up legs causes hull translational motion in the horizontal plane. As a result, the vertical soil reaction force no longer passes through the center of hull-leg connection and leads to an extra moment. Inclination of the legs, as

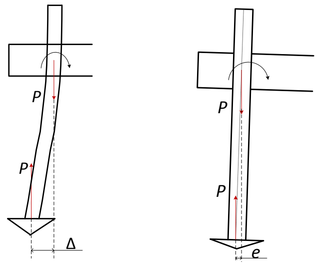

(a) P-Δ effect (b) Leg inclination

Figure 8: Illustration of P-Δ effect and leg inclination

illustrated in Figure 8(b), results in an eccentricity between the vertical soil force and the hull-leg connection. It also introduces extra bending moment in the legs at the hull-leg connections. These two effects are accounted for by the non-linear geometry feature in the finite element model in RIFLEX.

2.5. Modeling of system damping

For a typical jack-up type structure, the damping sources are mainly structural damping, soil damping and hydrodynamic damping.

The hydrodynamic damping is accounted for by incorporating the wave velocity relative to the movement of legs, which is the third term in Eq.(3).

The soil damping is typically around 2% of the system critical damping (DNVGL, 2015). In this study, the soil damping is considered by using equivalent linear dampers, which are presented as the second term in Eq.(1).

The structural damping of jack-up crane vessels also includes damping in guides, shock pads, locking devices and jacking mechanisms. In the present model, the structural damping corresponds to 0.5% of the system critical damping and is modeled by use of the Rayleigh damping model (Rayleigh, 1877).

3. System description of a typical jack-up crane vessel

A typical jack-up crane vessel is used in this study. The main properties of the vessel are listed in Table 1, including the parameters of the hull, legs and wind coefficients.

Table 1: Main properties of the vessel (Fred. Olsen Windcarrier AS, 2016)

Parameter	Value
Hull length, breadth and depth [m]	132, 39, 9
Total elevated load [t]	16,900
Total wind area A_{xn}, A_{yn} [m^2]	5372, 2119
Center of wind area (x_c, y_c, z_c) [m]	(0, 0, 7.5)
Leg length [m]	92.4
Leg diameter [m]	4.5
Longitudinal leg spacing [m]	68.3
Transverse leg spacing [m]	30.6

The structural properties of the crane are presented in Table 2. The detailed site-specific data for the vessel and the corresponding soil parameters are given in Table 3, which were obtained when the vessel installed offshore wind turbines at a 39m-deep site in the North Sea.

Table 2: Main parameters of the crane

Parameter	Value
Height of crane base [m]	25.5
Boom length [m]	107.6
Crane boom angle[deg]	67.6
No. of equivalent boom wires [-]	2
Equivalent boom wire stiffness [kN/m]	9048
Equivalent boom wire damping [kNs/m]	90.5

Table 3: Site specific data of the vessel

Parameter	Value
Water depth [m]	39.1
Airgap [m]	7.2
Penetration [m]	2.7
Leg below hull [m]	49
C_A (2D added mass coeff.)	1.0
C_D (2D drag coeff.)	0.8
Soil type	Dense sand
K_x, K_y [kN/m]	1.35×10^6
K_z [kN/m]	1.47×10^6
K_ϕ, K_θ [kNm/deg]	6.4×10^5
K_ψ [kNm/deg]	8.3×10^5

3.1. Definition of coordinate systems

A global coordinate system and a vessel-related coordinate system are introduced, as shown in Figure 9. For the vessel-related coordinate system $O_v - X_vY_vZ_v$, the origin O_v is located at the hull geometry center with X_v-axis along the hull length and Y_v-axis along the hull width while the

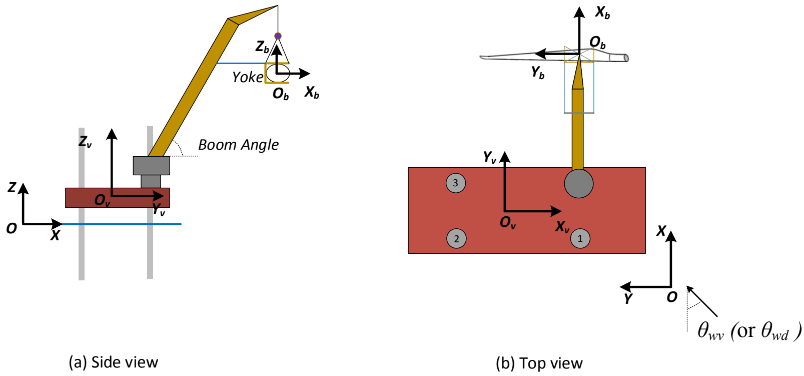

Figure 9: Definition of the global coordinate system $O - XYZ$ and the vessel-related coordinate system $O_v - X_vY_vZ_v$. A blade is also presented here to illustrate the scenario of wind turbine blade installation discussed in detail in Section 5. The wind turbine blade is along the y_g axis. A blade-related coordinate system $O_b - X_bY_bZ_b$ is defined for the blade; its origin is located at the blade COG and it is parallel with the global coordinate system when the blade is at rest.

z_v-axis follows the right hand rule.

The global coordinate system $O-XYZ$ has its origin located at the mean sea surface. The X and Z respectively parallel with Y_v and Z_v, when the vessel is at rest.

The crane boom angle is defined as the relative angle between the crane boom and the deck. The wave incident angle θ_{wv} is defined as the angle of the wave direction relative to the X and is positive counterclockwise. A similar definition is used for the wind inflow angle θ_{wd}.

The vessel is used to install a wind turbine blade, as shown in Figure 9. Detailed modeling of the blade and the lifting gear is discussed in Section 5.

3.2. Cancellation and enhancement periods of wave loads on the legs

Table 4 gives the critical wave periods that could lead to cancellation and enhancement effects of the global wave loads on the vessel legs due to wave phase, caused by the spacing between legs (DNVGL, 2015). The wave loads

Table 4: Cancellation and enhancement periods for the global wave loads on the vessel legs

Direction	0^o	65.87^o	90^o
T_{cancel}[s]	6.26	10.17	9.61
	3.61	5.65	5.40
$T_{enhance}$ [s]	4.43	6.93	6.62
	3.13	4.90	4.68

on individual legs are not affected. The resulting total loads on all of the legs would be reduced to zero due to the opposite phases of wave loads on the two legs in the wave propagation direction when the cancellation effect happens. Otherwise, the sum wave loads would be doubled in case of same phases, which is the enhancement effect of wave loads. Some of these cancellation and enhancement periods are likely to occur when the vessel works in the North sea (typical wave period 5$\sim$15s). The influences of wave cancellation and wave enhancement effects on the system dynamic response are studied in the later sections.

4. Evaluation of the vessel numerical model

The developed vessel model is evaluated in this section. The natural periods of the vessel motion obtained from the numerical model are compared against values estimated according to standard-recommended empirical formula. Verification against experimental data or on-site measurement is not carried out since these data are very difficult to obtain.

Eigen-value analysis is conducted to identify the eigen periods and eigen modes of vessel motion (excluding the crane), which are presented in Table 5 and Figure 10. The first two largest natural periods correspond to surge and sway motion, followed by that of yaw motion, which agrees with the general order of natural periods for typical elevated jack-up vessels given in DNV-RP-C104 (DNVGL, 2015).

Table 5: Eigen periods of the vessel motion defined in the vessel-related coordinate system in Figure 9

Mode	1	2	3	4	5	6
Eigen period (s)	3.087	2.912	2.363	0.594	0.479	0.451
Dominant hull motion	Sway	Surge	Yaw	Roll	Pitch	Heave

According to DNV-RP-C104 (DNVGL, 2015), the longest natural periods of a typical elevated unit can be approximated by:

$$T_n = 2\pi \sqrt{\frac{m_e}{k_e}} \tag{11}$$

where m_e and k_e are respectively the equivalent mass and stiffness associated with one leg, which have to be obtained from the complete model of the jack-up vessel and four legs, depending on the eigen modes. The natural periods of surge and sway motion for the vessel are calculated by using Eq.(11) and compared with the corresponding values obtained from the eigen-value analysis, as given in Table 6. The comparison shows that the eigen-periods

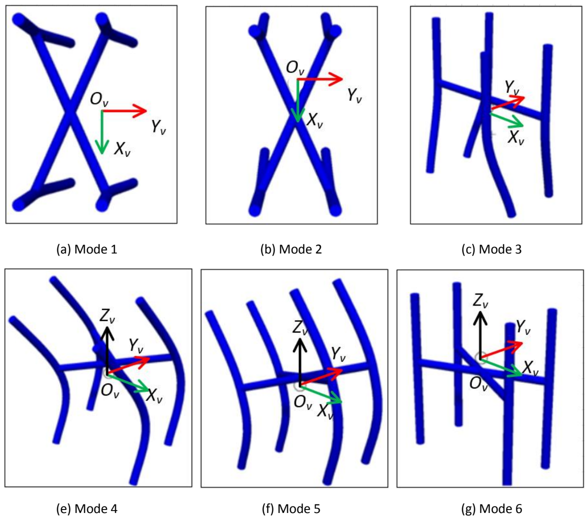

Figure 10: Illustration of mode shapes of the vessel motion (amplified by 2000 times). The vessel hull is illustrated by two rigid crossing beams. The crane and blade are not considered in the eigen value analysis while the soil-spudcan interaction is included.

of the eigen-value analysis agree fairly well with those estimated by the empirical formula. It implies that the established numerical model can provide reasonable estimation of the vessel dynamic response.

The natural period of the crane motion is identified by using decay tests while the vessel is fixed. A vertical force is applied at the crane tip and removed after some time. The natural period of the crane is calculated by analyzing the time series of the crane tip motion. The natural period is caused by the rotational motion of the crane boom around its hinged lower end due to the boom wire deformation. The crane boom itself has marginal deformation, compared to that of the boom wires. The natural period of

Table 6: Comparison of the natural periods of the vessel surge and sway motion (defined in the vessel-related coordinate system in Figure 9) from eigen value analyses and empirical formula

Mode	1	2
Dominant hull motion	Sway	Surge
Natural period from eigen value analysis (s)	3.087	2.912
Natural period calculated by Eq.(11) (s)	3.256	3.053

the crane is affected by the lifted components and lifting gears. The crane itself has a natural period of 2.0s without lifting anything. However, when the installed blade and the lifting gear given in Section 5 are considered, the crane natural period is shifted to approximately 2.9s.

5. Modeling of the installed wind turbine blade and the lifting gear

The developed vessel model is coupled with the SIMO-Aero code developed by Zhao et al. (2018) to establish a fully coupled aero-hydro-soil-elastic-mechanical code, SIMO-RIFLEX-Aero, for simulating offshore wind turbine blade installation using jack-up crane vessels. The coupled code is capable of accounting for the aerodynamics of the installed blade, the structural flexibility of the vessel legs and crane, the wave loads on the legs and wind loads on the hull, the soil-structure interaction, as well as the mechanical couplings between the crane and the blade. The vessel model is extensively discussed in Section 2. The detailed model of the blade and corresponding lifting gear is explained in this section.

The blade is modeled as a rigid body with 6 DOFs in SIMO. The structural flexibility of the blade is neglected since it has minor influence on the dynamic motion response of the blade during installation (Zhao et al., 2018). The aerodynamic loads acting on the blade are calculated by the external code Aero based on the cross-flow principle. Details of the Aero code can be found in Ref. (Zhao et al., 2018). The DTU 10 MW wind turbine blade (Bak et al., 2013) is considered in the present study.

A yoke is used to hold the blade. The yoke and the blade are considered as one rigid body in the numerical model. The yoke is lifted by the hook via four slings. The lift wire runs through the crane tip to the hook. In the present model, the lift wire and slings are modeled as bar elements with equivalent stiffness and damping properties. The hook is modeled as a point mass at the lower end of the lift wire. Tugger lines are used for blade heading control which run from the yoke to a trolley on the crane boom. Pretension is applied in tugger lines to prevent slack lines. The tugger line tension is modeled as bi-linear spring force (Zhao et al., 2018). The main properties of the blade lifting system are summarized in Table 7.

Table 7: Main properties of the blade and the lifting gear

Parameter	Value
Hook mass [tons]	10
Yoke mass [tons]	47
Blade mass [tons]	41.67
Blade length [m]	86.37
Installation height [m]	119
Tugger line arm length (relative to blade COG) [m]	10
Length of crane wire (from crane tip to hook) [m]	4.7
Length of slings [m]	20.4

Installation of the DTU 10MW wind turbine blade by the aforementioned jack-up crane vessel will be simulated by the coupled code SIMO-RIFLEX-Aero. As shown in Figure 11, the blade span is deployed along the vessel longitudinal direction. A blade body-related coordinate system is defined and used in the presented study. The its origin is at the blade center of gravity. The y_b-axis is along the blade span. The x_b-axis goes from the leading edge to the trailing edge of the blade while the z_b-axis follows the right hand rule. The blade body-related coordinate parallels with the global coordinate when the blade is at rest, as shown in Figure 9.

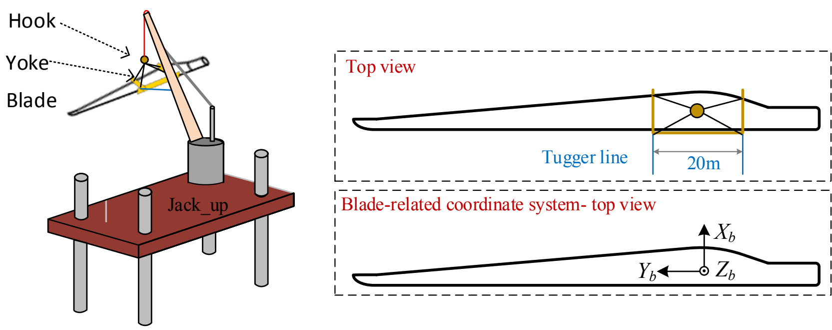

Figure 11: Illustration of blade orientation and its body-related coordinate system. Definition of the blade motion at its COG: the translational (rotational) motion along the X_b-, Y_b- and Z_b-axis are respectively denoted as surge (roll), sway (pitch) and heave (yaw).

Table 8 lists the first three longest natural periods and corresponding motion which dominate the blade rigid body motion (obtained when the crane tip is fixed). The first mode is caused by the blade pendulum motion around the hook, which is denoted by the blade roll resonant response in this study. The blade yaw resonant motion dominate the second mode. The

Table 8: Natural periods and corresponding dominant motions of the blade motion response(only blade)

Mode	$T_n[s]$	ω_n [rad/s]	Dominant response
1	12.0	0.524	Blade roll resonance (blade pendulum around the hook)
2	5.11	1.23	Blade yaw resonance
3	3.63	1.73	Blade-hook double pendulum around the crane tip in the $O_g y_g z_g$ plane (blade and hook motion out of phase)

third mode is caused by the double pendulum motion of the blade and hook around the crane tip in the vertical $O_g y_g z_g$ plane with the blade and hook motion out of phase (Zhao et al., 2018).

6. Time domain simulations and case studies

Time domain simulations are carried out to study the dynamic response of the vessel and the installed blade under different sea states, using the fully coupled SIMO-RIFLEX-Aero code. A series of load cases are defined, as given in Table 9.

LC1 and LC2 are turbulent wind only cases. The vessel and the crane tip are assumed to be fixed in LC1 and are free to move in LC2. These two cases are used to evaluate the wind induced motion of the vessel and the crane tip. Moreover, comparing results of LC1 and other cases can identify the effect of crane tip motion on the motion of the installed blade.

LC3 $\sim$ LC13 are load cases with combined turbulent wind and irregular waves. In LC6, the significant wave height and peak period are correlated with the wind condition at the North Sea Center site (Li et al., 2015). The wind turbulence intensity is calculated according to the IEC class A, which

Table 9: Load cases used in the time domain simulations

	Crane tip	Turbulent wind			Irregular waves		
		U_W [m/s]	T_I [%]	θ_{wd} [deg]	H_s [m]	T_p [s]	θ_{wv} [deg]
LC1	Fixed	10.23	20.8	0	-	-	-
LC2	Free	10.23	20.8	0	-	-	-
LC3	Free	10.23	20.8	0	2.4	8.55	0
LC4	Free	10.23	20.8	30	2.4	8.55	30
LC5	Free	10.23	20.8	65.87	2.4	8.55	65.87
LC6	Free	10.23	20.8	0	2.4	8.55	65.87
LC7	Free	10.23	20.8	0	2.4	8.55	90
LC8	Free	10.23	20.8	0	1.8	8.55	65.87
LC9	Free	10.23	20.8	0	1.2	8.55	65.87
LC10	Free	10.23	20.8	0	2.4	6.93	65.87
LC11	Free	10.23	20.8	0	2.4	5.65	65.87
LC12	Free	7.02	24.8	0	2.4	8.55	65.87
LC13	Free	4.86	30.4	0	2.4	8.55	65.87

U_W- mean wind speed; T_I- turbulent wind intensity; θ_{wd}- wind direction; H_s- significant wave height; T_p- wave peak period; θ_{wv}- wave direction.

is the design class for the DTU 10MW wind turbine (Bak et al., 2013). The wind and wave parameters are varied around LC6 to study the impacts of different factors on the system dynamic motion response, including wind and wave directions (aligned and misaligned), significant wave height, wave peak period and mean wind speed.

Turbulent winds are used in all load cases. The TurbSim (Jonkman, 2009) is used to generate the three dimensional turbulent wind field according to the Kaimal turbulence model. The irregular waves are long crested and are modeled by using the JONSWAP spectrum.

For each load case, the simulation lasts for one hour after removing the start-up transients. The statistical values and power spectra of the dynamic motion response are obtained based on the one hour simulation results.

7. Results and discussion

The results from the time domain simulations are discussed in this section. The characteristics of the vessel motion (6 DOFs), the crane tip movement (3 DOFs), the blade motion at its COG and the corresponding translational motion at the blade root (3 DOFs) are investigated. The blade root is considered as a point on the blade which is modeled as a rigid body. Therefore, the translational motion of the blade root are obtained from the 6 DOF rigid-body motion of the blade. Tensions in the boom wires, lift wire, slings and tugger lines are not discussed here due to their marginal fluctuations.

7.1. Motion of the vessel

The vessel motion is defined in the vessel-related coordinate system in Figure 9. Figure 12(a) show the standard deviations of the vessel translational motion in LC1 $\sim$ LC13 while those in Figure 12(b) present those of the vessel rotational motion. The vessel motion is zero in LC1 as it is fixed during the numerical simulation. The vessel heave motion is negligible.

Comparisons between LC2 and LC3$\sim$LC13 reveal that the wave-induced motion of the vessel dominates over the wind-induced response. The wind loads are further shown to have minor influence on the vessel motion, compared to the wave load, by comparing LC5 and LC6, and LC6, LC12 and LC13. The vessel motion is sensitive to the incident wave direction, as shown

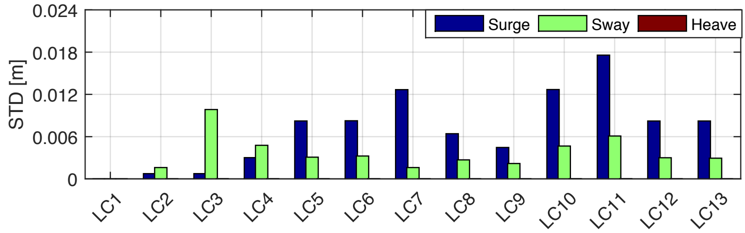

(a) Translational motion

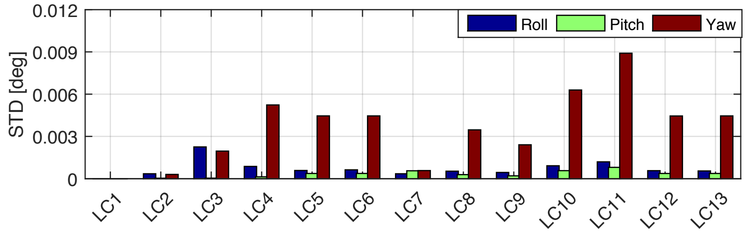

(b) Rotational motion

Figure 12: Standard deviations of the vessel motion in the vessel-related coordinate system defined in Figure 9

by comparing the results in LC3, LC6 and LC7. It is also dependent on the wave height, which can be observed in the results for LC6, LC8 and LC9. The vessel motion is marginally affected by the cancellation and enhancement effects in wave loads, as shown by the results in LC10 and LC11. The amplitudes of vessel motion show a increasing trend with decreasing wave peak period.

The vessel motion spectra are analyzed. Figure 13 shows the spectra of vessel motion in surge, sway and yaw. The spectra of vessel pitch and roll

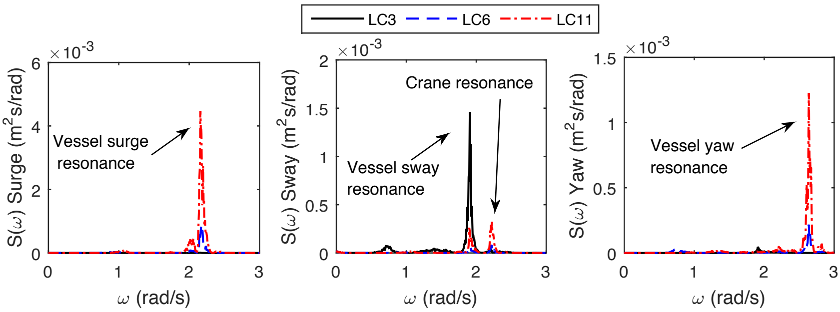

Figure 13: Power spectra of surge, sway and yaw motion of the vessel in LC3, LC6 and LC11 in the vessel-related coordinate system in Figure 9.

motion are similar to those of surge and sway motion, respectively. The power spectrum of vessel surge motion is dominated by the surge resonant response. The vessel sway motion is dominated by the vessel sway resonant response in LC3 ($\theta_{wv} = 0^o$) while notable contributions from the crane resonance response are observed in LC6 and LC11 ($\theta_{wv} = 65.87^o$). The vessel yaw motion is mainly dominated by the vessel yaw resonant response.

7.2. Motion at the crane tip

The crane tip motion is important for crane operations at a large lifting height. The characteristics of the crane tip motion are discussed in this section. The standard deviations of crane tip motion in the vessel related-coordinate system are presented in Figure 14.

Both the vessel motion and the crane deformation contribute to the crane tip motion. The crane deformation includes the deformation of the boom wires and the crane boom, while the deformation of the latter is much marginal compared to that of the former. The crane is deployed in the ver-

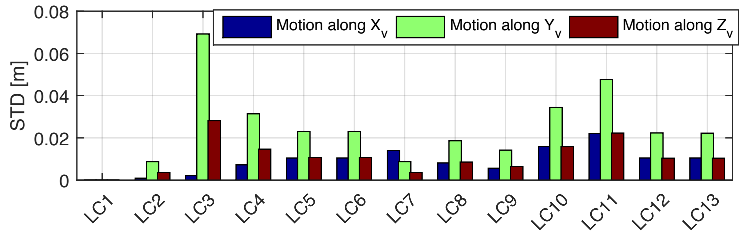

Figure 14: Standard deviations of the crane tip motion in the vessel-related coordinate system defined in Figure 9

tical $O_vY_vZ_v$ plane during the operation, as shown in Figure 9. As a result, the crane tip motion along Y_v and Z_v gets significant contributions from the crane resonant response due to crane deformation, as can be observed in their power spectra shown in Figure 15. The crane tip motion along X_v has minor contributions of crane resonant response and is mainly resulted from the vessel motion.

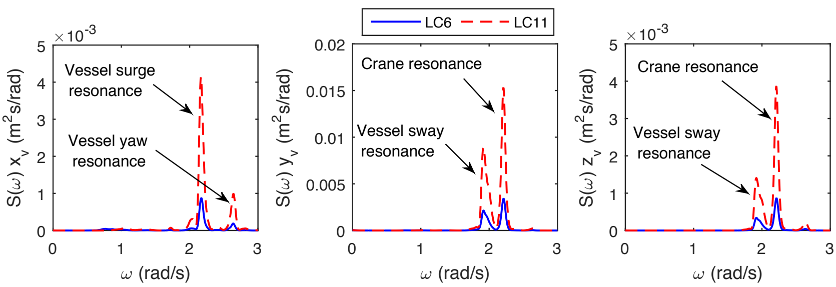

Figure 15: Power spectra of the crane tip motion in LC6 and LC11: from left to right- along X_v, Y_v and Z_v in the vessel-related coordinate system shown in Figure 9.

The crane tip motion is marginally affected by the variation of wind conditions, as shown by comparing it s standard deviations in LC5, LC6, LC12 and LC13 in Figure 14. Similar to the vessel motion, the crane tip motion is sensitive to the wave excitation. The comparisons among the results in LC6, LC10 and LC11, and LC6, LC8 and LC9 show that the crane tip motion decreases significantly with reduction in the significant wave height and wave peak period.

7.3. Motion of the installed blade

The 6 DOF rigid-body motions of the blade, with the reference point at its COG, are studied in this section. The motions are defined in the blade-related coordinate system in Figure 11. The first 3 DOF motions refer to the translational motions at the COG while the rest 3 DOF motions refer to the rotational motions around the COG. Their standard deviations in LC1∼13 are shown in Figure 16.

It can be observed that the blade roll motion is much larger than the blade yaw motion in Figure 16(b), since the latter is well controlled by the tugger lines deployed perpendicular to the blade span while the former experiences limited restoring force from the tugger lines.

Comparisons among LC1∼3 show that the blade surge, heave and pitch motions experience significant contributions from the vessel motion and crane movement. They show large dependency on the wave condition (LC3, LC6 ∼LC11) and are marginally affected by the wind properties (LC5, LC6, LC12 and LC13). They are dominated by a combination of the crane resonant response and the vessel sway resonant motion, as shown by the power spectra of blade surge motion in Figure 17. The dominance of these two contributions is dependent on the wave direction.

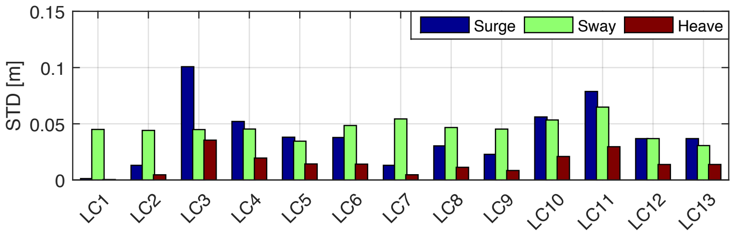

(a) Translational motion

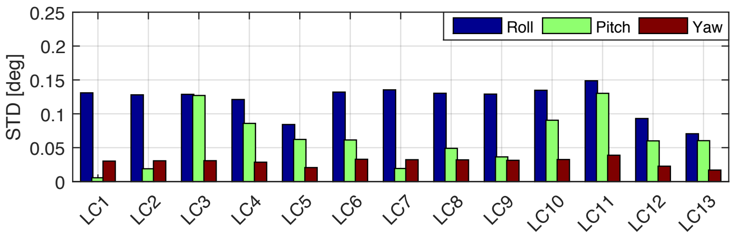

(b) Rotational motion

Figure 16: Standard deviations of the blade motion in the blade-related coordinate system defined in Figure 11

The blade motion in sway, roll and yaw is mainly induced by blade aerodynamic load. The power spectra of blade sway and yaw motions are presented in Figure 18. The blade sway motion is completely dominated by the blade roll resonant response in LC1. Consideration the vessel and crane motion introduces another two peaks into its power spectrum, due to the double pendulum induced response and the vessel surge resonant motion, as shown in Figure 18(a). These two peaks are negligible in the spectrum of blade yaw motion in Figure 18(b). The blade yaw motion is dominated by the blade

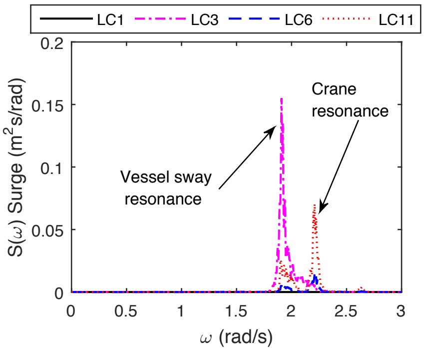

Figure 17: Power spectra of blade surge motion in LC1, LC3, LC6 and LC11

roll and yaw resonant responses. Consideration the vessel and crane motion increases the contribution from the blade yaw resonant motion. The effects of the vessel and crane motion on blade motion in sway, roll and yaw are significant in short waves.

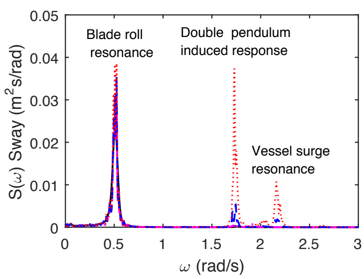

(a) Sway

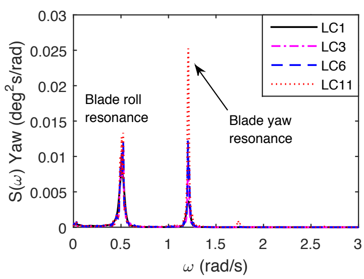

(b) Yaw

Figure 18: Power spectra of blade sway and yaw motion in LC1, LC6, LC11 and LC13

7.4. Motion at the blade root

The blade root motion is critical during the final mating phase of blade installation. The mating process is not possible if the blade root motion is too large. The characteristics of the translational motion at blade root in the blade related coordinate system in Figure 11 are studied in this section.

Figure 19 shows the standard deviations of the blade root motion. Comparing results in LC1∼LC3 indicates that the blade root motion would be significantly underestimated, especially along X_b, if the detailed modeling of vessel and crane motion is not considered. Larger underestimation is expected to occur in shorter waves, as indicated by comparing the power spectra of blade root motion in LC1, LC6 and LC11 in Figure 20.

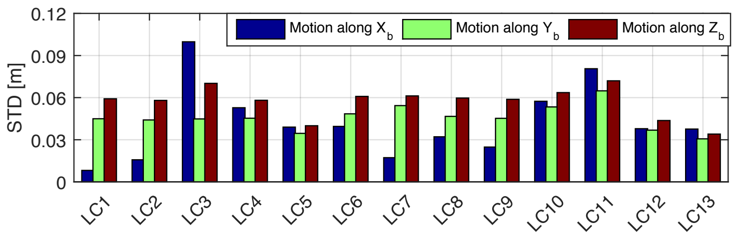

Figure 19: Standard deviations of the blade motion along X_b, Y_b and Z_b in the blade-related coordinate system defined in Figure 9

The displacements of blade root in the global coordinate system are further compared with those of the vessel origin, the crane tip and the blade COG, as shown in Table 10. The blade root motion along Y is mainly resulted from that of the blade COG. The blade root motion along Z is much larger than that of the blade COG, due to the notable contribution from blade roll motion. In LC3∼11, the blade root motion along X is close to that of blade

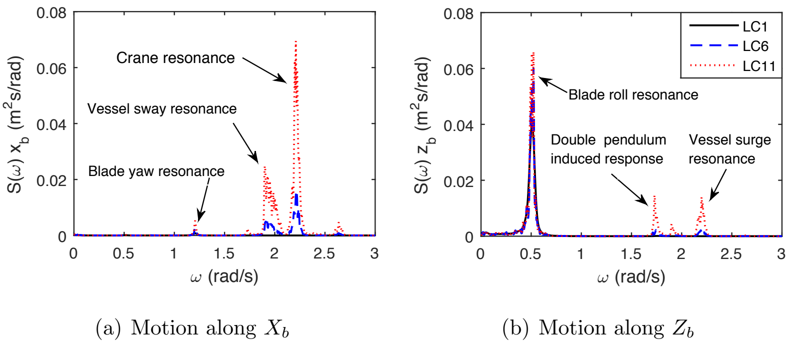

Figure 20: Power spectra of blade root motion along X_b and Z_b in LC1, LC6 and LC11 in the blade-related coordinate system defined in Figure 9

COG because the contribution from blade yaw motion becomes relatively less important. The displacements of the blade root and blade COG are much larger than those of the crane tip and the vessel origin. Detailed system modeling including the blade, the vessel and the crane is recommended for numerical analysis of offshore wind turbine blade installation.

8. Conclusions

This study deals with the development, evaluation and application of a fully integrated simulation tool, namely SIMO-RIFLEX-Aero, for modeling and dynamic response analysis of single blade installation for offshore wind turbines using a jack-up crane vessel. The developed simulation tool can account for aerodynamics, hydrodynamics, soil and structural dynamics and wire coupling mechanics.

A coupled SIMO-RIFLEX model for a typical elevated jack-up crane vessel is first developed, considering wave loads on the vessel legs, wind loads

Table 10: Comparison of displacement variations for the vessel origin (V), crane tip (C), blade (B) and blade root (BR) in the global coordinate system shown in Figure 9.

	σ_X [cm]				σ_Y [cm]				σ_Z [cm]			
	V	C	B	BR	V	C	B	BR	V	C	B	BR
LC1	-	-	0.13	0.82	-	-	4.50	4.50	-	-	0.05	5.92
LC3	0.99	6.92	10.08	9.98	0.08	0.21	4.49	4.48	0.00	2.82	3.55	7.02
LC6	0.33	2.31	3.78	3.95	0.83	1.05	4.85	4.85	0.00	1.07	1.42	6.09
LC9	0.22	1.42	2.29	2.48	0.45	0.57	4.53	4.53	0.00	0.64	0.85	5.88
LC11	0.61	4.76	7.88	8.06	1.76	2.21	6.49	6.48	0.00	2.23	2.96	7.20

on the vessel, structural flexibility of the legs and the crane, soil-structure interaction, as well as important non-linear effects, such as P-Δ effect and leg inclination. Eigen value analysis is conducted to analyze the eigen periods and mode shapes of the vessel motion. The natural periods of the vessel motion are found to be in the order of 0.4-3s, which are lower than typical wave periods. However, the vessel motion resonances in the longitudinal, transverse and torsional degrees can still be excited, especially in short waves. The first two longest periods are compared with values estimated by empirical formula recommended by standards and guidelines. The developed SIMO-RIFLEX model is then coupled with the SIMO-Aero code (Zhao et al., 2018) to achieve the integrated simulation tool SIMO-RIFLEX-Aero.

The fully coupled SIMO-RIFLEX-Aero code is then applied to simulate the dynamic response of the DTU 10MW wind turbine blade being installed by a jack-up crane vessel under different stochastic wave and wind conditions in time domain. The vessel motion is mainly induced by wave loads on the jack-up legs. A decrease in wave period and an increase in wave height can cause significant increase in the vessel motion. The vessel motion is dominated by the vessel's surge, sway and yaw resonant response with contribution from the crane's resonant response. Significant crane tip motion is induced by the vessel motion, together with the crane flexibility. The crane tip motion in sway and heave is dominated by the crane resonant response.

The motion of the installed blade are significantly affected by the crane motion caused by the vessel motion due to wave load on the legs. Crane tip motion contributes to much larger blade motion in surge, heave and pitch. Increases in the blade sway, roll and yaw motion are also caused by the crane tip motion in short waves while in long waves they are not. As a result, the blade root motion is significantly increased both along and normal to the hub axis. The blade root velocity is expected to experience larger increase in short waves, which can lead to high potential of damaged guide pins during the final connection phase.

It is essential to plan offshore operations by using an integrated numerical model and analysis. It is revealed in this study by taking the offshore wind turbine blade installation using a jack-up crane vessel as an example. In addition to the direct model of the blade motion under wind loads, modeling of the jack-up vessel and the crane is also of great importance for a more safe and efficient installation operation. The vessel motion can cause significant motion at the crane tip during lifting operations at large heights. The crane tip motion due to the vessel motion and crane flexibility can also greatly increase the motion of the lifted components, and hence affects the safety and efficiency of the operation.

The methodology developed in this study can also be applied to deal with other types of offshore lifting operations using jack-up crane vessels.

Acknowledgment

The authors appreciate the support from the Department of Marine Technology, Centre for Ships and Ocean Structures (CeSOS) and Centre for Autonomous Marine Operations and Systems (AMOS), NTNU. Thanks are also extended to Mr. Petter Faye Søyland in Fred Olsen Windcarrier for valuable discussions.

Reference

A2SEA, 2017. Sea installer - offshore wind turbine installation vessel. `https://www.a2sea.com/fleet/sea-installer/`, (Accessed on 12/24/2017).

Ahn, D., Shin, S.-C., Kim, S.-Y., Kharoufi, H., Kim, H.-C., 2017. Comparative evaluation of different offshore wind turbine installation vessels for korean west–south wind farm. International Journal of Naval Architecture and Ocean Engineering 9 (1), 45–54.

Bak, C., Zahle, F., Bitsche, R., Kim, T., Yde, A., Henriksen, L. C., Hansen, M. H., Natarajan, A., 2013. Description of the DTU 10 MW reference wind turbine. Tech. Rep. DTU Wind Energy Report-I-0092, Technical University of Denmark.

Carbon Brief Ltd, 2017. Installation of offshore floating wind turbines. `https://www.carbonbrief.org/qa-how-viable-are-floating-offshore-windfarms`, (Accessed on 02/08/2018).

DNVGL, 2015. Recommended practice DNVGL-RP-C104: Self-elevating units. Standard, DNVGL, Olso, Norway.

Duan, V., Olsson, F., 2014. Impact loads on a self-elevating unit during jacking operation. Master thesis, Chalmers University of Technology.

Fred. Olsen Windcarrier AS, 2016. Specifications for Jack-up Installation vessels Brave Tern and Bold Tern. Report, Fred. Olsen Windcarrier AS.

Fred. Olsen Windcarrier AS, 2017. Jack-up crane vessels for installation of offshore wind turbines. http://windcarrier.com/fleet/, (Accessed on 02/08/2018).

Friede & Goldman Ltd., 2017. Jack Up Products: Rack Chock. http://www.fng.com/engineered-products/jack-up-products, (Accessed on 12/24/2017).

Global Data, 2014. Offshore vessel and cables market- Market size, competitive landscape and key country analysis to 2020. Report GDAE1095MAR, GlobalData UK Ltd.

Global Maritime, 2003. Impact of changes to T&R 5-5A on jack-up system reliability levels. Research report 037, American Global Maritime, Houston, USA.

ISO, 2009. ISO/DIS 19905-1: Petroleum and natural gas industries- Site-specific assessment of mobile offshore units- Part 1: Jack-ups. Standard, International Organization for Standardization.

Jonkman, B. J., 2009. Turbsim user's guide: Version 1.50.

Li, L., Gao, Z., Moan, T., 2015. Joint distribution of environmental condition at five european offshore sites for design of combined wind and wave energy devices. Journal of Offshore Mechanics and Ocean engineering 137 (3).

Martin, C. M., 1994. Physical and numerical modelling of offshore foundations under combined loads. Ph.D. thesis, University of Oxford.

Paterson, J., DÁmico, F., Thies, P., Kurt, E., Harrison, G., 2017. Offshore wind installation vessels–a comparative assessment for uk offshore rounds 1 and 2. Ocean Engineering.

Rayleigh, L., 1877. Theory of Sound (two volumes). Dover Publications, New York.

Ringsberg, J. W., Daun, V., Olsson, F., 2017. Analysis of impact loads on a self-elevating unit during jacking operation. Journal of Offshore Mechanics and Arctic Engineering 139 (3), 031602.

Scaldis Salvage & Marine Contractors NV, 2018. Single lift of fully assembled offshore wind turbine tower installation. `http://www.scaldis-smc.com/en-GB/rambiz-3000/31`, (Accessed on 02/08/2018).

SINTEF Ocean, 2017a. RIFLEX 4.10.1 Theory Manual.

SINTEF Ocean, 2017b. Simo-theory manual version 4.10.

SNAME, 2008. Technical & Research Bulletin 5-5A: Guidelines for Site Specific Assessment of Mobile Jack-Up Units.

Van Dalfsen, A., 2016. Integral soil-jack-up modelling-modelling site-specific jack-up response and performing safety assessment. Master thesis, Delft University of Technology.

Zeng, J., Yuan, H., Wang, C., Wang, Y., Mo, J., 2015. The research on the fatigue analysis of the jack-ups leg based on sesam software. In: ASME 2015 34th International Conference on Ocean, Offshore and Arctic Engineering, May 31-June 5, 2015, St. John's, Newfoundland, Canada. American Society of Mechanical Engineers, pp. V007T06A068–V007T06A068.

Zhao, Y., Cheng, Z., Sandvik, P. C., Gao, Z., Moan, T., 2018. An integrated dynamic analysis method for simulating installation of a single blade for offshore wind turbines. Ocean Engineering 152, 72–88.

A.3 Paper 3

Paper 3:
Effect of foundation modeling on the dynamic motion response of an offshore wind turbine blade during installation by a jack-up crane vessel.
Authors: Yuna Zhao, Zhengshun Cheng, Zhen Gao, Torgeir Moan
Published in *Proceedings of the International Offshore Wind Technical Conference (IOWC)*, San Francisco, USA, November 4-7, 2018.

Is not included due to copyright
available at
https://doi.org/10.1115/IOWTC2018-1010

A.4 Paper 4

Paper 4:
Numerical study on the feasibility of offshore single blade installation by floating crane vessels.
Authors: Yuna Zhao, Zhengshun Cheng, Zhen Gao, Peter Christian Sandvik, Torgeir Moan
Published in *Marine Structures*, 2018,
DOI:10.1016/j.marstruc.2018.12.001.

Numerical study on the feasibility of offshore single blade installation by floating crane vessels

Yuna Zhao[a,c,*], Zhengshun Cheng[a,b,c], Zhen Gao[a,b,c], Peter Christian Sandvik[d], Torgeir Moan[a,b,c]

[a]*Centre for Autonomous Marine Operations and Systems (AMOS), NTNU, NO-7491 Trondheim, Norway*
[b]*Centre for Ship and Ocean Structures (CeSOS),NTNU, NO-7491 Trondheim, Norway*
[c]*Department of Marine Technology, NTNU, NO-7491 Trondheim, Norway*
[d]*PC Sandvik Marine, Trondheim, Norway*

Abstract

Compared with jack-up crane vessels that are now widely used in offshore wind turbine installation, floating crane vessels are more flexible with respect to working water depth and are much faster in relocation. They are thus a promising alternative to install offshore wind turbine components, especially in intermediate and deep water. However, the wave-induced motions of the floating vessels make the operations challenging. This study deals with a preliminary feasibility study on offshore single blade installation using floating crane vessels. Two typical floating crane vessels are considered, i.e., a mono-hull vessel and a semi-submersible vessel. They are assumed to be equipped with dynamic positioning systems that can well mitigate the slowly varying horizontal motions. Their overall performance during the blade installation is numerically evaluated by comparing their performance against a typical jack-up crane vessel. The crane dynamics plays a less important role for blade

*Corresponding author
Email address: yuna.zhao@ntnu.no (Yuna Zhao)

installation by floating vessels, compared to the jack-up crane vessel. The floating vessels' wave-induced motion greatly affects the blade motion. The semi-submersible vessel causes a much smaller blade motion than the mono-hull vessel. The results indicate that it is feasible to install offshore wind turbine blades by using floating crane vessels provided that the vessel type is properly selected. From the operability point of view, semi-submersible vessels are more feasible than mono-hull vessels for offshore single blade installations.
Keywords: Offshore wind turbine blade installation, floating crane vessels, feasibility study, fully coupled method, dynamic motion response

---

1. Introduction

Installation of offshore wind turbines can be carried out by using either jack-up or floating crane vessels. The jack-up crane vessels are now extensively used during the installation of bottom-fixed offshore wind turbines (Ahn et al., 2017). They can provide a stable elevated working platform. Nevertheless, they are limited by water depth, deck space and jacking duration. They are significantly less competitive when it comes to intermediate water and deep water. Therefore, shortage of crane vessels remains a critical issue (Paterson et al., 2018) for installation of wind turbines in intermediate water and deep water.

At present, floating wind turbines experience rapid development due to the potential of much higher power production in deep water zones (Wind Europe, 2018). For floating wind turbines, it is only possible to use floating crane vessels if on site installation is inevitable, since use of jack-up crane vessels is not feasible. The installation cost by floating crane vessels is usually much higher than that by jack-up crane vessels. When selecting the crane vessel in practical operations, technical feasibility and cost should be well balanced.

Compared to jack-up crane vessels, floating ones are flexible with respect to working water depth and fast in relocating. They are commonly used in the offshore oil and gas industry for installing sub-sea templates and topsides of platforms. At present, there are attempts of using floating crane vessels for offshore wind turbine installation, such as installing monopile foundations for bottom-fixed wind turbines shown in Figure 1(a), installing the tower-rotor-nacelle assembly for floating wind turbines in Figure 1(b) and installing tower-nacelle assembly and rotor for floating wind turbines in Figure 1(c). Up to now, wind turbine blades have not been installed by using floating crane vessels.

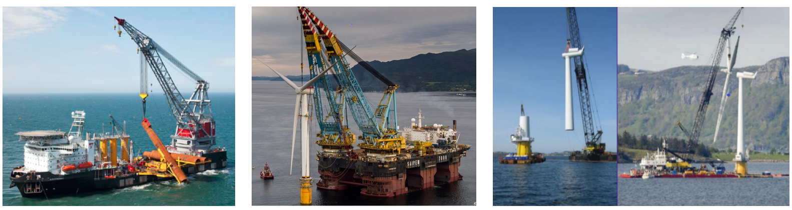

(a) (b) (c)

Figure 1: Examples of offshore wind turbine installation by using floating vessels. (a) installing a monopile for a bottom-fixed wind turbine by Oleg Strashnov, a mono-hull vessel (Seaway Heavy Lifting, 2018). (b) installing the tower and rotor-nacelle-assembly for a floating wind turbine by SAIPEM 7000, a semi-submersible vessel (Statoil, 2018). (c) installing tower-nacelle assembly (left) and rotor (right) for a floating wind turbine by a mono-hull vessel (Keseric, 2014).

There are studies on installation of offshore wind turbine components by floating cranes. Sarkar and Gudmestad (2013) proposed a method to install monopile foundations using a pre-installed submerged structure to isolate the foundation from the floating vessel motion. (Zhu et al., 2017) compared the dynamic motion response of a tripod foundation for offshore wind turbines during installation by a mono-hull and a jack-up crane vessel. Acero et al. (2017) studied the installation of an offshore wind turbine transition piece onto a monopile foundation by a mono-hull crane vessel. Ku and Roh (2015) studied the dynamic responses of an offshore wind turbine (tower-nacelle-rotor assembly) during lifting operation by a floating crane barge.

Installation of blades for offshore wind turbines is more challenging than other components (e.g. foundation, transition piece). This is because a high installation precision is required in the final blade mating phase and there is relative large motion between the turbine hub and the blade root at such large lifting height. Current industry practice is to use jack-up crane vessels to install offshore wind turbine blades. Jiang et al. (2018) studied the final mating phase of a 5MW wind turbine blade by a jack-up vessel onto a pre-assembled monopile and nacelle assembly. The blade root motion was found to be critical. The study found that the monopile hub motion can be important at certain wave periods when a resonant response is excited in the monopile. However, the blade root motion in this study is underestimated. Because it did not consider detailed modeling of the jack-up crane vessel, such as flexibility in jack-up legs and crane, jack-up leg soil-structure interaction and wave loads on jack-up legs, which are found to have significant influence on blade root motion during the final mating phase by Zhao et al. (2018b).

Compared to monopiles, the nacelle motions of typical jacket and tripod turbine foundations are much smaller (Shi et al., 2011). Therefore, for jacket and tripod wind turbines, the contribution of nacelle motion to the relative nacelle-blade root motion during blade mating is relatively small.

The present study aims at demonstrating the feasibility of offshore wind turbine blade installation by floating crane vessels. This is achieved by a detailed comparison of the blade dynamic motion response when installed by floating vessels with a representative jack-up crane vessel. Two different types of floating vessels are considered, i.e., a mono-hull and a semi-submersible vessel. The focus is placed on the blade final mating phase, addressing the blade motion response. It is assumed that the turbine has a jacket foundation and the nacelle motion is relatively less important and not addressed in the present study.

Fully coupled time domain simulations are carried out using the SIMO-RIFLEX-Aero code to study the dynamic responses of the three blade installation systems, including the motions of the vessel, crane tip, blade and blade root and tension in the tugger lines. The feasibility of using a floating vessel is demonstrated by showing that the motion and velocity of the blade root is within the limits experienced when a jack-up vessel is used. This approach is believed to be conservative since the installation of a jack-up crane vessel itself is weather sensitive.

2. System description

Figures 2 shows the overall configuration of offshore single blade installation set-up by the semi-submersible, mono-hull and jack-up crane vessels, respectively. An actual water depth of 39.1m is used in this study. Since bottom-fixed offshore wind turbines (e.g. monopiles) are more likely located in this water depth, and the motions of bottom-fixed offshore wind turbines are small, we neglected the motion of wind turbines during the numerical analysis.

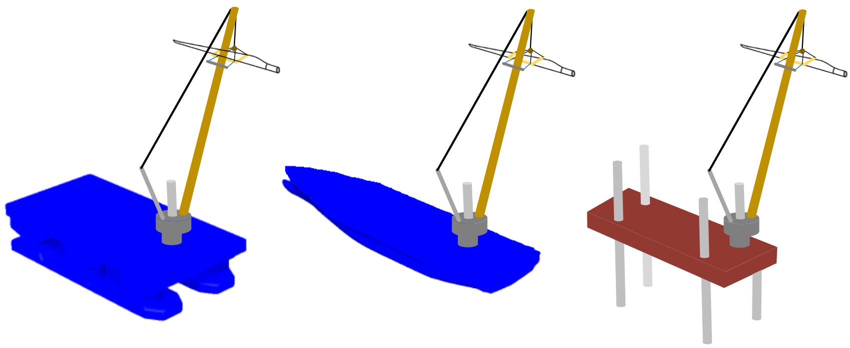

Figure 2: Offshore wind turbine installation using three different kinds of crane vessels: semi-submersible, mono-hull, jack-up.

The blade installation systems consist of three main parts, i.e., the vessel, the crane, and the installed blade and the lifting arrangements. Details of these three parts are provided in this section. The main properties of the three selected vessels are listed in Tables 1 and 2. The semi-submersible vessel has two longitudinal pontoons that are completely submerged. The pontoons are connected to the main deck via six vertical columns. The displaced volume of the mono-hull vessel is about 40% of the semi-submersible vessel. Both the semi-submersible vessel and the mono-hull vessel are assumed to be equipped with dynamic positioning (DP) systems to keep the vessels in position. The jack-up crane vessel has four legs with its hull elevated above the mean sea surface during operations.

Table 1: Main parameters of the floating crane vessels

Parameters		Semi-submersible	Mono-hull
Length	[m]	175	183
Breadth	[m]	87	47
Operational draught	[m]	26.1	12
Displacement	[m^3]	1.638×10^5	6.190×10^4

Table 2: Main parameters of the jack-up crane vessel

Parameters	Unit	Values
Hull length, breadth and depth	[m]	132, 39, 9
Displacement during transportation	[m^3]	2.20×10^4
Total elevated load	[t]	1.69×10^4
Leg length and diameter	[m]	92.4, 4.5
Long. and trans. leg spacing	[m]	68.3, 30.6
Airgap	[m]	7.2
Leg below hull	[m]	49
Soil type		Dense sand
K_x, K_y and K_z *	[kN/m]	1.35×10^6, 1.35×10^6, 1.47×10^6
K_ϕ, K_θ and K_ψ *	[kNm/deg]	6.4×10^5, 6.4×10^5, 8.3×10^5

* Equivalent linear spring stiffness of the soil in the global coordinate system defined in Figure 4(c).

The same typical pedestal crane is used for all three crane vessels in this study, as shown in Figure 3. The pedestal crane consists of crane supports, a wire overhang system and a lattice boom. The crane is connected to the vessel via the crane supports. In the numerical model, the boom is modeled using flexible beam elements with its lower end hinged on the crane base. The boom wires control the boom inclination and are represented by bar elements. The deformation of the crane supports, including king, pedestal and back-stay, is neglected (Zhao et al., 2018b). The main parameters of the crane are listed in Table 3.

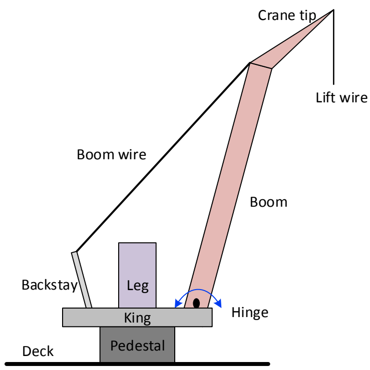

Figure 3: Illustration of a typical offshore pedestal crane (Zhao et al., 2018b)

The DTU 10 MW wind turbine blade (Bak et al., 2013) is used in this study. As shown in Figure 2, the blade is held by a yoke and lifted by the hook via four slings. The lift wire runs through the crane tip to the hook. Tugger lines are used for blade heading control which run from the yoke to a trolley on the crane boom. Pretension is applied in tugger lines to prevent slack lines. The main properties of the blade lifting system are summarized in Table 4.

As shown in Figure 4, three right-handed coordinate systems are defined and used for each blade installation system, i.e., a global coordinate system

Table 3: Main parameters of the crane

Crane properties (Zhao et al., 2018b)	
Boom length [m]	107.6
Crane boom angle [deg]	67.6
No. of equivalent boom wires [-]	2
Equivalent boom wire stiffness [kN/m]	9048
Equivalent boom wire damping [kNs/m]	90.5
Crane tip positions on the vessels *	
Semi-submersible vessel	(66m, 65.3m, 144.9m)
Mono-hull vessel	(74.2m,65.6m,144.9m)
Jack-up vessel	(34.2m,49.3m,133.2m)

* It is given in the vessel-related coordinate system. The height of crane tip on all three vessel are the same in the global coordinate system, i.e., 144.9m above the mean sea surface.

$O-XYZ$, a vessel-related coordinate system $O_v-X_vY_vZ_v$ and a blade-related coordinate system $O_b - X_bY_bZ_b$.

The blade-related coordinate system $O_b - X_bY_bZ_b$ has its origin on the blade's center of gravity. Y_b is in the blade's longitudinal direction and is positive towards the blade tip; Z_b is positive upwards; X_b follows the right-hand rule. The $O_b - X_bY_bZ_b$ parallels with the global coordinate system $O - XYZ$ when the blade is at rest.

For the vessel-related coordinate system $O_v-X_vY_vZ_v$, its origin is located at the center of the waterplane of the floating vessel at rest, while it sits on the geometrical center of the elevated jack-up hull. X_v is in the vessels' longitudinal direction and Z_v is positive upwards; Y_v follows the right-hand rule. When the vessel is at rest, $O_v - X_vY_vZ_v$ will parallel with the global

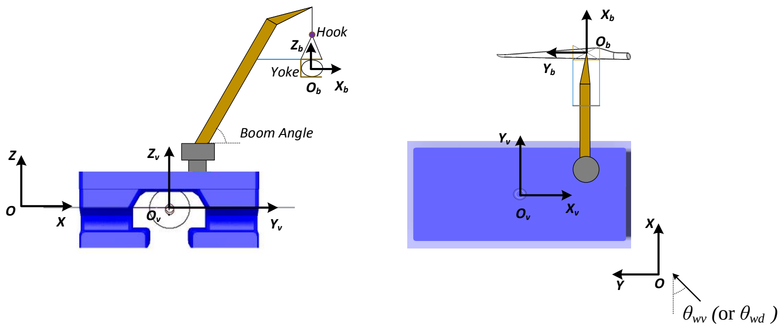

(a) Semi-submersible vessel: side view and top view

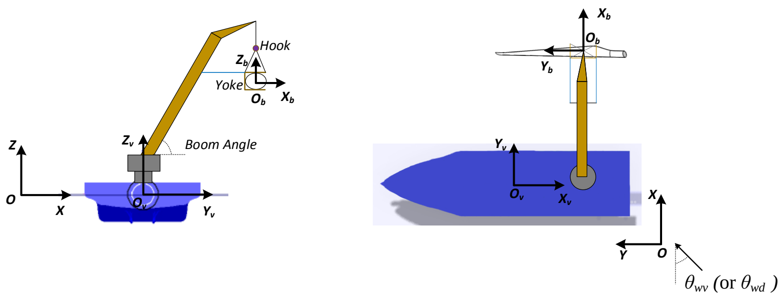

(b) Mono-hull vessel: side view and top view

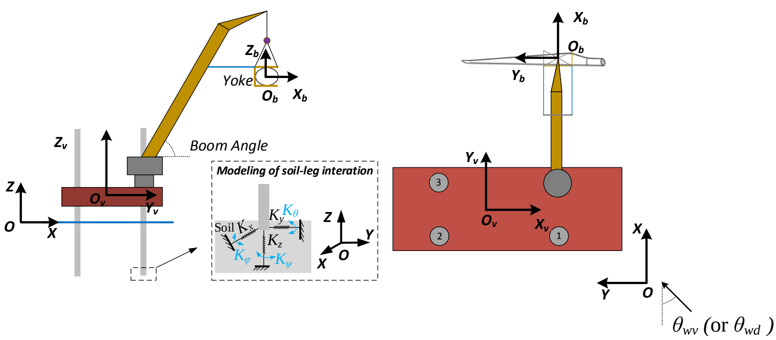

(c) Jack-up vessel: side view and top view

Figure 4: Definition of coordinate systems for the blade installation system: θ_{wv} is the incident wave angle while θ_{wd} is the wind inflow angle.

Table 4: Main properties of the blade and the lifting arrangement (Zhao et al., 2018a)

Parameter	Value
Hook mass [tons]	10
Yoke mass [tons]	47
Blade mass [tons]	41.67
Blade length [m]	86.37
Installation height [m]	119
Length of crane wire (from crane tip to hook) [m]	4.7
Length of slings [m]	20.4
Tugger line arm length (relative to blade COG) [m]	10
Length of tugger line [m]	5.7
Stiffness of tugger line [kN/m]	525

coordinate system $O-XYZ$ if it rotates around the Z_v axis by 90 deg.

The global coordinate system $O-XYZ$ has its origin located at the mean sea surface. Z is positive upwards. X parallels with the Y_v when the vessels are at rest. The Y follows the right hand rule.

The incident wave angle, i.e., θ_{wv}, is defined as the relative angle of wave direction and the positive X direction in the global coordinate system. The incident wind angle θ_{wd} has a similar definition while the wind and waves do not always have the same incident angle.

3. Methodology

The fully coupled code, the SIMO-RIFLEX-Aero (Zhao et al., 2018b) is used to conduct the integrated dynamic analysis of single blade installation by three crane vessels in time domain. The coupled code is an integration of three programs, i.e., SIMO (SINTEF Ocean, 2017b), RIFLEX (SINTEF

Ocean, 2017a) and Aero (Zhao et al., 2018a). Detailed structural models for the blade installation systems are shown in Table 5.

Table 5: Structural model for the blade installation systems

Component	Modeling
Blade	Rigid body with 6 DOFs in SIMO
Hook	Point mass at the lower end of lift wire in RIFLEX
Boom wire, lift wire and slings	Bar elements in RIFLEX
Tugger lines	Bi-linear springs (only tension, no compression) in SIMO
Crane boom	Beam elements with circular cross-section, hinged at the lower end in RIFLEX
Crane base	Rigid (master slave connections between the nodes) in RIFLEX
Jack-up hull	Rigid body with 6 DOFs in SIMO
Jack-up hull-leg connections	Rigid
Jack-up legs	Beam elements with ring cross-sections in RIFLEX
Jack-up soil-structure interaction	Linear springs and dampers in 6 DOFs at the lower ends of all legs in RIFLEX
Floating vessels	Rigid bodies with 6 DOFs in SIMO

The external force models for the blade installation systems are presented in Table 6. The aerodynamic loads acting on the installed blade are computed in the Aero code based on the cross-flow principle (Horner, 1965; Hoerner and Borst, 1985). At each time step, the Aero code calculates the aerodynamic loads using the instantaneous blade position provided by SIMO and the relative wind velocity seen by the blade. The aerodynamic loads are then imported by SIMO (Zhao et al., 2018a).

The hydrodynamic load modeling for the jack-up vessel and the floating vessels are different, as shown in Table 6. The hydrodynamic loads on the jack-up legs are calculated based on the Morison's formula (diameter to wave length ration$< 1/5$), with integration to the instantaneous sea surface considering the presence of water inside the legs (Zhao et al., 2018b).

For the floating vessels, the hydrodynamics loads are calculated based on

Table 6: External force model for the blade installation systems

Component	Force model
Blade	Aerodynamic load calculated in the Aero code, including influence of wind shear, wind turbulence and dynamic stall
Jack-up hull	Wind loads with equivalent wind area and wind coefficients
Jack-up legs	Hydrodynamic loads calculated using Morison's formula with integration to the instantaneous sea surface considering water inside the legs
Floating vessels	Hydrodynamic loads calculated by using the 1st and 2nd order potential theory considering viscous roll damping; dynamic forces from the DP systems are modeled as equivalent linear stiffness terms with 70% of critical damping in surge, sway and yaw

the potential flow theory. The hydrostatic restoring coefficients are computed using the mean position of the vessels. The added mass, potential damping and first order wave excitation forces are obtained using a first order potential flow model and applied in the time domain using the convolution techniques (SINTEF Ocean, 2017b). Additional viscous roll damping is incorporated as 3% of the vessel's critical damping in roll (Pedersen, 2012). In addition to the first order hydrodynamic forces, the mean wave drift loads are also considered. The Newman's approximation is used to estimate the second order difference frequency wave excitation loads on the mono-hull vessel in surge, sway and yaw. For the semi-submersible vessel, integration of second order mean wave pressure over its wetted surface is used to estimate the second order difference frequency wave excitation forces in all 6 DOFs, as recommended in the DNV-RP-C205 guideline (DNV, 2007). The restoring forces of the DP system are simplified into equivalent linear stiffness terms in surge, sway and yaw. Besides, large damping, i.e., 70% of the critical damping of the vessels' surge, sway and yaw motion, is applied to eliminate the corresponding slowly varying motion. This is a reasonable assumption since it can be achieved by use of DP systems in practical operations (SINTEF Ocean, 2017c).

4. Identification of system natural periods

The natural periods of the three blade installation systems are estimated in this section. Since the blade installation systems are complex, the natural periods are identified module by module.

4.1. Vessels

Eigenvalue analyses are conducted to identify the natural periods of the vessels' motion, excluding the crane and blade.

For the floating vessels, their natural frequencies are obtained by solving Eq.(1).

$$[-\omega^2(\mathbf{M} + \mathbf{A}_\infty) + \mathbf{K}] \cdot \mathbf{x} = 0 \tag{1}$$

where $\mathbf{M}$ is the vessel mass matrix; $\mathbf{A}_\infty$ is the added mass matrix at infinite frequency; $\mathbf{K}$ is the restoring matrix which is the sum of the hydrostatic restoring and the equivalent restoring from the DP system.

The eigenvalue analysis for the jack-up vessel is solved by using the Lanczos method (SINTEF Ocean, 2017a), considering the flexibilities in the jack-up legs and the soil foundations.

The results are presented in Table 7. The natural periods of the semi-submersible vessel are above 18s. The natural periods of the mono-hull vessel motion in heave, roll and pitch are between 9s∼14s, which are within typical wave period range. The natural periods of the jack-up vessel motion are much shorter than those of the two floating vessels.

Table 7: Natural periods of vessels' motions (defined in the vessel-related coordinate systems in Figure 4)

Vessel	Surge	Sway	Heave	Roll	Pitch	Yaw
Semi-submersible	83.68 s	75.29 s	22.64 s	23.56 s	18.20 s	86.72 s
Mono-hull	87.27 s	75.23 s	10.00 s	13.51 s	9.07 s	85.69 s
Jack-up	2.912 s	3.087 s	2.363 s	0.479 s	0.594 s	0.451 s

4.2. Crane

The crane boom is hinged at its lower end, The crane motion is mainly caused by the deformation of the boom wires. The natural period of the crane motion is identified by conducting decay tests while the vessel is fixed. In the current blade installation scenario, the crane motion has a natural period of 2.9s.

4.3. Blade

The natural frequencies of blade rigid body motion are obtained by eigenvalue analysis, together with the hook while keeping the vessel and the crane fixed, based on Eq.(1). Since the blade and the hook are in air, the corresponding added mass matrix $\mathbf{A}_\infty$ is neglected. The restoring matrix $\mathbf{K}$ is mainly resulted from the mechanical wire coupling forces from the lift wire, slings and tugger lines.

The dominant motions of the blade rigid body motion and corresponding periods and frequencies are listed in Table 8. The blade-hook in-phase pendulum motion has the longest natural period of 12s, followed by the blade

Table 8: Natural periods and dominant motion of the blade motion (defined in the blade-related coordinate systems in Figure 4)

Dominant response	Period [s]	Frequency [rad/s]
Blade roll resonance (in phase pendulum motion)	12.0	0.52
Blade yaw resonance (due to tugger lines)	5.11	1.23
Blade-hook double pendulum around the crane tip in the $O_b - Y_bZ_b$ plane (blade and hook motion out of phase)	3.63	1.73
Blade surge resonance (due to tugger lines)	1.90	3.31

yaw resonant motion with a period around 5s. The third mode is caused by the out-of-phase double pendulum motion of the blade and hook around the crane tip in the vertical $O_bY_bZ_b$ plane (Zhao et al., 2018a). The natural period of blade surge motion due to tugger line restoring effects is around 1.9 s. As a result, the blade surge resonance is generally not excited.

5. Load cases and environmental conditions

A series of load cases (LCs) are defined for the blade installation systems and used in the time domain simulations, as shown in Table 9. LC1 is a turbulent wind only case. LC2 is an irregular wave only case. They are used to formulate a comparison against LC3 to reveal the influence of wind and waves on the system dynamic responses.

LC3∼LC7 have correlated turbulent wind and irregular waves. In these load cases, the significant wave height and peak period are correlated with the mean wind speed. The correlation is based on the measurement and analysis of data obtained at the North Sea Center site (Li et al., 2015). The wind turbulence intensity is calculated according to the IEC class A, which is the design class for the DTU 10MW wind turbine (Bak et al., 2013). The

Table 9: Load cases: turbulent wind and irregular waves

LC	U_w [m/s]	T_I [%]	H_s [m]	T_p [s]	θ_{wd} [deg]	θ_{wv} [deg]	Sim. length [s]
LC1	7.0	24.8	-	-	0	-	3600×5
LC2	-	-	1.0	7.3	-	0	3600×5
LC3	7.0	24.8	1.0	7.3	0	0	3600×5
LC4	7.0	24.8	1.0	7.3	0	315	3600×5
LC5	7.0	24.8	1.0	7.3	0	270	3600×5
LC6	8.3	22.9	1.5	7.7	0	0	3600×5
LC7	5.6	28.0	0.5	6.8	0	0	3600×5
LC8	7.0	24.8	1.0	[5,6,7,8,9,10]	0	285	6×(3600×5)

U_w- mean wind speed; T_I - turbulence intensity factor; θ_{wd} - wind inflow angle; θ_{wv} - wave incident angle; $\theta_{wv} = 0^o$ - beam sea; $\theta_{wv} = 315^o$ - quarter sea; $\theta_{wv} = 270^o$- head sea.

wave direction is varied in LC3∼LC5, i.e., beam sea, quarter sea and head sea, to study the impacts of misalignment of wind and wave on the system motion responses. LC6 and LC7 are two correlated wind and wave conditions that are different from LC3. They are used to identify the dynamic response characteristics of system under various sea states.

A parametric study is carried out in LC8, to further investigate the effect of wave peak period on the performance of floating crane vessels. The wave peak period varies from 5s to 10s, while the significant wave height and wind condition are kept the same as LC3. The wave direction in LC8 is assumed to be 285 deg, close to the vessel head sea direction to utilize the wave orientation to improve vessel performance. The 15 deg offset from the head sea direction is recommended by DNV-RP-H103 (DNV, 2014) to represent a practical head sea condition during operation.

During the simulations, the turbulent wind field is generated by using the TurbSim code (Jonkman, 2009) according to the Kaimal turbulence model.

The irregular waves are long crested and are modeled by using the JONSWAP spectrum with $\gamma = 1$ (DNV, 2007).

Five identical and independent simulations are carried out for each load case. Each simulation lasts for one hour after removing the start-up transient part. The statistical values and power spectra of the dynamic motion responses presented in the next section are obtained based on the average of five one-hour simulations.

6. Results and discussion

6.1. Hydrodynamic performance of the floating vessels

Prior to the comparative study of the dynamic responses of the three blade installation systems, the hydrodynamic properties of the two floating vessels are investigated. Their hydrodynamic coefficients, i.e., the added mass, potential damping, first order wave excitation force transfer function and first order motion transfer function, are calculated in frequency domain. The water depth considered is 39.1m. The results in vessel roll (ϕ_v) are shown in Figure 5. The former three are non-dimensionalized using the following definitions:

- A_{44} is non-dimensionalized by $\rho V L^2$.
- B_{44} is non-dimensionalized by $\rho V L\sqrt{gL}$.
- H_4^1 is non-dimensionalized by $\rho V g A_{wave}$.

where ρ is the water density; V is the vessel displaced volume; L is the vessel length; g is the acceleration of gravity; A_{wave} is the unit wave height.

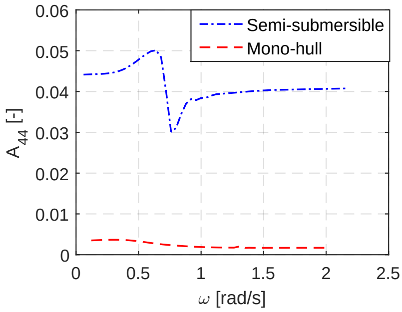

(a) Added mass A_{44}

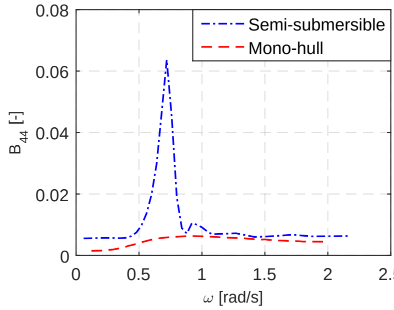

(b) Potential damping B_{44}

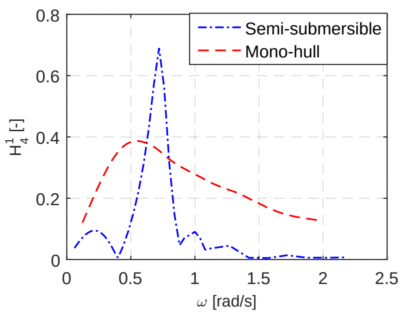

(c) RAO of first order excitation force H_4^1

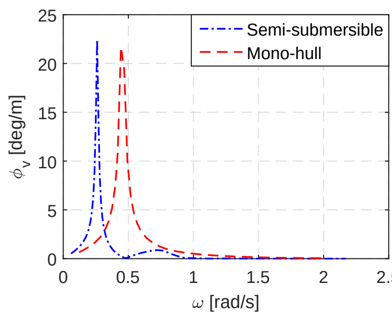

(d) RAO of first order motion in roll

Figure 5: Non-dimensional added mass, potential damping and transfer function of the first order wave excitation force and motion of the floating vessels in roll. The transfer functions of first order wave excitation force and first order motion are estimated with incident wave angle of 0^o. It should be noted that the RAO of wave excitation fore, rather than the motion RAO is used in the time domain analysis. The RAO of vessel roll motion shown here just aims to illustrate the variation of vessel motion with incident wave period.

The layout of the semi-submersible vessel contributes to a large added mass coefficient in roll, i.e., A_{44}, which is larger than the corresponding mass moment of inertia I_{44}. For the mono-hull vessel, its A_{44} is less than 20% of its I_{44}.

The RAO of the first order wave excitation force H_4^1 of the semi-submersible vessel is overall smaller than the mono-hull vessel. Even though the former exceeds the latter in the frequency range of 0.65∼0.75 rad/s (by less than 50%). The large added mass and potential damping of the former help to limit its dynamic response. Overall, the former has better hydrodynamic performance than the latter within typical wave frequency range, as shown in Figure 5(d).

6.2. Characteristics of system motion responses

The system dynamic motion characteristics are discussed in this section based on the time domain simulation results, including the vessel motion (6 DOFs) and the crane tip motion (3 DOFs) in the vessel-related coordinate systems, and the blade motion (6 DOFs) and the blade root motion (3 DOFs) in the blade-related coordinate systems. The standard deviations of positions of the crane tip, the blade center of gravity and the blade root are compared in the global coordinate system.

6.2.1. Vessels

The standard deviations of the vessel motion in LC1∼ LC7 are presented in Figure 6.

The vessel motions are mainly wave-induced, as indicated by the comparisons among LC1, LC2 and LC3. Compared to the jack-up vessel, the floating vessels have larger motions in all 6 DOFs. The semi-submersible vessel has smaller motions than the mono-hull, due to its better hydrodynamic performance as discussed in Section 6.1.

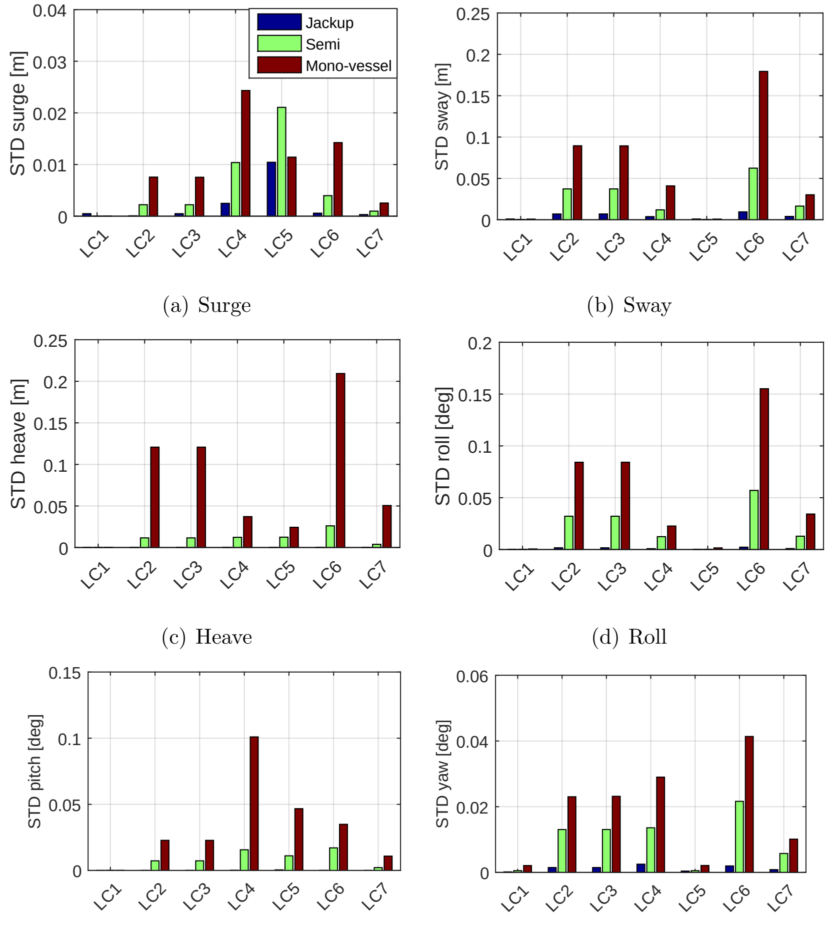

(a) Surge

(b) Sway

(c) Heave

(d) Roll

(e) Pitch

(f) Yaw

Figure 6: Standard deviations of vessel motion in LC1∼LC7 in the vessel-related coordinate system.

The power spectra of vessel motion in sway and roll in LC3 are shown in Figure 7. The jack-up vessel has minor wave frequency response and is dominated by the vessel sway resonant motion. The mono-hull vessel's sway motion experiences a large contribution from the slowly varying sway motion, which is dominant in short waves. For both of the floating vessels, the wave frequency response is found to be significant, especially in roll motion, as shown in Figure 7(b). The mono-hull vessel roll motion has its natural period close to the wave peak period and hence gets significant wave load excitations, leading to large wave frequency response. The mono-hull vessel's motion in heave and pitch has a similar trend.

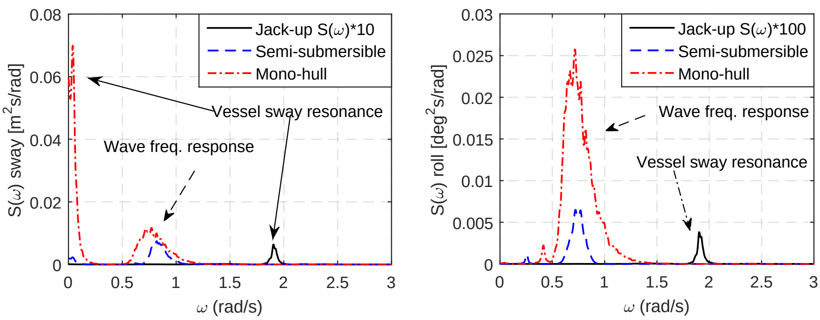

(a) Sway (b) Roll

Figure 7: Power spectra of vessel motion in LC3

6.2.2. Crane tip

The crane tip motion is given in the vessel-related coordinate system. Its standard deviations are shown in Figure 8.

For crane operations at large lifting height, the vessel's rotational motion greatly contributes to the crane tip motion. As a result, the amplitude of crane tip motion is generally larger than the vessel translational motion, which can be observed by comparing Figures 6(a) and 8(a), and by comparing

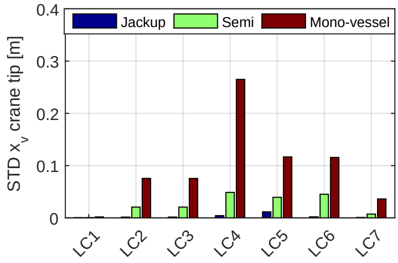

(a) Crane tip motion along X_v

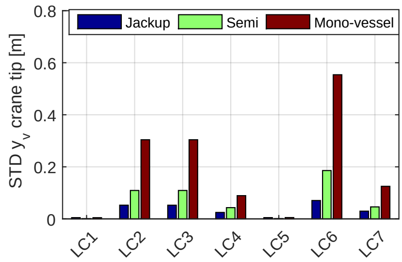

(b) Crane tip motion along Y_v

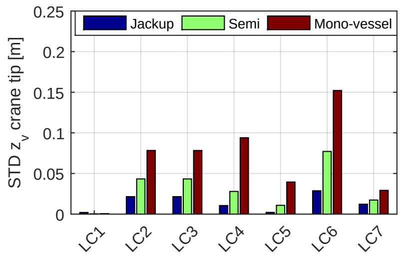

(c) Crane tip motion along Z_v

Figure 8: Standard deviations of crane tip motion in LC1∼LC7 in the vessel-related coordinate system.

6(b) and 8(b), respectively. However, the former can be smaller than the latter in some cases. For example, the crane tip motion in Z_v direction (in the vessel-related coordinate system) is smaller than the vessel heave motion for the mono-hull vessel in LC3, LC6 and LC7, as can be found by comparing Figures 6(c) and 8(c). The corresponding time series in LC3 are further analyzed, as shown in Figure 9(a). The contributions of the mono-hull vessel's heave and roll motions dominate the crane tip motion in Z_v direction in LC3. The contribution from vessel roll motion is out of phase with that of vessel heave motion, resulting in the crane tip motion in Z_v

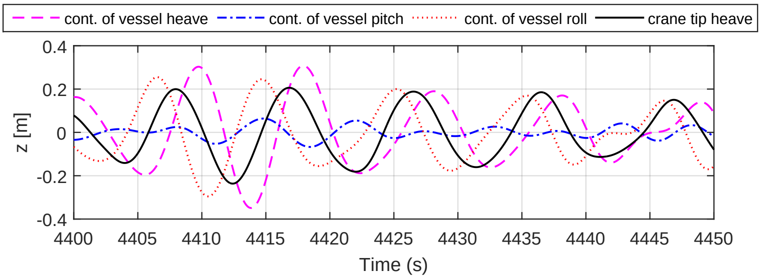

(a) LC3

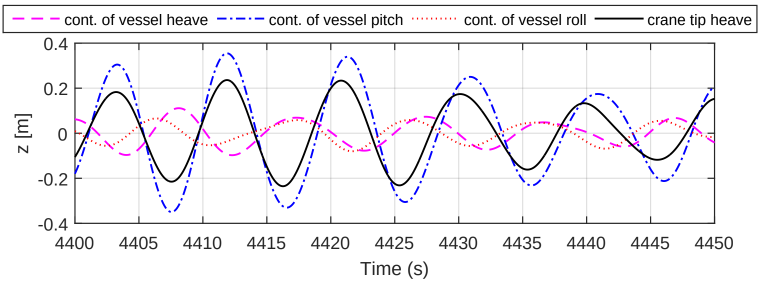

(b) LC4

Figure 9: Contributions of mono-hull vessel's motion to the crane tip motion in Z_v direction in the vessel-related coordinate system in LC3 and LC4.

direction smaller than the vessel heave motion. In LC4, the vessel pitch is remarkable. It has much larger contribution to the crane tip motion in Z_v direction than vessel heave and roll motions, as shown in Figure 9(b). As a result, the crane tip motion in Z_v direction has a larger amplitude than the vessel heave motion.

Overall, the crane tip on the jack-up vessel has the smallest motion, followed by that on the semi-submersible vessel and that on the mono-hull vessel. Spectral analysis is carried out to further identify the differences. As shown in Figure 10, the crane tip motion on the floating vessels is highly dominated by the wave frequency response due to floating vessels' motion. The motion contribution from the crane movement caused by crane elastic deformation is relatively less important on the floating vessels. Nevertheless, it has a notable contribution for the crane tip motion on the jack-up crane vessel, as shown in Figure 10(b).

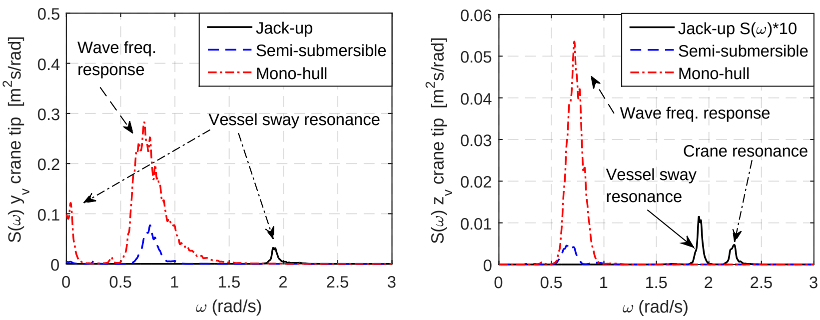

(a) Crane tip motion along Y_v in LC3 (b) Crane tip motion along Z_v in LC4

Figure 10: Power spectra of crane tip motion in LC3 and LC4 in the vessel-related coordinate system.

Similar to the vessel motion, the dynamic responses of the crane tip are sensitive to the variations in wave conditions, as can be found by comparing LC3$\sim$LC7 in Figure 8. Comparison among LC3, LC6 and LC7 shows that the crane tip motion increases significantly with increasing wave height. The crane tip motion along X_v has the maximum response in LC4 with quartering sea. The crane tip motions along Y_v and Z_v reach their maximum values in LC5 with head sea. It shows that the crane tip motion can be reduced by adjusting the vessel heading relative to the wave direction.

6.2.3. Blade

The standard deviations of the blade motion in the blade-related coordinate system are presented in Figure 11.

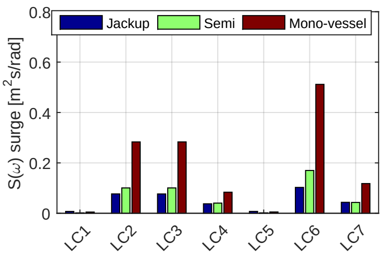

(a) Surge

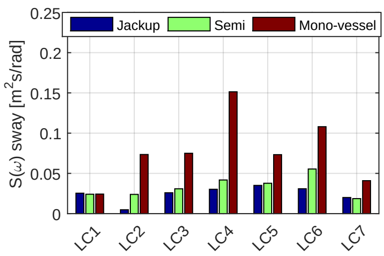

(b) Sway

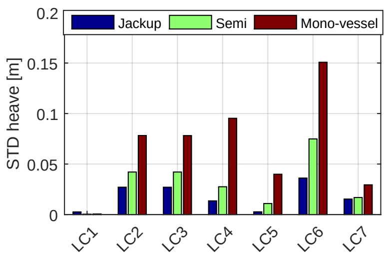

(c) Heave

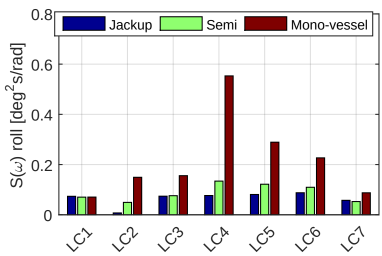

(d) Roll

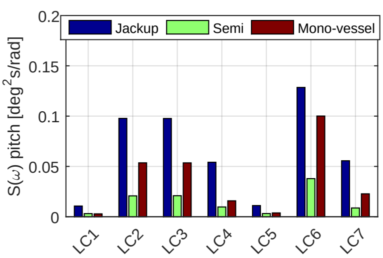

(e) Pitch

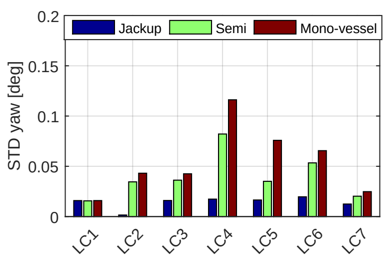

(f) Yaw

Figure 11: Standard deviations of blade motion in LC1∼LC7 in the blade-related coordinate system.

Comparisons among LC1∼LC3 show the relative importance of wave-induced vessel motion and blade aerodynamic loads in the blade dynamic response. The former is the main contributor to the blade motion in surge, heave and pitch. The blade motion in other DOFs shows remarkable dependency on both of them. Nevertheless, their relative contribution varies from vessel to vessel, as shown in Figure 12. For the jack-up vessel, the blade roll motion is mainly induced by the blade aerodynamic loads. When installed by the floating vessels, the blade roll motion is also affected by the vessels' wave-induced motion. For the semi-submersible vessel, the wave frequency response is slightly excited. The wave frequency response is remarkable for the mono-hull vessel and as a result, the double-pendulum motion is excited. Overall, the effect of wave-induced vessel motion dominates over that of the aerodynamic loads in blade roll motion for the mono-hull vessel, as can be observed in Figures 11(d) and 12(c). A similar trend exists for the blade motion in sway on the mono-hull vessel.

The contribution of wave-induced vessel response in the blade dynamic motion experiences a significant variation under different wave conditions, which is revealed by comparing the results of LC3∼LC7 in Figure 11. The maximum contributions from the wave frequency responses are seen in LC6 which is the severest sea state within LC1∼LC7. The amplitudes of blade motion are dependent on the wave direction. The blade surge, heave and pitch motions reach their minimum values in head sea condition in LC5, as shown in Figure 11. The blade motion in sway, roll and yaw reaches minimum in beam sea in LC3 and maximum in quartering sea in LC4. The

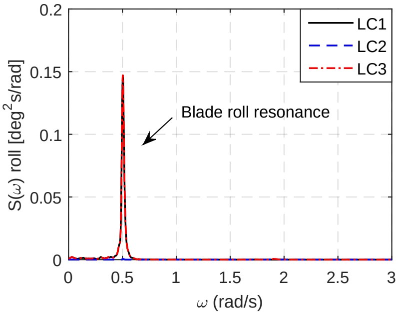

(a) By jack-up vessel

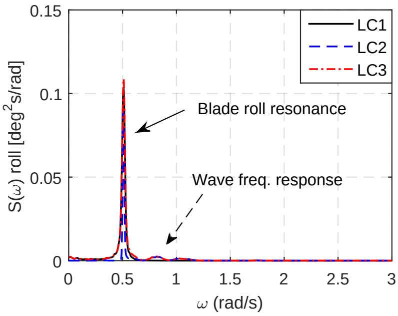

(b) By semi-submersible vessel

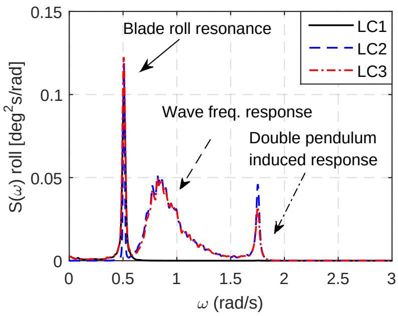

(c) By mono-hull vessel

Figure 12: Power spectra of blade roll motion in LC1∼LC3

power spectra of the blade yaw motion in LC3∼LC5 are presented in Figure 13. The blade yaw motion on the semi-submersible vessel has a relatively small contribution from the wave-frequency response. It is mainly dominated by the blade yaw resonant motion which is significantly excited in quartering sea in LC4. On the mono-hull vessel, the blade yaw motion also has a remarkable contribution from the wave frequency response. It excites the blade roll resonance as well in LC4 and leads to a large increase in blade yaw

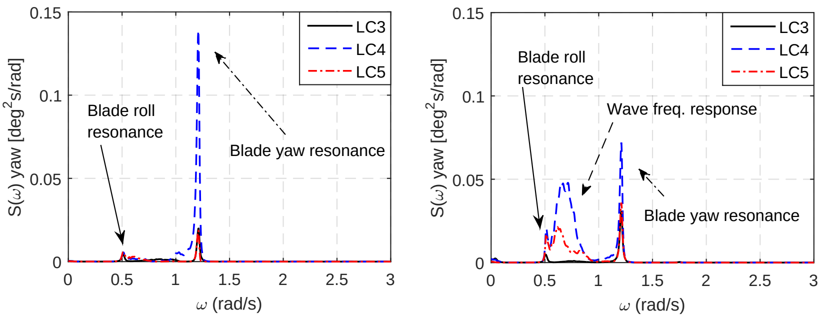

(a) By semi-submersible vessel

(b) By mono-hull vessel

Figure 13: Power spectra of blade yaw motion in LC3∼LC5

motion.

Similar to the crane tip motion, the blade motion on the floating vessels has relatively less important contributions from the crane dynamics, as shown in Figure 14. On the jack-up vessel, the crane resonant response is important for the blade motion because it is excited by the jack-up vessel motion since their natural periods are very close.

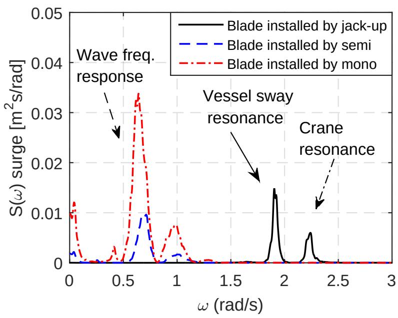

Figure 14: Power spectra of blade surge motion in LC4

6.2.4. Blade root

The dynamic motion at the blade root is critical for the mating process of blade root into the turbine hub. The blade root motion is given in the blade-related coordinate system. The standard deviations of blade root motion are shown in Figure 15.

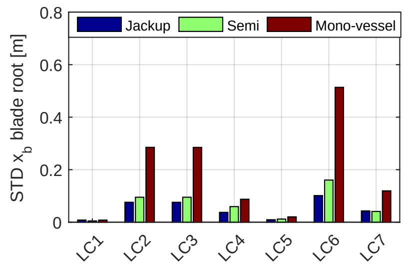

(a) Blade root motion along X_b

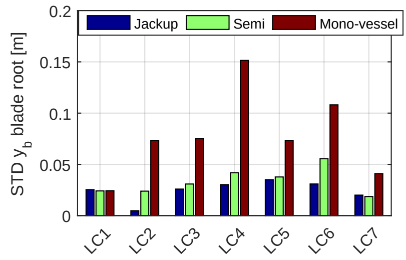

(b) Blade root motion along Y_b

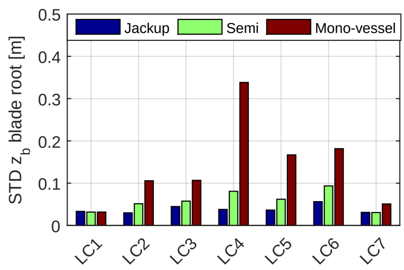

(c) Blade root motion along Z_b

Figure 15: Standard deviations of blade root motion in LC1~LC7 in the blade-related coordinate system.

The blade root motion along X_b is mainly resulted from the blade surge and yaw motions. The latter has very limited contribution since it is well controlled by the tugger lines. The blade root motion along Y_b is mainly caused by the blade sway; thus, their dynamic characteristics are similar. The blade root motion along Z_b is a result of the blade heave and roll motions. It has larger amplitudes than the blade heave motion because of the significant contribution from the blade roll motion.

The blade root motion is affected by both wind and wave loads, as indicated by the comparison among LC1$\sim$LC3, and LC3$\sim$LC7 in Figure 15. Figure 16 shows the power spectra of blade root motion in X_b and Z_b in LC3. The blade root motion along X_b has significant wave frequency response for the floating vessels, as shown in Figure 16(a); it is thus sensitive to the wave condition. The blade root motion along Z_b shows significant dependency on blade motion caused by both aerodynamic loads and wave-induced vessel motion, which can be observed in Figure 16(b). Hence it is sensitive to both wind and wave conditions.

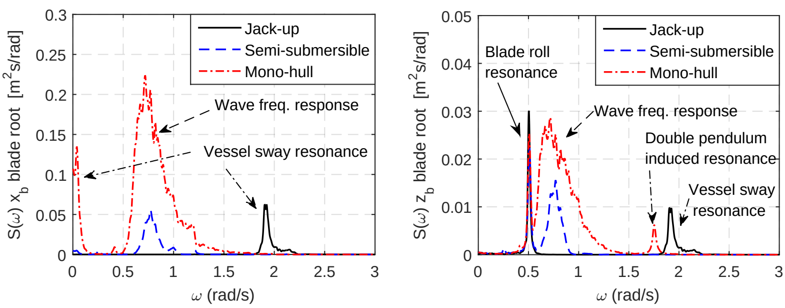

(a) Blade root motion along X_b (b) Blade root motion along Z_b

Figure 16: Power spectra of blade root motion along X_b and Z_b in the blade-related coordinate system in LC3

Compared with the semi-submersible vessel, the blade root motion on the mono-hull vessel is much larger and shows more significant variations with changing wave conditions, which can be found by comparisons within

LC3∼LC7 in Figure 15. Because it has much more contributions from the wave-frequency response caused by vessel motion since the mono-hull vessel gets larger wave load excitation due to its hydrodynamic properties, as shown in Figure 16. The power spectra of blade root motion along Y_b on the mono-hull and the semi-submersible vessels in LC3, LC6 and LC7 are compared in Figure 17. The blade root motion along Y_b on the mono-hull vessel has significant wave frequency response which increases dramatically from LC7, LC3 to LC6. For the semi-submersible vessel, the blade root motion along Y_b has much less contribution from the wave-induced vessel motion and thus has a lower amplitude.

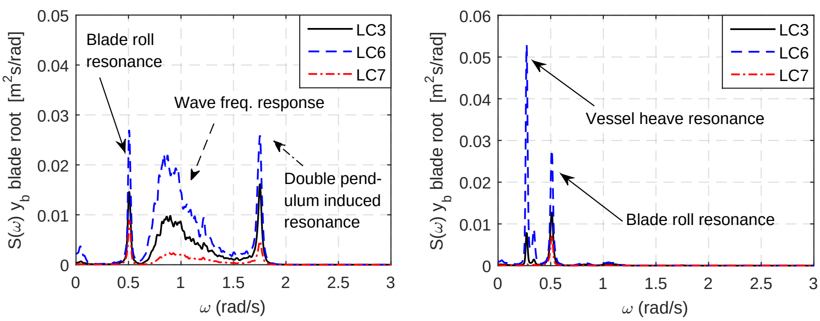

(a) Mono-hull vessel

(b) Semi-submersible vessel

Figure 17: Power spectra of blade root motion along Y_b in the blade-related coordinate system for the mono-hull and semi-submersible vessels in LC3, LC6 and LC7

6.2.5. Effect of wave period on blade root motion

Figure 18 shows the standard deviations of the blade root motion in the blade-related coordinate system in LC8 with varying wave peak period (5∼10s). By taking advantage of the vessel weather orientation, the amplitudes of blade root motion along X_b in LC8 with $T_p = 7s$ are greatly reduced, compared to LC3.

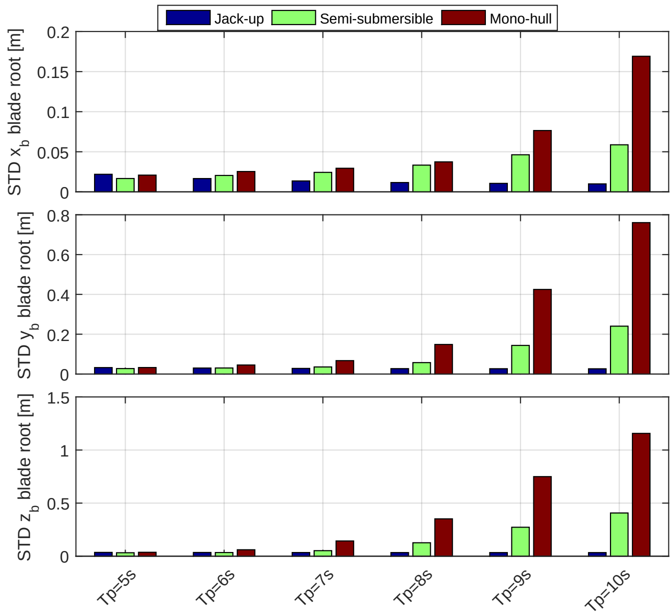

Figure 18: Standard deviations of blade root motion in the blade-related coordinate system in LC8 with varying wave peak period.

As can be observed in Figure 18, the root motion of the blade installed by the jack-up crane vessel decreases with the increasing wave peak period. Because the vessel gets less wave load excitations as the wave peak period shifts further away from the natural periods of vessel motion. On the contrary, the blade root motion increases significantly on the floating crane vessels. The mono-hull vessel causes the largest increase in blade root motion, since the vessel motion in the vertical plane is highly excited with the increasing wave peak period. Compared to the mono-hull vessel, the semi-submersible vessel causes a much smaller increase in blade root motion, since its motion natural periods are much larger than the wave periods considered. The results indicate that a floating vessel with motion natural frequencies far from typical wave frequency range helps reduce the blade root motion during installation.

6.2.6. Comparison of motions in the global coordinate system

The translational movements at crane tip, blade COG and blade root are further compared in the global coordinate system. Figure 19 shows their corresponding standard deviations.

It can be found in Figure 19 that the blade COG movement is quite different from that of the crane tip. When the jack-up crane vessel is used, the former is overall larger than the latter. Nevertheless, the former is observed to be smaller than the latter on the mono-hull vessel, especially along global X and Y directions. Compared to the jack-up and mono-hull vessels, the semi-submersible vessel experiences smaller differences in crane tip and blade COG movement. Besides, the blade root movement along the global Z direction is found to be much larger than that of the blade COG during installations by all three vessels in Figure 19(c). Hence, detailed system modeling is recommended for offshore wind turbine installation, including the modeling of vessel motion, crane dynamics, lifting arrangement and lifted component.

6.3. Tension in tugger lines

Identical tugger line system with two horizontally deployed tugger lines are used to control the heading of the blade during installation by the three

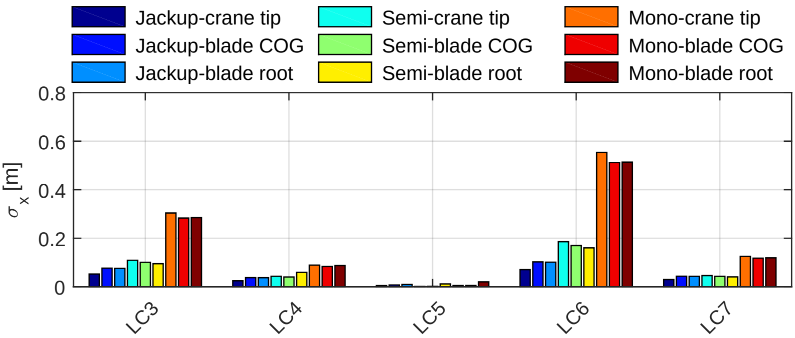

(a) Along global X axis

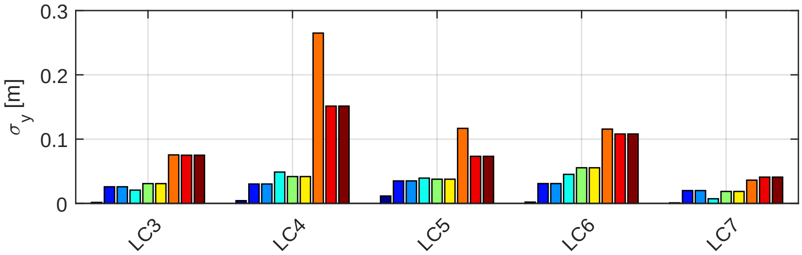

(b) Along global Y axis

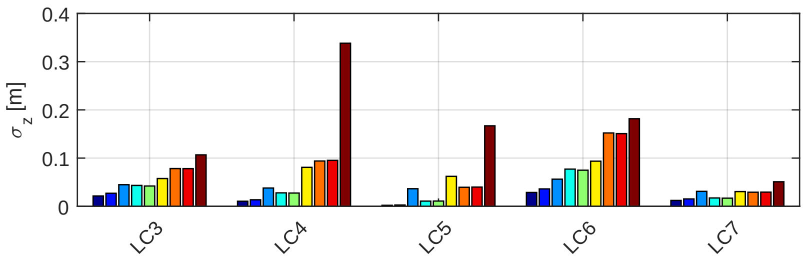

(c) Along global Z axis

Figure 19: Standard deviation of positions crane tip, blade COG and blade root in the global coordinate system.

crane vessels. The tugger line 1 is close to blade root while tugger line 2 is close to blade tip. During the simulations, no slack event is observed within the tugger lines. The standard deviations of tension in both tugger lines in LC1~LC7 are presented in Figure 20.

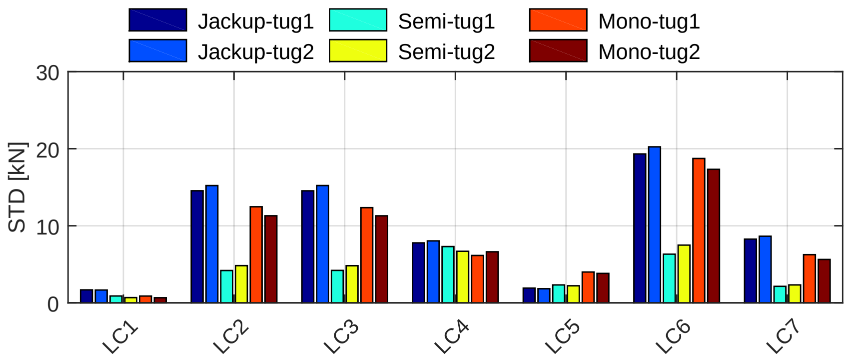

Figure 20: Standard deviations of tension in tugger lines in LC1~LC7

The variation of tugger line tension is affected by both wind and wave conditions, as shown by comparing LC1, LC2 and LC3 in Figure 20. However, the latter has highly dominant influence over the former. As a result, the standard deviations of tugger line tension vary significantly with changes in wave conditions, as shown by comparison among LC3~LC7 in Figure 20.

The tugger lines on the semi-submersible vessel experience the lowest level of fluctuation in tension. Those on the mono-hull vessel and on the jack-up vessel have a similar level of fluctuation while the former is slightly larger than the latter.

Spectral analysis is conducted to further investigate the differences. The results are presented in Figure 21. The tugger line tension for the jack-up

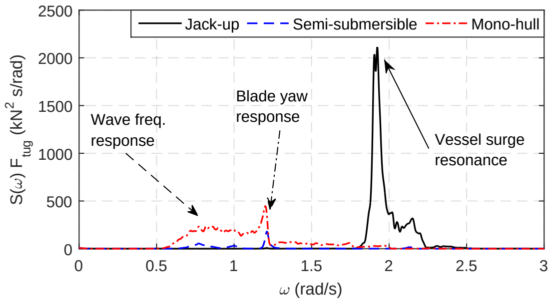

Figure 21: Power spectra of tension in tugger line 1 in LC3

crane vessel is dominated by the vessel surge resonant and crane resonant responses. For the mono-hull vessel, the main contributions are the wave frequency response and the blade yaw resonant response. The tugger line tension for the semi-submersible vessel gets low excitations in all three parts, and thus has the lowest fluctuation.

6.4. Discussion

During single blade installation for offshore wind turbines, the critical event occurs during the mating phase, i.e. mating the blade root into the turbine hub. The operation is not feasible or successful if one of the following scenarios occur during the mating phase:

- Too large blade root displacement in the radial direction of the hub opening, since it can make mating operation not possible.
- Excessive blade root velocity, especially in the radial direction of the hub opening, since it can cause impact with the hub opening and consequently damage guide pins at the blade root. It should be noted that

the guide pins are much stronger in taking axial force than bending moment (Verma et al., 2018).

Therefore, the blade root displacement and velocity in the radial direction of the hub opening are two critical parameters that strongly affect the feasibility of single blade installation. Nevertheless, relevant quantitative criteria with respect to these two critical parameters are difficult to obtain.

In order to assess the feasibility of single blade installation offshore by floating crane vessels in the present study, the criteria are taken as the characteristic values of blade root displacement and velocity in the radial direction of the hub opening during installation by a typical jack-up crane vessel. Figure 15 indicates that among the LCs considered, LC6 gives the largest blade root displacement during installation by the jack-up crane vessel. Hence the characteristic blade root displacement and velocity in LC6 installed by the jack-up crane vessel are assumed to be the criteria. It should be noted that the criteria considered are conservative as the environmental conditions in LC6 are below the operational limits for installation by jack-up crane vessels.

Figure 22 presents the comparison of blade root displacement and velocity in the radial direction of the hub opening in LC8, against the selected criteria. The wave peak period T_p varies in LC8 while the significant wave height ($H_s = 1m$) and wind condition are kept constant. As shown in Figure 22, both R_{xz} and V_{xz} increase significantly with increasing T_p. Single blade installation by the mono-hull crane vessel is feasible under wave conditions with T_p less than 7s. The semi-submersible vessel installation is feasible with a larger T_p of about 8s. Therefore, the feasibility of single blade installation by floating vessels is dependent on the probability of peak period T_p, or the

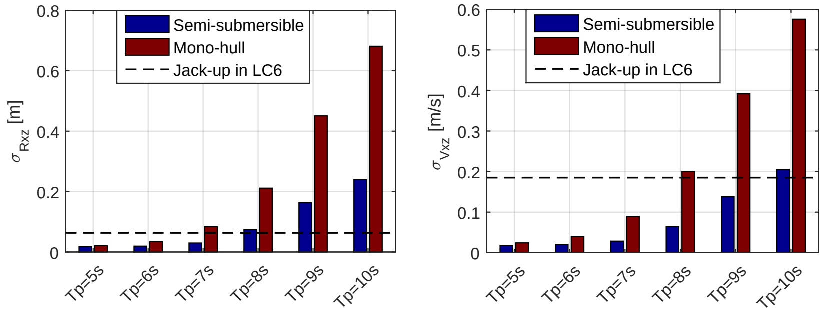

(a) Displacement (b) Velocity

Figure 22: Comparison of blade root motion (displacement and velocity) in the radial direction of the hub opening in the global coordinate system during installation by floating vessels in LC8 (with varying wave peak period) to the corresponding values of the jack-up crane vessel in LC6.

probability of operational weather window.

The feasibility of single blade installation by floating vessels is expected to be larger at offshore wind farm sites characterized by relatively short waves, such as in the North Sea, rather than sites dominated by long waves. Because the blade during installation by floating vessels has smaller motion in short waves than in long waves, as shown in Figure 22.

The semi-submersible vessel has a larger feasibility with respect to single blade installation, compared to the mono-hull vessel. Because the blade motion is larger when installed by the mono-hull vessel, due to larger wave-induced vessel motion partially caused by the difference in vessel displacement. The displacement of the mono-hull vessel considered is about 40% of the semi-submersible vessel. The mono-hull vessel's performance is expected to be improved by increasing the vessel size. However, the geometrical layout of the mono-hull vessel results in motion natural periods close to (or within) typical wave period range, e.g., in heave, roll and pitch.

To increase feasibility and performance of floating crane vessels in single blade installation, the vessels should be carefully selected. Increase of vessel size is one possible solution from the technical point of view, but it will increase the vessel construction cost and consequently the operational cost. Another possible solution is to use a floating vessel with better hydrodynamic performance, e.g., with natural periods of vessel motion outside typical wave period range. A suitable vessel type is semi-submersible. The geometrical parameters of a semi-submersible vessel, such as pontoons, columns, cross section and overall size, usually can make its natural periods of motion beyond upper limit of typical wave periods.

Utilization of weather orientation is another way to improve the floating vessels' performance when installing wind turbine blades, as shown by comparing LC3$\sim$LC5 in Figure 23. By adjusting the vessel heading relative to the wave direction, such as head sea in LC5, the blade root radial motion is greatly reduced for both of the floating vessels.

Floating crane vessels can more easily be relocated during offshore wind turbine installation, than jack-up vessels. The installation process of a jack-up vessel, such as leg lowering and retrieval, is sensitive to wave conditions and very time consuming (over 4 hours in total) (Fred. Olsen Windcarrier AS, 2016). Nevertheless, it is not necessary for floating vessels, and hence the time spent on relocation can be significantly shorter.

It should be noted that this paper focuses on a preliminary feasibility study of offshore single blade installation by floating crane vessels, therefore,

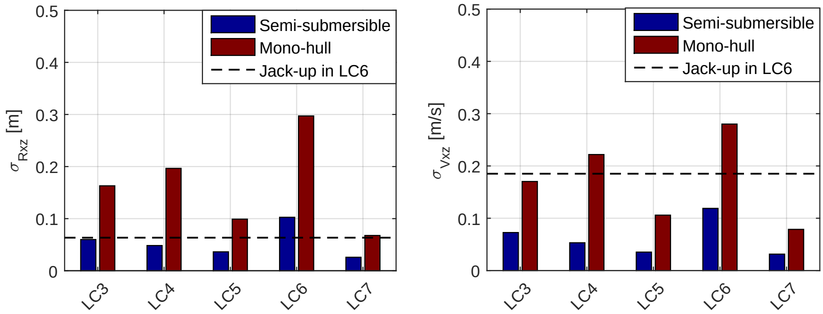

(a) Displacement (b) Velocity

Figure 23: Comparison of blade root motion (displacement and velocity) in the radial direction of the hub opening in the global coordinate system during installation by floating vessels in LC3∼LC7 (correlated wind and wave conditions) to the corresponding values of the jack-up crane vessel in LC6.

only a limited number of wind and wave conditions are considered. The wind and wave conditions in LC3∼LC7 are correlated and they are based on the long term hindcast data from the North Sea Center Site (Li et al., 2015).

The feasibility of floating vessel installation in this study is evaluated from the perspective of vessel performance. However, there are also many other factors to be considered when selecting vessels during planning phase of operations, such as environmental conditions, vessel availability, budget of operation, etc., which need specific coordination according to projects.

7. Conclusions

This paper deals with a feasibility study of using floating crane vessels during installation of offshore wind turbine blades, by a detailed comparison of system dynamic responses with a typical jack-up crane vessel. The comparison is conservative because the installation of a jack-up vessel is weather sensitive. Two typical floating crane vessels, i.e., a mono-hull vessel and a semi-submersible vessel, are considered to install the DTU 10 MW wind turbine blade. The floating vessels are assumed to be equipped with good dynamic positioning systems to mitigate the slowly varying horizontal motions. Fully coupled time domain simulations are carried out to investigate the dynamic responses of the three blade installation systems, including the motions of the vessel, the crane tip, the installed blade and the blade root, and tension in tugger lines.

The crane tip movement caused by the crane's elastic deformation plays a relatively less important role in blade installation by floating crane vessels, than for the jack-up crane vessel. This is because the crane tip motion on the floating vessels mainly follows the vessels' rigid body motion. The semi-submersible vessel causes much smaller blade motion than the mono-hull vessel. It also causes much smaller variation of the tugger line tension than the mono-hull vessel and the jack-up vessel.

It is feasible to use floating crane vessels to install offshore wind turbine blades provided that the slowly varying motion of floating vessels are well mitigated by the DP system. The feasibility lies in the allowable operational weather window, and is site- and vessel-dependent. Offshore sites with short wave conditions has higher feasibility in floating vessel installation than at sites with long wave conditions. Floating vessels with small wave frequency motion responses are expected to have a higher feasibility. Utilization of weather orientation for floating vessels can greatly reduce the motion of the installed blade and hence increase the feasibility and reduce the operational cost.

Acknowledgment

The authors appreciate the support from the Department of Marine Technology, Centre for Ships and Ocean Structures (CeSOS) and Centre for Autonomous Marine Operations and Systems (AMOS), NTNU. Thanks are extended to Mr. Petter Faye Søyland and Mr. Eric Van Buren in Fred Olsen Windcarrier for valuable input data of and discussions on the numerical modeling of the jack-up crane vessel. Thanks are also extended to Dr. Chenyu Luan for valuable discussions.

Reference

Acero, W. G., Gao, Z., Moan, T., 2017. Methodology for assessment of the allowable sea states during installation of an offshore wind turbine transition piece structure onto a monopile foundation. Journal of Offshore Mechanics and Arctic Engineering 139 (6), 061901.

Ahn, D., Shin, S.-C., Kim, S.-Y., Kharoufi, H., Kim, H.-C., 2017. Comparative evaluation of different offshore wind turbine installation vessels for Korean west-south wind farm. International Journal of Naval Architecture and Ocean Engineering 9 (1), 45–54.

Bak, C., Zahle, F., Bitsche, R., Kim, T., Yde, A., Henriksen, L. C., Hansen, M. H., Natarajan, A., 2013. Description of the DTU 10 MW reference wind turbine. Tech. Rep. DTU Wind Energy Report-I-0092, Technical University of Denmark.

DNV, 2007. DNV-RP-C205 Environmental conditions and environmental loads. Standard, DET NORSKE VERITAS, Olso, Norway.

DNV, 2014. Recommended Practice DNV-RP-H103, Modelling and Analysis of Marine Operations. Standard, DET NORSKE VERITAS, Olso, Norway.

Fred. Olsen Windcarrier AS, 2016. Specifications for Jack-up Installation vessels Brave Tern and Bold Tern. Report, Fred. Olsen Windcarrier AS, Oslo.

Hoerner, S. F., Borst, H. V., 1985. Fluid-dynamic lift: practical information on aerodynamic and hydrodynamic lift. Hoerner Fluid Dynamics, Vancouver, WA.

Horner, S., 1965. Fluid dynamic drag: Practical information on aerodynamic drag and hydrodynamic resistance. Hoerner Fluid Dyn., Midland Park, NJ.

Jiang, Z., Gao, Z., Ren, Z., Li, Y., Duan, L., 2018. A parametric study on the final blade installation process for monopile wind turbines under rough environmental conditions. Engineering Structures 172, 1042–1056.

Jonkman, B. J., 2009. Turbsim user's guide: Version 1.50.

Keseric, N., 2014. Norway's solution: Hywind world's first full scale floating turbine. Report, Statoil.

Ku, N., Roh, M.-I., 2015. Dynamic response simulation of an offshore wind turbine suspended by a floating crane. Ships and Offshore Structures 10 (6), 621–634.

Li, L., Gao, Z., Moan, T., 2015. Joint distribution of environmental condition at five european offshore sites for design of combined wind and wave energy devices. Journal of Offshore Mechanics and Ocean engineering 137 (3), 031901.

Paterson, J., D'Amico, F., Thies, P., Kurt, R., Harrison, G., 2018. Offshore wind installation vessels–A comparative assessment for UK offshore rounds 1 and 2. Ocean Engineering 148, 637 – 649.

Pedersen, E. A., 2012. Motion analysis of semi-submersible. Master's thesis, Department of Marine Technology, Norwegian University of Science and Technology.

Sarkar, A., Gudmestad, O. T., 2013. Study on a new method for installing a monopile and a fully integrated offshore wind turbine structure. Marine Structures 33, 160–187.

Seaway Heavy Lifting, 2018. Oleg strashnov. `https://www.seawayheavylifting.com.cy/vessels/oleg-strashnov`, (Accessed on 04/15/2018).

Shi, W., Park, H.-c., Chung, C.-w., Kim, Y.-c., et al., 2011. Comparison of dynamic response of monopile, tripod and jacket foundation system for a 5-mw wind turbine. In: The Twenty-first International Offshore and Polar Engineering Conference, Hawaii, USA, June 19-24, 2011.

SINTEF Ocean, 2017a. RIFLEX- Theory Manual 4.10.1. SINTEF Ocean, Trondheim, Norway.

SINTEF Ocean, 2017b. SIMO-Theory Manual Version 4.10. SINTEF Ocean, Trondheim, Norway.

SINTEF Ocean, 2017c. SIMO-User Manual Version 4.10. SINTEF Ocean, Trondheim, Norway.

Statoil, 2018. Hywind-the leading solution for floating offshore wind power. https://www.statoil.com/en/what-we-do/hywind-where-the-wind-takes-us.html, (Accessed on 05/01/2018).

Verma, A. S., Jiang, Z., Vedvik, N. P., Gao, Z., Ren, Z., 2018. Impact assessment of a wind turbine blade root during an offshore mating process. Engineering structures (under review).

Wind Europe, 2018. Offshore wind in Europe- Key trends and statistics 2017. Report, Wind Europe.

Zhao, Y., Cheng, Z., Sandvik, P. C., Gao, Z., Moan, T., 2018a. An integrated dynamic analysis method for simulating installation of a single blade for offshore wind turbines. Ocean Engineering 152, 72–88.

Zhao, Y., Cheng, Z., Sandvik, P. C., Gao, Z., Moan, T., Buren, E. V., 2018b. Numerical modeling and analysis of the dynamic motion response of an offshore wind turbine blade during installation by a jack-up crane vessel. Ocean Engineering (under review).

Zhu, H., Li, L., Ong, M., 2017. Study of lifting operation of a tripod foundation for offshore wind turbine. In: IOP Conference Series: Materials Science and Engineering. Vol. 276(1). p. 012012.

A.5 Paper 5

Paper 5:

Explicit structural response-based methodology for assessment of operational limits for single blade installation for offshore wind turbines.

Authors: Amrit Shankar Verma, Yuna Zhao, Zhen Gao, Nils Petter Vedvik

Published in *Proceedings of the 4th International Conference in Ocean Engineering (ICOE 2018)*, Chennai, India, November 4-7, 2018.

Explicit structural response-based methodology for assessment of operational limits for single blade installation for offshore wind turbines

Amrit Shankar Verma[1*], Yuna Zhao[1], Zhen Gao[1], and Nils Petter Vedvik[2]

[1] Department of Marine Technology, Norwegian University of Science and Technology (NTNU) Trondheim, NO-7491, Norway
[2] Department of Mechanical and Industrial Engineering, NTNU Richard Birkelandsvei 2B, NO-7491, Trondheim, Norway
*Contact author : amrit.s.verma@ntnu.no

Abstract. The growing requirements of large size turbines require heavier components to be lifted at larger heights using installation vessels primarily jack-ups and floating vessels. This imposes an inherent and significant risk of impact and contact in the components in particular, when floating installation vessels are used. This is due to excessive wave induced dynamic motion of vessel and its crane tip along with significant motion of the lifted object and could cause significant damage to the lifted blades. Currently, the planning for such weather sensitive operation does not include explicitly the risk of contact/impact or damage in the components to determine the operational limits. Such a study becomes very important for the blade owing to the fact that the blades are made of composite materials and is extremely vulnerable to damage from contact/impact loads. The present paper proposes a novel methodology to determine response based operational limit for the blade installation by considering the structural damage criteria for the lifted blade linked under accidental loads in combination with the global response analysis of the installation system under stochastic wind and wave loads. The methodology is explained further for a case study on the DTU 10 MW reference blade model lifted horizontally using jackup crane vessel with zero degree pitch angle which impacts the pre-assembled turbine tower at the tip region of the blade. The environmental condition with a mean wind speed of 10 m/s was considered. The results further shows that under such conditions, it is safe to install blade from structural damage perspective when no damage level is acceptable in the blade.

Keywords: Offshore wind turbine blade; Operational limits; Contact/Impact behaviour; Marine operation; Jack up vessel; Floating crane vessel

1 Introduction

The average rated capacity of offshore wind turbine has raised by over 62 % in the last decade[1]. Moreover, the latest commercial 8 MW capacity offshore wind turbine has been successfully grid connected for the Dong Energy's Burbo bank extension project at the coast of Liverpool in UK [2]. The hub height for this turbine was around 105 m with length of the blade around 80 m. This requirement of bigger turbines along with large rotor diameters would continue to increase in the near future. This would present a great challenge during the installation phase of the blade using installation vessels owing to the fact that the installation would require larger blades to be lifted to a very large height and would require very high precision [3, 4]. One of the most important challenge can be the risk of impact/contact to the blade especially when being lifted at larger heights using floating vessels where it is expected to get larger wind speed and the vessel exhibits high dynamic motion under the action of waves. This demands improved and optimized methodology to estimate operability limits for planning and execution of such operations especially from a structural safety perspective as the blades are made of composite materials with sandwich configurations and can be in principle quite vulnerable to such undesirable impact/contact events when compared with the components like transition piece and monopile made of steel structures. Steel structure presents a ductile behaviour where as composite material on the other hand exhibits brittle behaviour and most of the energy absorbed during impact is dissipated either in elastic deformation or damage mechanism with not always feasible to visually inspect such damages [5,6]. Moreover, they exhibit quite complex and many simultaneous and interacting failure modes which could affect the residual strength of the blade in different ways [7-9]. Currently, the blades can be installed using jack up crane vessels under mean wind speed of 10 m/s which gives less than 2 months of weather window in the North Sea. Some of the new and advanced installation equipment claim to be able to install the blade till 15 m/s [3, 4]. These improvised installation concepts do not consider the structural damage criteria into account for establishing these operability limits and are mostly based on safe dynamic responses in the system. In principle, these methodology for deriving allowable limits should also guarantee the safety of the components from structural perspective along with the stability of the installation systems. The present paper proposes such a novel methodology which could establish response based operational limits in terms of allowable sea states which would also represent the measure of the safe responses in the system also from a structural safety perspective under such accidental contact/impact loads on the lifted blade.

In the past, *Guachamin Acero, et al. 2016* [10] has proposed a very generic methodology which could derive quite systematically a very practical response based operational limits for any particular installation phase by measuring the responses in the system due to normal environmental loads. Li, et al. 2016 has successfully utilized this approach to study the operability limits for initial hammering process of the monopile using heavy lift floating vessel [12]. *Guachamin Acero, et al. 2016* has also utilized this methodology to derive the operational limits for mating phase of the transition piece with monopile [11]. The methodology proposed by *Guachamin Acero, et al. 2016* also includes some guidelines and procedures which can be utilized to study operability limits based on structural damage criteria for impact/contact risks. However, the criteria recommended in the approach is explicitly suited for the steel components involved in such installation like monopiles and transition pieces. Moreover, it was further studied by *Li, et al. 2014* that the damages to the monopile and transition piece due to impact while installation were not significant at acceptable levels of allowable sea states[13]. This is not true for the blade as *Verma, et al. 2017* has studied that the blade could suffer significant damages and exhibit quite complex failure mode under impact with the tower also at a very low velocity of impact [5]. Thus in order to estimate the operability limits for the installation phase of the blade from a structural safety perspective, it is very important to first understand the damage development in the blade for different impact scenario along with the dynamic motion of the lifted blade and then study the effects of such impact induced damages on their structural integrity to identify allowable and critical damages. The proposed methodology in this paper takes into consideration all these factors and is explained in section 2 of this paper. The methodology is explained with a case study on the DTU 10 MW blade model which is discussed in section 3 and 4. Finally conclusions are presented in section 5 of this paper.

2 Explicit structural response based methodology

The choice of installation method for any offshore wind turbine is the compromise between number of lifts, weight and number of components, water depth of the site and many times availability of the vessels [10]. Split type installation method is one of the most common methods of installing offshore turbines where all the components are individually installed [14]. Fig. 1 presents a very general installation sequence for the components of a typical offshore wind turbine at the offshore site. The installation phase for the offshore wind blade onsets (Operation 5) after the monopile, transition piece, tower, nacelle and hub are successfully installed (Operation 1, 2, 3, 4). In principle, an offshore wind blade is lifted with a crane vessel from the deck and is finally mounted on the hub. Generally, it is horizontally lifted (Fig. 2), tilt lifted or vertically lifted [3, 4]. The most common type of lifting method is the horizontal single blade mounting method [4]. It comes with an advantage that the blade do not require a rotation because the blade are horizontally stored on the deck of the vessel. However, this method of lift presents different choices of pitch angle for the lift (varying from $0°$ to $180°$) (Fig. 3) which again decides variation in lift and drag forces on the lifted blade. This would give varying dynamic responses in the blade as different aerodynamic shaped sections of the blade would be exposed in the wind. It is to be also noted that the behaviour and the nature of loads on the blade during lifting compared to the operational phase are different in nature and would also vary with change in the lift height towards hub [3].

For simplicity, the entire lifting phase of the blade can be divided into three different sub operations/phases (Fig.1,Fig.3). When the blade is lift-up from the deck and is in close vicinity with other structure and equipment (Sub-operation 1), when the blade is in full liftoff phase moving towards the nacelle (Sub-operation 2) and when the blade root part is going towards the hub for

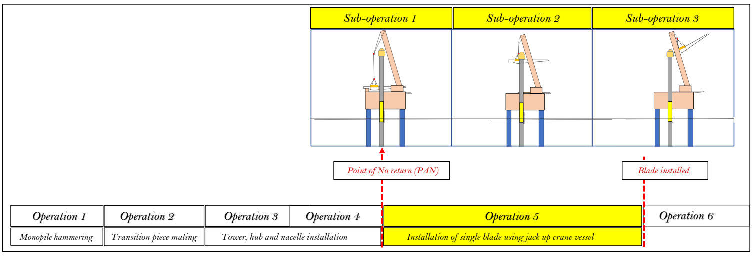

Fig. 1. Different stages of offshore wind turbine installation

Fig. 2. Horizontal lifting of blade [16]

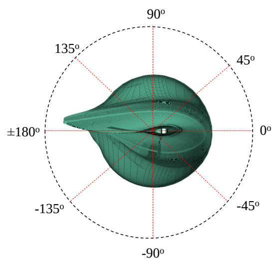

Fig. 3. Pitch angle variation for lifting [4]

the mating phase (Sub-operation 3). These different sub-operations along with varying choices of pitch angle for the lift presents different impact scenarios and contact regions along the blade. For sup-operations 1 and 2, the horizontal lifting with 0° (180°) pitch angle can cause the leading edge or the trailing edge vulnerable to impact whereas lifting with 90° pitch angle can cause pressure or suction side vulnerable (Fig.3) [5]. These scenarios exposes the composite laminate section of the blade (as well as the adhesive joints and the sandwich sections) to impact. However, for sub-operation 3 (Fig.3), the bolts of the blade root section which is made up of steel material and embedded in the composite skin is vulnerable to impact. Also, for sub-operation 1 and sub-operation 2, the impact can occur at any section of the blade and thus different damage behaviour is expected as different sections of the blade has different layups with varying thickness implying varying strength and stiffness. Again, from structural safety perspective, impact induced damages under each sub-operation phase for different exposed region in impact will have varying influence on the strength of blade. The delamination in the composite ply during impact in sub-operation 1 (or 2) can cause sub-laminate buckling and thus effects the buckling strength [7]. However, any damage to the bolts of the blade root region during sub-operation 3 can affect the fatigue life of the blade.

The present paper presents explicit structural response based methodology (Fig.5) which can estimate allowable sea state for the blade installation under accidental contact/impact loads by linking the stochastic global response motion analysis of the installation system (with lifted blade) (Step-1) with the deterministic structural analysis on the blade at different impact locations (Step-2) by estimating the distribution for impact velocity. The deterministic structural analysis considers damage assessment study on the blade (Analysis 2a) along with the residual strength analysis (Analysis 2b) on the damaged blade (Fig.5). The methodology to estimate the operational limits for the installing blade based on this structural damage criteria is described below:

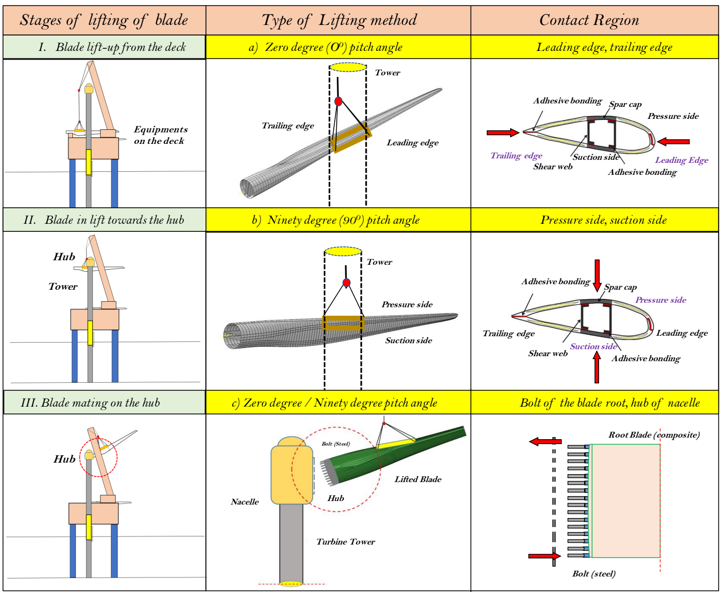

Fig. 4. Different impact scenarios and contact regions possible during lifting

Assumptions and restrictions : The methodology is applied to such cases where the installation philosophy of the wind turbine is assumed to be a split type. It is further assumed that the other components of the turbine like monopile, transition piece, nacelle and hub are successfully installed (Fig.1). It is also assumed that the installation phase of the blade can be regarded as a weather restricted marine operation which is mostly the case. The entire installation phase of the blade is considered to be a point of no return (PAN), meaning that once the blade is lifted, the operation cannot be reversed back (Fig.1). The operational limits can be derived for each sub-operation based on structural damage criteria with relevant impact regions mentioned. The final operational limit for installing blade is the minimum value derived for all the three sub-operations.

Step 1: Stochastic global response analysis of the installation system with the lifted blade: The first step involves the stochastic rigid body global response analysis of the installation system with the lifted blade for a chosen sea state described by a suitable sea state parameter (Hs, Tp, Uw) to determine the relationship between the environmental conditions and the impact velocity (Fig.5). Finally, because of the stochastic nature of the operating environment, for any particular sea state, the distribution for the impact velocity can be obtained. This distribution will be used in connection with the structural impact analysis of blade to determine the distribution of damage energy.

Step 2: Non-linear structural analysis on the blade model: This is an independent step in which, a nonlinear time domain impact analysis (damage assessment study) is performed on a structural blade finite element model for different random impact velocities (Analysis 2a) to obtain the threshold velocity of impact below which there is no damage obtained in the blade as well as to determine the deterministic relationship between damage energy and impact velocity post this threshold value (Fig.5). The operational limit derived based on this threshold value is called ND (No damage) approach where as operational limit derived with some level of damage allowed in the blade is called DT (Damage tolerance) approach (Fig.5). In order to consider the later approach, which facilitate in increasing the operational limit, residual strength analysis on the damaged blade is performed to study the structural behavior of the blade post damage (Analysis 2b) and to determine the deterministic relation between damage in the blade and its residual ultimate strength post impact.

Step 3: Assessment of operational limit: The stochastic nature of the environmental condition implies that for any given sea state, the impact velocity, the blade damage and the residual strength would have a distribution and are linked with each other from the relationship obtained from previous steps. The allowable environmental conditions are the conditions that will lead to the same failure probability which is considered as standard 10^{-4} for unmanned structure. For ND (No damage approach), the failure probability is estimated by assuming an acceptable limit of the threshold value of impact velocity and for DT (damage tolerance) approach the failure probability is estimated based on allowable strength reduction of 5% in the blade post impact from the distribution of residual strength obtained from previous step. The sea state parameters for which the failure probability is less than 10^{-4} is considered allowable.

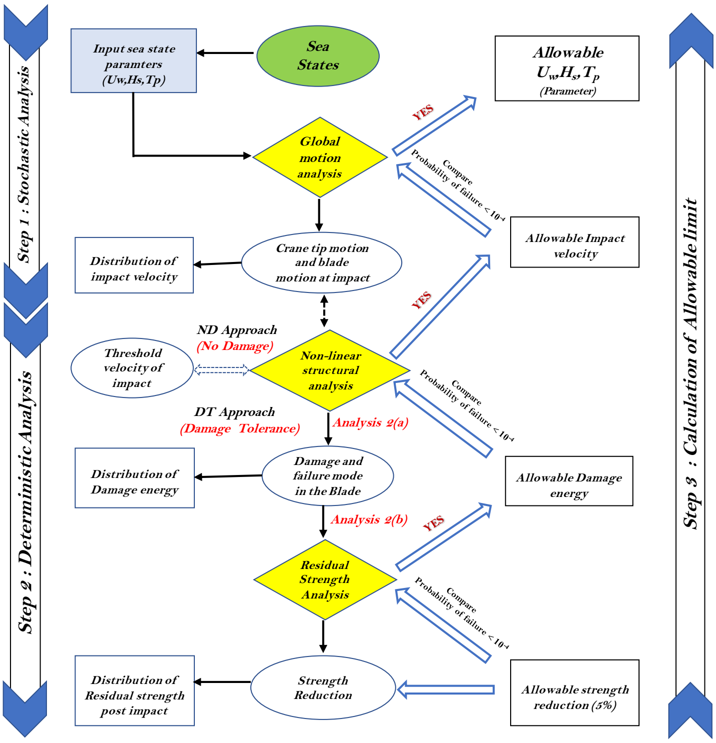

Fig. 5. Explicit structural resposne based methodolgy

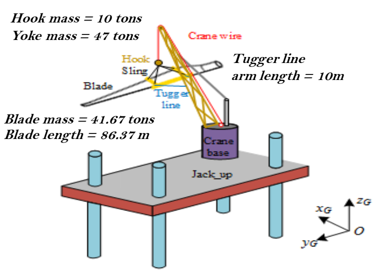

Fig. 6. Global response analysis of the installation system in SIMO-Aero [3]

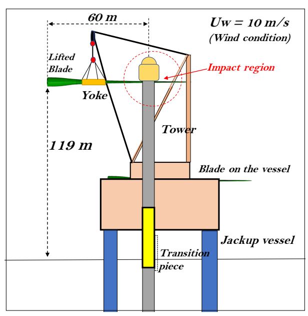

Fig. 7. Case study- Sub-operation 2 of the installation phase

3 Case study

The present paper illustrate the above mentioned methodology for the *sub-operation 2* of the blade installation (Fig.7) where the DTU 10 MW blade [15] lifted in a turbulent wind with zero degree pitch angle using a jackup crane vessel suffers a contact at the tip region of the blade (60 m from root, along the leading edge) with the tower at the installation height of 119 m. The reason for choosing this section of the blade as the impact region is because this region has the least laminate thickness (18 mm, Fig.11) and is more sensitive to damage from impact for the same level of impact energy compared to the other regions along the leading edge. The turbulent wind chosen for installation in the case study has a mean wind speed of 10 m/s and turbulence intensity of 15.72%. The complete illustration of the explicit response based methodology based on damage tolerance (DT) approach is out of the scope of this paper and the paper focuses on the estimating whether the chosen turbulent wind with Uw =10 m/s is safe for blade installation or not based on ND (No damage) approach.

4 Analysis, results and discussion

As per the methodology, the first step is the stochastic dynamic motion response analysis of the installation system (Fig.6). Steady state time domain simulations were carried out by coupled Aero-Hydro-Mechanical code, i.e., SIMO-Aero [3] to calculate the dynamic characteristics of blade motion during installation. The installation system includes a crane vessel, the blade to be installed, yoke and the hook modelled as rigid body (Fig.6). A simplified non-linear spring model was used to model the tugger lines under constant tension control. In this study, the target mean tension in the tugger lines is 80 kN. SIMO-Aero accounts for hydrodynamics of the installation vessel, mechanical couplings among bodies in the system and aerodynamics of the lifted blade. Moreover, it was assumed that the jackup vessel was rigidly sited on the seabed without any motion (Hydro module was unchecked). Details regarding the lift wire and slings could be found in Ref [3]. A set of 30 steady state time domain simulations were run in turbulent wind conditions (Uw =10 m/s, Iz=15.72%) to get the characteristics of the impact velocity. Each simulation has a duration of 1100 s with the first 100 s removed to exclude transient effect. The total duration of data was 30,000 s. It was found that the motion of the blade is dominating in the x-direction and thus the velocity in x-direction was chosen for further study. The maximum velocity (Vx) in each 500s (60 data points) were selected for extreme distribution analysis and were fitted to Gumbel probability plot which showed good fit (Fig.8) The parameters for the distribution were further estimated based on method of moments and is reported as (μ= 0.0241 and β = 0.0017). Fig.9 shows the extreme value probability density function (PDF) for the impact velocity of the blade based on the above parameters for the particular chosen wind condition. These distributions connects stochastic analysis with deterministic analysis.

After the distribution of the characteristics of the motion of the lifted blade is obtained, the next step is the non-linear time domain impact analysis on the

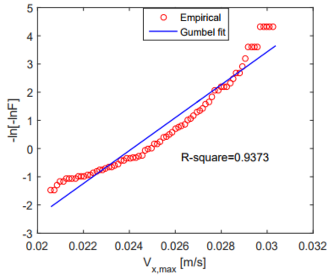

Fig. 8. Fitting of data for the velocity into Gumbel probability paper

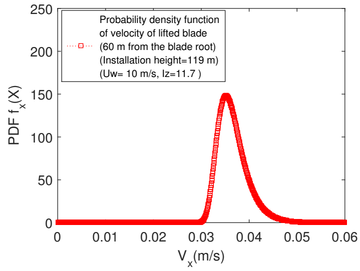

Fig. 9. Extreme value distribution of impact velocity of the blade (PDF)

blade. Fig. 10 and Fig. 11 shows the contact scenario (bird view) and the composite layup respectively for the impact location (A, 0.68<r/R<0.71) considered for the structural analysis in ABAQUS explicit environment. The numerical modelling details for the blade along with the damage criteria and the non linear material and contact formulation implemented in this study can be found in [5].

The first step for this damage assessment study (Analysis 2a) is to find the threshold velocity of impact below which there is no initiation of damage in the blade. The blade was given initial velocity of impact starting at a very low velocity (Fig.14). It can be seen that for the case of 0.08m/s, none of the ply in the laminate has reached Hashin failure criterion equal to one (Fig.12). This indicates that the damage initiation criteria has not been met and there was no damage in the blade which is consistent with the results for the damage energy presented in Fig.14. However, for the case of 0.095m/s, Ply no.2 (Fig. 13) has HSNMCCRT (matrix compression failure) criterion equal to one which confirms our understanding that the damage has initiated in the blade and there is development of damage energy as shown in Fig. 14. From the above discussion it can be said that the damage threshold velocity would lie somewhere below 0.095 m/s (Fig.14). From further analysis, it was found that 0.094 m/s is the threshold velocity of impact and any impact velocity above it would initiate the damage.The threshold velocity of impact obtained from this study (0.094 m/s) can now be utilized to calculate the operability limit based on reliability based approach explained before. It was found that the exceedence probability calculated based on this threshold value from the extreme value distribution (Fig.9) is of the order 10^{-6} and was very less than the acceptable limit of 10^{-4}. Thus from this observation, it can be said that the average mean wind speed of 10 m/s is safe for blade installation from structural damage perspective when no damage (ND) approach (i.e allowing no damage in the blade even after impact and setting a limit before initiation of damage onsets) is applied.

Further, in order to utilize the damage tolerance approach, it is very important to understand and estimate the dependency of damage energy with velocity

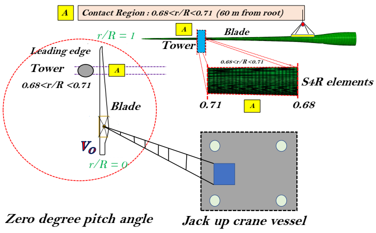

Fig. 10. Impact scenario and contact region considered for damage analysis (bird view)

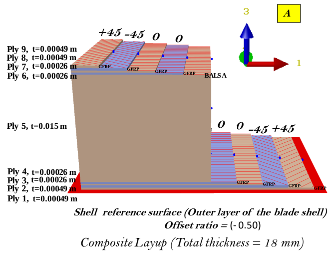

Fig. 11. Composite Layup at the contact region $[+45/-45/0_2/\mathrm{Balsa}]_s$

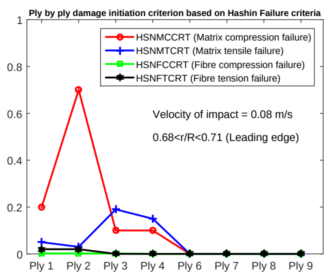

Fig. 12. Ply by Ply Hashin failure criterion (a) 0.08 m/s (No damage initiation)

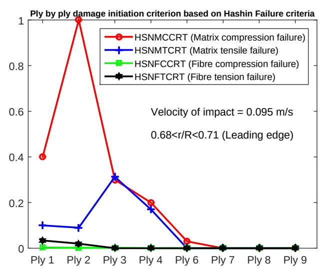

Fig. 13. Ply by Ply Hashin failure criterion (b) 0.095 m/s (Damage initiation)

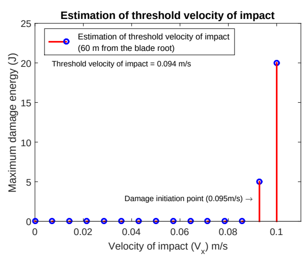

Fig. 14. Estimation of threshold velocity of impact (No damage approach)

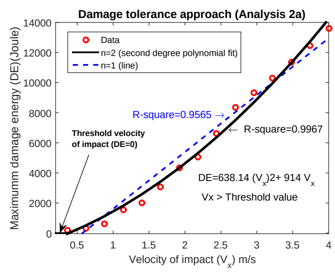

Fig. 15. Estimation of dependency of damage energy with the velocity of impact post damage threshold velocity (Damage tolerance approach)

of impact post threshold impact velocity. For this, the blade was given further translational velocity of impact ranging from 0.1 m/s to 4 m/s. Fig.15 presents the maximum damage energy developed in the blade for these impact velocities. The maximum damage energy obtained for each case were fitted to a straight line as well as second degree polynomial fit to describe the best fit with later describing the data more accurately. After the relation between damage energy and impact velocity is determined ($638.14V_x^2 + 914V_x$) distribution of damage energy can be obtained from the transformation of variables from the extreme value distribution of the velocity (Vx) obtained from Step 1 (stochastic analysis). However, one important note to consider here is that this relation between the distribution of damage energy and impact velocity is highly dependent upon the composite layup plan, details for the numerical model and will also vary with the choice of blade and thus require a broader statistical distribution utilizing large variety of blade or laminate layup sequence. This can be quite challenging as very limited no of blade are available in research domain like Sandia 100 m blade, DTU 10MW reference blade model. Alternatively, an experimental investigation on the blade could give some real time reference data to compare. Moreover, such an approach is very important especially when the industry plans to go into deeper water and would require floating vessel to install the blade which would present these accidental impact events with a higher impact velocity as they will be also influenced by wave induced motion.

5 Conclusions

This paper presented a novel explicit structural response based methodology to investigate the operational limit for the single blade installation by emphasizing the importance of structural safety for the blade in installation linked under accidental loads. The methodology mentioned in the paper maps the stochastic motion analysis of the installation system with different choices of pitch angle for the lifted blade with the deterministic structural analysis for impact/contact at different blade sections and finally calculates the operational limit based on reliability based approach. The methodology broadly mentions two different categories for calculation of such limits. The first category involves the No damage (ND) approach where the operational limits are calculated based on threshold impact velocity with no damage allowed in the blade. Another category is based on the damage tolerance (DT) approach which involves the utilization of residual strength of the blade post impact and can be applied further when the industry plans to extend its operational limit. The paper also illustrates the mentioned methodology based on ND approach for the DTU 10 MW blade model lifted horizontally with jackup crane vessel for zero degree pitch angle under mean wind speed of 10 m/s which impacts the tip region of the leading edge of the blade almost at the nacelle height. The global response analysis was performed in SIMO Aero along with structural impact analysis in ABAQUS Explicit. Further, it was found that the blade was safe to install from structural safety perspective in such a wind condition if such accidental contact/impact event occurs.

6 Acknowledgement

This work was made possible through the SFI MOVE projects supported by the Norwegian Research Council, NFR project number 237929.

References

1. W. Europe, "Key Trends and statistics of the the European offshore wind industry 2016."
2. M. V. O. WIND, "First V164-8.0 MW turbine installed at Burbo Bank Extension," http://www.mhivestasoffshore.com
3. Y. Zhao, Z. Cheng, P.C Sandvikd ,T. Moan and Z. Gao, "An integrated dynamic analysis method for simulating installation of a single blade for offshore wind turbines " (Inpress) Ocean Engieering 2017.
4. L. Kuijken, "Single Blade Installation for Large Wind Turbines in Extreme Wind Conditions," Master of Science Thesis, Technical University of Denmark
5. A. Verma, Z. Gao, and N. Vedvik, "Numerical assessment of wind turbine blade damage due to contact/impact with tower during installation," (In press),COTech -Computational methods in Offshore Technology, University of Stavanger (UiS), 2017
6. S. Agrawal, K. K. Singh, and P. Sarkar, "Impact damage on fibre-reinforced polymer matrix compositea review," Journal of Composite Materials, vol. 48, no. 3, pp. 317-332, 2014.
7. P. U. Haselbach,"Ultimate Strength of Wind Turbine Blades under Multiaxial Loading," *Ph.D Thesis*, DTU Wind Energy, 2015.
8. H. G. Lee, M. G. Kang, and J. Park, "Fatigue failure of a composite wind turbine blade at its root end," Composite Structures, vol. 133, pp. 878-885, 2015.
9. M. McGugan, G. Pereira, B. F. Srensen, H. Toftegaard, and K. Branner, "Damage tolerance and structural monitoring for wind turbine blades," Phil. Trans. R. Soc. A, vol. 373, no. 2035, p. 20140077, 2015.
10. W. G. Acero, L. Li, Z. Gao, and T. Moan, "Methodology for assessment of the operational limits and operability of marine operations," Ocean Engineering, vol. 125, pp. 308-327, 2016.
11. W. G. Acero, Z. Gao, and T. Moan, "Methodology for assessment of the allowable sea states during installation of an offshore wind turbine transition piece structure onto a monopile foundation," Journal of Offshore Mechanics and Arctic Engineering.
12. L. Li, Z. Gao, and T. Moan, "Operability analysis of monopile lowering operation using different numerical approaches," International Journal of Offshore and Polar Engineering, vol. 26, no. 02, pp. 88-99, 2016.
13. C. Li, Z. Gao, T. Moan, and N. Lu, "Numerical Simulation of Transition Piece-Monopile Impact during Offshore Wind Turbine Installation," in The Twenty-fourth International Ocean and Polar Engineering Conference, 2014: International Society of Offshore and Polar Engineers.
14. W. Wang and Y. Bai, "Investigation on installation of offshore wind turbines," Journal of Marine Science and Application, vol. 9, no. 2, pp. 175-180, 2010.
15. C. Bak; F. Zahle; R. Bitsche; T. Kim; A. Yde; L.C. Henriksen; P.B. Andersen; A. Natarajan, M.H. Hansen; Design and performance of a 10 MW wind turbine, J. Wind Energy, To be accepted.
16. Picture taken from London array website http://www.londonarray.com/the-project-3/offshore-construction.

A.6 Report 1

Report 1:
Assessment of operational environmental limits for offshore single blade installation using response-based criteria.
Authors: Yuna Zhao, Zhen Gao, Torgeir Moan, Peter Christian Sandvik.
Report, Norwegian University of Science and Technology, 2019.

Assessment of operational environmental limits for offshore single blade installation using response-based criteria

Yuna Zhao[a,b,*], Zhen Gao[a,b], Torgeir Moan[a,b], Peter Christian Sandvik[c]

[a] *Centre for Autonomous Marine Operations and Systems (AMOS), NTNU, NO-7491 Trondheim, Norway*
[b] *Department of Marine Technology, NTNU, NO-7491 Trondheim, Norway*
[c] *PC Sandvik Marine, Trondheim, Norway*

Abstract

Installation of offshore wind turbine blades needs detailed planning to increase efficiency and reduce costs. Well assessed operational limits, with respect to both wind and wave conditions, can greatly assist the planning of such operations. This study presents an approach for assessing the operational environmental limits of offshore single blade installation. The approach combines the general installation procedure, identification of critical events and limiting response parameters, and detailed modelling of the installation system. The final blade mating operation is most crucial. The critical events are identified to be the guide pins not entering the hub in the monitoring phase before mating, and bent guide pins during the mating phase. The limiting response parameters are respectively the blade root motion relative to the hub radial direction for the former and the blade root radial velocity for the latter. The criterion of blade root motion is assumed for demonstra-

*Corresponding author
Email address: `yuna.zhao@ntnu.no` (Yuna Zhao)

tion while that of blade radial velocity is obtained via finite element analysis of the collision event. More effects need to be considered in these criteria during practical offshore installation. The characteristic values of the limiting response parameters are calculated by stochastic time domain analysis using the coupled numerical model of the installation system. The model accounts for blade aerodynamic loads, vessel hydrodynamics, crane flexibility and lifting arrangements. Based on the characteristic values of the limiting parameters and corresponding criteria, the approach to find the allowable environmental conditions is discussed. Demonstration of the approach is carried out using a simple case study with a DTU 10MW wind turbine blade installed by a semi-submersible crane vessel onto a jacket wind turbine.
Keywords: Offshore wind turbine blade installation, final mating phase, critical events, limiting parameters, dynamic motion response, assessment of operational environmental limits

---

1. Introduction

The offshore wind energy industry has developed fast in recent years. The global cumulative capacity of offshore wind increased by 300% from 2011 to 2017, reaching 19GW in 2017 (Global Wind Energy Council, 2018). The capacity and size per wind turbine also experience a fast increase, from 3MW to 8MW or even larger, such as recently announced Haliade-X 12MW (GE Renewable Energy, 2018). The increase in turbine capacity implies increasing turbine size and hub height, as shown by the comparison of turbine capacity and blade dimensions for various offshore wind turbines in Table 1. These developments represent increasing challenges to the installation of offshore wind turbines.

Table 1: Offshore wind turbine capacity and blade dimensions

Turbine model	Capacity	Blade weight	Blade length	Hub height	Reference wind farm
Bonus B76/2000 (Wind-turbine-models, 2012)	2MW	6.5tons	36.5m	64m	Middelgrunden
Siemens SWT-3.6-107 (Siemens, 2015)	3.6MW	15.8tons	52m	83.5m	Burbo Bank
Senvion 5MW (Alpha ventus, 2015)	5MW	20.8 tons	61.5m	92m	Alpha Ventus
Vestas V164-8.0MW(Vestas, 2012)	8MW	35tons	80m	105m	Burbo Bank Extension
DTU 10MW(Bak et al., 2013)	10MW	41.7tons	86.4m	119m	Research model
Haliade-X 12MW (GE Renewable Energy, 2018)	12MW	Unknown	107m	150m	Recently announced

Offshore wind turbine components are typically installed separately and in sequence by lifting operations using offshore crane vessels. The unstable offshore environmental conditions induce significant motions in the installation system, leading to high risks, low installation efficiency and high costs. Particularly, the wind turbine blades are fragile and require high installation precision. The rapid increases in turbine blade size, weight and installation height make the installation process more difficult to conduct. Under such circumstances, it is important to establish advanced numerical models to study the dynamic characteristics of offshore wind turbine blade installation, to assess the allowable operational limits and to predict the available weather windows.

To date, there are a few numerical studies on offshore wind turbine blade installation. An integrated dynamic analysis method for simulating installation of a single blade for wind turbines has been developed and applied to study the dynamic blade motion response during installation using jack-up and floating crane vessels by Zhao et al. (2018a, 2019, 2018b,c). The coupled method accounts for blade aerodynamics, vessel hydrodynamics, crane flexibilities and system mechanical couplings. The vessels' (even jack-ups) motion and crane deformation were found to have significant contributions to the motion of the installed blade. Jiang et al. (2018) studied the blade installation process for a monopile supported offshore wind turbine and found that the monopile hub motion can be important at certain wave periods when a resonant response is excited in the monopile. When different types of support structures are considered, the hub motion differs. Compared to monopiles, the hub motions of jackets and tripods supporting the same-size wind turbines are much smaller (Shi et al., 2011). Verma et al. (2018) studied the installation process with respect to blade structural integrity if collisions occur between blade root and hub using advanced finite element methods. The results give references on structural response criteria that causes no damage in blade during installation.

Based on numerical modelling and analysis of offshore single blade installation, the operational limits can be established, considering the limiting criteria and the safety factors. The operational limits can be expressed in terms of environmental conditions which can be tracked prior to and during execution of operations. Typically, the operational limits vary from operation to operation, due to differences in operational requirements and in system characteristics. For instance, the operational limits for wind turbine support structure installation are mainly dependent on wave conditions (Li et al., 2016b). However, for wind turbine blade installation, wind condition is also important since it causes significant aerodynamic loads on the installed blade, leading to notable influence on the installation.

To assess the environmental limits for offshore wind turbine installation, a generic methodology was developed by Acero et al. (2016a) and applied to establish the operational limits of transition piece mating (Acero et al., 2017), monopile hammering (Li et al., 2016a) and fully assembled turbine installation (Acero et al., 2016b). In those applications, only waves were considered as the main source of loads. When assessing the operational limits of wind turbine blade installation, both wind and wave conditions need to be considered.

In this study, a systematic approach to assess the operational limits based on response criteria for offshore blade mating operation is presented. A general description of the wind turbine blade installation procedures is given. The critical events and corresponding limiting parameters are identified. The allowable environmental limits for the blade final mating phase are established based on a fully coupled numerical model. Safety factors are not accounted for. The approach is demonstrated by a case study considering single blade installation for a jacket wind turbine by a semi-submersible crane vessel. The hub motion of a typical jacket wind turbine is assumed small and hence not considered in this study.

2. System components

The system for offshore single blade installation typically consists of crane vessel, wind turbine blade and lifting arrangement, as illustrated in Figure 1. The lifting arrangement includes lift wire, hook, slings, yoke and tugger lines. The tugger lines control the blade orientation during installation. Numerical modelling of typical blade installation systems is discussed in Section 6.

Figure 1: Illustration of system components for offshore single blade installation (DEEPWATER WIND, 2019) (Note: the jack-up vessel graphically represents the crane vessel in the system components. A floating crane vessel is used in the case study.)

3. Installation procedures

The wind turbine blades are typically transported on board the installation vessel and are installed using lifting operations, as shown in Figure 1. The installation procedure is summarized into the following steps:

Step 1. The blade is loaded in the yoke. The blade yoke is lifted off the vessel deck by running the crane winch.

Step 2. The blade is lifted to the installation height. The orientation of the blade is controlled by the pre-tensioned tugger line system

Step 3. The blade approaches the turbine hub by operating the crane. The blade is suspended in a safe position, minimizing risk for impacts.

Step 4. The crane and the tugger lines are adjusted to ensure good alignment of the blade root with the hub opening. The blade root motion is monitored to decide whether the mating operation is possible or not.

Step 5. Once mating is expected to be possible, the blade root is mated into the hub.

Figure 2 shows a detailed view of the blade mating operation.

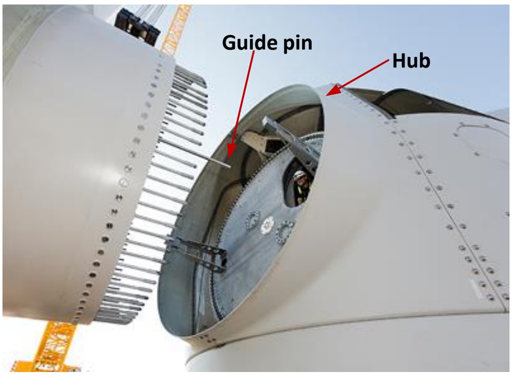

Figure 2: Final mating operation of blade onto turbine hub (Siemens, 2012)

4. Critical events and limiting response parameters

Among the blade installation activities, steps 4 and 5 are critical. The motion monitoring phase, i.e., step 4, is pre-requisite for the mating operation. A mating attempt is considered to be successful if the guide pins manage to enter into the hub opening. The critical event is failure of mating attempts due to excessive radial blade root motion. The physical limit is the radial mating gap. The corresponding limiting response parameter is the blade root motion in the hub opening's radial direction which is named as blade radial motion in this report for simplicity. The entering is considered to be possible when the guide pins outcrosses the mating boundary, i.e., the hub opening within an acceptable crossing rate range. If the blade root outcrosses the mating boundary too frequently, mating attempts are not likely to be successful.

During the mating phase, structural damage in blade root guide pins may occur when the blade root collides with the hub. Particularly, radial impacts are much more critical than axial impacts. Because radial impacts may result in bent guide pins, leading to failure of mating operation. Thus, the physical limit is no plastic bending deformation in guide pins. The critical event of the operation is bent guide pins. The limiting response parameter can be taken as the radial impact velocity.

In addition, the structural integrity in wires and ropes needs to be ensured during the whole operation. On one hand, the maximum wire tension should be within the wire design capacity. The wires are assumed to have sufficient capacities since they are also used to install much heavier wind turbine components such as nacelles. On the other hand, slack in wires should be avoided, especially in tugger lines. The lift wire and slings are found to be always tensioned during the operation due to the gravity of the installed blade. Slacks in tugger wires can be avoided by adjusting the pretension, they are considered as a restrictive event.

A summary of the critical events and limiting response parameters are listed in Figure 3.

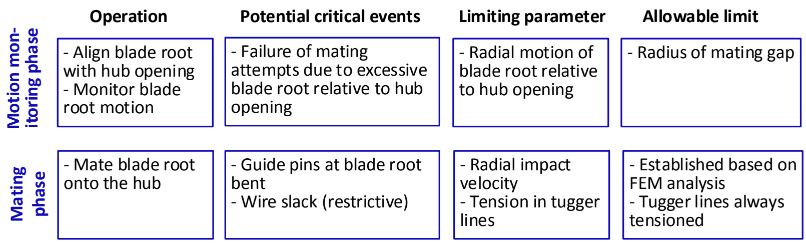

Figure 3: Potential critical events, corresponding limiting parameters and allowable limits for the blade mating operation

5. Methodology

The detailed procedure for establishing operational environmental limits for offshore single blade installation is given in this section.

First of all, the potentially restrictive and critical events are identified based on the system configuration, installation procedure and numerical modelling of the sequentially defined installation activities. Then the response parameters which will limit the operations in the critical events are identified and their corresponding criteria (allowable maximum responses) are determined. By comparing the characteristic values of the limiting response parameter with its criteria, the operational environmental limits for each critical event can be identified in various environmental conditions. The characteristic value of a response parameter, which can be estimated using numerical modelling and analysis, is the response value at a certain exceedance probability so that the safety of different operations can be directly compared.

In principle, safety factors need to be considered in the operational limits due to uncertainties, for instance, from numerical modelling and human actions in practical operations. However, safety factors are not considered in this study.

5.1. Criteria of the limiting response parameters for blade mating

In the monitoring phase, mating attempts are assumed to be possible as long as the blade root can enter the hub opening. Detailed operation procedures after that for the entering are not considered in this study. The allowable limit is the annular mating gap between the hub opening and the blade root, as illustrated in Figure 4. In practical operations, the size of the annual gap depends on the dimensions of the blades and the turbine hub.

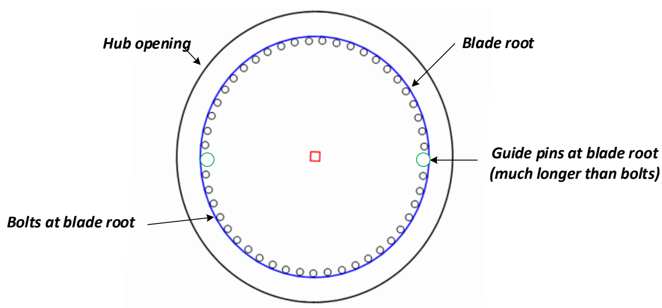

Figure 4: Illustration of the blade mating gap

In the mating phase, it is important to ensure that deformation of the guide pins are elastic and no permanent bent damage occurs when they collide with the hub opening. The impact velocity can be considered as a representative response parameter. Due to the blade's structural non-linearity, the corresponding criteria, i.e., the maximum allowable impact velocity needs to be established based on FEM analysis of the impact scenario, which has been studied by Verma et al. (2018).

5.2. Characteristic values of the limiting parameters

For the blade installation system, the system components are strongly coupled. Besides, both wind and wave excitations are important for such installation activities.

The dynamic responses of the identified limiting parameters need to be calculated based on time domain coupled analysis of the operational scenario. Repeated runs with different random seeds are needed in the time domain analysis to reduce statistical uncertainty. This has been considered in the case study in Section 7.

The characteristic values of the limiting parameters can be derived on the basis of extreme value distribution using either exceedance probability or target percentile. The exceedance probability is dependent on the consequences of failure events. In the monitoring phase, the mating attempts can always be tried again. Thus, the consequence of failure is relatively less severe and a larger exceedance probability can be designed. However, damaged guide pins in the mating phase lead to expensive repairs, delay of operations and hence additional costs. Therefore, a small exceedance probability should be considered. Specific values of the exceedance probabilities may vary from operation to operation due to the installation conditions and requirements. The values of exceedance probabilities used in this study are given in Section 7.

5.3. Operational environmental limits for the complete mating operation

The complete blade mating operation consists of the motion monitoring phase and the mating phase. The operational limits of environmental conditions for each of these two activities can be identified by comparing the characteristic value of the limiting parameter with the corresponding allowable limit, under various possible environmental conditions. By combining the environmental limits of both activities and taking the lower envelope, the limits for the complete operation can be obtained. It is assumed that the environment is unchanged since the mating time is considered to be short.

The procedures are summarized in the flowchart shown in Figure 5. It is established based on stationary time domain analysis where the transient effects, such as , transient effects such as entry and exit of the blade root into the hub, and guide pins fail to enter the hub due to transient motion of the blade caused by guide pin impact forces, are not considered at this stage. Such transient effects may lead to reduced environmental limits.

6. Numerical modelling of offshore single blade installation

An integrated numerical model is important for time domain analysis of offshore wind turbine blade installation. In the numerical model, modelling of vessel and crane is essential, in addition to the direct model of blade motion under wind loads. Due to the large lifting height, the vessel motion under wave loads and crane deformation can cause significant blade motion during installation.

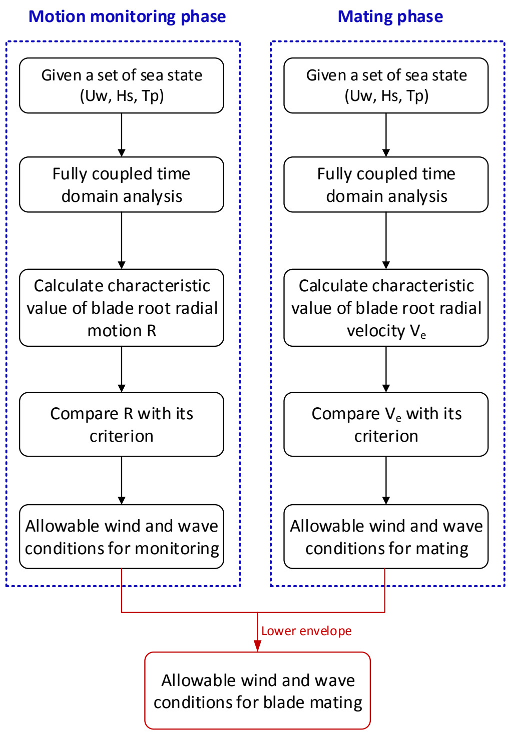

Figure 5: Flowchart of assessing allowable wind and wave conditions for the blade mating operation. The criteria are based on the deterministic geometrical constraints of the mating boundary and the deterministic strength parameters of the structures.

6.1. Modelling of installed blade and the lifting arrangement

During numerical modelling, the structural flexibility of the wind turbine blade can be neglected since it has minor influence on the blade's dynamic motion response during installation (Zhao et al., 2018b). Thus, the blade can be modelled as a rigid body. The aerodynamic loads on the blade are important and need to be considered. The characteristics of aerodynamic loads on a blade during installation are quite different from those of a rotating blade. The cross-flow principle (Hoerner and Borst, 1985) has been used to calculate the aerodynamic loads on a installed blade. In the computation of aerodynamic loads, it is important to consider the blade motion which is an important source of damping. Details of the aerodynamic load calculation of a single blade during installation are described in Ref. (Zhao et al., 2018b).

The blade is held by a yoke rigidly during installation. They can be considered as one body in the numerical model. The hook is represented by a point mass. The lift wire and slings are modelled as flexible bar elements with equivalent stiffness and damping properties. Tugger lines are used for blade heading control which run from the yoke to a trolley on the crane boom. Pretension is applied in tugger lines to prevent slack lines. The tugger line tension is modeled as bi-linear spring force (Zhao et al., 2018b).

6.2. Modelling of vessel and crane

For floating crane vessels, the wave-induced motions are significant. The slowly varying motions can be well mitigated by using dynamic positioning (DP) systems. While the wave-frequency motion responses plays an important role (Zhao et al., 2019).

In addition to the vessel motions, deformation of crane also contributes to the motion of the blade being installed. Thus, it is essential to model the structural flexibility of the crane. Take pedestal cranes as an example, the deformation is mainly resulted from boom wires, rather than the crane boom. The crane flexibility is relatively less important for floating crane vessels than for jack-up crane vessels (Zhao et al., 2019).

More detailed discussion about the advanced modelling of offshore single blade installation are discussed in Ref. Zhao et al. (2019, 2018b,c).

7. Case study

In this section, the methodology is demonstrated by using the scenario that a semi-submersible crane vessel installing a DTU 10MW wind turbine blade onto a jacket foundation located at water depth of 39m. Figure 6 shows an illustration of the system. Table 2 lists the main parameters of the vessel, crane, blade and lifting arrangement. Typically, jacket wind turbines have relatively small hub motion. Hence, the hub motion is not considered in the case study.

Table 2: Main parameters of the blade installation system (detailed parameters of the jacket wind turbine support structure is not given since it is assumed to be rigid with neglecting hub motion)

	Parameters	Value	Parameters	Value
Vessel	Length [m]	175	Breadth [m]	87
	Draught [m]	26.1	Displacement [m^3]	1.638×10^5
Crane	Boom length [m]	107.6	Boom angle [deg]	67.6
	No. of boom wires [-]	2	Boom wire stiffness [kN/m]	9048
	Boom wire damping [kNs/m]	90.5		
Blade	Mass [tons]	41.67	Length [m]	86.37
	Hub height [m]	119	Root radius [m] 2.69	
Lifting arrangement	Length of crane wire [m]	4.7	Length of slings [m]	20.4
	Tugger line arm length [m]	10	Length of tugger line [m]	5.7
	Stiffness of tugger line [kN/m]	525	Hook / Yoke mass [tons]	10 / 47

For the motion monitoring phase, the mating attempts are assumed to be possible as long as the guide pins enter the hub opening. Failure of

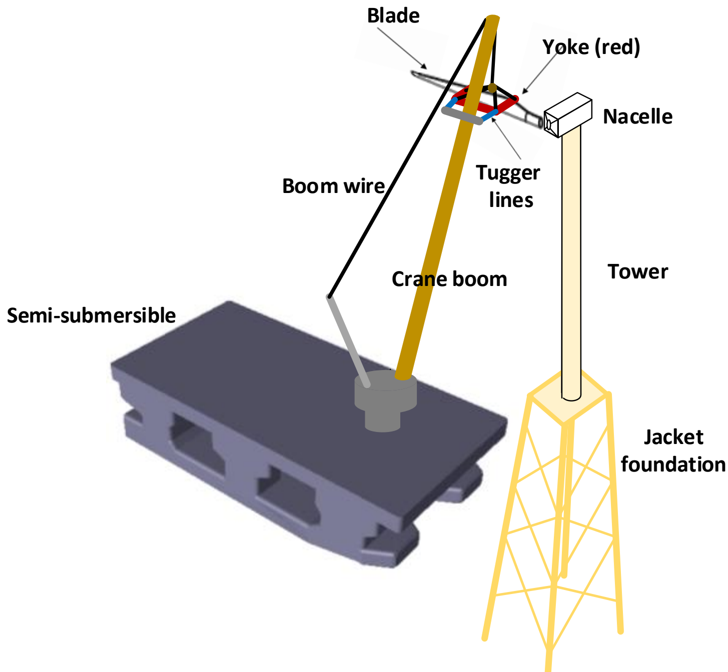

Figure 6: Illustration of offshore single blade installation system (The system is simply for demonstration purpose. The components' dimensions are not in scale.)

mating attempts will not lead to structural failure, it decides whether or not the installation should continue for the rest of the mating operation. The corresponding criterion is the mating gap which is the difference between the hub radius and blade root radius. The actual value of the criterion is dependent on turbine size and turbine design. In this case study, it is assumed to be proportional with the radius of blade root:

$$r = \lambda R_{root} \tag{1}$$

where λ is a factor assumed to be around 10%~20% for demonstration purposes, due to unavailability of practical and reliable data. The characteristic value of blade root radial motion (R) is quantified based on average outcrossing rate which has been frequently used for mating boundary issues (Acero et al., 2017; Jiang et al., 2018). It is assumed that the mating is possible if the blade root crosses the circular boundary once per minute. More accurate value can be assigned based on specific operations. The characteristic value of the blade root radial motion is the value corresponding to a mean upcorssing rate of $\nu^+ = 0.0167$, as illustrated in Figure 7.

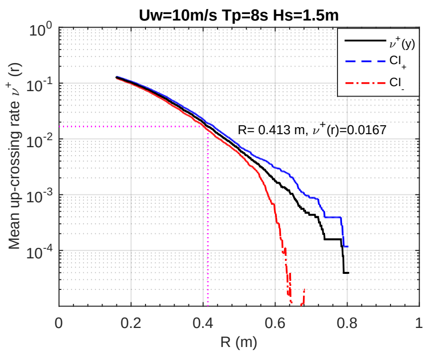

Figure 7: Example of getting characteristic values of blade root radial motion based on mean upcrossing rate. Legends: time domain simulation(-), empirical 95% confidence band (——, −·−·).

In the blade mating phase, it should be ensured that plastic bending deformation (damage) occurs in the guide pins. The limiting response parameter can be taken as the blade radial velocity. The maximum allowable impact velocity is found to be around 0.7m/s, based on non-linear finite element analysis of the impact scenario of DTU 10MW wind turbine blade by

Verma et al. (2018). The consequence of a possible damaged guide pins is significant. It requires to bring the blade back to deck of the installation vessel and needs repair or replacement of guide pins, leading to delayed operation and extra costs. The probability of occurrence is limited to 10^{-4}, which is a representative value for typical marine operations, according to DNV-OS-H101 (DNV, 2011). The characteristic value of blade root radial impact velocity (V_e) is taken as the 10-min extreme value with a exceedance probility to 10^{-4}. Figure 8 shows an example. The results do not include any memory effect following the impact since modeling of impacts between the blade root and hub is not accounted for. Safety factors are not addressed in this study and a value of 1.0 is assumed.

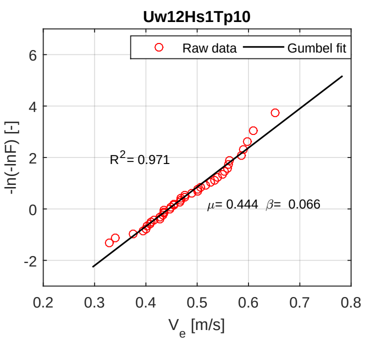

(a) Gumbel probability paper

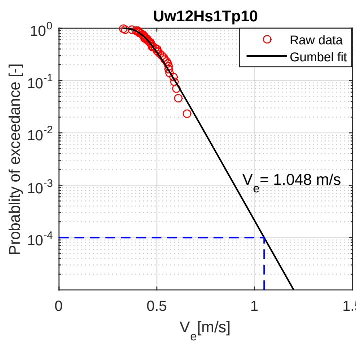

(b) Probability of exceedance

Figure 8: Example of getting blade root radial velocity based on Gumbel distribution fit and extrapolation technique: $U_w = 12m/s$, $T_p = 10s$ and $H_s = 1m$.

7.1. Dynamic response

Time domain system dynamic response analysis are carried out, under various combined wind and wave conditions, to identify characteristic values of limiting parameters which may reach the dangerous level.

A wide range of wind and wave conditions are considered. The mean wind speed at hub height varies from 2 m/s to 12 m/s in steps of 2m/s. The significant wave height varies from 0.5 m to 3.0 m in steps of 0.5 m and the wave peak period varies from 4 s to 12 s in steps of 2 s. The wind inflow angle is $\theta_{wd} = 0 \ deg$. The incident wave angle is $\theta_{wv} = 285 \ deg$, slightly off head sea.

The characteristic values of R and V_e under various wind and wave conditions are shown in Figures 9(a) and 9(b) respectively. Both R and V_e increase with the increasing wave peak period. In short waves ($T_p \leq 8s$), both R and V_e increase with increasing wind speed, indicating that wind is the dominant excitation. In long waves, they decrease with the increasing wind speed. Hence, the aerodynamic loads act as damping, compared to the significant contributions of wave-induced vessel motion.

The dynamic tension in tugger lines are checked against slacks in lines. Figure 10 presents example statistics of the tugger line tensions. It is found that the tugger lines remain in tension under typical allowable operational sea states. These sea states are selected based on the allowable operational limits discussed in Section 8.

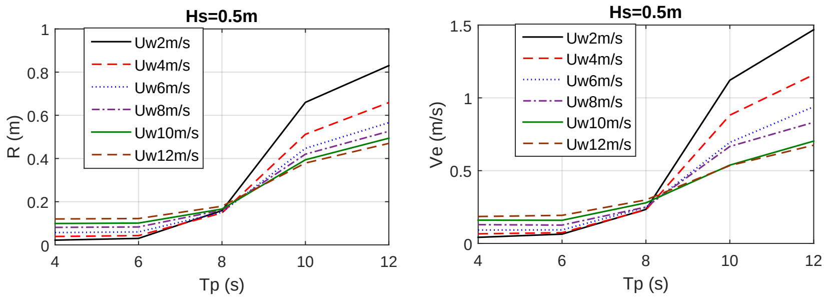

(a) Radial motion

(b) Radial velocity

Figure 9: Characteristic values of blade root motion and velocity with varying wind and wave conditions: $H_s = 0.5m$.

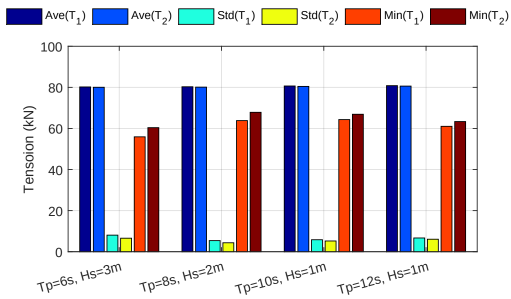

Figure 10: Example statistics of tugger line tension under typical sea states, with $U_w = 2m/s$: statistical value averaged from 42 10-min runs

8. Operational environmental limits

The allowable operational sea states for each phase were identified by mapping the characteristic values of limiting parameters against their allowable limits.

8.1. *Motion monitoring phase*

Figure 7 shows the mapping of R for the blade motion monitoring phase. In short waves ($T_p <= 6s$), mating attempts are sufficiently safe to carry out for H_s of 3m and wind speed of 12m/s. The allowable limit of H_s decreases sharply with the increase of T_p. At $T_p = 8s$, mating attempts (mating gap $r = 0.1R_{root}$) are feasible with H_s below 1.0m with slight variations depending on wind speed. When T_p increases to 12s, mating attempts are not possible for H_s larger than 0.5m, for all considered wind conditions.

The wind condition is also an important part of the operational limits for the blade motion monitoring phase. Table 3 compares the allowable limit of H_s under varying wind speed. With $T_p = 8s$, the upper boundary of H_s is increased by 15% when the wind speed increases from 2m/s to 12m/s. At $T_p = 12s$, the corresponding increase is more significant, i.e., almost 90%.

A larger radius of the mating gap can increase the allowable limits for the motion monitoring phase, as can be observed in Figure 7. When the mating gap radius increases from $0.1R_{root}$ to $0.2R_{root}$, the allowable limit of H_s is almost doubled at $T_p = 8s$ for wind speed within 6m/s to 12m/s.

Table 3: Allowable limit of H_s with varying wind speed (mating gap of $r = 0.2R_{root}$)

T_p \ U_w	2m/s	4m/s	6m/s	8m/s	10m/s	12m/s
8s	1.72m	1.86m	1.92m	1.92m	1.96m	1.97m
12s	0.31m	0.41m	0.48m	0.51m	0.55m	0.58m

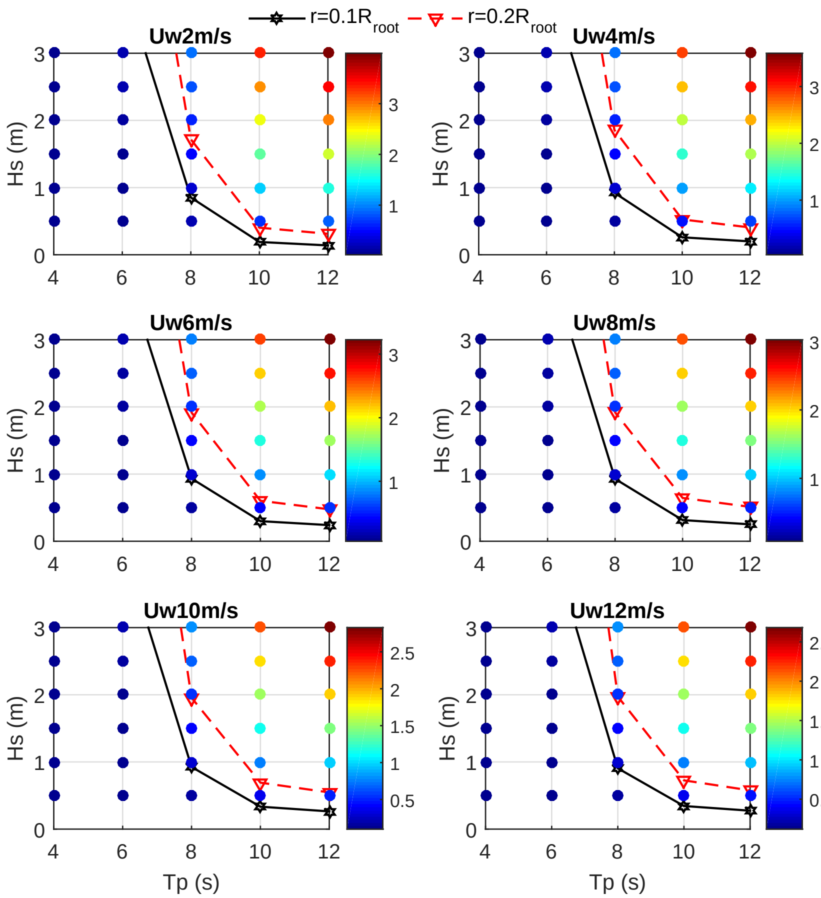

Figure 11: Mapping of blade root radial motion (R, characteristic value corresponding to an mean upcrossing rate of $\nu^+ = 0.0167$) against allowable limit ($r = [0.1, 0.2] \times R_{root}$, $R_{root} = 2.69m$) under various combined wind and wave conditions.

8.2. Blade mating phase

The mapping of V_e against its limiting criteria for the blade mating phase is shown in Figure 12. As revealed by the results, the mating phase is safe

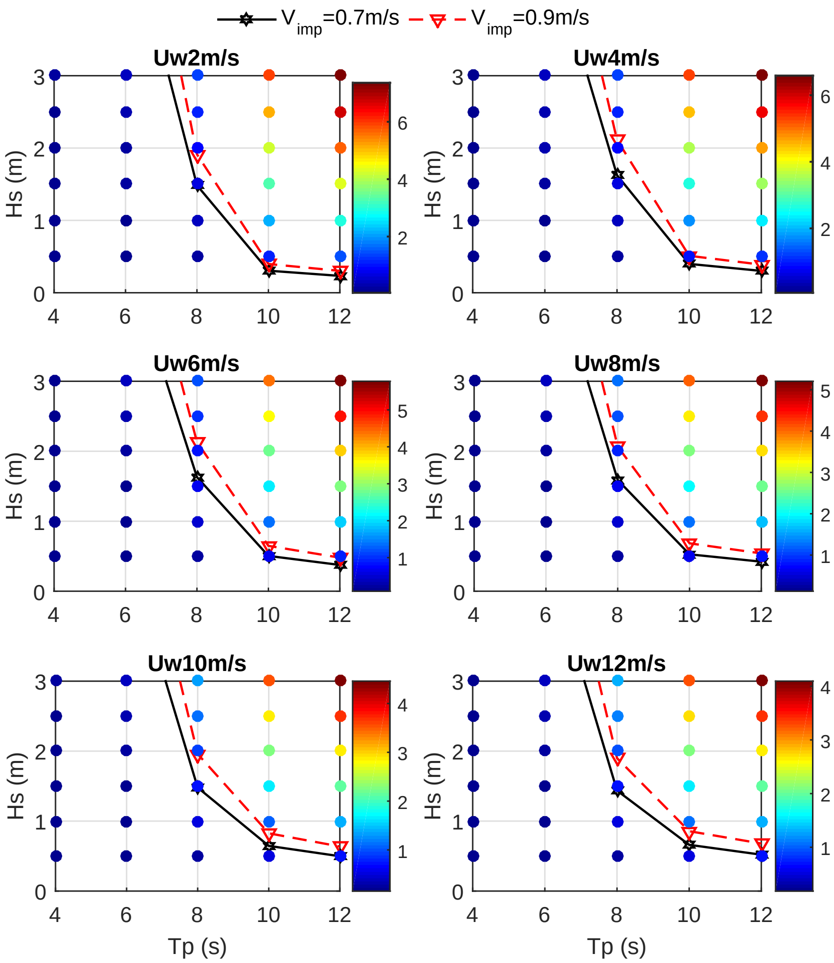

Figure 12: Mapping of blade root radial velocity (V_e, 10-min extreme value corresponding to a probability of exceedance 10^{-4}) against allowable limit ($v_{imp} = [0.7, 0.9]\ m/s$) under various combined wind and wave conditions. The 0.7 m/s is estimated based on nonlinear FEM analysis while 0.9m/s is an assumed varied value.

to operate under H_s of 3m in short wave conditions with T_p less than 6s, and wind speed up to 12m/s. The blade mating is more challenging in long wave conditions, as the allowable limit of H_s is much smaller, compared to the short wave conditions. When T_p is 12s, bending damage in guide pins ($V_{imp} = 0.7m/s$) would occur with H_s larger than 0.5m, for all considered wind conditions. Under such a condition, the effect of wind becomes important. At $T_p = 12s$, a larger wind speed helps increase the allowable limit of H_s, from 0.23m at wind speed of 2m/s to 0.52m of H_s at wind speed of 12m/s.

Increasing V_{imp} from 0.7m/s to 0.9m/s, the allowable limit of H_s can be increased by approximately 0.5m for waves with T_p of 8s, by 0.1∼0.2m for waves with T_p of 12s, for all considered wind speeds.

8.3. Complete blade mating operation

The overall allowable wind and wave conditions for the complete blade mating operation can be found by combining those of the monitoring and mating phases, and taking the lower envelope, as illustrated in Figure 13.

As can be observed in Figure 13, the mating operation is governed by the motion monitoring phase when the mating gap $r = 0.1R_{root}$. In such a case, the complete blade mating operation is mainly failed by unsuccessful mating attempts during the motion monitoring phase. In this case, increasing the limiting criteria of impact velocity does not necessarily lead to increases in the overall operational limits. However, if the mating gap is $0.2R_{root}$ and the allowable impact velocity is 0.7m/s, the overall operational limit would be governed by the bent guide pins in the mating phase. Under such a circumstance, an increase in the allowable impact velocity can widen the overall operational limits.

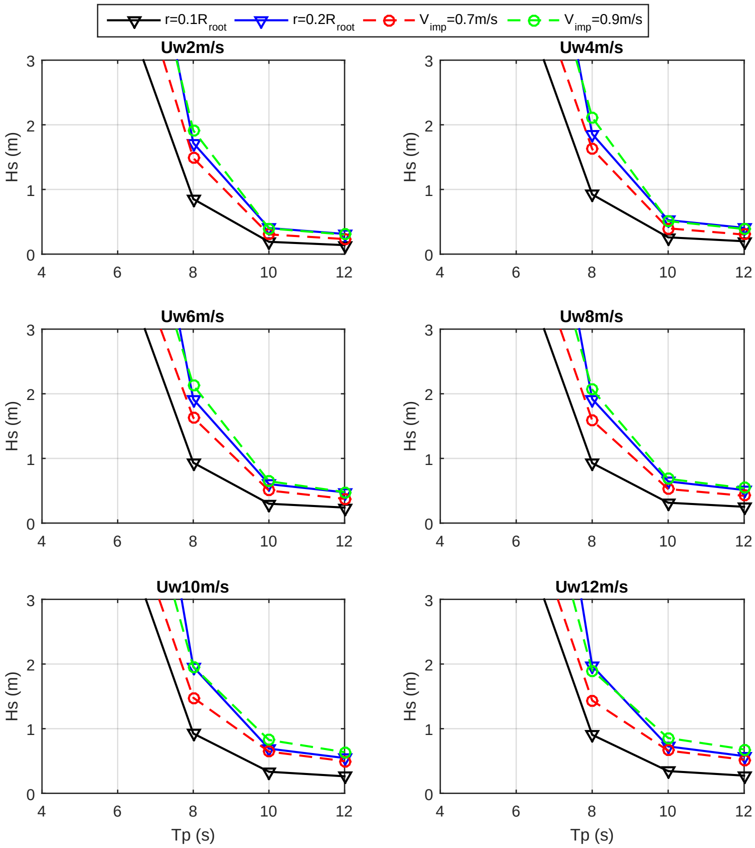

Figure 13: Allowable limits of wave and wind conditions for complete blade mating operation

9. Conclusions

This study presents an approach for assessing the operational environmental limits of single blade installation for offshore wind turbines in terms of combined wind and wave conditions. The installation procedure is discussed followed by an identification of the critical events and corresponding limiting response parameters. The criteria of the response parameters are determined assuming a safety factor of 1.0. Characteristic values of the limiting parameters are obtained using fully coupled time domain analysis based on stochastic methods. This study also provides a demonstration of the approach to find out the allowable operational limits. The main conclusions are provided as follows.

The final blade mating operation is found to be critical during the whole installation phase. The critical events include failed mating attempts in the motion monitoring phase and bent guide pins in the mating phase. The corresponding limiting response parameters are found to be respectively blade root motion relative to the hub radial direction and blade root radial velocity. The limiting criterion for the blade root motion is chosen for demonstration purpose, while the actual criterion should be decided in relevant operations.

Numerical analysis based on a fully coupled model is essential to assess the dynamic responses of the blade installation system. The model should include blade aerodynamics, vessel hydrodynamics, crane flexibility and lifting arrangements. The system is affected by non-linear features, hence time domain simulations should be used. The vessel motion and crane flexibility have significant contributions to the blade motion.

Both wind and waves are important for offshore single blade installation.

When a floating crane vessel is considered, the dynamic responses of limiting parameters increase significantly with increasing wave peak period. In relatively short wave conditions, e.g, with periods less than 8s in the case study, wind excitation dominates. The dynamic responses of limiting parameters increase with the increase of wind speed. While in long wave conditions, the wind loads act as damping forces. Hence, they decreases remarkably with the increasing wind speed.

The approach is applied in a case study with a DTU 10MW wind turbine blade installed by a semi-submersible crane vessel onto a jacket wind turbine. The hub motion of the jacket wind turbine is not considered. The overall operational limits are obtained by taking the lower envelope of the operational limits for both the monitoring phase.

10. Limitations

The case study serves as a simple demonstration of the presented approach, focusing on establishing the allowable environmental limits based on characteristic values of limiting parameters and allowable environmental limits. Uncertainties from human decision-making, properties of structural components and numerical modelling are not considered. Future efforts can be devoted to account for these uncertainties.

The characteristic values of the limiting parameters are estimated without accounting for the influence of turbine hub motion since a jacket with relatively small motion is considered. Future work could be carried out to account for turbine hub motion into allowable limits and compare the effects of hub motion for different types of offshore wind turbines, such as monopiles, tripods, jackets, etc., on the operational environmental limits.

Uncertainties in derivation of allowable environmental conditions for offshore wind turbine installation should be addressed in future work. The uncertainties consists of numerical modelling uncertainties, stochastic uncertainties in extreme value computation and uncertainties in implementation of the allowable environmental limits.

References

Acero, G. W., Li, L., Gao, Z., Moan, T., 2016a. Methodology for assessment of the operational limits and operability of marine operations. Ocean Engineering 125, 308–327.

Acero, W., Gao, Z., Moan, T., 2016b. Assessment of the dynamic responses and allowable sea states for a novel offshore wind turbine installation concept based on the inverted pendulum principle. Energy Procedia 94, 61–71.

Acero, W. G., Gao, Z., Moan, T., 2017. Methodology for assessment of the allowable sea states during installation of an offshore wind turbine transition piece structure onto a monopile foundation. Journal of Offshore Mechanics and Arctic Engineering 139 (6), 061901.

Alpha ventus, 2015. Alpha ventus offshore wind farm. `https://www.alpha-ventus.de/english/`, (Accessed on 12/28/2018).

Bak, C., Zahle, F., Bitsche, R., Kim, T., Yde, A., Henriksen, L. C., Hansen, M. H., Natarajan, A., 2013. Description of the DTU 10 MW reference wind turbine. Tech. Rep. DTU Wind Energy Report-I-0092, Technical University of Denmark.

DEEPWATER WIND, 2019. Block Island Wind Farm - Deepwater Wind. http://dwwind.com/project/block-island-wind-farm/, (Accessed on 02/09/2019).

DNV, 2011. Recommended Practice DNV-OS-H101: marine operations. Standard, DET NORSKE VERITAS, Olso, Norway.

GE Renewable Energy, 2018. World's Largest Offshore Wind Turbine: Haliade-X. https://www.ge.com/renewableenergy/wind-energy/turbines/haliade-x-offshore-turbine, (Accessed on 12/28/2018).

Global Wind Energy Council, 2018. GLOBAL WIND STATISTICS 2017. Report, Global Wind Energy Council.

Hoerner, S. F., Borst, H. V., 1985. Fluid-dynamic lift: practical information on aerodynamic and hydrodynamic lift. Hoerner Fluid Dynamics, Vancouver, WA.

Jiang, Z., Gao, Z., Ren, Z., Li, Y., Duan, L., 2018. A parametric study on the final blade installation process for monopile wind turbines under rough environmental conditions. Engineering Structures 172, 1042–1056.

Li, L., Acero, W. G., Gao, Z., Moan, T., 2016a. Assessment of allowable sea states during installation of offshore wind turbine monopiles with shallow penetration in the seabed. Journal of Offshore Mechanics and Arctic Engineering 138 (4), 041902.

Li, L., Gao, Z., Moan, T., 2016b. Operability analysis of monopile lowering operation using different numerical approaches. International Journal of Offshore and Polar Engineering 26(2), 88–99.

Shi, W., Park, H.-C., Chung, C.-W., Kim, Y.-C., et al., 2011. Comparison of dynamic response of monopile, tripod and jacket foundation system for a 5-mw wind turbine. In: The Twenty-first International Offshore and Polar Engineering Conference, Hawaii, USA, June 19-24, 2011.

Siemens, 2012. Offshore wind turbine blade installation. https://www.siemens.com/press/en/feature/2012/energy/2012-07-rotorblade.php, (Accessed on 12/27/2018).

Siemens, 2015. Siemens SWT-3.6-107 specifications. https://www.siemens.com/content/dam/internet/siemens-com/global/market-specific-solutions/wind/data_sheets/data-sheet-wind-turbine-swt-3-6-107.pdf, (Accessed on 12/28/2018).

Verma, A. S., Jiang, Z., Vedvik, N. P., Gao, Z., Ren, Z., 2018. Impact assessment of a wind turbine blade root with the hub during an offshore mating process. Engineering Structures 80(C), 205–222.

Vestas, 2012. V164-8MW specifications. http://www.homepages.ucl.ac.uk/~uceseug/Fluids2/Wind_Turbines/Turbines/V164-8MW.pdf, (Accessed on 12/28/2018).

Wind-turbine-models, 2012. Bonus b76/2000 - 2,00 mw - wind turbine. https://en.wind-turbine-models.com/turbines/121-bonus-b76-2000, (Accessed on 12/28/2018).

Zhao, Y., Cheng, Z., Gao, Z., Moan, T., 2018a. Effect of foundation modeling of a jack-up crane vessel on the dynamic motion response of an offshore wind turbine blade during installation. In: Proceedings of the International Offshore Wind Technical Conference (IOWC), San Francisco, USA, November 4-7, 2018.

Zhao, Y., Cheng, Z., Gao, Z., Sandvik, P. C., Moan, T., 2019. Numerical study on the feasibility of offshore single blade installation by floating crane vessels. Marine Structures 64, 442–462.

Zhao, Y., Cheng, Z., Sandvik, P. C., Gao, Z., Moan, T., 2018b. An integrated dynamic analysis method for simulating installation of a single blade for offshore wind turbines. Ocean Engineering 152, 72–88.

Zhao, Y., Cheng, Z., Sandvik, P. C., Gao, Z., Moan, T., Buren, E. V., 2018c. Numerical modeling and analysis of the dynamic motion response of an offshore wind turbine blade during installation by a jack-up crane vessel. Ocean Engineering 165, 353–364.

284

Appendix B

List of previous PhD theses at Dept. of Marine Tech.

Previous PhD theses published at the Department of Marine Technology
(earlier: Faculty of Marine Technology)
NORWEGIAN UNIVERSITY OF SCIENCE AND TECHNOLOGY

Report No.	**Author**	**Title**
	Kavlie, Dag	Optimization of Plane Elastic Grillages, 1967
	Hansen, Hans R.	Man-Machine Communication and Data-Storage Methods in Ship Structural Design, 1971
	Gisvold, Kaare M.	A Method for non-linear mixed -integer programming and its Application to Design Problems, 1971
	Lund, Sverre	Tanker Frame Optimalization by means of SUMT-Transformation and Behaviour Models, 1971
	Vinje, Tor	On Vibration of Spherical Shells Interacting with Fluid, 1972
	Lorentz, Jan D.	Tank Arrangement for Crude Oil Carriers in Accordance with the new Anti-Pollution Regulations, 1975
	Carlsen, Carl A.	Computer-Aided Design of Tanker Structures, 1975
	Larsen, Carl M.	Static and Dynamic Analysis of Offshore Pipelines during Installation, 1976
UR-79-01	Brigt Hatlestad, MK	The finite element method used in a fatigue evaluation of fixed offshore platforms. (Dr.Ing. Thesis)
UR-79-02	Erik Pettersen, MK	Analysis and design of cellular structures. (Dr.Ing. Thesis)
UR-79-03	Sverre Valsgård, MK	Finite difference and finite element methods applied to nonlinear analysis of plated structures. (Dr.Ing. Thesis)
UR-79-04	Nils T. Nordsve, MK	Finite element collapse analysis of structural members considering imperfections and stresses due to fabrication. (Dr.Ing. Thesis)
UR-79-05	Ivar J. Fylling, MK	Analysis of towline forces in ocean towing systems. (Dr.Ing. Thesis)
UR-80-06	Nils Sandsmark, MM	Analysis of Stationary and Transient Heat Conduction by the Use of the Finite Element Method. (Dr.Ing. Thesis)
UR-80-09	Sverre Haver, MK	Analysis of uncertainties related to the stochastic modeling of ocean waves. (Dr.Ing. Thesis)
UR-81-15	Odland, Jonas	On the Strength of welded Ring stiffened cylindrical Shells primarily subjected to axial Compression
UR-82-17	Engesvik, Knut	Analysis of Uncertainties in the fatigue Capacity of Welded Joints

Report No.	Author	Title
UR-82-18	Rye, Henrik	Ocean wave groups
UR-83-30	Eide, Oddvar Inge	On Cumulative Fatigue Damage in Steel Welded Joints
UR-83-33	Mo, Olav	Stochastic Time Domain Analysis of Slender Offshore Structures
UR-83-34	Amdahl, Jørgen	Energy absorption in Ship-platform impacts
UR-84-37	Mørch, Morten	Motions and mooring forces of semi submersibles as determined by full-scale measurements and theoretical analysis
UR-84-38	Soares, C. Guedes	Probabilistic models for load effects in ship structures
UR-84-39	Aarsnes, Jan V.	Current forces on ships
UR-84-40	Czujko, Jerzy	Collapse Analysis of Plates subjected to Biaxial Compression and Lateral Load
UR-85-46	Alf G. Engseth, MK	Finite element collapse analysis of tubular steel offshore structures. (Dr.Ing. Thesis)
UR-86-47	Dengody Sheshappa, MP	A Computer Design Model for Optimizing Fishing Vessel Designs Based on Techno-Economic Analysis. (Dr.Ing. Thesis)
UR-86-48	Vidar Aanesland, MH	A Theoretical and Numerical Study of Ship Wave Resistance. (Dr.Ing. Thesis)
UR-86-49	Heinz-Joachim Wessel, MK	Fracture Mechanics Analysis of Crack Growth in Plate Girders. (Dr.Ing. Thesis)
UR-86-50	Jon Taby, MK	Ultimate and Post-ultimate Strength of Dented Tubular Members. (Dr.Ing. Thesis)
UR-86-51	Walter Lian, MH	A Numerical Study of Two-Dimensional Separated Flow Past Bluff Bodies at Moderate KC-Numbers. (Dr.Ing. Thesis)
UR-86-52	Bjørn Sortland, MH	Force Measurements in Oscillating Flow on Ship Sections and Circular Cylinders in a U-Tube Water Tank. (Dr.Ing. Thesis)
UR-86-53	Kurt Strand, MM	A System Dynamic Approach to One-dimensional Fluid Flow. (Dr.Ing. Thesis)
UR-86-54	Arne Edvin Løken, MH	Three Dimensional Second Order Hydrodynamic Effects on Ocean Structures in Waves. (Dr.Ing. Thesis)
UR-86-55	Sigurd Falch, MH	A Numerical Study of Slamming of Two-Dimensional Bodies. (Dr.Ing. Thesis)
UR-87-56	Arne Braathen, MH	Application of a Vortex Tracking Method to the Prediction of Roll Damping of a Two-Dimension Floating Body. (Dr.Ing. Thesis)

Report No.	Author	Title
UR-87-57	Bernt Leira, MK	Gaussian Vector Processes for Reliability Analysis involving Wave-Induced Load Effects. (Dr.Ing. Thesis)
UR-87-58	Magnus Småvik, MM	Thermal Load and Process Characteristics in a Two-Stroke Diesel Engine with Thermal Barriers (in Norwegian). (Dr.Ing. Thesis)
MTA-88-59	Bernt Arild Bremdal, MP	An Investigation of Marine Installation Processes – A Knowledge - Based Planning Approach. (Dr.Ing. Thesis)
MTA-88-60	Xu Jun, MK	Non-linear Dynamic Analysis of Space-framed Offshore Structures. (Dr.Ing. Thesis)
MTA-89-61	Gang Miao, MH	Hydrodynamic Forces and Dynamic Responses of Circular Cylinders in Wave Zones. (Dr.Ing. Thesis)
MTA-89-62	Martin Greenhow, MH	Linear and Non-Linear Studies of Waves and Floating Bodies. Part I and Part II. (Dr.Techn. Thesis)
MTA-89-63	Chang Li, MH	Force Coefficients of Spheres and Cubes in Oscillatory Flow with and without Current. (Dr.Ing. Thesis
MTA-89-64	Hu Ying, MP	A Study of Marketing and Design in Development of Marine Transport Systems. (Dr.Ing. Thesis)
MTA-89-65	Arild Jæger, MH	Seakeeping, Dynamic Stability and Performance of a Wedge Shaped Planing Hull. (Dr.Ing. Thesis)
MTA-89-66	Chan Siu Hung, MM	The dynamic characteristics of tilting-pad bearings
MTA-89-67	Kim Wikstrøm, MP	Analysis av projekteringen for ett offshore projekt. (Licenciat-avhandling)
MTA-89-68	Jiao Guoyang, MK	Reliability Analysis of Crack Growth under Random Loading, considering Model Updating. (Dr.Ing. Thesis)
MTA-89-69	Arnt Olufsen, MK	Uncertainty and Reliability Analysis of Fixed Offshore Structures. (Dr.Ing. Thesis)
MTA-89-70	Wu Yu-Lin, MR	System Reliability Analyses of Offshore Structures using improved Truss and Beam Models. (Dr.Ing. Thesis)
MTA-90-71	Jan Roger Hoff, MH	Three-dimensional Green function of a vessel with forward speed in waves. (Dr.Ing. Thesis)
MTA-90-72	Rong Zhao, MH	Slow-Drift Motions of a Moored Two-Dimensional Body in Irregular Waves. (Dr.Ing. Thesis)
MTA-90-73	Atle Minsaas, MP	Economical Risk Analysis. (Dr.Ing. Thesis)
MTA-90-74	Knut-Aril Farnes, MK	Long-term Statistics of Response in Non-linear Marine Structures. (Dr.Ing. Thesis)

Report No.	Author	Title
MTA-90-75	Torbjørn Sotberg, MK	Application of Reliability Methods for Safety Assessment of Submarine Pipelines. (Dr.Ing. Thesis)
MTA-90-76	Zeuthen, Steffen, MP	SEAMAID. A computational model of the design process in a constraint-based logic programming environment. An example from the offshore domain. (Dr.Ing. Thesis)
MTA-91-77	Haagensen, Sven, MM	Fuel Dependant Cyclic Variability in a Spark Ignition Engine - An Optical Approach. (Dr.Ing. Thesis)
MTA-91-78	Løland, Geir, MH	Current forces on and flow through fish farms. (Dr.Ing. Thesis)
MTA-91-79	Hoen, Christopher, MK	System Identification of Structures Excited by Stochastic Load Processes. (Dr.Ing. Thesis)
MTA-91-80	Haugen, Stein, MK	Probabilistic Evaluation of Frequency of Collision between Ships and Offshore Platforms. (Dr.Ing. Thesis)
MTA-91-81	Sødahl, Nils, MK	Methods for Design and Analysis of Flexible Risers. (Dr.Ing. Thesis)
MTA-91-82	Ormberg, Harald, MK	Non-linear Response Analysis of Floating Fish Farm Systems. (Dr.Ing. Thesis)
MTA-91-83	Marley, Mark J., MK	Time Variant Reliability under Fatigue Degradation. (Dr.Ing. Thesis)
MTA-91-84	Krokstad, Jørgen R., MH	Second-order Loads in Multidirectional Seas. (Dr.Ing. Thesis)
MTA-91-85	Molteberg, Gunnar A., MM	The Application of System Identification Techniques to Performance Monitoring of Four Stroke Turbocharged Diesel Engines. (Dr.Ing. Thesis)
MTA-92-86	Mørch, Hans Jørgen Bjelke, MH	Aspects of Hydrofoil Design: with Emphasis on Hydrofoil Interaction in Calm Water. (Dr.Ing. Thesis)
MTA-92-87	Chan Siu Hung, MM	Nonlinear Analysis of Rotordynamic Instabilities in Highspeed Turbomachinery. (Dr.Ing. Thesis)
MTA-92-88	Bessason, Bjarni, MK	Assessment of Earthquake Loading and Response of Seismically Isolated Bridges. (Dr.Ing. Thesis)
MTA-92-89	Langli, Geir, MP	Improving Operational Safety through exploitation of Design Knowledge - an investigation of offshore platform safety. (Dr.Ing. Thesis)
MTA-92-90	Sævik, Svein, MK	On Stresses and Fatigue in Flexible Pipes. (Dr.Ing. Thesis)
MTA-92-91	Ask, Tor Ø., MM	Ignition and Flame Growth in Lean Gas-Air Mixtures. An Experimental Study with a Schlieren System. (Dr.Ing. Thesis)

Report No.	Author	Title
MTA-86-92	Hessen, Gunnar, MK	Fracture Mechanics Analysis of Stiffened Tubular Members. (Dr.Ing. Thesis)
MTA-93-93	Steinebach, Christian, MM	Knowledge Based Systems for Diagnosis of Rotating Machinery. (Dr.Ing. Thesis)
MTA-93-94	Dalane, Jan Inge, MK	System Reliability in Design and Maintenance of Fixed Offshore Structures. (Dr.Ing. Thesis)
MTA-93-95	Steen, Sverre, MH	Cobblestone Effect on SES. (Dr.Ing. Thesis)
MTA-93-96	Karunakaran, Daniel, MK	Nonlinear Dynamic Response and Reliability Analysis of Drag-dominated Offshore Platforms. (Dr.Ing. Thesis)
MTA-93-97	Hagen, Arnulf, MP	The Framework of a Design Process Language. (Dr.Ing. Thesis)
MTA-93-98	Nordrik, Rune, MM	Investigation of Spark Ignition and Autoignition in Methane and Air Using Computational Fluid Dynamics and Chemical Reaction Kinetics. A Numerical Study of Ignition Processes in Internal Combustion Engines. (Dr.Ing. Thesis)
MTA-94-99	Passano, Elizabeth, MK	Efficient Analysis of Nonlinear Slender Marine Structures. (Dr.Ing. Thesis)
MTA-94-100	Kvålsvold, Jan, MH	Hydroelastic Modelling of Wetdeck Slamming on Multihull Vessels. (Dr.Ing. Thesis)
MTA-94-102	Bech, Sidsel M., MK	Experimental and Numerical Determination of Stiffness and Strength of GRP/PVC Sandwich Structures. (Dr.Ing. Thesis)
MTA-95-103	Paulsen, Hallvard, MM	A Study of Transient Jet and Spray using a Schlieren Method and Digital Image Processing. (Dr.Ing. Thesis)
MTA-95-104	Hovde, Geir Olav, MK	Fatigue and Overload Reliability of Offshore Structural Systems, Considering the Effect of Inspection and Repair. (Dr.Ing. Thesis)
MTA-95-105	Wang, Xiaozhi, MK	Reliability Analysis of Production Ships with Emphasis on Load Combination and Ultimate Strength. (Dr.Ing. Thesis)
MTA-95-106	Ulstein, Tore, MH	Nonlinear Effects of a Flexible Stern Seal Bag on Cobblestone Oscillations of an SES. (Dr.Ing. Thesis)
MTA-95-107	Solaas, Frøydis, MH	Analytical and Numerical Studies of Sloshing in Tanks. (Dr.Ing. Thesis)
MTA-95-108	Hellan, Øyvind, MK	Nonlinear Pushover and Cyclic Analyses in Ultimate Limit State Design and Reassessment of Tubular Steel Offshore Structures. (Dr.Ing. Thesis)
MTA-95-109	Hermundstad, Ole A., MK	Theoretical and Experimental Hydroelastic Analysis of High Speed Vessels. (Dr.Ing. Thesis)

Report No.	Author	Title
MTA-96-110	Bratland, Anne K., MH	Wave-Current Interaction Effects on Large-Volume Bodies in Water of Finite Depth. (Dr.Ing. Thesis)
MTA-96-111	Herfjord, Kjell, MH	A Study of Two-dimensional Separated Flow by a Combination of the Finite Element Method and Navier-Stokes Equations. (Dr.Ing. Thesis)
MTA-96-112	Æsøy, Vilmar, MM	Hot Surface Assisted Compression Ignition in a Direct Injection Natural Gas Engine. (Dr.Ing. Thesis)
MTA-96-113	Eknes, Monika L., MK	Escalation Scenarios Initiated by Gas Explosions on Offshore Installations. (Dr.Ing. Thesis)
MTA-96-114	Erikstad, Stein O., MP	A Decision Support Model for Preliminary Ship Design. (Dr.Ing. Thesis)
MTA-96-115	Pedersen, Egil, MH	A Nautical Study of Towed Marine Seismic Streamer Cable Configurations. (Dr.Ing. Thesis)
MTA-97-116	Moksnes, Paul O., MM	Modelling Two-Phase Thermo-Fluid Systems Using Bond Graphs. (Dr.Ing. Thesis)
MTA-97-117	Halse, Karl H., MK	On Vortex Shedding and Prediction of Vortex-Induced Vibrations of Circular Cylinders. (Dr.Ing. Thesis)
MTA-97-118	Igland, Ragnar T., MK	Reliability Analysis of Pipelines during Laying, considering Ultimate Strength under Combined Loads. (Dr.Ing. Thesis)
MTA-97-119	Pedersen, Hans-P., MP	Levendefiskteknologi for fiskefartøy. (Dr.Ing. Thesis)
MTA-98-120	Vikestad, Kyrre, MK	Multi-Frequency Response of a Cylinder Subjected to Vortex Shedding and Support Motions. (Dr.Ing. Thesis)
MTA-98-121	Azadi, Mohammad R. E., MK	Analysis of Static and Dynamic Pile-Soil-Jacket Behaviour. (Dr.Ing. Thesis)
MTA-98-122	Ulltang, Terje, MP	A Communication Model for Product Information. (Dr.Ing. Thesis)
MTA-98-123	Torbergsen, Erik, MM	Impeller/Diffuser Interaction Forces in Centrifugal Pumps. (Dr.Ing. Thesis)
MTA-98-124	Hansen, Edmond, MH	A Discrete Element Model to Study Marginal Ice Zone Dynamics and the Behaviour of Vessels Moored in Broken Ice. (Dr.Ing. Thesis)
MTA-98-125	Videiro, Paulo M., MK	Reliability Based Design of Marine Structures. (Dr.Ing. Thesis)
MTA-99-126	Mainçon, Philippe, MK	Fatigue Reliability of Long Welds Application to Titanium Risers. (Dr.Ing. Thesis)

Report No.	Author	Title
MTA-99-127	Haugen, Elin M., MH	Hydroelastic Analysis of Slamming on Stiffened Plates with Application to Catamaran Wetdecks. (Dr.Ing. Thesis)
MTA-99-128	Langhelle, Nina K., MK	Experimental Validation and Calibration of Nonlinear Finite Element Models for Use in Design of Aluminium Structures Exposed to Fire. (Dr.Ing. Thesis)
MTA-99-129	Berstad, Are J., MK	Calculation of Fatigue Damage in Ship Structures. (Dr.Ing. Thesis)
MTA-99-130	Andersen, Trond M., MM	Short Term Maintenance Planning. (Dr.Ing. Thesis)
MTA-99-131	Tveiten, Bård Wathne, MK	Fatigue Assessment of Welded Aluminium Ship Details. (Dr.Ing. Thesis)
MTA-99-132	Søreide, Fredrik, MP	Applications of underwater technology in deep water archaeology. Principles and practice. (Dr.Ing. Thesis)
MTA-99-133	Tønnessen, Rune, MH	A Finite Element Method Applied to Unsteady Viscous Flow Around 2D Blunt Bodies With Sharp Corners. (Dr.Ing. Thesis)
MTA-99-134	Elvekrok, Dag R., MP	Engineering Integration in Field Development Projects in the Norwegian Oil and Gas Industry. The Supplier Management of Norne. (Dr.Ing. Thesis)
MTA-99-135	Fagerholt, Kjetil, MP	Optimeringsbaserte Metoder for Ruteplanlegging innen skipsfart. (Dr.Ing. Thesis)
MTA-99-136	Bysveen, Marie, MM	Visualization in Two Directions on a Dynamic Combustion Rig for Studies of Fuel Quality. (Dr.Ing. Thesis)
MTA-2000-137	Storteig, Eskild, MM	Dynamic characteristics and leakage performance of liquid annular seals in centrifugal pumps. (Dr.Ing. Thesis)
MTA-2000-138	Sagli, Gro, MK	Model uncertainty and simplified estimates of long term extremes of hull girder loads in ships. (Dr.Ing. Thesis)
MTA-2000-139	Tronstad, Harald, MK	Nonlinear analysis and design of cable net structures like fishing gear based on the finite element method. (Dr.Ing. Thesis)
MTA-2000-140	Kroneberg, André, MP	Innovation in shipping by using scenarios. (Dr.Ing. Thesis)
MTA-2000-141	Haslum, Herbjørn Alf, MH	Simplified methods applied to nonlinear motion of spar platforms. (Dr.Ing. Thesis)
MTA-2001-142	Samdal, Ole Johan, MM	Modelling of Degradation Mechanisms and Stressor Interaction on Static Mechanical Equipment Residual Lifetime. (Dr.Ing. Thesis)

Report No.	Author	Title
MTA-2001-143	Baarholm, Rolf Jarle, MH	Theoretical and experimental studies of wave impact underneath decks of offshore platforms. (Dr.Ing. Thesis)
MTA-2001-144	Wang, Lihua, MK	Probabilistic Analysis of Nonlinear Wave-induced Loads on Ships. (Dr.Ing. Thesis)
MTA-2001-145	Kristensen, Odd H. Holt, MK	Ultimate Capacity of Aluminium Plates under Multiple Loads, Considering HAZ Properties. (Dr.Ing. Thesis)
MTA-2001-146	Greco, Marilena, MH	A Two-Dimensional Study of Green-Water Loading. (Dr.Ing. Thesis)
MTA-2001-147	Heggelund, Svein E., MK	Calculation of Global Design Loads and Load Effects in Large High Speed Catamarans. (Dr.Ing. Thesis)
MTA-2001-148	Babalola, Olusegun T., MK	Fatigue Strength of Titanium Risers – Defect Sensitivity. (Dr.Ing. Thesis)
MTA-2001-149	Mohammed, Abuu K., MK	Nonlinear Shell Finite Elements for Ultimate Strength and Collapse Analysis of Ship Structures. (Dr.Ing. Thesis)
MTA-2002-150	Holmedal, Lars E., MH	Wave-current interactions in the vicinity of the sea bed. (Dr.Ing. Thesis)
MTA-2002-151	Rognebakke, Olav F., MH	Sloshing in rectangular tanks and interaction with ship motions. (Dr.Ing. Thesis)
MTA-2002-152	Lader, Pål Furset, MH	Geometry and Kinematics of Breaking Waves. (Dr.Ing. Thesis)
MTA-2002-153	Yang, Qinzheng, MH	Wash and wave resistance of ships in finite water depth. (Dr.Ing. Thesis)
MTA-2002-154	Melhus, Øyvin, MM	Utilization of VOC in Diesel Engines. Ignition and combustion of VOC released by crude oil tankers. (Dr.Ing. Thesis)
MTA-2002-155	Ronæss, Marit, MH	Wave Induced Motions of Two Ships Advancing on Parallel Course. (Dr.Ing. Thesis)
MTA-2002-156	Økland, Ole D., MK	Numerical and experimental investigation of whipping in twin hull vessels exposed to severe wet deck slamming. (Dr.Ing. Thesis)
MTA-2002-157	Ge, Chunhua, MK	Global Hydroelastic Response of Catamarans due to Wet Deck Slamming. (Dr.Ing. Thesis)
MTA-2002-158	Byklum, Eirik, MK	Nonlinear Shell Finite Elements for Ultimate Strength and Collapse Analysis of Ship Structures. (Dr.Ing. Thesis)
IMT-2003-1	Chen, Haibo, MK	Probabilistic Evaluation of FPSO-Tanker Collision in Tandem Offloading Operation. (Dr.Ing. Thesis)

Report No.	Author	Title
IMT-2003-2	Skaugset, Kjetil Bjørn, MK	On the Suppression of Vortex Induced Vibrations of Circular Cylinders by Radial Water Jets. (Dr.Ing. Thesis)
IMT-2003-3	Chezhian, Muthu	Three-Dimensional Analysis of Slamming. (Dr.Ing. Thesis)
IMT-2003-4	Buhaug, Øyvind	Deposit Formation on Cylinder Liner Surfaces in Medium Speed Engines. (Dr.Ing. Thesis)
IMT-2003-5	Tregde, Vidar	Aspects of Ship Design: Optimization of Aft Hull with Inverse Geometry Design. (Dr.Ing. Thesis)
IMT-2003-6	Wist, Hanne Therese	Statistical Properties of Successive Ocean Wave Parameters. (Dr.Ing. Thesis)
IMT-2004-7	Ransau, Samuel	Numerical Methods for Flows with Evolving Interfaces. (Dr.Ing. Thesis)
IMT-2004-8	Soma, Torkel	Blue-Chip or Sub-Standard. A data interrogation approach of identity safety characteristics of shipping organization. (Dr.Ing. Thesis)
IMT-2004-9	Ersdal, Svein	An experimental study of hydrodynamic forces on cylinders and cables in near axial flow. (Dr.Ing. Thesis)
IMT-2005-10	Brodtkorb, Per Andreas	The Probability of Occurrence of Dangerous Wave Situations at Sea. (Dr.Ing. Thesis)
IMT-2005-11	Yttervik, Rune	Ocean current variability in relation to offshore engineering. (Dr.Ing. Thesis)
IMT-2005-12	Fredheim, Arne	Current Forces on Net-Structures. (Dr.Ing. Thesis)
IMT-2005-13	Heggernes, Kjetil	Flow around marine structures. (Dr.Ing. Thesis
IMT-2005-14	Fouques, Sebastien	Lagrangian Modelling of Ocean Surface Waves and Synthetic Aperture Radar Wave Measurements. (Dr.Ing. Thesis)
IMT-2006-15	Holm, Håvard	Numerical calculation of viscous free surface flow around marine structures. (Dr.Ing. Thesis)
IMT-2006-16	Bjørheim, Lars G.	Failure Assessment of Long Through Thickness Fatigue Cracks in Ship Hulls. (Dr.Ing. Thesis)
IMT-2006-17	Hansson, Lisbeth	Safety Management for Prevention of Occupational Accidents. (Dr.Ing. Thesis)
IMT-2006-18	Zhu, Xinying	Application of the CIP Method to Strongly Nonlinear Wave-Body Interaction Problems. (Dr.Ing. Thesis)
IMT-2006-19	Reite, Karl Johan	Modelling and Control of Trawl Systems. (Dr.Ing. Thesis)
IMT-2006-20	Smogeli, Øyvind Notland	Control of Marine Propellers. From Normal to Extreme Conditions. (Dr.Ing. Thesis)

Report No.	Author	Title
IMT-2007-21	Storhaug, Gaute	Experimental Investigation of Wave Induced Vibrations and Their Effect on the Fatigue Loading of Ships. (Dr.Ing. Thesis)
IMT-2007-22	Sun, Hui	A Boundary Element Method Applied to Strongly Nonlinear Wave-Body Interaction Problems. (PhD Thesis, CeSOS)
IMT-2007-23	Rustad, Anne Marthine	Modelling and Control of Top Tensioned Risers. (PhD Thesis, CeSOS)
IMT-2007-24	Johansen, Vegar	Modelling flexible slender system for real-time simulations and control applications
IMT-2007-25	Wroldsen, Anders Sunde	Modelling and control of tensegrity structures. (PhD Thesis, CeSOS)
IMT-2007-26	Aronsen, Kristoffer Høye	An experimental investigation of in-line and combined inline and cross flow vortex induced vibrations. (Dr. avhandling, IMT)
IMT-2007-27	Gao, Zhen	Stochastic Response Analysis of Mooring Systems with Emphasis on Frequency-domain Analysis of Fatigue due to Wide-band Response Processes (PhD Thesis, CeSOS)
IMT-2007-28	Thorstensen, Tom Anders	Lifetime Profit Modelling of Ageing Systems Utilizing Information about Technical Condition. (Dr.ing. thesis, IMT)
IMT-2008-29	Refsnes, Jon Erling Gorset	Nonlinear Model-Based Control of Slender Body AUVs (PhD Thesis, IMT)
IMT-2008-30	Berntsen, Per Ivar B.	Structural Reliability Based Position Mooring. (PhD-Thesis, IMT)
IMT-2008-31	Ye, Naiquan	Fatigue Assessment of Aluminium Welded Box-stiffener Joints in Ships (Dr.ing. thesis, IMT)
IMT-2008-32	Radan, Damir	Integrated Control of Marine Electrical Power Systems. (PhD-Thesis, IMT)
IMT-2008-33	Thomassen, Paul	Methods for Dynamic Response Analysis and Fatigue Life Estimation of Floating Fish Cages. (Dr.ing. thesis, IMT)
IMT-2008-34	Pákozdi, Csaba	A Smoothed Particle Hydrodynamics Study of Two-dimensional Nonlinear Sloshing in Rectangular Tanks. (Dr.ing.thesis, IMT/ CeSOS)
IMT-2007-35	Grytøyr, Guttorm	A Higher-Order Boundary Element Method and Applications to Marine Hydrodynamics. (Dr.ing.thesis, IMT)
IMT-2008-36	Drummen, Ingo	Experimental and Numerical Investigation of Nonlinear Wave-Induced Load Effects in Containerships considering Hydroelasticity. (PhD thesis, CeSOS)

Report No.	Author	Title
IMT-2008-37	Skejic, Renato	Maneuvering and Seakeeping of a Singel Ship and of Two Ships in Interaction. (PhD-Thesis, CeSOS)
IMT-2008-38	Harlem, Alf	An Age-Based Replacement Model for Repairable Systems with Attention to High-Speed Marine Diesel Engines. (PhD-Thesis, IMT)
IMT-2008-39	Alsos, Hagbart S.	Ship Grounding. Analysis of Ductile Fracture, Bottom Damage and Hull Girder Response. (PhD-thesis, IMT)
IMT-2008-40	Graczyk, Mateusz	Experimental Investigation of Sloshing Loading and Load Effects in Membrane LNG Tanks Subjected to Random Excitation. (PhD-thesis, CeSOS)
IMT-2008-41	Taghipour, Reza	Efficient Prediction of Dynamic Response for Flexible amd Multi-body Marine Structures. (PhD-thesis, CeSOS)
IMT-2008-42	Ruth, Eivind	Propulsion control and thrust allocation on marine vessels. (PhD thesis, CeSOS)
IMT-2008-43	Nystad, Bent Helge	Technical Condition Indexes and Remaining Useful Life of Aggregated Systems. PhD thesis, IMT
IMT-2008-44	Soni, Prashant Kumar	Hydrodynamic Coefficients for Vortex Induced Vibrations of Flexible Beams, PhD thesis, CeSOS
IMT-2009-45	Amlashi, Hadi K.K.	Ultimate Strength and Reliability-based Design of Ship Hulls with Emphasis on Combined Global and Local Loads. PhD Thesis, IMT
IMT-2009-46	Pedersen, Tom Arne	Bond Graph Modelling of Marine Power Systems. PhD Thesis, IMT
IMT-2009-47	Kristiansen, Trygve	Two-Dimensional Numerical and Experimental Studies of Piston-Mode Resonance. PhD-Thesis, CeSOS
IMT-2009-48	Ong, Muk Chen	Applications of a Standard High Reynolds Number Model and a Stochastic Scour Prediction Model for Marine Structures. PhD-thesis, IMT
IMT-2009-49	Hong, Lin	Simplified Analysis and Design of Ships subjected to Collision and Grounding. PhD-thesis, IMT
IMT-2009-50	Koushan, Kamran	Vortex Induced Vibrations of Free Span Pipelines, PhD thesis, IMT
IMT-2009-51	Korsvik, Jarl Eirik	Heuristic Methods for Ship Routing and Scheduling. PhD-thesis, IMT
IMT-2009-52	Lee, Jihoon	Experimental Investigation and Numerical in Analyzing the Ocean Current Displacement of Longlines. Ph.d.-Thesis, IMT.

Report No.	Author	Title
IMT-2009-53	Vestbøstad, Tone Gran	A Numerical Study of Wave-in-Deck Impact usin a Two-Dimensional Constrained Interpolation Profile Method, Ph.d.thesis, CeSOS.
IMT-2009-54	Bruun, Kristine	Bond Graph Modelling of Fuel Cells for Marine Power Plants. Ph.d.-thesis, IMT
IMT-2009-55	Holstad, Anders	Numerical Investigation of Turbulence in a Sekwed Three-Dimensional Channel Flow, Ph.d.-thesis, IMT.
IMT-2009-56	Ayala-Uraga, Efren	Reliability-Based Assessment of Deteriorating Ship-shaped Offshore Structures, Ph.d.-thesis, IMT
IMT-2009-57	Kong, Xiangjun	A Numerical Study of a Damaged Ship in Beam Sea Waves. Ph.d.-thesis, IMT/CeSOS.
IMT-2010-58	Kristiansen, David	Wave Induced Effects on Floaters of Aquaculture Plants, Ph.d.-thesis, CeSOS.
IMT-2010-59	Ludvigsen, Martin	An ROV-Toolbox for Optical and Acoustic Scientific Seabed Investigation. Ph.d.-thesis IMT.
IMT-2010-60	Hals, Jørgen	Modelling and Phase Control of Wave-Energy Converters. Ph.d.thesis, CeSOS.
IMT-2010- 61	Shu, Zhi	Uncertainty Assessment of Wave Loads and Ultimate Strength of Tankers and Bulk Carriers in a Reliability Framework. Ph.d. Thesis, IMT/ CeSOS
IMT-2010-62	Shao, Yanlin	Numerical Potential-Flow Studies on Weakly-Nonlinear Wave-Body Interactions with/without Small Forward Speed, Ph.d.thesis,CeSOS.
IMT-2010-63	Califano, Andrea	Dynamic Loads on Marine Propellers due to Intermittent Ventilation. Ph.d.thesis, IMT.
IMT-2010-64	El Khoury, George	Numerical Simulations of Massively Separated Turbulent Flows, Ph.d.-thesis, IMT
IMT-2010-65	Seim, Knut Sponheim	Mixing Process in Dense Overflows with Emphasis on the Faroe Bank Channel Overflow. Ph.d.thesis, IMT
IMT-2010-66	Jia, Huirong	Structural Analysis of Intect and Damaged Ships in a Collission Risk Analysis Perspective. Ph.d.thesis CeSoS.
IMT-2010-67	Jiao, Linlin	Wave-Induced Effects on a Pontoon-type Very Large Floating Structures (VLFS). Ph.D.-thesis, CeSOS.
IMT-2010-68	Abrahamsen, Bjørn Christian	Sloshing Induced Tank Roof with Entrapped Air Pocket. Ph.d.thesis, CeSOS.
IMT-2011-69	Karimirad, Madjid	Stochastic Dynamic Response Analysis of Spar-Type Wind Turbines with Catenary or Taut Mooring Systems. Ph.d.-thesis, CeSOS.

Report No.	Author	Title
IMT-2011-70	Erlend Meland	Condition Monitoring of Safety Critical Valves. Ph.d.-thesis, IMT.
IMT–2011-71	Yang, Limin	Stochastic Dynamic System Analysis of Wave Energy Converter with Hydraulic Power Take-Off, with Particular Reference to Wear Damage Analysis, Ph.d. Thesis, CeSOS.
IMT – 2011-72	Visscher, Jan	Application of Particla Image Velocimetry on Turbulent Marine Flows, Ph.d.Thesis, IMT.
IMT – 2011-73	Su, Biao	Numerical Predictions of Global and Local Ice Loads on Ships. Ph.d.Thesis, CeSOS.
IMT – 2011-74	Liu, Zhenhui	Analytical and Numerical Analysis of Iceberg Collision with Ship Structures. Ph.d.Thesis, IMT.
IMT – 2011-75	Aarsæther, Karl Gunnar	Modeling and Analysis of Ship Traffic by Observation and Numerical Simulation. Ph.d.Thesis, IMT.
IMT – 2011-76	Wu, Jie	Hydrodynamic Force Identification from Stochastic Vortex Induced Vibration Experiments with Slender Beams. Ph.d.Thesis, IMT.
IMT – 2011-77	Amini, Hamid	Azimuth Propulsors in Off-design Conditions. Ph.d.Thesis, IMT.
IMT – 2011-78	Nguyen, Tan-Hoi	Toward a System of Real-Time Prediction and Monitoring of Bottom Damage Conditions During Ship Grounding. Ph.d.thesis, IMT.
IMT- 2011-79	Tavakoli, Mohammad T.	Assessment of Oil Spill in Ship Collision and Grounding, Ph.d.thesis, IMT.
IMT- 2011-80	Guo, Bingjie	Numerical and Experimental Investigation of Added Resistance in Waves. Ph.d.Thesis, IMT.
IMT- 2011-81	Chen, Qiaofeng	Ultimate Strength of Aluminium Panels, considering HAZ Effects, IMT
IMT- 2012-82	Kota, Ravikiran S.	Wave Loads on Decks of Offshore Structures in Random Seas, CeSOS.
IMT- 2012-83	Sten, Ronny	Dynamic Simulation of Deep Water Drilling Risers with Heave Compensating System, IMT.
IMT- 2012-84	Berle, Øyvind	Risk and resilience in global maritime supply chains, IMT.
IMT- 2012-85	Fang, Shaoji	Fault Tolerant Position Mooring Control Based on Structural Reliability, CeSOS.

Report No.	Author	Title
IMT- 2012-86	You, Jikun	Numerical studies on wave forces and moored ship motions in intermediate and shallow water, CeSOS.
IMT- 2012-87	Xiang ,Xu	Maneuvering of two interacting ships in waves, CeSOS
IMT- 2012-88	Dong, Wenbin	Time-domain fatigue response and reliability analysis of offshore wind turbines with emphasis on welded tubular joints and gear components, CeSOS
IMT-2012-89	Zhu, Suji	Investigation of Wave-Induced Nonlinear Load Effects in Open Ships considering Hull Girder Vibrations in Bending and Torsion, CeSOS
IMT-2012-90	Zhou, Li	Numerical and Experimental Investigation of Station-keeping in Level Ice, CeSOS
IMT-2012-91	Ushakov, Sergey	Particulate matter emission characteristics from diesel enignes operating on conventional and alternative marine fuels, IMT
IMT-2013-1	Yin, Decao	Experimental and Numerical Analysis of Combined In-line and Cross-flow Vortex Induced Vibrations, CeSOS
IMT-2013-2	Kurniawan, Adi	Modelling and geometry optimisation of wave energy converters, CeSOS
IMT-2013-3	Al Ryati, Nabil	Technical condition indexes doe auxiliary marine diesel engines, IMT
IMT-2013-4	Firoozkoohi, Reza	Experimental, numerical and analytical investigation of the effect of screens on sloshing, CeSOS
IMT-2013-5	Ommani, Babak	Potential-Flow Predictions of a Semi-Displacement Vessel Including Applications to Calm Water Broaching, CeSOS
IMT- 2013-6	Xing, Yihan	Modelling and analysis of the gearbox in a floating spar-type wind turbine, CeSOS
IMT-7-2013	Balland, Océane	Optimization models for reducing air emissions from ships, IMT
IMT-8-2013	Yang, Dan	Transitional wake flow behind an inclined flat plate-----Computation and analysis, IMT
IMT-9-2013	Abdillah, Suyuthi	Prediction of Extreme Loads and Fatigue Damage for a Ship Hull due to Ice Action, IMT
IMT-10-2013	Ramìrez, Pedro Agustìn Pèrez	Ageing management and life extension of technical systems- Concepts and methods applied to oil and gas facilities, IMT
IMT-11-2013	Chuang, Zhenju	Experimental and Numerical Investigation of Speed Loss due to Seakeeping and Maneuvering. IMT

Report No.	Author	Title
IMT-12-2013	Etemaddar, Mahmoud	Load and Response Analysis of Wind Turbines under Atmospheric Icing and Controller System Faults with Emphasis on Spar Type Floating Wind Turbines, IMT
IMT-13-2013	Lindstad, Haakon	Strategies and measures for reducing maritime CO2 emissons, IMT
IMT-14-2013	Haris, Sabril	Damage interaction analysis of ship collisions, IMT
IMT-15-2013	Shainee, Mohamed	Conceptual Design, Numerical and Experimental Investigation of a SPM Cage Concept for Offshore Mariculture, IMT
IMT-16-2013	Gansel, Lars	Flow past porous cylinders and effects of biofouling and fish behavior on the flow in and around Atlantic salmon net cages, IMT
IMT-17-2013	Gaspar, Henrique	Handling Aspects of Complexity in Conceptual Ship Design, IMT
IMT-18-2013	Thys, Maxime	Theoretical and Experimental Investigation of a Free Running Fishing Vessel at Small Frequency of Encounter, CeSOS
IMT-19-2013	Aglen, Ida	VIV in Free Spanning Pipelines, CeSOS
IMT-1-2014	Song, An	Theoretical and experimental studies of wave diffraction and radiation loads on a horizontally submerged perforated plate, CeSOS
IMT-2-2014	Rogne, Øyvind Ygre	Numerical and Experimental Investigation of a Hinged 5-body Wave Energy Converter, CeSOS
IMT-3-2014	Dai, Lijuan	Safe and efficient operation and maintenance of offshore wind farms ,IMT
IMT-4-2014	Bachynski, Erin Elizabeth	Design and Dynamic Analysis of Tension Leg Platform Wind Turbines, CeSOS
IMT-5-2014	Wang, Jingbo	Water Entry of Freefall Wedged – Wedge motions and Cavity Dynamics, CeSOS
IMT-6-2014	Kim, Ekaterina	Experimental and numerical studies related to the coupled behavior of ice mass and steel structures during accidental collisions, IMT
IMT-7-2014	Tan, Xiang	Numerical investigation of ship's continuous- mode icebreaking in leverl ice, CeSOS
IMT-8-2014	Muliawan, Made Jaya	Design and Analysis of Combined Floating Wave and Wind Power Facilities, with Emphasis on Extreme Load Effects of the Mooring System, CeSOS
IMT-9-2014	Jiang, Zhiyu	Long-term response analysis of wind turbines with an emphasis on fault and shutdown conditions, IMT
IMT-10-2014	Dukan, Fredrik	ROV Motion Control Systems, IMT

Report No.	Author	Title
IMT-11-2014	Grimsmo, Nils I.	Dynamic simulations of hydraulic cylinder for heave compensation of deep water drilling risers, IMT
IMT-12-2014	Kvittem, Marit I.	Modelling and response analysis for fatigue design of a semisubmersible wind turbine, CeSOS
IMT-13-2014	Akhtar, Juned	The Effects of Human Fatigue on Risk at Sea, IMT
IMT-14-2014	Syahroni, Nur	Fatigue Assessment of Welded Joints Taking into Account Effects of Residual Stress, IMT
IMT-1-2015	Bøckmann, Eirik	Wave Propulsion of ships, IMT
IMT-2-2015	Wang, Kai	Modelling and dynamic analysis of a semi-submersible floating vertical axis wind turbine, CeSOS
IMT-3-2015	Fredriksen, Arnt Gunvald	A numerical and experimental study of a two-dimensional body with moonpool in waves and current, CeSOS
IMT-4-2015	Jose Patricio Gallardo Canabes	Numerical studies of viscous flow around bluff bodies, IMT
IMT-5-2015	Vegard Longva	Formulation and application of finite element techniques for slender marine structures subjected to contact interactions, IMT
IMT-6-2015	Jacobus De Vaal	Aerodynamic modelling of floating wind turbines, CeSOS
IMT-7-2015	Fachri Nasution	Fatigue Performance of Copper Power Conductors, IMT
IMT-8-2015	Oleh I Karpa	Development of bivariate extreme value distributions for applications in marine technology,CeSOS
IMT-9-2015	Daniel de Almeida Fernandes	An output feedback motion control system for ROVs, AMOS
IMT-10-2015	Bo Zhao	Particle Filter for Fault Diagnosis: Application to Dynamic Positioning Vessel and Underwater Robotics, CeSOS
IMT-11-2015	Wenting Zhu	Impact of emission allocation in maritime transportation, IMT
IMT-12-2015	Amir Rasekhi Nejad	Dynamic Analysis and Design of Gearboxes in Offshore Wind Turbines in a Structural Reliability Perspective, CeSOS

Report No.	Author	Title
IMT-13-2015	Arturo Jesùs Ortega Malca	Dynamic Response of Flexibles Risers due to Unsteady Slug Flow, CeSOS
IMT-14-2015	Dagfinn Husjord	Guidance and decision-support system for safe navigation of ships operating in close proximity, IMT
IMT-15-2015	Anirban Bhattacharyya	Ducted Propellers: Behaviour in Waves and Scale Effects, IMT
IMT-16-2015	Qin Zhang	Image Processing for Ice Parameter Identification in Ice Management, IMT
IMT-1-2016	Vincentius Rumawas	Human Factors in Ship Design and Operation: An Experiential Learning, IMT
IMT-2-2016	Martin Storheim	Structural response in ship-platform and ship-ice collisions, IMT
IMT-3-2016	Mia Abrahamsen Prsic	Numerical Simulations of the Flow around single and Tandem Circular Cylinders Close to a Plane Wall, IMT
IMT-4-2016	Tufan Arslan	Large-eddy simulations of cross-flow around ship sections, IMT
IMT-5-2016	Pierre Yves-Henry	Parametrisation of aquatic vegetation in hydraulic and coastal research,IMT
IMT-6-2016	Lin Li	Dynamic Analysis of the Instalation of Monopiles for Offshore Wind Turbines, CeSOS
IMT-7-2016	Øivind Kåre Kjerstad	Dynamic Positioning of Marine Vessels in Ice, IMT
IMT-8-2016	Xiaopeng Wu	Numerical Analysis of Anchor Handling and Fish Trawling Operations in a Safety Perspective, CeSOS
IMT-9-2016	Zhengshun Cheng	Integrated Dynamic Analysis of Floating Vertical Axis Wind Turbines, CeSOS
IMT-10-2016	Ling Wan	Experimental and Numerical Study of a Combined Offshore Wind and Wave Energy Converter Concept
IMT-11-2016	Wei Chai	Stochastic dynamic analysis and reliability evaluation of the roll motion for ships in random seas, CeSOS
IMT-12-2016	Øyvind Selnes Patricksson	Decision support for conceptual ship design with focus on a changing life cycle and future uncertainty, IMT
IMT-13-2016	Mats Jørgen Thorsen	Time domain analysis of vortex-induced vibrations, IMT

Report No.	Author	Title
IMT-14-2016	Edgar McGuinness	Safety in the Norwegian Fishing Fleet – Analysis and measures for improvement, IMT
IMT-15-2016	Sepideh Jafarzadeh	Energy effiency and emission abatement in the fishing fleet, IMT
IMT-16-2016	Wilson Ivan Guachamin Acero	Assessment of marine operations for offshore wind turbine installation with emphasis on response-based operational limits, IMT
IMT-17-2016	Mauro Candeloro	Tools and Methods for Autonomous Operations on Seabed and Water Coumn using Underwater Vehicles, IMT
IMT-18-2016	Valentin Chabaud	Real-Time Hybrid Model Testing of Floating Wind Tubines, IMT
IMT-1-2017	Mohammad Saud Afzal	Three-dimensional streaming in a sea bed boundary layer
IMT-2-2017	Peng Li	A Theoretical and Experimental Study of Wave-induced Hydroelastic Response of a Circular Floating Collar
IMT-3-2017	Martin Bergström	A simulation-based design method for arctic maritime transport systems
IMT-4-2017	Bhushan Taskar	The effect of waves on marine propellers and propulsion
IMT-5-2017	Mohsen Bardestani	A two-dimensional numerical and experimental study of a floater with net and sinker tube in waves and current
IMT-6-2017	Fatemeh Hoseini Dadmarzi	Direct Numerical Simualtion of turbulent wakes behind different plate configurations
IMT-7-2017	Michel R. Miyazaki	Modeling and control of hybrid marine power plants
IMT-8-2017	Giri Rajasekhar Gunnu	Safety and effiency enhancement of anchor handling operations with particular emphasis on the stability of anchor handling vessels
IMT-9-2017	Kevin Koosup Yum	Transient Performance and Emissions of a Turbocharged Diesel Engine for Marine Power Plants
IMT-10-2017	Zhaolong Yu	Hydrodynamic and structural aspects of ship collisions
IMT-11-2017	Martin Hassel	Risk Analysis and Modelling of Allisions between Passing Vessels and Offshore Installations

Report No.	Author	Title
IMT-12-2017	Astrid H. Brodtkorb	Hybrid Control of Marine Vessels – Dynamic Positioning in Varying Conditions
IMT-13-2017	Kjersti Bruserud	Simultaneous stochastic model of waves and current for prediction of structural design loads
IMT-14-2017	Finn-Idar Grøtta Giske	Long-Term Extreme Response Analysis of Marine Structures Using Inverse Reliability Methods
IMT-15-2017	Stian Skjong	Modeling and Simulation of Maritime Systems and Operations for Virtual Prototyping using co-Simulations
IMT-1-2018	Yingguang Chu	Virtual Prototyping for Marine Crane Design and Operations
IMT-2-2018	Sergey Gavrilin	Validation of ship manoeuvring simulation models
IMT-3-2018	Jeevith Hegde	Tools and methods to manage risk in autonomous subsea inspection,maintenance and repair operations
IMT-4-2018	Ida M. Strand	Sea Loads on Closed Flexible Fish Cages
IMT-5-2018	Erlend Kvinge Jørgensen	Navigation and Control of Underwater Robotic Vehicles
IMT-6-2018	Bård Stovner	Aided Intertial Navigation of Underwater Vehicles
IMT-7-2018	Erlend Liavåg Grotle	Thermodynamic Response Enhanced by Sloshing in Marine LNG Fuel Tanks
IMT-8-2018	Børge Rokseth	Safety and Verification of Advanced Maritime Vessels
IMT-9-2018	Jan Vidar Ulveseter	Advances in Semi-Empirical Time Domain Modelling of Vortex-Induced Vibrations
IMT-10-2018	Chenyu Luan	Design and analysis for a steel braceless semi-submersible hull for supporting a 5-MW horizontal axis wind turbine
IMT-11-2018	Carl Fredrik Rehn	Ship Design under Uncertainty
IMT-12-2018	Øyvind Ødegård	Towards Autonomous Operations and Systems in Marine Archaeology
IMT-13- 2018	Stein Melvær Nornes	Guidance and Control of Marine Robotics for Ocean Mapping and Monitoring

Report No.	Author	Title
IMT-14-2018	Petter Norgren	Autonomous Underwater Vehicles in Arctic Marine Operations: Arctic marine research and ice monitoring
IMT-15-2018	Minjoo Choi	Modular Adaptable Ship Design for Handling Uncertainty in the Future Operating Context
MT-16-2018	Ole Alexander Eidsvik	Dynamics of Remotely Operated Underwater Vehicle Systems
IMT-17-2018	Mahdi Ghane	Fault Diagnosis of Floating Wind Turbine Drivetrain- Methodologies and Applications
IMT-18-2018	Christoph Alexander Thieme	Risk Analysis and Modelling of Autonomous Marine Systems
IMT-19-2018	Yugao Shen	Operational limits for floating-collar fish farms in waves and current, without and with well-boat presence
IMT-20-2018	Tianjiao Dai	Investigations of Shear Interaction and Stresses in Flexible Pipes and Umbilicals
IMT-21-2018	Sigurd Solheim Pettersen	Resilience by Latent Capabilities in Marine Systems
IMT-22-2018	Thomas Sauder	Fidelity of Cyber-physical Empirical Methods. Application to the Active Truncation of Slender Marine Structures
IMT-23-2018	Jan-Tore Horn	Statistical and Modelling Uncertainties in the Design of Offshore Wind Turbines
IMT-24-2018	Anna Swider	Data Mining Methods for the Analysis of Power Systems of Vessels
IMT-1-2019	Zhao He	Hydrodynamic study of a moored fish farming cage with fish influence
IMT-2-2019	Isar Ghamari	Numerical and Experimental Study on the Ship Parametric Roll Resonance and the Effect of Anti-Roll Tank
IMT-3-2019	Håkon Strandenes	Turbulent Flow Simulations at Higher Reynolds Numbers
IMT-4-2019	Siri Mariane Holen	Safety in Norwegian Fish Farming – Concepts and Methods for Improvement
IMT-5-2019	Ping Fu	Reliability Analysis of Wake-Induced Riser Collision
IMT-6-2019	Vladimir Krivopolianskii	Experimental Investigation of Injection and Combustion Processes in Marine Gas Engines using Constant Volume Rig

Report No.	Author	Title
IMT-7-2019	Anna Maria Kozlowska	Hydrodynamic Loads on Marine Propellers Subject to Ventilation and out of Water Condition.
IMT-8-2019	Hans-Martin Heyn	Motion Sensing on Vessels Operating in Sea Ice: A Local Ice Monitoring System for Transit and Stationkeeping Operations under the Influence of Sea Ice
IMT-9-2019|	Stefan Vilsen	Method for Real-Time Hybrid Model Testing of Ocean Structures – Case on Slender Marine Systems
IMT-10-2019	Finn-Christian W. Hanssen	Non-Linear Wave-Body Interaction in Severe Waves
IMT-11-2019	Trygve Fossum	Adaptive Sampling for Marine Robotics
IMT-12-2019	Jørgen Bremnes Nielsen	Modeling and Simulation for Design Evaluation
IMT-13-2019	Yuna Zhao	Numerical modelling and dyncamic analysis of offshore wind turbine blade installation

Doctoral theses at NTNU, 2019:190

Yuna Zhao

Numerical Modeling and Dynamic Analysis of Offshore Wind Turbine Blade Installation

Doctoral Thesis

Yuna Zhao

Doctoral theses at NTNU, 2019:190

NTNU
Norwegian University of Science and Technology
Faculty of Engineering
Department of Marine Technology

ISBN 978-82-326-3976-2 (printed version)
ISBN 978-82-326-3977-9 (electronic version)
ISSN 1503-8181

NTNU
Norwegian University of Science and Technology

NTNU

NTNU
Norwegian University of Science and Technology